2021

Mechanisms Of Early Arterial Stiffening And Reduced Smooth Muscle Contractility In The Premature Aging Disease Hutchinson-Gilford Progeria Syndrome

Ryan Von Kleeck
University of Pennsylvania

Mechanisms Of Early Arterial Stiffening And Reduced Smooth Muscle Contractility In The Premature Aging Disease Hutchinson-Gilford Progeria Syndrome

Abstract

Hutchinson-Gilford Progeria syndrome (HGPS) is a rare premature aging disease in which children present with a rapid onset of clinical characteristics of aging. Ultimately, HGPS children die in their teen years due to severe cardiovascular disease leading to heart attack and stroke. Despite discovering the mutation resulting in HGPS, a single nucleotide point mutation in the Lamin A gene, how this mutated form of Lamin A, termed progerin, results in such severe cardiovascular pathology is not well understood. Although HGPS children do not have altered blood lipid profiles, they present with increased arterial stiffness, a cholesterol-independent risk factor for cardiovascular disease that is also increased in the normal aging population. Toward the end of their lifespan, the arteries of HGPS patients display a dramatic loss of smooth muscle cells (SMCs) and a highly collagenous, fibrotic environment. However, the initial driving factors of arterial stiffening and the decline in smooth muscle cell function are not well characterized. In this work, I use the LMNAG609G/G609G mouse model (hereafter referred to as HGPS mice), which harbors the equivalent mutation to that seen in the human disease, to study causal factors initiating arterial stiffening and SMC decline in young mice. I found that the onset of arterial stiffening in HGPS mice highly correlates with an increase in the collagen cross linking enzyme Lysyl Oxidase (LOX), and pharmacologic inhibition of LOX in vivo corrected arterial stiffening and heart defects, such as diastolic dysfunction, present in HGPS mice. Interestingly, I found that normally aged mouse arteries also present with arterial stiffening and increased LOX abundance, although distinct from that seen in HGPS. Furthermore, I found that SMC function declines well before the loss of SMCs from HGPS mouse arteries, as young HGPS mice presented with decreased arterial contractility at an early age. I correlated this decrease in arterial contractility with a reduction in smooth muscle myosin heavy chain (SM-MHC), and restoration of SM-MHC corrected the decreased force generation exhibited by isolated HGPS SMCs. Consistent with observations in HGPS mice, aged mouse arteries also presented with decreased contractility and SM-MHC, although whether the mechanisms are similar or distinct from that of HGPS requires further study. Overall, these studies demonstrate that arterial stiffening and decline in SMC function occur at a very early age in HGPS and replicate many of the phenotypes seen in normal aged arteries. Insight from this study provides new understanding of the early driving factors of arterial stiffening and decline in SMC function and sheds light on potential therapeutic approaches to reduce the burden of cardiovascular disease in HGPS.

Degree Type

Dissertation

Degree Name

Doctor of Philosophy (PhD)

Graduate Group

Pharmacology

First Advisor

Richard K. Assoian

Keywords

Arterial contractility, Arterial Stiffening, Cardiovascular, Progeria, Rare disease

MECHANISMS OF EARLY ARTERIAL STIFFENING AND REDUCED SMOOTH MUSCLE CONTRACTILITY IN THE PREMATURE AGING DISEASE HUTCHINSON-GILFORD PROGERIA SYNDROME

Ryan von Kleeck

A DISSERTATION

in

Pharmacology

Presented to the Faculties of the University of Pennsylvania

in

Partial Fulfillment of the Requirements for the

Degree of Doctor of Philosophy

2021

Supervisor of Dissertation	**Graduate Group Chairperson**
_____	_____
Richard Assoian	**Julie Blendy**
Professor of Pharmacology	Professor of Pharmacology

Dissertation Committee

Rebecca Wells, Professor of Medicine, Perelman School of Medicine
Tilo Grosser, Research Associate Professor of Pharmacology, Perelman School of Medicine
Robert Mauck, Professor for Education and Research in Orthopaedic Surgery, Perelman School of Medicine
Zoltan Arany, Professor of Cardiology, Perelman School of Medicine

ABSTRACT

MECHANISMS OF EARLY ARTERIAL STIFFENING AND REDUCED SMOOTH MUSCLE CONTRACTILITY IN THE PREMATURE AGING DISEASE HUTCHINSON-GILFORD PROGERIA SYNDROME

Ryan von Kleeck

Richard Assoian

Hutchinson-Gilford Progeria syndrome (HGPS) is a rare premature aging disease in which children present with a rapid onset of clinical characteristics of aging. Ultimately, HGPS children die in their teen years due to severe cardiovascular disease leading to heart attack and stroke. Despite discovering the mutation resulting in HGPS, a single nucleotide point mutation in the Lamin A gene, how this mutated form of Lamin A, termed progerin, results in such severe cardiovascular pathology is not well understood. Although HGPS children do not have altered blood lipid profiles, they present with increased arterial stiffness, a cholesterol-independent risk factor for cardiovascular disease that is also increased in the normal aging population. Toward the end of their lifespan, the arteries of HGPS patients display a dramatic loss of smooth muscle cells (SMCs) and a highly collagenous, fibrotic environment. However, the initial driving factors of arterial stiffening and the decline in smooth muscle cell function are not well characterized.

In this work, I use the $LMNA^{G609G/G609G}$ mouse model (hereafter referred to as HGPS mice), which harbors the equivalent mutation to that seen in the human disease, to study causal factors initiating arterial stiffening and SMC decline in young mice. I

found that the onset of arterial stiffening in HGPS mice highly correlates with an increase in the collagen cross linking enzyme Lysyl Oxidase (LOX), and pharmacologic inhibition of LOX *in vivo* corrected arterial stiffening and heart defects, such as diastolic dysfunction, present in HGPS mice. Interestingly, I found that normally aged mouse arteries also present with arterial stiffening and increased LOX abundance, although distinct from that seen in HGPS.

Furthermore, I found that SMC function declines well before the loss of SMCs from HGPS mouse arteries, as young HGPS mice presented with decreased arterial contractility at an early age. I correlated this decrease in arterial contractility with a reduction in smooth muscle myosin heavy chain (SM-MHC), and restoration of SM-MHC corrected the decreased force generation exhibited by isolated HGPS SMCs. Consistent with observations in HGPS mice, aged mouse arteries also presented with decreased contractility and SM-MHC, although whether the mechanisms are similar or distinct from that of HGPS requires further study.

Overall, these studies demonstrate that arterial stiffening and decline in SMC function occur at a very early age in HGPS and replicate many of the phenotypes seen in normal aged arteries. Insight from this study provides new understanding of the early driving factors of arterial stiffening and decline in SMC function and sheds light on potential therapeutic approaches to reduce the burden of cardiovascular disease in HGPS.

TABLE OF CONTENTS

LIST OF TABLES

LIST OF ILLUSTRATIONS

Chapter 1: Introduction

1.1 Hutchinson-Gilford Progeria Syndrome (HGPS): mutation, consequences, and therapies

1.1a History and identification of HGPS

Hutchinson-Gilford Progeria Syndrome (HGPS) was a disease first discovered by Dr. Jonathan Hutchinson in 1886 and later reported by Dr. Hastings Gilford in 1897 in England (Hutchinson 1886). It was first diagnosed when Dr. Hutchinson noticed a boy who had loss of hair and atrophic condition of the skin and appendages. Dr. Hutchinson noted the boy as having a generally aged appearance with a short stature and “pinched facial features” (Kashyap et al. 2014; Hutchinson 1886; McKusick 2005). This rare disease soon became commonly referred to as a disease of premature aging, with the name Progeria derived from Greek meaning “prematurely old.” Intriguingly, although these patients displayed severe growth defects, cognitive function remained intact (Saxena & Kumar 2020). Interest and widespread knowledge of the disease became prevalent after the birth of Sam Berns, the son of two medical doctors, who was diagnosed with Progeria. Sam soon became a public figure and icon of Progeria, giving TedX talks and participating in an HBO documentary about the disease to spread awareness. Sam’s parents, Dr. Scott Berns and Dr. Leslie Gordon, devoted their work to understanding the disease, later establishing the Progeria Research Foundation. This

disease is now called Hutchinson-Guilford Progeria Syndrome (HGPS) to distinguish it from other forms of premature aging.

HGPS is classified as an ultra-rare genetic disease, affecting around 1 in 4 to 8 million births (Sinha et al. 2014). There is no predisposition to HGPS and it has been shown to affect all genders and ethnicities (Sinha et al. 2014). In 2003, the genetic basis of HGPS was discovered to be a single nucleotide point mutation in the LMNA gene (Lamin A) (Goldman et al. 2004; Eriksson et al. 2003; De Sandre-Giovannoli et al. 2003). The median age for diagnosis of children with HGPS is around 3 years of age (Hennekam 2006), and currently genetic testing (c.1824C>T in the LMNA gene) is used to confirm diagnosis (Gordon et al. 2003; Saxena & Kumar 2020). Children diagnosed generally present with alopecia, prominent scalp veins, and low bone density. Histopathology is generally conducted on the skin and reveals abnormal nuclear morphology (Gordon et al. 2003; Saxena & Kumar 2020).

The mutation causing nearly all cases of HGPS had been identified as a de novo single nucleotide 1824C>T substitution in exon 11 of the LMNA gene (chromosome 1q21.2-q21.3) (De Sandre-Giovannoli et al. 2003; Eriksson et al. 2003; Goldman et al. 2004). Although this single nucleotide substitution does not result in a change in amino acid (LMNAG608G), it creates a cryptic splice site toward the end of exon 11 of LMNA. This abnormal splicing event leads to the deletion of 150 nucleotides, and subsequent deletion of 50 amino acids, from exon 11 near the C-terminal end of pre-Lamin A (Saxena & Kumar 2020). These 50 amino acids are critical for the recognition by ZMPSTE24 endoprotease, which normally cleaves 14 amino acids and a farnesyl and carboxymethyl group off the C-terminus of pre-Lamin A to generate mature Lamin A protein. This mutated form of Lamin A in HGPS, termed progerin, retains the C-terminal

farnesyl and carboxymethylated CAAX motif that would normally be cleaved off during natural processing by ZMPSTE24 (Fig. 1.01) (Hamczyk et al. 2018). The retention of this farnesyl group causes progerin to accumulate on the nucleoplasmic side of the inner nuclear membrane and progerin is unable to form a proper nuclear lamina network (Saxena & Kumar 2020). The aberrant splicing of LMNA seen in HGPS also occurs at very small levels in natural aging in skin fibroblasts and in the arterial wall leading to accumulation of progerin with age in healthy individuals (Scaffidi & Misteli 2006; Olive et al. 2010). This has brought a lot of attention toward Progeria, as it may share commonalities and a mechanistic relation with normal aging, though the very low amount of progerin in normal aging confounds this simple idea.

Much work has been done in evaluating whether the toxicity of progerin originates from the loss of 50 amino acids or from the retention of the farnesyl and carboxyl moieties. Evidence for the hypothesis that the major driver of progerin toxicity comes from its farnesylation can be seen from other atypical progeria syndromes such as restrictive dermopathy, where patients present with specific mutations to ZMPSTE24 – the protease important for the cleavage of the farnesyl group from LMNA (Mazereeuw-Hautier et al. 2007; Yang et al. 2005; Navarro et al. 2005; Navarro et al. 2004). These patients present with even more severe progeria-like symptoms, dying in the first week of life. Indeed, ZMPSTE24-deficient mice also present with many common characteristics of HGPS (Fong et al. 2004). In addition, mouse models such as the LMNA-nHG transgenic mouse have been generated that replicate the loss of 150 nucleotides from exon 11 of *LMNA* typically seen in HGPS but have modified the CAAX farnesylation motif into SAAX or CAX (Yang et al. 2008; Yang et al. 2011). This mouse model produces unfarnesylated progerin protein (that still has the 50 amino acid

deletion) and shows a less severe HGPS phenotype, highlighting the toxicity of the farnesyl group.

One of the major functions of the nuclear lamina is to serve as a scaffold to structurally support the nucleus. The improper lamina network formed by progerin accumulation has been shown to cause a stiffer and thicker nuclear lamina, which leaves the nucleus brittle and more susceptible to mechanical damage (Verstraeten et al. 2008). This altered lamina network is also associated with the characteristic nuclear blebbing phenotype seen in HGPS (Dahl et al. 2006; Verstraeten et al. 2008; Goldman et al. 2004). In addition to structural support, it has become appreciated that the nuclear lamina plays an important role in chromatin organization and signaling pathways. The nuclear lamina binds heterochromatin, and loss of peripheral heterochromatin (Gesson et al. 2016) and dramatic chromatin remodeling have been reported in HGPS nuclei (Shumaker et al. 2006; Pegoraro et al. 2009). Nuclei with progerin accumulation also display altered nuclear pore complex organization and changes in nuclear import and export (Kelley et al. 2011; García-Aguirre et al. 2019) in addition to increased DNA damage as visualized through γHAX staining (Gonzalo et al. 2016; Liu et al. 2005).

1.1b Systemic consequences of Progerin expression

One of the major phenomena of HGPS is the severe growth retardation and loss of hair in HGPS children. Clinical symptoms begin manifesting themselves around 1-2 years of age, as it is hypothesized that is when many cell types begin terminal differentiation and commence increased expression of Lamin A (Merideth et al. 2008; Saxena & Kumar 2020). Cognitive abilities of HGPS patients remain rather unaffected,

likely due to the low expression levels of Lamin A in the brain due to the presence of microRNA-9 in neural cells (Nissan et al. 2012).

Additional abnormalities present in HGPS children include loss of subcutaneous fat, reduced hearing, altered dentition, increased platelet number, absence of puberty, extra-skeletal calcification, stiff joints, angina, and hip dislocation (Domingo et al. 2009; Kieran et al. 2007; Gordon et al. 2019; Guardiani et al. 2011; Monnerat et al. 2019; Merideth et al. 2008; Rork et al. 2014; Ullrich & Gordon 2015). However, the major complication leading to death at a mean age of 14.5 years is the onset of cardiovascular disease leading to heart attack or stroke. Children present with severe atherosclerosis of coronary and cerebrovascular arteries (Merideth et al. 2008). Moreover, these progeria children do not present with common risk factors for cardiovascular disease such as hyperlipidemia or diabetes. HGPS patients present with low high-density lipoprotein levels, but normal low-density lipoprotein and cholesterol levels (Szamosi et al. 1984; Gordon et al. 2005). These findings suggest that progerin plays a pathogenic role in promoting cardiovascular disease independent of dyslipidemia.

As mentioned, the main cause of death in HGPS children is complications arising from severe atherosclerosis (Merideth et al. 2008; Saxena & Kumar 2020). Arterial stenosis can affect HGPS children of all ages and has been used as an early indicator of plaque formation and noninvasive imaging has been used to detect carotid plaques at late stages in HGPS children (Gerhard-Herman et al. 2011; Merideth et al. 2008). In addition, severe vascular smooth muscle cell (SMC) loss is also observed in HGPS arteries, with late-stage patients presenting with little to no SMCs present and a highly fibrotic arterial environment (Gerhard-Herman et al. 2011; Olive et al. 2010). Vascular

calcification has also been observed in HGPS arteries along with adventitial thickening and fibrosis (Villa-Bellosta et al. 2013; Ullrich & Gordon 2015).

Heart abnormalities are also present in HGPS patients (Prakash et al. 2018). In a clinical study evaluating heart function through echocardiography, HGPS patients presented with increased left ventricular hypertrophy and left ventricular diastolic dysfunction. Calcification of the mitral and aortic valves was also observed and lead to stenosis and regurgitation, especially as children became older (Prakash et al. 2018).

Additionally, HGPS children present with arterial vessel stiffening (Olive et al. 2010; Gerhard-Herman et al. 2011)**.** Intriguingly, arterial stiffening is also seen in the normal aging population (Mitchell et al. 2010). Clinical studies evaluating arterial stiffness through pulse-wave velocity measurements have shown that the vascular stiffening in HGPS children is similar to adults of 60 years or older (Gerhard-Herman et al. 2011). The arterial stiffening in these children has attracted a lot of attention from the research community because arterial stiffening remains one of the most prominent cholesterol-independent risk factors for cardiovascular disease (Mitchell et al. 2010), and understanding the rapid stiffening process in HGPS may uncover molecular mechanisms responsible for arterial stiffening in normal aging. Many of the cardiovascular abnormalities in HGPS are also present in the normal aging population. Table 1, modified from a review by from Hamczyk (2018), evaluates the common cardiovascular characteristics between normal aging and HGPS (Hamczyk, del Campo, et al. 2018).

1.1c Current cell and animal models to study HGPS

Cell models

As HGPS is such a rare disease, many animal and cell models have been created to study the disease and develop therapies. Currently, over 200 cell lines are available from the Progeria Research Foundation tissue bank (Gordon 2019). The majority of cell studies use HGPS patient fibroblasts and induced pluripotent stem cells (iPSCs) in order to study cell behavior in vitro. These cells recapitulate many of the clinical observations seen in HGPS patients including nuclear blebbing, increased cellular senescence, altered nuclear trafficking and export, altered epigenetic markers, increased DNA double-stranded breaks, and altered signaling pathways (Saxena & Kumar 2020). Potential therapies that have been used on cell models include farnesyl transferase inhibitors, to block the toxic farnesylation of progerin; all-trans-retinoic acid, to reduced LMNA transcription; and mTOR inhibitors, to promote autophagy and clearance of progerin protein (Pellegrini et al. 2015; Capell et al. 2005; Capell et al. 2008; Cao et al. 2011; Cenni et al. 2011; DuBose et al. 2018; Gabriel et al. 2016). However, one disadvantage to cell models is that they lack critical information needed to carry over to the clinic such as the pharmacodynamics of a drug and additional toxicity to other organs and body systems. They also lack the ability to study progerin's effect on an entire organ system. Thus, many animal models have been generated to study HGPS and evaluate potential therapeutic options.

ZMPSTE24-null mouse model

The first preclinical mouse model for HGPS was a ZMPSTE24-null mouse generated in 2002 (Pendás et al. 2002; Bergo et al. 2002). This model knocked out the protease essential for cleaving the C-terminal end of Lamin-A, thus leading to the accumulation of farnesylated pre-Lamin A. Although it shared many similar phenotypes with HGPS children such as slow growth, lipodystrophy, low body weight, cardiac dysfunction, and

premature death (Mayoral et al. 2018), it lacks the equivalent mutation seen in human HGPS patients, as progerin harbors an additional 50 amino acid deletion in comparison to pre-Lamin A.

LmnaHG mouse model

The LmnaHG mouse model was generated, which has intron 10 and 11 as well as the last 150 nucleotides of exon 11 deleted (Yang et al. 2005). This mouse produces progerin protein, but not through the creation of a cryptic splice site as seen in the human disease. The deletion of introns 10 and 11 also abolish Lamin C synthesis, which is normally present in HGPS. However, this model also phenocopies many of the symptoms of HGPS (Yang et al. 2005; Mayoral et al. 2018; Yang et al. 2006).

BAC G608G mouse model

An additional mouse model termed the BAC G608G mouse was developed by Varga et al. in 2006 and contains the mutant LMNAG608G (as found in HGPS patients) as a transgene in a human bacterial artificial chromosome (Varga et al. 2006). These mice especially model the arterial defects seen in the human disease, showing progressive loss of medial SMCs, arterial calcification, adventitial thickening, and increased extracellular matrix (ECM) deposition. However, these mice did not recapitulate many clinical symptoms of progeria aside from defects in the cardiovascular system.

LMNA G609G mouse model and characterization

In 2011, Osorio et al. developed a transgenic mouse model harboring the equivalent mutation to the human HGPS syndrome in the mouse genome (c.1827C>T; p.G609G), termed the $LMNA^{G609G}$ model (Osorio et al. 2011). These mice mirrored many of the features of the human disease, including depletion of SMCs and cardiovascular and heart defects (Osorio et al. 2011). It was found that the homozygous $LMNA^{G609G/G609G}$

mice (hereafter referred to as HGPS mice), presented with swift onset of the progeroid symptoms and displayed premature death with a median survival of around 100 days. The HGPS mice displayed progressive weight loss, with a plateau in weight starting as early as 5 weeks of age and slowly declining until death (Osorio et al. 2011). The heterozygous $LMNA^{+/G609G}$ mice displayed a delayed onset of progeroid symptoms, but still displayed premature death at approximately 240 days (Osorio et al. 2011). Because it effectively models the same point mutation and reproduces the exact molecular situation that occurs at the LMNA locus seen in the human syndrome, the $LMNA^{G609G}$ mouse model has become a widely used animal model in the field of HGPS.

Many groups in addition to Osorio et al. have characterized the $LMNA^{G609G}$ mouse model. Like the human syndrome, the mice showed loss of the subcutaneous fat layer, an increase in senescence associated β-galactosidase staining, and thinning and loss of fur toward the end of their lifespan (Zaghini et al. 2020). The $LMNA^{G609G}$ mice displayed reduced bone density and alterations in the bone structure of their skull. The mutant mice displayed a loss of SMCs, specifically in the aortic arch. Although cause of death is unclear in $LMNA^{G609G}$ mice, Zaghini et al. (2020) propose that it is likely a result of cardiovascular abnormalities in addition to malnutrition (Zaghini et al. 2020).

Osmanagic-Myers (2018) found extensive myocardial and perivascular fibrosis when characterizing cardiovascular defects in mice selectively expressing the $LMNA^{G609G}$ mutation in endothelial cells driven by the endothelium-specific *Cdh5* promoter (Osmanagic-Myers et al. 2018). Although these mice did not present with SMC loss, which is a hallmark of the human syndrome, they did present with left ventricular hypertrophy and significant diastolic dysfunction. This study suggested that the potent effect progerin has on the SMC population is due to intrinsic expression of

progerin in the SMC population and not caused by a dysfunctional endothelium. However, endothelial-specific progerin expression was enough to induce cardiac fibrosis with enhanced levels of Col3a1 transcript present in the heart (Osmanagic-Myers et al. 2018). The enhanced col3a1 expression was likely due to endothelial cells signaling other cell types to increase collagen production, as the endothelial cells themselves did not have increased col3a1 expression. However, since endothelial specific progerin expression still led to left ventricular hypertrophy and diastolic dysfunction, endothelial dysfunction may be responsible for a portion of the cardiac abnormalities in HGPS. This study linked the profibrotic response of progerin-expressing endothelial cells to a defect in nitric oxide signaling due to reduced nitric oxide synthase 3 (NOS3) levels, as nitric oxide (NO) generally acts in a paracrine manner to cause an antifibrotic effect on surrounding tissues (Osmanagic-Myers et al. 2018).

Work from the laboratory of Dr. Vicente Andres has further characterized the effect of progerin expression on cardiovascular abnormalities in HGPS mice. Hamczyk et al. (2018) used $LMNA^{G609G}$ mice crossed with ApoE-null mice to evaluate the formation of atherosclerotic lesions due to progerin expression. They found that $LMNA^{G609G}$/Apoe-null mice which were fed a high fat diet developed more severe atherosclerotic lesions in comparison Apoe-null mice. Furthermore, they discovered that these findings were replicated even when restricting progerin expression solely to the SMCs, indicating that SMC progerin expression is critical for the generation of severe atherosclerotic lesions seen in HGPS (Hamczyk, Villa-Bellosta, et al. 2018).

In addition, work from del Campo et al. (2019) and Murtada et al. (2020) revealed that older $LMNA^{G609G}$ mice displayed increased aortic stiffness between 13-15 weeks of age (toward the end of their lifespan). Mice expressing progerin selectively in endothelial

cells did not present with increased aortic stiffness (del Campo et al. 2019). However, restricting progerin expression to SMCs was able to reproduce this increase in aortic stiffness, suggesting that arterial stiffening in HGPS is a consequence of altered vascular SMC function. Furthermore, treatment of aortas with collagenase prevented stiffening of G609G aortas, whereas treatment with elastase or mycalolide B had no effect on vessel stiffness, indicating that altered collagen is likely the cause of increased arterial stiffness rather than elastin abnormalities or cytoskeletal integrity (del Campo et al. 2019). This idea was substantiated by the observed increased levels of collagens III, IV, V and XII present through arterial staining. In addition, recent work by del Campo et al. (2020) showed that SMC-specific progerin expression also results in decreased arterial contraction and relaxation in response to vasoconstrictors and vasodilators, whereas endothelial specific progerin expression had no effect on vessel contractility (del Campo et al. 2020). It is important to note that these studies have evaluated HGPS mice at a very late stage in their lifespan, when there has been significant reported loss of SMCs (Murtada et al. 2020; Osorio et al. 2011). Thus, findings of increased arterial stiffness and decreased arterial contractility at this late timepoint may be confounded by the loss of SMCs from HGPS mice. In conclusion, although it is likely a combinatorial effect of progerin expression in the endothelium as well as the smooth muscle cell layer that presents HGPS children with such a high risk of cardiovascular disease, the SMC population is critical in causing increased arterial stiffening and reduced contractility in HGPS.

1.1d Current therapeutic options to treat HGPS

Currently, the major approved treatment for HGPS consists of the administration of farnesyl transferase inhibitors (FTIs). FTIs that were originally used for the treatment of cancer have proven effective in HGPS patients and animal models (Toth et al. 2005; Capell et al. 2005; Capell et al. 2008; Yang et al. 2006; Yang et al. 2005; Glynn & Glover 2005; Pacheco et al. 2014). FTIs work through binding to the farnesytransferase enzyme at the CAAX-binding domain, preventing the enzyme from recognizing the CAAX motif and inhibiting farnesylation of the protein. It is believed that the de-farnesylated form of progerin is then targeted for degradation (Columbaro et al. 2005). In a clinical study following children treated with FTI Lonafarnib (Gordon et al. 2018), it was found that Lonafarnib significantly lowered mortality during a 2.2-year study. Initial trials with Lonafarnib also showed reduced arterial stiffening as measured by pulse wave velocity and carotid artery wall echo density. One of the limitations of FTI therapy is that in place of farnesylation, prelamin A can still undergo prenylation with the addition of geranylgeranyl groups. In this case, combination treatment with statins is effective because statins reduce geranylgeranylation (Varela et al. 2008).

Additional therapies currently undergoing clinical trials include mTOR inhibitors, including the rapamycin analog everolimus. These mTOR inhibitors increase autophagic clearance of progerin (Cao et al. 2011; DuBose et al. 2018; Gabriel et al. 2016). Combinatorial therapies of lonafarnib and everoliumus correct altered genome organization and DNA damage in an HGPS fibroblast model (Bikkul et al. 2018) and are currently undergoing clinical trials.

Lastly, attempts at genome editing using CRISPR-cas9 have also been promising in reducing the effects of progerin in mouse models (Beyret et al. 2019; Santiago-Fernández et al. 2019). Adenoviral delivery of a CRISPR-cas9 vector targeting

progerin was shown to reduce both progerin and Lamin A levels and prolong lifespan of $LMNA^{G609G}$ HGPS mice. However, some of the current downsides to this treatment are potential off-target effects that may cause mutations at undesired sites in the genome as well as the efficacy and distribution of the CRISPR-cas9 vector throughout the body. Currently, technology is not sufficient for a large portion of cells within a tissue to receive and incorporate the viral genome. An exciting new technology of base editing has also been applied to HGPS mouse models to correct the C>T mutation at the Lamin A locus. A single injection containing the base-editing technology packaged in an adeno-associated virus corrected the pathogenic mutation by 20-60% in various tissues, greatly extended lifespan, and corrected the vascular pathology in an HGPS mouse model (Koblan et al. 2021).

1.2 Arterial stiffening and mechanical properties of the ECM

1.2a Changes in artery structure in aging and disease

The arterial wall is composed of three major layers (Fig. 1.02). The lumen of the vessel is primarily composed of endothelial cells. These endothelial cells sit anchored on a basement membrane which is majorly composed of laminin and collagen proteins synthesized from the endothelial cells, but over 20 additional basement-matrix proteins have been identified in arteries (Xu & Shi 2014). An inner elastic lamina composed of elastin fibers separates the endothelial layer from the smooth muscle cell layer. This

layer of SMCs, or media layer, is highly rich in collagen and elastin fibers. In addition, an abundance of microfibrils, proteoglycans, and glycoproteins are also synthesized by the SMCs residing in this layer. The outer layer of the artery, or adventitia layer, is separated from the media by an external elastic lamina (Wagenseil & Mecham 2009; Xu & Shi 2014). This exterior layer of connective tissue is primarily synthesized by resident (adventitial) fibroblasts and consists mainly of fibrillar collagens, proteoglycans, and fibronectin among many other ECM proteins. It is important to note that the ECM in the vessel wall is constantly undergoing change and remodeling in response to stimuli such as pressure and flow, and these changes can affect the mechanics of arteries and signaling to cells over time (Wagenseil & Mecham 2009; Xu & Shi 2014).

Mechanisms of arterial stiffening have been well-studied in the normal aging population. The composition of the ECM plays a critical role in arterial stiffness (Cox & Erler 2011). The stiffness of the major arteries relies on a balance of elastin and collagen fibers (Humphrey et al. 2014; Wagenseil & Mecham 2012) to maintain a proper response to blood pressure. Elastin allows for recoil at lower load and dampens cyclic loading from the beating heart while fibrillar collagens contribute to the strain-stiffening property of arteries at high load (Kohn et al. 2015). Arteries express three main fibrillar collagens, with collagen-I>collagen-III>collagen-V in abundance (Hulmes 2008; Prockop & Kivirikko 1995). Increased collagen deposition as well as elastin fragmentation has been observed in the arteries of HGPS children at autopsy (Olive et al. 2010; Gerhard-Herman et al. 2011; Merideth et al. 2008) and in aged arteries (Kohn et al. 2015; Tsamis et al. 2013).

In addition to increases in fibrillar collagens, the mechanical properties of tissues are further regulated by matrix remodeling enzymes (Freitas-Rodríguez et al. 2017;

Lampi & Reinhart-King 2018), and especially Lysyl Oxidase (LOX) and its family members (LOXL1, LOXL2, LOXL3 and LOXL4) (Yamauchi & Sricholpech 2012; Nilsson et al. 2016; Steppan et al. 2019). These enzymes covalently cross-link newly synthesized collagen and elastin fibers to enhance their tensile strength (Tsamis et al. 2013; Baker et al. 2013; Herchenhan et al. 2015), and their overexpression is commonly seen in stiffness-related pathologies (Desmoulière et al. 1997; Kagan 1994). However, since elastin biosynthesis ends early in life (Tsamis et al. 2013; Wagenseil & Mecham 2012; Davidson et al. 1986; Mithieux & Weiss 2005; Kelleher et al. 2004), LOX-mediated crosslinking is thought to target newly synthesized collagens in normal aging. While increased collagens and matrix modifying enzymes such as LOX can promote pathology through increasing arterial stiffness, it is important to note that decreases in these proteins can also cause arterial pathologies. For example, degradation of elastin and reduction in collagen cross-linking promote the formation of aortic aneurysms (Xu & Shi 2014). Thus, the arterial wall relies on a delicate balance of ECM proteins to maintain an appropriate stiffness to properly handle the mechanical load from the heart, and changes to arterial stiffness in either direction can have drastic consequences.

Ultimately, changes in stiffness of the arteries can cause downstream effects on the heart and increased pressure on the arterial network. Increased arterial stiffening can lead to increased afterload on the heart which has been linked to left ventricular hypertrophy and ventricular stiffening, conditions commonly observed in HGPS (Mottram et al. 2005; Kim et al. 2017; Prakash et al. 2018). As the left ventricle wall remodels to become thicker, its capacity for blood decreases in comparison to a healthy ventricle. This results in a decreased stroke volume and less blood supplied to the body, ultimately leading to heart failure. In addition, prior evidence from our lab supports the idea that

increased arterial stiffness may promote atherosclerosis by increasing macrophage binding to endothelial cells, as macrophages preferentially adhere to stiffer surfaces (Kothapalli et al. 2012). Because arterial stiffness is correlated with many of the additional negative cardiovascular outcomes seen in HGPS, it offers a very promising point of study and therapeutic intervention.

1.2b Collagens, crosslinking, and lysyl oxidase

Collagens are the most abundant proteins in mammals, comprising around 30% of total protein mass (Ricard-Blum 2011). The most abundant class of collagens expressed in the body are the type-1 fibrillar collagens. However, there are currently 28 members of the collagen family, and each collagen type can have multiple alpha chains (i.e. Col1a1, Col1a2) (Ricard-Blum 2011). At their core, all collagens possess the common structural feature of a triple helix domain, a combination of three alpha chains. These triple helix domains are generally composed of Gly-X-Y repeats and depending on the type of collagen can be rather flexible if there are imperfections or short interruptions in these repeats (Bella et al. 2006; Khoshnoodi et al. 2008; Ricard-Blum 2011). Fibril forming collagens, such as Collagens-I, III, and V have one large triple helix domain, and play a structural role, where they contribute to tissue shape and mechanical properties (Ricard-Blum 2011). Fibril-associated collagens with interrupted triple-helices (FACIT) such as collagens IX, XII, and XIV have multiple triple helices (Shaw & Olsen 1991). In addition, non-fibrillar network-forming collagens such as collagen-IV can form stable basement membranes for cells and serve as anchors for the binding of other collagen molecules (Ricard-Blum 2011).

Fibrillar collagens are synthesized as a procollagen peptide and secreted into the extracellular space (Gelse et al. 2003). Then, the N- and C- terminal propeptides are cleaved by BMP-1/Tolloid like proteinases, leaving the collagen molecule with N- and C-terminal telopeptides. The fibrillar collagen molecules then self-assemble into fibrils and can be stabilized through covalent crosslinks between lysine residues in the telopeptide regions between collagen molecules (Yamauchi & Sricholpech 2012). Covalent crosslinks of collagens include oxidative deamination of lysines by the Lysyl Oxidase enzyme family, disulfide bonds, and the N^{ε}(γ-glutamyl)lysine isopeptide catalyzed by the transglutaminase-2 enzyme (Ricard-Blum 2011).

Collagens can be degraded by several types of proteases among which is the matrix metalloproteinase family of enzymes (MMPs). MMPs are zinc-dependent endopeptidases that normally are responsible for physiological tissue repair processes but also play a role in tumorigenesis and metastasis. The fibrillar collagens are generally cleaved by MMP-1 and MMP-8 at specific MMP cleavage sites (Ricard-Blum 2011; Klein & Bischoff 2011).

One of the major enzymes responsible for the lysine crosslinking of the telopeptides of collagens are of the Lysyl Oxidase (LOX) family of enzymes, consisting of 5 family members including LOX, and four LOX-Like proteins, LOXL 1-4 (Mäki 2009; Eyre & Wu 2005; Trackman 2016). Collagen-1 contains two possible lysines available for crosslinking in the C-terminal telopeptide and three in the N-terminal. LOX works by performing an oxidative deamination reaction to convert the amino group in the lysine residue into a more reactive aldehyde moiety. This lysine-aldehyde can then condense with lysine or hydroxylysine residues from telopeptides of other collagen molecules (Yamauchi & Sricholpech 2012; Lucero & Kagan 2006). This covalent modification

between collagen molecules stabilizes the collagen and increased cross-linking is observed in many stiffness-related pathologies (Fig. 1.03).

LOX works extracellularly on newly synthesized collagens and itself is secreted as a pro-LOX protein. Like pro-collagens, pro-LOX must also be cleaved by BMP-1/Tolloid-like proteinases, thus providing a mechanism by which BMP1 catalytically activates LOX in addition to preparing its collagen substrate (Yamauchi & Sricholpech 2012). LOX also requires a copper ion and cofactor LTQ (Lysine tyrosylquinone) to oxidize its lysine substrate. Beta-aminopropionitrile (BAPN) is a well-known inhibitor of LOX isoforms, acting in an irreversible manner through the formation of a dead-end complex with essential cofactor LTQ (Yamauchi & Sricholpech 2012). BAPN can inhibit all LOX isoforms (Nilsson et al. 2016). Although BAPN is a highly effective inhibitor in vitro, the compound can be oxidized by additional amine oxidases, such as serum amine oxidases, and lead to accumulation of toxic products *in vivo* (Trackman 2016).

In the majority of tissues, LOX is the most abundantly expressed of the family isoforms and is required for completion of proper collagen and elastin biosynthesis (Trackman 2016). LOX knockout mice die perinatally due to vascular defects (Sharma-Bhandari et al. 2015; Atsawasuwan et al. 2005; Mäki et al. 2002). In addition, the LOX isoform is commonly upregulated in fibrotic diseases, and its crosslinking of collagens is thought to provide resistance of the extracellular matrix to degradation (Mäki et al. 2002). LOXL-1 is primarily linked to elastin maturation, as LOXL1-knockout mice show skin, uterine, and lung abnormalities and LOXL-1 closely associates with elastic fibers in vivo (Liu et al. 2004; Lee et al. 2008). Studies of LOXL-2 have focused on the protein's upregulation in many cancers (Torres et al. 2015; Moon et al. 2013; Trackman 2016). Additional roles (aside from crosslinking) for LOXL2 in signal transduction have also

been studied, and a direct interaction of LOXL2 with nuclear proteins, such as HSP90, has been demonstrated (Mccready et al. 2014). Currently, aside from its upregulation in fibrosis like other LOX isoforms, not much is known about LOXL3 (Trackman 2016). LOXL4 is highly expressed in the vascular tissues and has also been linked to fibrotic pathologies (Trackman 2016).

1.2c Elastin synthesis and maturation

Elastin is the major component of the ECM that provides elasticity to the tissue and is predominantly found in the large arteries, tendons, skin, and lungs (Mithieux & Weiss 2005). In contrast to the high Young's modulus of collagen ($1x10^6$ kPa), elastin has a relatively low Young's modulus of 300-600 kPa and can extend from 100-220% of its unstretched length (Gosline 1976; Fung 1993). Bundles of elastin form elastic fibers, in which elastin comprises the core of the fiber (approximately 90% of the fiber); smaller microfibrils surround the sheathe of elastin. Elastin comprises around 30-57% of the aorta and in large arteries is organized into concentric rings around the lumen of the vessel, with a layer of smooth muscle cells between each elastic lamina (Vrhovski & Weiss 1998; Li et al. 1998). These elastic fibers undergo billions of cycles of extension and recoil without mechanical failure (Keeley et al. 2002). Elastin has a very long half-life, estimated to be around 70 years in humans (Petersen et al. 2002; Mithieux & Weiss 2005), and as such there is very little turnover in healthy tissues. Elastogenesis takes place during the late fetal and early neonatal period, with smooth muscle cells being the primary cell-type depositing elastin in the large arteries (Uitto et al. 1991). Before the deposition of elastin, microfibrils are first deposited and thought to act as a scaffold for

orientation of the elastic fibrils (Kielty et al. 2002; Davis & Mecham 1993). These microfibrils are composed of several molecules that help aid in hydration, growth factor association, and regulation of cellular activities, including proteoglycans such as fibrillin-1 and -2. When initially synthesized, elastin is formed by the cross-linking of lysines on tropoelastin monomers (Mithieux & Weiss 2005). This cross-linking is performed similar to collagen cross-linking and is also done by the lysyl oxidase family of enzymes (Kagan & Sullivan 1982; Liu et al. 2004; Noblesse et al. 2004). Cross-linking of lysine residues is the only known post-translational modification of elastin. Because of the extensive crosslinking by LOX family members, elastin degradation is very slow (Mithieux & Weiss 2005). However, elastin fiber breakdown is increased, particularly during aging, due to elastases (Faury 2001). Elastin degradation products can then produce responses such as increased ECM synthesis, cell migration, and cell proliferation (Mithieux & Weiss 2005).

1.3 Arterial contractility and smooth muscle cell biology

1.3a Regulators of smooth muscle contractility

Vascular smooth muscle cells (SMCs) line the medial layer of arteries, and one of their major functions is to regulate blood flow to target organs by modulating arterial tone and peripheral resistance (Webb 2003; Hathaway et al. 1991). Vascular tone is regulated through tonic contraction and dilation of the larger arteries. Similar to other

muscle cells, the major contractile components in SMCs consists of actin and myosin. However, in contrast to skeletal muscle, smooth muscle cells undergo tonic, or prolonged contraction (Webb 2003; Hathaway et al. 1991). Thus, they possess cell-type specific forms of actin and myosin.

A smooth muscle specific form of myosin heavy chain (encoded by the myh11 gene, SM MHC protein) and smooth muscle alpha-actin (acta2 gene, SMA protein) exist in SMCs and have been designated critical components for cellular contraction (Lehman & Morgan 2012; Babu et al. 2000; Martin et al. 2007). The smooth muscle-specific myosin isoforms have greater force generating capacity than striated muscle myosins and allow for the prolonged tonic contraction of SMCs (Babu et al. 2000). Smooth muscle myosins are composed of two heavy chains, two essential light chains, and two regulatory light chains and associate with the contractile SMA filaments which anchor to dense bodies and adhesion plaques on the cell membrane (Lehman & Morgan 2012). Additionally, SMCs contain other cell-specific contractile proteins such as transgelin (gene *Tagln*), an actin cross-linking protein, and calponin (gene *Cnn1*), which can regulate ATPase activity of myosin in smooth muscle (Webb 2003; Hathaway et al. 1991). Inability to properly regulate vascular tone through contraction and dilation may lead to impaired blood flow to target tissues.

The contraction of SMCs is largely calcium-dependent (Fig. 1.04) (Morgan 1990; Webb 2003; Somlyo et al. 2004; Hathaway et al. 1991). Influx of calcium into the cytoplasm by either calcium channels on the cell membrane or release of intracellular calcium stores can allow calcium to bind to calmodulin and activate myosin light chain kinase (MLCK). Phosphorylation of the regulatory light chain of smooth muscle myosin by MLCK allows for cycling of cross bridges between actin and myosin to initiate

contraction. This phosphorylation of myosin light chain allows for enhanced inorganic phosphate release to increase the rate of the actomyosin ATPase cycle. Additionally, alpha adrenergic agonists such as norepinephrine and phenylephrine can cause release of calcium through signaling cascades involving the activation of heterotrimeric G-proteins and activation of the second messengers IP3 (inositol triphosphate) and DAG (Diacylglycerol). Binding of IP3 to the sarcoplasmic reticulum promotes calcium release, and DAG signaling activates protein kinase C (PKC) to phosphorylate ion channels and promote intracellular calcium transport (Webb 2003; Hathaway et al. 1991; Ahmed & Warren 2018; Zhu et al. 2019; Ringvold & Khalil 2017).

Acting antagonistic to MLCK, myosin light chain phosphatase (MLCP) can dephosphorylate the regulatory light chain of smooth muscle myosin to lessen the rate of the actomyosin ATPase cycle. RhoA and Rho-associated protein kinase (ROCK) signaling can phosphorylate MLCP in order to inhibit its function and promote contractility. The Rho pathway is thought to be activated upon receptor binding of phenylephrine or other alpha adrenergic agonists by release of Rho-GEFs from the cell membrane (Webb 2003; Hathaway et al. 1991; Szasz & Webb 2017). To promote relaxation of smooth muscle, calcium is removed from the cytoplasm by Calcium-magnesium-ATPase pumps on the sarcoplasmic reticulum or the cell membrane in addition to sodium calcium exchange pumps. Additionally, activation of MLCP also promotes relaxation (Webb 2003; Hathaway et al. 1991).

1.3b Smooth muscle myosins and smooth muscle actin

SMCs possess 4 unique isoforms of the myosin heavy chain subunit (SM-MHC) which originate from alternative splicing of the *Myh11* gene. These four isoforms result from the addition of an insert in either the head region or on the COOH terminus of the protein (Fig. 1.05) (Eddinger & Meer 2007). Smooth muscle also has two smooth muscle myosin light chain-17 (SM-MLC17) isoforms and two regulatory SM-MLC20 isoforms (Lenzs et al. 1989; Lash et al. 1990; Eddinger & Meer 2007). In addition to smooth muscle specific myosins, SMCs also contain non-muscle myosin heavy chain (NM-MHC) isoforms IIA, IIB, and IIC, and in contrast to SM-MHC, these NM-MHC isoforms do not possess a head or tail insert (Eddinger & Meer 2007). There is currently no data supporting combination of NM- MHC and SM-MHC to form active myosins. However, there is data suggesting non-muscle myosin light chain subunits may combine with SM-MHC subunits, although this may be tissue specific (Eddinger & Meer 2007).

Although containing both NM-MHC and SM-MHC, as SMCs begin to differentiate, the abundance of NM-MHC decreases over time from around 50% of total myosin in neonates to around 10% of total myosin in mature adults as observed in swine, rat, and mouse, and SM-MHC increases to become the predominant myosin present (Eddinger & Murphy 1991; Eddinger & Wolf 1993; Frid et al. 1994; Gaylinn et al. 1989). This suggests that SM-MHC has a critical role in the function of SMCs and arterial physiology that differs from the role of non-muscle myosins. Indeed, in contrast to other muscles, smooth muscle can shorten by 80% of its original length (Eddinger & Meer 2007). This is in part due to the smooth muscle specific isoforms of myosin present, and that smooth muscle thick filaments possess four myosins per 14.5nm in contrast to three myosins in tissue like striated muscle (Tonino et al. 2002). Furthermore, smooth muscle thick filaments are thought to be more labile than other muscle filaments,

so assembly and disassembly of actomyosin filaments may also contribute to the unique contractility of SMCs (Eddinger & Meer 2007). The NM-MHC isoforms present in SMCs have been proposed to be involved in housekeeping processes instead of contractility, as SMCs can still experience large tonic forces when there is little or no NM-MHC (Eddinger & Meer 2007).

In addition to myosins, SMCs also have four isoforms of actin (Fatigati & Murphy 1984; Kim et al. 2008). The alpha isoform of SMA dominates in supporting the contractile ability of SMCs in comparison to the gamma isoform (Lehman & Morgan 2012). Additionally, SMCs have two non-muscle beta and gamma actin isoforms which play a maintenance role in cell structure (Drew et al. 1991; Fatigati & Murphy 1984; Kim et al. 2008). Some studies support that the actin isoforms segregate into separate filaments in the cell, with the alpha smooth muscle actin filaments running along the length of the cell and the gamma isoform localized at the cortex (Gallant et al. 2011; Lehman & Morgan 2012). Both of these actin filaments anchor to dense bodies, which are strong focal adhesions that form on the cell membrane and provide anchoring structures to allow for contraction of the actomyosin skeleton. What may set the actin cytoskeleton of smooth muscle apart from skeletal muscle is that the exchange of smooth muscle actin is much more rapid, and increased polymerization of actin has been shown to correlate with an increase in the magnitude of contractile force generated (Lehman & Morgan 2012; Mehta & Gunst 1999; Jones et al. 1999; Gunst & Zhang 2008). Overall, the unique isoforms smooth muscle cells possess of actin and myosin allow for their distinct physiological function of tonic contraction and regulation of vascular tone.

1.3c Smooth muscle biology and phenotypic switching

SMCs exist along a range of phenotypes from “contractile” to “synthetic.” In relation to regulating blood pressure, vascular tone, and blood distribution, it is important that SMCs possess a contractile ability (Owens et al. 2004; Davis-Dusenbery et al. 2011). However, in response to specific conditions such as vascular injury, it is important that the SMCs are capable of migrating, proliferating and synthesizing large amounts of extracellular matrix to repair the wound, all of which are characteristic of the synthetic state. The ability of SMCs to transition from a contractile state to matrix-remodeling state is called phenotypic switching (Hao et al. 2003; Owens et al. 2004; Rensen et al. 2007). Major markers of the contractile cell phenotype include, but are not limited to, SM-MHC, SMA, myocardin (see below), and calponin - all proteins involved in the contractility of SMCs. Synthetic molecular markers include increased collagen I and osteopontin expression, and increased synthesis of MMP isoforms, in addition to other markers (Rensen et al. 2007; Owens et al. 2004; Beamish et al. 2010; Long et al. 2008; Miano 2003; Rzucidlo et al. 2007). It is important to note that SMCs do not exist in either a solely contractile or synthetic state but exist instead along a spectrum ranging from either end.

Phenotypic switching can occur due to chemical or mechanical cues. For instance, platelet-derived growth factor (PDGF) induces a more synthetic phenotype (Li et al. 1997; Hao et al. 2002; Kotani et al. 2003) while transforming growth factor beta (TGF-β) signaling induces a contractile phenotype (Hautmann et al. 1997; Hao et al. 2002). Mechanical stimuli can also play a role in SMC differentiation, as stretch (caused by variations in arterial pressure) and flow (caused by blood passing through arteries)

can also alter phenotype. Shear stress caused by flow promotes a more synthetic phenotype, showing reduced SMA and SM-MHC expression (Hao et al. 2002; Rensen et al. 2007). Stretch increases the abundance of both contractile proteins and matrix proteins (O'Callaghan & Williams 2000; Reusch et al. 1996; Birukov et al. 1998; Lehoux & Tedgui 1998; Reusch et al. 1997). Fibronectin and collagen abundance are increased upon mechanical strain of SMCs, and it is thought that constant strain on the SMCs can lead to build-up of matrix proteins to cause stiffening of the arteries (O'Callaghan & Williams 2000).

At a genetic level, SMC phenotype is regulated by several transcription factors and transcriptional co-activators that control the expression of contractile genes (Fig. 1.06) (Davis-Dusenbery et al. 2011). Cis-acting elements termed CArG boxes (CC(AT)6GG) are upstream of many SMC contractile genes, which allows for the binding of serum response factor (SRF) and activation of transcription (Kim et al. 1997; Li et al. 1996; Mack & Owens 1999; Manabe & Owens 2001). SRF affinity for the CArG motif is dramatically enhanced by the binding of myocardins or MRTFs (myocardin-related transcription factors) and negatively regulated by KLF4 (Du et al. 2003; Chen et al. 2002; Wang et al. 2003; Hinson et al. 2007; Davis-Dusenbery et al. 2011). Furthermore, microRNAs such as mir-143/145 also play a role in regulating SMC differentiation by targeting and degrading KLF4 transcript to promote the contractile phenotype (Boettger et al. 2009; Zhang 2009; Hutcheson et al. 2013). Overall, a wide variety of stimuli and signals can influence the gene profile of SMCs to allow for varying phenotypic state, and overabundance or loss of particular signals can be devastating for SMC and arterial function.

1.4 Mechanotransduction from the ECM

In addition to contributing to the mechanical properties of tissues, the ECM, in combination with cell force generation, can also modulate inter and intra-cellular signaling pathways (Figure 1.07). Cells adhere to the ECM through transmembrane receptors. The most common cellular attachments to the ECM are transmembrane proteins called integrins. These integrins are associated with matrix components outside of the cell and linker proteins inside the cell that connect integrins to the cytoskeleton. Thus, integrins are transmembrane adhesions that form a mechanism to transduce mechanical signals from outside the cell into biochemical signals inside the cell (Humphrey et al. 2014; Ciobanasu et al. 2013; Ingber 2008). The clustering of integrins and collection of signaling molecules at these clustering sites has been termed a focal adhesion, and it has been demonstrated that cells on stiffer substrates generate larger and more stable focal adhesions, as the integrin adhesions strengthen under force. Inside the cell, linker proteins which consist of Talin, Vinculin, and Paxillin among many others, connect the integrin to the actomyosin cytoskeleton. The coupling of the actomyosin skeleton to the rigid ECM allows the cell to generate tension and unfold signaling and docking proteins, such as Talin and Vinculin, to allow for biochemical signaling events to take place (Humphrey et al. 2014; Martino et al. 2018; Geiger et al. 2009; Burridge & Guilluy 2016).

The increased generation of cellular tension on stiff substrates can enforce the stabilization of the actin cytoskeleton, leading to increased polymerization of actin filaments to form large bundles called stress fibers. For example, intracellular tension has been shown to activate Rho signaling and downstream Rho associated kinase

(ROCK) and LIM Kinase to phosphorylate cofilin and stabilize actin filaments (Martino et al. 2018; Fukata et al. 2001; Hayakawa et al. 2011). This polymerization of actin can further influence downstream biochemical signaling. For instance, the transcriptional coactivator MKL-1 (or MRTF-A; myocardin-related transcription factor) is generally sequestered in the cytoplasm by monomeric G-actin. As actin fibers form due to increased polymerization, the abundance of G-actin decreases and MKL becomes freed of its binding from G-actin and can translocate to the nucleus to transcribe many contractility-related genes (Martino et al. 2018; Ho et al. 2013).

Similar to the connections that exist between the ECM and the cytoplasmic actin skeleton, force can also be transduced from the actin cytoskeleton to the nucleus through the Linker of Nucleoskeleton and Cytoskeleton (LINC) complex. The LINC complex connects to the actin cytoskeleton and intermediate filaments through Nesprin proteins which cross the outer nuclear membrane. Nesprins connect to SUN proteins in the nuclear envelope, and SUN proteins connect to the nuclear lamina meshwork on the inner nuclear membrane (Dahl et al. 2008; Dahl & Kalinowski 2011; Crisp et al. 2006; Martino et al. 2018).

Another example of force transduction signaling has been demonstrated through transcriptional regulators YAP/TAZ (Yes-associated protein 1, and WW-domain-containing transcription regulator 1, respectively). Dupont et al. (2011) showed that YAP/TAZ are mechanically activated transcriptional regulators that are predominantly cytosolic on softer substrates, but translocate to the nucleus on stiff substrates (Dupont et al. 2011). Novel studies by Elosegui-Artola et al. (2017) have shown that force on LINC connections can act to open nuclear pores and promote entry of transcription factors such as YAP/TAZ into the nucleus (Elosegui-Artola et al. 2017). In addition, it has

been hypothesized that force generation on the LINC complex can act to regulate epigenetics (van Steensel & Belmont 2017; Lelièvre 2009).

In HGPS, progerin expression and the consequently altered nuclear lamina has been shown to influence mechanotransduction. Dahl and colleagues (2006) have shown that the nuclear lamina of HGPS cells has reduced nuclear deformability and a reduced ability to rearrange under mechanical stress (Dahl et al. 2006). Supporting this study, Verstraeten et al. (2008) showed that HGPS nuclei are much stiffer and HGPS cells are more susceptible to mechanical stress than cells with a healthy nuclear lamina (Verstraeten et al. 2008). Others have shown dysregulated interactions between progerin and SUN proteins, further suggesting progerin expression can cause altered mechanotransduction to the nucleus (Chen et al. 2014). As Lamin A plays such a critical role in structural integrity of the nucleus and mechanotransduction, it is no surprise progerin can alter both of these integral functions.

1.4 Rationale and objectives

Arterial stiffening and reduced arterial contractility have been reported in HGPS children and animal models, but the initial drivers and molecular mechanisms remain unknown. Previously, arterial stiffening and reduced contractility have been reported in HGPS mouse models at late-stage time-points, near the end of the animal's lifespan (Murtada et al. 2020; del Campo et al. 2020). However, the interpretation of these results in terms of vascular biology is confounded by the low numbers of arterial SMCs at this late stage. The work in this thesis seeks to understand the initial molecular regulators of arterial stiffening and reduced contractility. By using the $LMNA^{G609G}$ mouse model and

evaluating cardiovascular abnormalities at a young age before the onset of severe HGPS pathology, we can understand some of the molecular drivers leading to altered cardiovascular function.

In Chapter 2, I show that arterial stiffening and diastolic dysfunction begins at a very early time-point in HGPS mice and correlates with an increase in LOX abundance. *In vivo* administration of LOX inhibitor BAPN corrected arterial stiffening and diastolic dysfunction. Genome-wide profiling revealed reduced miR-145 as a mechanism for the increased LOX abundance, and restoration of miR-145 in primary cultured HGPS SMCs reduced LOX transcript to WT levels. We also compare the arterial stiffening of young HGPS mice to normally aged WT mice and show unique differences in axial versus circumferential stiffening. Interestingly, although we report increased LOX abundance in normally aged arteries, we did not find reduced miR-145 levels. This indicates that the arterial stiffening in normal aging versus premature aging may occur through differential mechanisms.

In Chapter 3, I explore the mechanism of reduced arterial contractility in HGPS. I show that HGPS carotid arteries have reduced vasoconstriction in response to potassium chloride. In surveying key SMC contractility markers, I discovered HGPS SMCs display reduced SM-MHC levels. This reduction in SM-MHC is causal for decreased force generation in isolated HGPS SMCs as restoration of SM-MHC significantly increased traction force. Lastly, I show that normally aged arteries of both mice and humans display decreased SM-MHC levels, indicating that a reduction in SM-MHC and arterial contractility may be a common phenomenon of normal and premature aging.

In Chapter 4, I will present early findings to understand the direct effects of progerin expression on LOX and SM-MHC. I show that acute progerin expression in WT SMCs does not recapitulate the high LOX or reduced miR-145 observed in HGPS but does result in the selective decrease in SM-MHC. Additionally, I show decreased nuclear localization of myocardin-related transcription factor-A (MRTF-A), a key regulator of SMC contractile gene expression, in HGPS SMCs. Furthermore, I show that knockdown of MRTF-A in WT SMCs partially mimics the contractile gene profile of HGPS SMCs.

In Chapter 5, I summarize the findings of this work and discuss hypotheses relating to how and why HGPS SMCs may be altering the arterial ECM, and I consider ideas of how progerin may be directly causing decreased force generation in SMCs. I also discuss potential implications of my work in the context of therapies for HGPS and normal aging and explore the commonalities and differences I have observed between premature and natural aging.

1.5 Figures

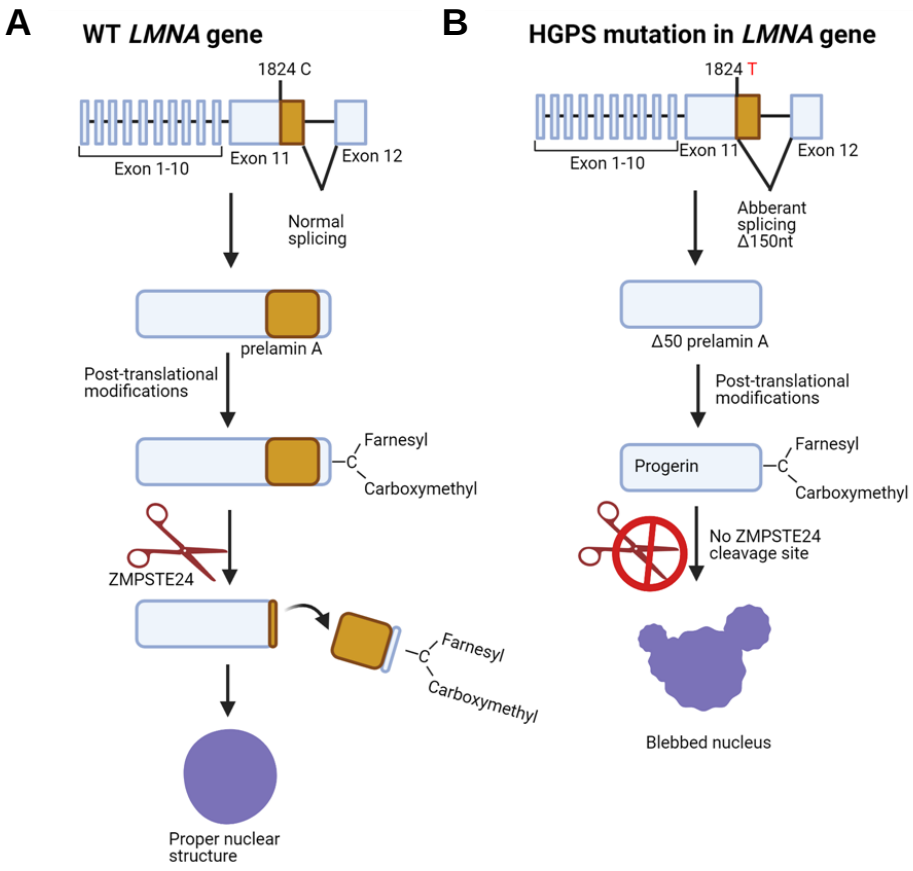

Figure 1.01. Post-translational processing of Lamin A and Progerin. (A) In healthy cells, the Prelamin A precursor protein is produced from proper splicing of the *LMNA* gene and subsequently processed with post-translational modifications. In a final step, ZMPSTE24 cleaves the farnesylated and carboxymethylated C-terminus of Prelamin A to produce mature Lamin A protein. In cases of ZMPSTE24 deficiency, a farnesylated and carboxymethylated Prelamin A protein produces a progeroid phenotype. **(B)** In classic HGPS, the c.1824C>T mutation in *LMNA* results in aberrant splicing between exons 11-12 and the loss of 50 amino acids from the resultant protein. These 50 amino

acids are critical for the recognition of progerin by ZMPSTE24, and the farnesyl and carboxymethyl moieties remain attached to the C-terminus, leading to nuclear defects. Figure made in BioRender (biorender.com).

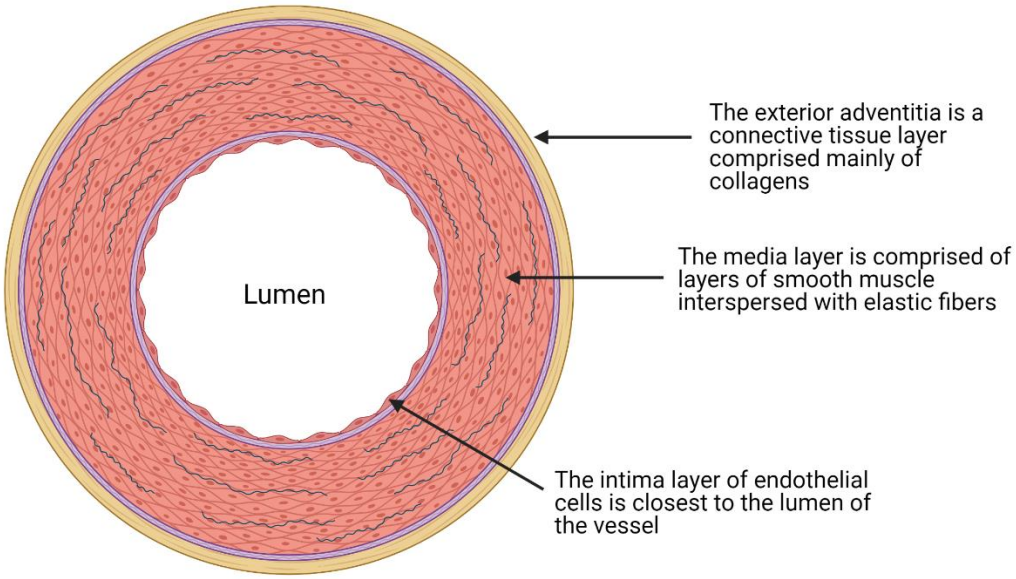

Figure 1.02. Large elastic artery structure. The large elastic arteries such as the aorta have three distinct layers. The inward most layer facing the lumen of the vessel is comprised of endothelial cells, which are essential in responding to changes in blood flow and additional soluble factors present in the blood. The endothelial layer is separated from the media layer by the inner elastic lamina. The media layer is comprised of smooth muscle cells which are essential for regulating vascular tone. Layers of smooth muscle are separated by concentric rings of elastin fibers. The media layer is separated from the outer adventitia layer by an external elastic lamina. The adventitia layer is a highly collagenous connective tissue synthesized by fibroblasts. Figure made in BioRender (biorender.com).

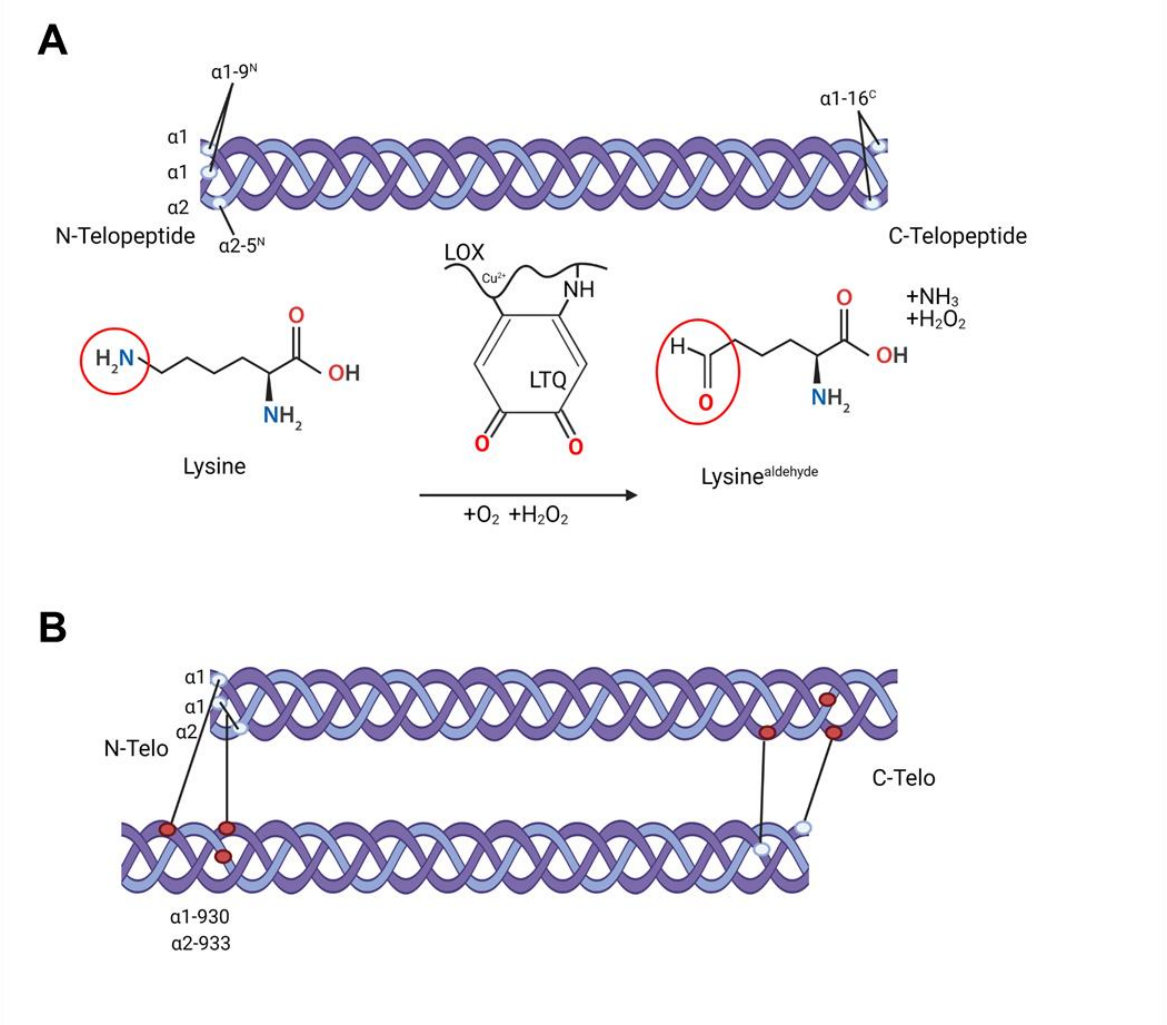

Figure 1.03. Lysyl Oxidase (LOX)-mediated crosslinking of collagen. (A) Crosslinking locations of the 5 lysine or hydroxylysine residues on the telo-peptide region of type-I collagen (denoted by blue circles). LOX mediates collagen crosslinking through conversion of Lysine to a more reactive Lysine-aldehyde and requires Cu^{2+} and cofactor LTQ. **(B)** Inter-peptide crosslinking sites between triple helices on type-I collagen. Figure prepared in Biorender (biorender.com).

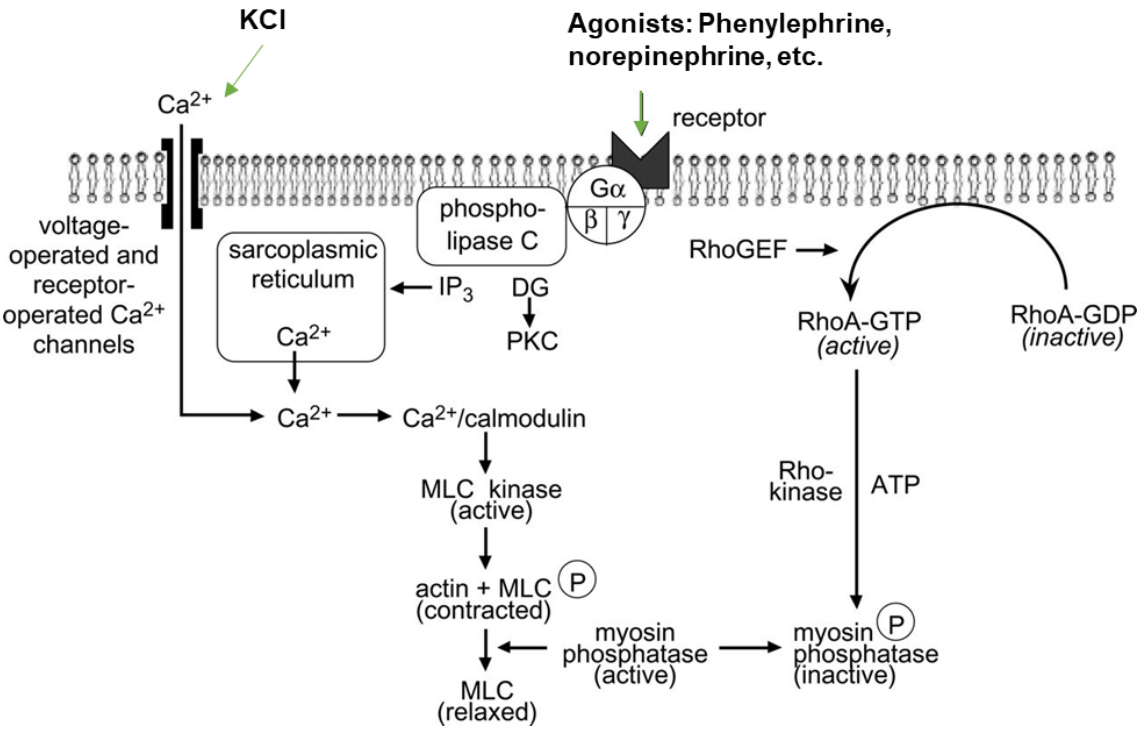

Figure 1.04. Mechanisms of smooth muscle cell contraction. Agonist binding (such as phenylephrine) to G-protein coupled receptors can induce the production of two second messengers through activation of phospholipase C. Diacylglycerol (DG) triggers contraction through activation of protein kinase C (PKC), which can phosphorylate calcium ion channels and additional proteins that regulate myosin cross-bridge cycling. Inositol 1,4,5-trisphosphate (IP3), binds to the sarcoplasmic reticulum to trigger calcium release. Alternatively, increased KCl can cause membrane depolarization and activation of voltage-gated calcium channels on the cell membrane. Calcium binding to calmodulin activates myosin light chain kinase (MLCK) to promote a contracted state through the phosphorylation of myosin light chain. Additionally, receptor binding can activate RhoA and downstream Rho-kinase to phosphorylate and inactivate myosin phosphatase and promote contraction. Figure modified from Webb (2003).

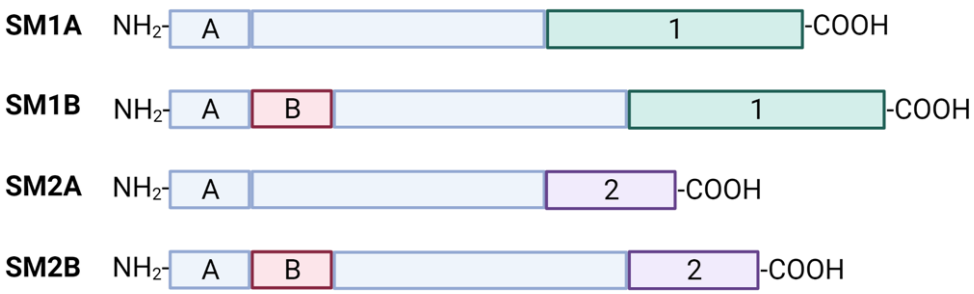

Figure 1.05. Smooth muscle myosin heavy chain (SM-MHC) isoforms. Alternative splicing of the *Myh11* gene generates four distinct isoforms of SM-MHC. The SM1 isoform contains an additional insert in the –COOH terminus of the protein not present in the SM2 isoform. The SMA isoform lacks an insert near the N-terminus in comparison to the SMB isoform. Figure made in BioRender (biorender.com).

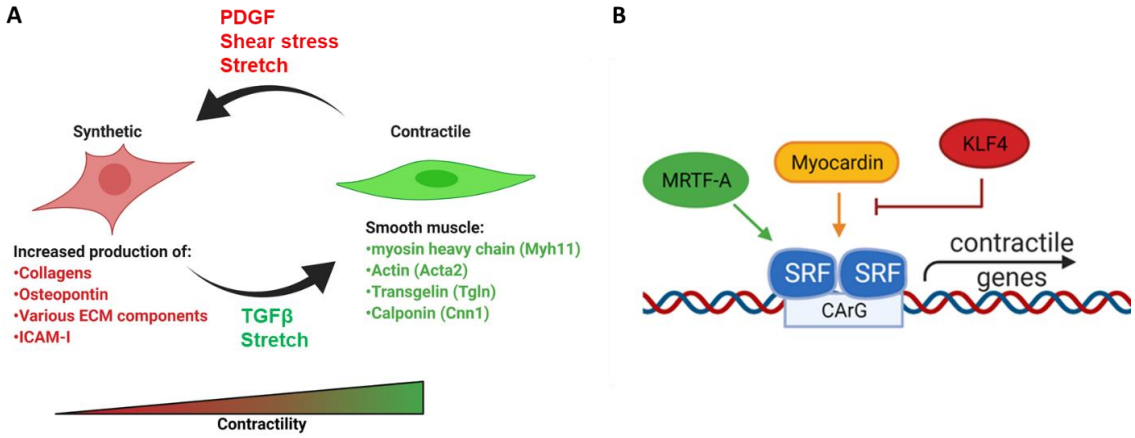

Figure 1.06. Regulation of SMC phenotypic switching and contractility. (A) SMCs exist along a phenotypic spectrum ranging from synthetic, proliferating and ECM-producing cells, to contractile cells expressing an abundance of contractile machinery. Various stimuli such as platelet derived growth factor (PDGF), shear stress, or stretch have been reported to promote a more synthetic phenotype. Transforming growth factor beta (TGFβ) and stretch have been reported to promote a contractile phenotype. **(B)** Regulation of contractile gene transcription relies on CArG box motifs on DNA upstream of contractile genes that bind serum response factor (SRF). Binding of myocardin or myocardin like transcription factors (MRTFs) enhance the transcriptional activity of SRF. In contrast, KLF4 can negatively regulate contractile gene expression.

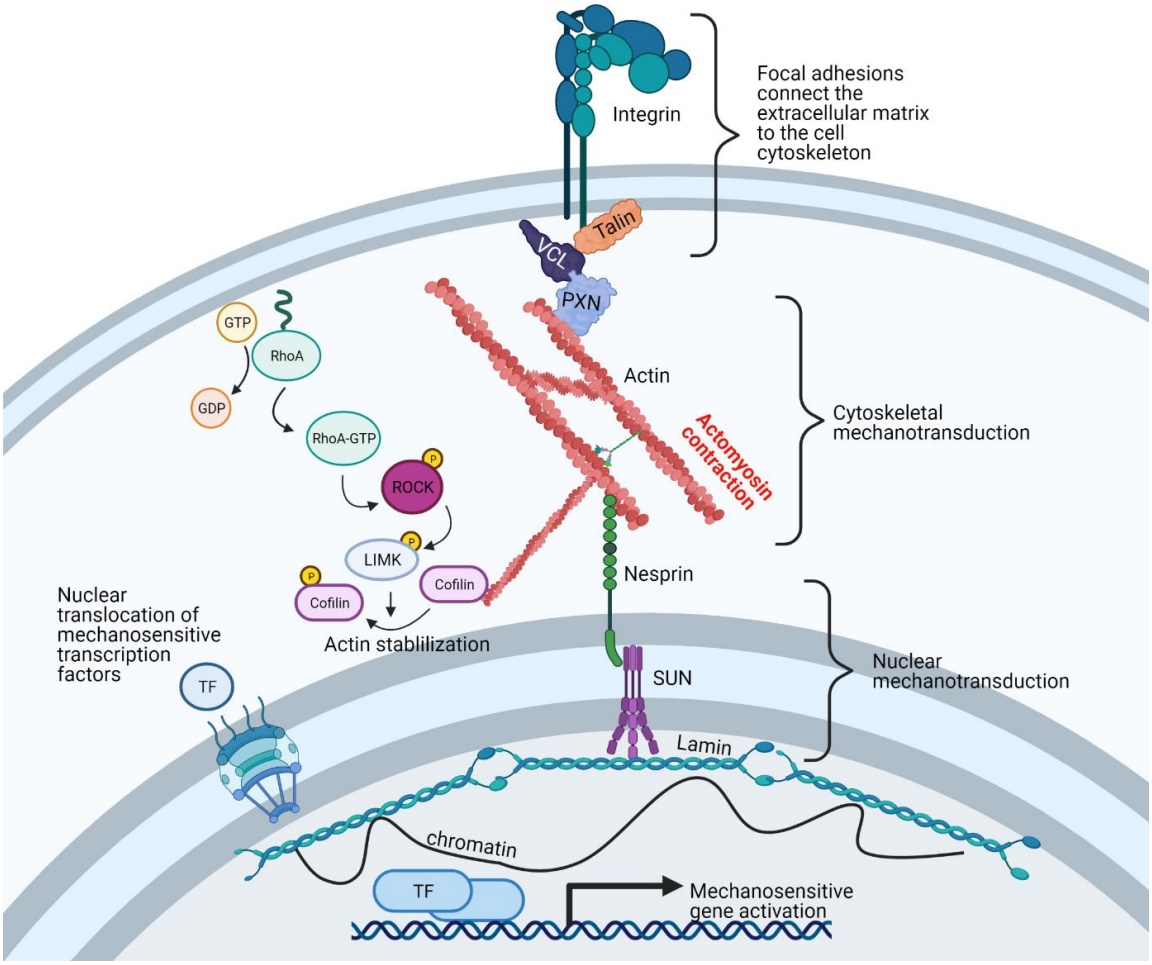

Figure 1.07. Mechanotransduction from the ECM to the nucleus. Extracellular mechanical signals are transmitted to the nucleus through connections of the cyto- and nucleo-skeleton. Integrins bind to various extracellular matrix components and form focal adhesions, recruiting proteins such as talin, vinculin (VCL), and paxillin (PXN) to their intracellular domain and link the integrin to the actomyosin cytoskeleton. Stabilization of the actomyosin skeleton is enforced by the activation of RhoA and downstream LIM Kinase (LIMK) to phosphorylate cofilin. Force generated from the contraction of actomyosin filaments is transmitted to the nucleus through the Linker of Nucleoskeleton

and Cytoskeleton (LINC) complex. Nesprin proteins anchor to cytoskeletal filaments in the cytoplasm and SUN proteins in the inner nuclear space. In turn, SUN proteins anchor to the nuclear lamin network. Mechanosensitive gene transcription is activated by the nuclear localization of mechanosensitive transcription factors or transcriptional regulators and through changes in chromatin structure. Figure made in BioRender (biorender.com).

1.6 Tables

Table 1. Common cardiovascular complications present in physiological aging and in the premature aging disease Hutchinson-Gilford Progeria Syndrome. Table adapted from Hamczyk et al. (2018)

Cardiovascular Complications	Physiological aging	Premature aging
Heart failure	Yes	Yes
Left ventricular diastolic dysfunction	Yes	Yes
Ventricular hypertrophy	Yes	Yes
Cardiac fibrosis	Yes	Yes
Heart valve dysfunction	Yes	Yes
Increased sympathetic activity	Yes	Yes
Decreased baroreflex sensitivity	Yes	Yes
Intima-media thickening	Yes	Yes
Vascular stiffening	Yes	Yes
Vascular fibrosis	Yes	Yes
Endothelial dysfunction	Yes	No
Atherosclerosis	Yes	Yes
Vascular calcification	Yes	Yes
Hypertension	Yes	Yes
Elevated platelet count	No	Yes
Prolonged prothrombin time	No	Yes

1.7 References

Ahmed S & Warren DT (2018) Vascular smooth muscle cell contractile function and mechanotransduction. *Vessel Plus* 2, 36.

Atsawasuwan P, Mochida Y, Parisuthiman D & Yamauchi M (2005) Expression of lysyl oxidase isoforms in MC3T3-E1 osteoblastic cells. *Biochem. Biophys. Res. Commun.* 327, 1042–1046.

Babu GJ, Warshaw DM & Periasamy M (2000) Smooth muscle myosin heavy chain isoforms and their role in muscle physiology. *Microsc. Res. Tech.* 50, 532–540.

Baker A-M, Bird D, Lang G, Cox TR & Erler JT (2013) Lysyl oxidase enzymatic function increases stiffness to drive colorectal cancer progression through FAK. *Oncogene* 32, 1863–1868.

Beamish JA, He P, Kottke-Marchant K & Marchant RE (2010) Molecular regulation of contractile smooth muscle cell phenotype: implications for vascular tissue engineering. *Tissue Eng. Part B. Rev.* 16, 467–91.

Bella J, Liu J, Kramer R, Brodsky B & Berman HM (2006) Conformational Effects of Gly-X-Gly Interruptions in the Collagen Triple Helix. *J. Mol. Biol.* 362, 298–311.

Bergo MO, Gavino B, Ross J, Schmidt WK, Hong C, Kendall L V., Mohr A, Meta M, Genant H, Jiang Y, Wisner ER, Van Bruggen N, Carano RAD, Michaelis S, Griffey SM & Young SG (2002) Zmpste24 deficiency in mice causes spontaneous bone fractures, muscle weakness, and a prelamin A processing defect. *Proc. Natl. Acad. Sci. U. S. A.* 99, 13049–13054.

Beyret E, Liao HK, Yamamoto M, Hernandez-Benitez R, Fu Y, Erikson G, Reddy P &

Izpisua Belmonte JC (2019) Single-dose CRISPR–Cas9 therapy extends lifespan of mice with Hutchinson–Gilford progeria syndrome. *Nat. Med.* 25, 419–422.

Bikkul MU, Clements CS, Godwin LS, Goldberg MW, Kill IR & Bridger JM (2018) Farnesyltransferase inhibitor and rapamycin correct aberrant genome organisation and decrease DNA damage respectively, in hutchinson-gilford progeria syndrome fibroblasts. *Biogerontology* 19, 579–602.

Birukov KG, Bardy N, Lehoux S, Merval R, Shirinsky VP & Tedgui A (1998) Intraluminal pressure is essential for the maintenance of smooth muscle caldesmon and filamin content in aortic organ culture. *Arterioscler. Thromb. Vasc. Biol.* 18, 922–927.

Boettger T, Beetz N, Kostin S, Schneider J, Krüger M, Hein L & Braun T (2009) Acquisition of the contractile phenotype by murine arterial smooth muscle cells depends on the Mir143/145 gene cluster. *J. Clin. Invest.* 119, 2634–2647.

Burridge K & Guilluy C (2016) Focal adhesions, stress fibers and mechanical tension. *Exp. Cell Res.* 343, 14–20.

del Campo L, Sánchez-López A, González-Gómez C, Andrés-Manzano MJ, Dorado B & Andrés V (2020) Vascular Smooth Muscle Cell-Specific Progerin Expression Provokes Contractile Impairment in a Mouse Model of Hutchinson-Gilford Progeria Syndrome that Is Ameliorated by Nitrite Treatment. *Cells* 9, 656.

del Campo L, Sánchez-López A, Salaices M, von Kleeck RA, Expósito E, González-Gómez C, Cussó L, Guzmán-Martínez G, Ruiz-Cabello J, Desco M, Assoian RK, Briones AM & Andrés V (2019) Vascular smooth muscle cell-specific progerin expression in a mouse model of Hutchinson–Gilford progeria syndrome promotes arterial stiffness: Therapeutic effect of dietary nitrite. *Aging Cell*, e12936.

Cao K, Graziotto JJ, Blair CD, Mazzulli JR, Erdos MR, Krainc D & Collins FS (2011)

Rapamycin reverses cellular phenotypes and enhances mutant protein clearance in Hutchinson-Gilford progeria syndrome cells. *Sci. Transl. Med.* 3.

Capell BC, Erdos MR, Madigan JP, Fiordalisi JJ, Varga R, Conneely KN, Gordon LB, Der CJ, Cox AD & Collins FS (2005) Inhibiting farnesylation of progerin prevents the characteristic nuclear blebbing of Hutchinson-Gilford progeria syndrome. *Proc. Natl. Acad. Sci. U. S. A.* 102, 12879–12884.

Capell BC, Olive M, Erdos MR, Cao K, Faddah DA, Tavarez UL, Conneely KN, Qu X, San H, Ganesh SK, Chen X, Avallone H, Kolodgie FD, Virmani R, Nabel EG & Collins FS (2008) A farnesyltransferase inhibitor prevents both the onset and late progression of cardiovascular disease in a progeria mouse model. *Proc. Natl. Acad. Sci. U. S. A.* 105, 15902–15907.

Cenni V, Capanni C, Columbaro M, Ortolani M, D'Apice MR, Novelli G, Fini M, Marmiroli S, Scarano E, Maraldi NM, Squarzoni S, Prencipe S & Lattanzi G (2011) Autophagic degradation of farnesylated prelamin A as a therapeutic approach to lamin-linked progeria. *Eur. J. Histochem.* 55, 200–205.

Chen J, Kitchen CM, Streb JW & Miano JM (2002) Myocardin: A Component of a Molecular Switch for Smooth Muscle Differentiation. *J. Mol. Cell. Cardiol.* 34, 1345–1356.

Chen Z-J, Wang W-P, Chen Y-C, Wang J-Y, Lin W-H, Tai L-A, Liou G-G, Yang C-S & Chi Y-H (2014) Dysregulated interactions between lamin A and SUN1 induce abnormalities in the nuclear envelope and endoplasmic reticulum in progeric laminopathies. *J. Cell Sci.* 127.

Ciobanasu C, Faivre B & Le Clainche C (2013) Integrating actin dynamics, mechanotransduction and integrin activation: The multiple functions of actin binding

proteins in focal adhesions. *Eur. J. Cell Biol.* 92, 339–348.

Columbaro M, Capanni C, Mattioli E, Novelli G, Parnaik VK, Squarzoni S, Maraldi NM & Lattanzi G (2005) Rescue of heterochromatin organization in Hutchinson-Gilford progeria by drug treatment. *Cell. Mol. Life Sci.* 62, 2669–2678.

Cox TR & Erler JT (2011) Remodeling and homeostasis of the extracellular matrix: implications for fibrotic diseases and cancer. *Dis. Model. Mech.* 4, 165–178.

Crisp M, Liu Q, Roux K, Rattner JB, Shanahan C, Burke B, Stahl PD & Hodzic D (2006) Coupling of the nucleus and cytoplasm: Role of the LINC complex. *J. Cell Biol.* 172, 41–53.

Dahl KN & Kalinowski A (2011) Nucleoskeleton mechanics at a glance. *J. Cell Sci.* 124, 675–678.

Dahl KN, Ribeiro AJS & Lammerding J (2008) Nuclear shape, mechanics, and mechanotransduction. *Circ. Res.* 102, 1307–1318.

Dahl KN, Scaffidi P, Islam MF, Yodh AG, Wilson KL & Misteli T (2006) Distinct structural and mechanical properties of the nuclear lamina in Hutchinson-Gilford progeria syndrome. *Proc. Natl. Acad. Sci. U. S. A.* 103, 10271–6.

Davidson JM, Hill KE & Alford JL (1986) Developmental changes in collagen and elastin biosynthesis in the porcine aorta. *Dev. Biol.* 118, 103–11.

Davis-Dusenbery BN, Wu C & Hata A (2011) Micromanaging vascular smooth muscle cell differentiation and phenotypic modulation. *Arterioscler. Thromb. Vasc. Biol.* 31, 2370–2377.

Davis EC & Mecham RP (1993) Elastic Fiber Organization. In *Tissue Engineering*. Birkhäuser Boston, pp.26–34.

Desmoulière A, Darby I, Costa AM, Raccurt M, Tuchweber B, Sommer P & Gabbiani G

(1997) Extracellular matrix deposition, lysyl oxidase expression, and myofibroblastic differentiation during the initial stages of cholestatic fibrosis in the rat. *Lab. Invest.* 76, 765–78.

Domingo DL, Trujillo MI, Council SE, Merideth MA, Gordon LB, Wu T, Introne WJ, Gahl WA & Hart TC (2009) Hutchinson-Gilford progeria syndrome: Oral and craniofacial phenotypes. *Oral Dis.* 15, 187–195.

Drew JS, Moos C & Murphy RA (1991) Localization of isoactins in isolated smooth muscle thin filaments by double gold immunolabeling. *Am. J. Physiol. - Cell Physiol.* 260.

Du KL, Ip HS, Li J, Chen M, Dandre F, Yu W, Lu MM, Owens GK & Parmacek MS (2003) Myocardin Is a Critical Serum Response Factor Cofactor in the Transcriptional Program Regulating Smooth Muscle Cell Differentiation. *Mol. Cell. Biol.* 23, 2425–2437.

DuBose AJ, Lichtenstein ST, Petrash NM, Erdos MR, Gordon LB & Collins FS (2018) Everolimus rescues multiple cellular defects in laminopathy-patient fibroblasts. *Proc. Natl. Acad. Sci. U. S. A.* 115, 4206–4211.

Dupont S, Morsut L, Aragona M, Enzo E, Giulitti S, Cordenonsi M, Zanconato F, Le Digabel J, Forcato M, Bicciato S, Elvassore N & Piccolo S (2011) Role of YAP/TAZ in mechanotransduction. *Nature* 474, 179–183.

Eddinger TJ & Meer DP (2007) Myosin II isoforms in smooth muscle: Heterogeneity and function. *Am. J. Physiol. - Cell Physiol.* 293, 493–508.

Eddinger TJ & Murphy RA (1991) Developmental changes in actin and myosin heavy chain isoform expression in smooth muscle. *Arch. Biochem. Biophys.* 284, 232–237.

Eddinger TJ & Wolf JA (1993) Expression of four myosin heavy chain isoforms with development in mouse uterus. *Cell Motil. Cytoskeleton* 25, 358–368.

Elosegui-Artola A, Andreu I, Beedle AEM, Lezamiz A, Uroz M, Kosmalska AJ, Oria R, Kechagia JZ, Rico-Lastres P, Le Roux AL, Shanahan CM, Trepat X, Navajas D, Garcia-Manyes S & Roca-Cusachs P (2017) Force Triggers YAP Nuclear Entry by Regulating Transport across Nuclear Pores. *Cell* 171, 1397-1410.e14.

Eriksson M, Brown WT, Gordon LB, Glynn MW, Singer J, Scott L, Erdos MR, Robbins CM, Moses TY, Berglund P, Dutra A, Pak E, Durkin S, Csoka AB, Boehnke M, Glover TW & Collins FS (2003) Recurrent de novo point mutations in lamin A cause Hutchinson-Gilford progeria syndrome. *Nature* 423, 293–298.

Eyre DR & Wu JJ (2005) Collagen cross-links. *Top. Curr. Chem.* 247, 207–229.

Fatigati V & Murphy RA (1984) Actin and Tropomyosin Variants in Smooth Muscles. Dependence on tissue type. *J. Biol. Chem.* 259, 14383–14388.

Faury G (2001) Function-structure relationship of elastic arteries in evolution: From microfibrils to elastin and elastic fibres. *Pathol. Biol.* 49, 310–325.

Fong LG, Ng JK, Meta M, Coté N, Yang SH, Stewart CL, Sullivan T, Burghardt A, Majumdar S, Reue K, Bergo MO & Young SG (2004) Heterozygosity for Lmna deficiency eliminates the progeria-like phenotypes in Zmpste24-deficient mice. *Proc. Natl. Acad. Sci. U. S. A.* 101, 18111–18116.

Freitas-Rodríguez S, Folgueras AR & López-Otín C (2017) The role of matrix metalloproteinases in aging: Tissue remodeling and beyond. *Biochim. Biophys. Acta - Mol. Cell Res.* 1864, 2015–2025.

Frid MG, Moiseeva EP & Stenmark KR (1994) Multiple phenotypically distinct smooth muscle cell populations exist in the adult and developing bovine pulmonary arterial

media in vivo. *Circ. Res.* 75, 669–681.

Fukata Y, Kaibuchi K, Amano M & Kaibuchi K (2001) Rho-Rho-kinase pathway in smooth muscle contraction and cytoskeletal reorganization of non-muscle cells. *Trends Pharmacol. Sci.* 22, 32–39.

Fung Y-C (1993) *Biomechanics*, New York, NY: Springer New York.

Gabriel D, Gordon LB & Djabali K (2016) Temsirolimus partially rescues the Hutchinson-Gilford progeria cellular phenotype. *PLoS One* 11.

Gallant C, Appel S, Graceffa P, Leavis P, Lin JJC, Gunning PW, Schevzov G, Chaponnier C, DeGnore J, Lehman W & Morgan KG (2011) Tropomyosin variants describe distinct functional subcellular domains in differentiated vascular smooth muscle cells. *Am. J. Physiol. - Cell Physiol.* 300.

García-Aguirre I, Alamillo-Iniesta A, Rodríguez-Pérez R, Vélez-Aguilera G, Amaro-Encarnación E, Jiménez-Gutiérrez E, Vásquez-Limeta A, Samuel Laredo-Cisneros M, Morales-Lázaro SL, Tiburcio-Félix R, Ortega A, Magaña JJ, Winder SJ & Cisneros B (2019) Enhanced nuclear protein export in premature aging and rescue of the progeria phenotype by modulation of CRM1 activity. *Aging Cell* 18.

Gaylinn BD, Eddinger TJ, Martino PA, Monical PL, Hunt DF & Murphy RA (1989) Expression of nonmuscle myosin heavy and light chains in smooth muscle. *Am. J. Physiol. - Cell Physiol.* 257.

Geiger B, Spatz JP & Bershadsky AD (2009) Environmental sensing through focal adhesions. *Nat. Rev. Mol. Cell Biol.* 10, 21–33.

Gelse K, Pöschl E & Aigner T (2003) Collagens--structure, function, and biosynthesis. *Adv. Drug Deliv. Rev.* 55, 1531–46..

Gerhard-Herman M, Smoot LB, Wake N, Kieran MW, Kleinman ME, Miller DT, Schwartzman A, Giobbie-Hurder A, Neuberg D & Gordon LB (2011) Mechanisms of Premature Vascular Aging in Children With Hutchinson-Gilford Progeria Syndrome. *Hypertension* 59.

Gesson K, Rescheneder P, Skoruppa MP, Von Haeseler A, Dechat T & Foisner R (2016) A-type Lamins bind both hetero- and euchromatin, the latter being regulated by lamina-associated polypeptide 2 alpha. *Genome Res.* 26, 462–473.

Glynn MW & Glover TW (2005) Incomplete processing of mutant lamin A in Hutchinson-Gilford progeria leads to nuclear abnormalities, which are reversed by farnesyltransferase inhibition. *Hum. Mol. Genet.* 14, 2959–2969.

Goldman RD, Shumaker DK, Erdos MR, Eriksson M, Goldman AE, Gordon LB, Gruenbaum Y, Khuon S, Mendez M, Varga R & Collins FS (2004) Accumulation of mutant lamin A progressive changes in nuclear architecture in Hutchinson-Gilford progeria syndrome. *Proc. Natl. Acad. Sci. U. S. A.* 101, 8963–8968.

Gonzalo S, Kreienkamp R & Askjaer P (2016) Hutchinson-Gilford Progeria Syndrome: A premature aging disease caused by LMNA gene mutations. *Ageing Res. Rev.*

Gordon CM, Cleveland RH, Baltrusaitis K, Massaro J, D'Agostino RB, Liang MG, Snyder B, Walters M, Li X, Braddock DT, Kleinman ME, Kieran MW & Gordon LB (2019) Extraskeletal Calcifications in Hutchinson-Gilford Progeria Syndrome. *Bone* 125, 103–111.

Gordon L (2019) The Progeria Research Foundation Cell and Tissue Bank. *Progeria Res. Found.*

Gordon L, Brown W & Collins F (2003) *Hutchinson-Gilford Progeria Syndrome*, University of Washington, Seattle.

Gordon LB, Harten IA, Patti ME & Lichtenstein AH (2005) Reduced adiponectin and HDL cholesterol without elevated C-reactive protein: Clues to the biology of premature atherosclerosis in Hutchinson-Gilford Progeria Syndrome. *J. Pediatr.* 146, 336–341.

Gordon LB, Shappell H, Massaro J, D'Agostino RB, Brazier J, Campbell SE, Kleinman ME & Kieran MW (2018) Association of Lonafarnib Treatment vs No Treatment With Mortality Rate in Patients With Hutchinson-Gilford Progeria Syndrome. *JAMA* 319, 1687.

Gosline JM (1976) The physical properties of elastic tissue. *Int. Rev. Connect. Tissue Res.* Vol. 7, 211–249.

Guardiani E, Zalewski C, Brewer C, Merideth M, Introne W, Smith ACM, Gordon L, Gahl W & Kim HJ (2011) Otologic and audiologic manifestations of Hutchinson-Gilford progeria syndrome. *Laryngoscope* 121, 2250–2255.

Gunst SJ & Zhang W (2008) Actin cytoskeletal dynamics in smooth muscle: A new paradigm for the regulation of smooth muscle contraction. *Am. J. Physiol. - Cell Physiol.* 295.

Hamczyk M, del Campo L & Andrés V (2018) Aging in the Cardiovascular System: Lessons from Hutchinson-Gilford Progeria Syndrome. *Annu. Rev. Physiol.* 80, 27–48.

Hamczyk MR, Villa-Bellosta R, Gonzalo P, Andrés-Manzano MJ, Nogales P, Bentzon JF, López-Otín C & Andrés V (2018) Vascular Smooth Muscle-Specific Progerin Expression Accelerates Atherosclerosis and Death in a Mouse Model of Hutchinson-Gilford Progeria Syndrome. *Circulation*, CIRCULATIONAHA.117.030856.

Hao H, Gabbiani G & Bochaton-Piallat ML (2003) Arterial smooth muscle cell

heterogeneity: Implications for atherosclerosis and restenosis development. *Arterioscler. Thromb. Vasc. Biol.* 23, 1510–1520.

Hao H, Ropraz P, Verin V, Camenzind E, Geinoz A, Pepper MS, Gabbiani G & Bochaton-Piallat ML (2002) Heterogeneity of smooth muscle cell populations cultured from pig coronary artery. *Arterioscler. Thromb. Vasc. Biol.* 22, 1093–1099.

Hathaway DR, March KL, Lash JA, Adam LP & Wilensky RL (1991) Vascular smooth muscle. A review of the molecular basis of contractility. *Circulation* 83, 382–90.

Hautmann MB, Madsen CS & Owens GK (1997) A transforming growth factor β (TGFβ) control element drives TGFβ- induced stimulation of smooth muscle α-actin gene expression in concert with two CArG elements. *J. Biol. Chem.* 272, 10948–10956.

Hayakawa K, Tatsumi H & Sokabe M (2011) Actin filaments function as a tension sensor by tension-dependent binding of cofilin to the filament. *J. Cell Biol.* 195, 721–727.

Hennekam RCM (2006) Hutchinson-Gilford progeria syndrome: Review of the phenotype. In *American Journal of Medical Genetics, Part A*. Am J Med Genet A, pp.2603–2624.

Herchenhan A, Uhlenbrock F, Eliasson P, Weis M, Eyre D, Kadler KE, Magnusson SP & Kjaer M (2015) Lysyl Oxidase Activity Is Required for Ordered Collagen Fibrillogenesis by Tendon Cells. *J. Biol. Chem.* 290, 16440–16450.

Hinson JS, Medlin MD, Lockman K, Taylor JM & Mack CP (2007) Smooth muscle cell-specific transcription is regulated by nuclear localization of the myocardin-related transcription factors. *Am. J. Physiol. - Hear. Circ. Physiol.* 292.

Ho CY, Jaalouk DE, Vartiainen MK & Lammerding J (2013) Lamin A/C and emerin regulate MKL1-SRF activity by modulating actin dynamics. *Nature* 497, 507–11.

Hulmes DJS (2008) Collagen Diversity, Synthesis and Assembly. In *Collagen*. Boston,

MA: Springer US, pp.15–47.

Humphrey JD, Dufresne ER & Schwartz MA (2014) Mechanotransduction and extracellular matrix homeostasis. *Nat. Rev. Mol. Cell Biol.* 15, 802–812.

Hutcheson R, Terry R, Chaplin J, Smith E, Musiyenko A, Russell JC, Lincoln T & Rocic P (2013) MicroRNA-145 restores contractile vascular smooth muscle phenotype and coronary collateral growth in the metabolic syndrome. *Arterioscler. Thromb. Vasc. Biol.* 33, 727–736.

Hutchinson J (1886) Congenital Absence of Hair and Mammary Glands with Atrophic Condition of the Skin and its Appendages in a Boy Whose Mother Had Been Almost Wholly Bald from Alopecia Areata from the Age of Six. *J. R. Soc. Med.* MCT-69, 473–477.

Ingber DE (2008) Tensegrity-based mechanosensing from macro to micro. *Prog. Biophys. Mol. Biol.* 97, 163–179.

Jones KA, Perkins WJ, Lorenz RR, Prakash YS, Sieck GC & Warner DO (1999) F-actin stabilization increases tension cost during contraction of permeabilized airway smooth muscle in dogs. *J. Physiol.* 519, 527–538.

Kagan HM (1994) Lysyl Oxidase: Mechanism, Regulation and Relationship to Liver Fibrosis. *Pathol. - Res. Pract.* 190, 910–919.

Kagan HM & Sullivan KA (1982) Lysyl Oxidase: Preparation and Role in Elastin Biosynthesis. *Methods Enzymol.* 82, 637–650.

Kashyap S, Shanker V & Sharma N (2014) Hutchinson - Gilford progeria syndrome: A rare case report. *Indian Dermatol. Online J.* 5, 478.

Keeley FW, Bellingham CM & Woodhouse KA (2002) Elastin as a self-organizing biomaterial: Use of recombinantly expressed human elastin polypeptides as a

model for investigations of structure and self-assembly of elastin. *Philos. Trans. R. Soc. B Biol. Sci.* 357, 185–189.

Kelleher CM, McLean SE & Mecham RP (2004) Vascular Extracellular Matrix and Aortic Development. *Curr. Top. Dev. Biol.* 62, 153–188.

Kelley JB, Datta S, Snow CJ, Chatterjee M, Ni L, Spencer A, Yang C-S, Cubenas-Potts C, Matunis MJ & Paschal BM (2011) The Defective Nuclear Lamina in Hutchinson-Gilford Progeria Syndrome Disrupts the Nucleocytoplasmic Ran Gradient and Inhibits Nuclear Localization of Ubc9. *Mol. Cell. Biol.* 31, 3378–3395.

Khoshnoodi J, Pedchenko V & Hudson BG (2008) Mammalian collagen IV. *Microsc. Res. Tech.* 71, 357–370.

Kielty CM, Sherratt MJ & Shuttleworth CA (2002) Elastic fibres. *J. Cell Sci.* 115, 2817 LP – 2828.

Kieran MW, Gordon L & Kleinman M (2007) New approaches to Progeria. *Pediatrics* 120, 834–841.

Kim HL, Lim WH, Seo J Bin, Chung WY, Kim SH, Kim MA & Zo JH (2017) Association between arterial stiffness and left ventricular diastolic function in relation to gender and age. *Med. (United States)* 96.

Kim HR, Gallant C, Leavis PC, Gunst SJ & Morgan KG (2008) Cytoskeletal remodeling in differentiated vascular smooth muscle is actin isoform dependent and stimulus dependent. *Am. J. Physiol. - Cell Physiol.* 295.

Kim S, Ip HS, Lu MM, Clendenin C & Parmacek MS (1997) A serum response factor-dependent transcriptional regulatory program identifies distinct smooth muscle cell sublineages. *Mol. Cell. Biol.* 17, 2266–2278.

Klein T & Bischoff R (2011) Physiology and pathophysiology of matrix metalloproteases.

Amino Acids 41, 271–290.

Koblan LW, Erdos MR, Wilson C, Cabral WA, Levy JM, Xiong ZM, Tavarez UL, Davison LM, Gete YG, Mao X, Newby GA, Doherty SP, Narisu N, Sheng Q, Krilow C, Lin CY, Gordon LB, Cao K, Collins FS, Brown JD & Liu DR (2021) In vivo base editing rescues Hutchinson–Gilford progeria syndrome in mice. *Nature* 589, 608–614.

Kohn JC, Lampi MC & Reinhart-King CA (2015) Age-related vascular stiffening: causes and consequences. *Front. Genet.* 06, 112.

Kotani M, Fukuda N, Ando H, Hu WY, Kunimoto S, Saito S & Kanmatsuse K (2003) Chimeric DNA-RNA hammerhead ribozyme targeting PDGF A-chain mRNA specifically inhibits neointima formation in rat carotid artery after balloon injury. *Cardiovasc. Res.* 57, 265–276.

Kothapalli D, Liu S-L, Bae YH, Monslow J, Xu T, Hawthorne EA, Byfield FJ, Castagnino P, Rao S, Rader DJ, Puré E, Phillips MC, Lund-Katz S, Janmey PA & Assoian RK (2012) Cardiovascular Protection by ApoE and ApoE-HDL Linked to Suppression of ECM Gene Expression and Arterial Stiffening. *Cell Rep.* 2, 1259–1271.

Lampi MC & Reinhart-King CA (2018) Targeting extracellular matrix stiffness to attenuate disease: From molecular mechanisms to clinical trials. *Sci. Transl. Med.* 10, eaao0475.

Lash JA, Helper DJ, Klug M, Nicolozakes AW & Hathaway DR (1990) Nucleotide and deduced amino acid sequence of cDNAs encoding two isoforms for the 17,000 dalton myosin light chain in bovine aortic smooth muscle. *Nucleic Acids Res.* 18, 7176.

Lee UJ, Gustilo-Ashby AM, Daneshgari F, Kuang M, Vurbic D, Dan LL, Flask CA, Li T & Damaser MS (2008) Lower urogenital tract anatomical and functional phenotype in

lysyl oxidase like-1 knockout mice resembles female pelvic floor dysfunction in humans. *Am. J. Physiol. - Ren. Physiol.* 295.

Lehman W & Morgan KG (2012) Structure and dynamics of the actin-based smooth muscle contractile and cytoskeletal apparatus. *J. Muscle Res. Cell Motil.* 33, 461–469.

Lehoux S & Tedgui A (1998) Signal transduction of mechanical stresses in the vascular wall. In *Hypertension*. Lippincott Williams and Wilkins, pp.338–345.

Lelièvre SA (2009) Contributions of extracellular matrix signaling and tissue architecture to nuclear mechanisms and spatial organization of gene expression control. *Biochim. Biophys. Acta* 1790, 925–35.

Lenzs S, Lohseo P, Seidel U & Arnoldll H-H (1989) *The Alkali Light Chains of Human Smooth and Nonmuscle Myosins Are Encoded by a Single Gene. Tissue-specific expression by alternative splicing pathways. J Biol Chem* 264, 9009-15.

Li DY, Brooke B, Davis EC, Mecham RP, Sorensen LK, Boak BB, Eichwald E & Keating MT (1998) Elastin is an essential determinant of arterial morphogenesis. *Nature* 393, 276–280.

Li L, Miano JM, Cserjesi P & Olson EN (1996) SM22α, a marker of adult smooth muscle, is expressed in multiple myogenic lineages during embryogenesis. *Circ. Res.* 78, 188–195.

Li X, Van Putten V, Zarinetchi F, Nicks ME, Thaler S, Heasley LE & Nemenoff RA (1997) Suppression of smooth-muscle α-actin expression by platelet-derived growth factor in vascular smooth-muscle cells involves Ras and cytosolic phospholipase A2. *Biochem. J.* 327, 709–716.

Liu B, Wang J, Chan KM, Tjia WM, Deng W, Guan X, Huang JD, Li KM, Chau PY, Chen

DJ, Pei D, Pendas AM, Cadiñanos J, López-Otín C, Tse HF, Hutchison C, Chen J, Cao Y, Cheah KSE, Tryggvason K & Zhou Z (2005) Genomic instability in laminopathy-based premature aging. *Nat. Med.* 11, 780–785.

Liu X, Zhao Y, Gao J, Pawlyk B, Starcher B, Spencer JA, Yanagisawa H, Zuo J & Li T (2004) Elastic fiber homeostasis requires lysyl oxidase-like 1 protein. *Nat. Genet.* 36, 178–182.

Long X, Bell RD, Gerthoffer WT, Zlokovic B V. & Miano JM (2008) Myocardin Is Sufficient for a Smooth Muscle-Like Contractile Phenotype. *Arterioscler. Thromb. Vasc. Biol.* 28.

Lucero HA & Kagan HM (2006) Lysyl oxidase: an oxidative enzyme and effector of cell function. *Cell. Mol. Life Sci.* 63, 2304–2316.

Mack CP & Owens GK (1999) Regulation of smooth muscle α-actin expression in vivo is dependent on CArG elements within the 5' and first intron promoter regions. *Circ. Res.* 84, 852–861.

Mäki JM (2009) Lysyl oxidases in mammalian development and certain pathological conditions. *Histol. Histopathol.* 24, 651–660.

Mäki JM, Räsänen J, Tikkanen H, Sormunen R, Mäkikallio K, Kivirikko KI & Soininen R (2002) Inactivation of the Lysyl Oxidase Gene *Lox* Leads to Aortic Aneurysms, Cardiovascular Dysfunction, and Perinatal Death in Mice. *Circulation* 106, 2503–2509.

Manabe I & Owens GK (2001) CArG elements control smooth muscle subtype-specific expression of smooth muscle myosin in vivo. *J. Clin. Invest.* 107, 823–34.

Martin AF, Bhatti S, Pyne-Geithman GJ, Farjah M, Manaves V, Walker L, Franks R, Strauch AR & Paul RJ (2007) Expression and function of COOH-terminal myosin

heavy chain isoforms in mouse smooth muscle. *Am. J. Physiol. Physiol.* 293, C238–C245.

Martino F, Perestrelo AR, Vinarský V, Pagliari S & Forte G (2018) Cellular mechanotransduction: From tension to function. *Front. Physiol.* 9, 824.

Mayoral P, Bárcena C & López-Otín C (2018) Progeria mouse models. In *Conn's Handbook of Models for Human Aging*. Elsevier, pp.689–701.

Mazereeuw-Hautier J, Wilson LC, Mohammed S, Smallwood D, Shackleton S, Atherton DJ & Harper JI (2007) Hutchinson-Gilford progeria syndrome: Clinical findings in three patients carrying the G608G mutation in LMNA and review of the literature. *Br. J. Dermatol.* 156, 1308–1314.

Mccready J, Wong DS, Burlison JA, Ying W & Jay DG (2014) An impermeant ganetespib analog inhibits extracellular Hsp90-mediated cancer cell migration that involves Lysyl oxidase 2-like protein. *Cancers (Basel).* 6, 1031–1046.

McKusick VA (2005) The Gordon Wilson Lecture: The clinical legacy of Jonathan Hutchinson (1828-1913): syndromology and dysmorphology meet genomics. *Trans. Am. Clin. Climatol. Assoc.* 116, 15–38.

Mehta D & Gunst SJ (1999) Actin polymerization stimulated by contractile activation regulates force development in canine tracheal smooth muscle. *J. Physiol.* 519, 829–840.

Merideth MA, Gordon LB, Clauss S, Sachdev V, Smith ACM, Perry MB, Brewer CC, Zalewski C, Kim HJ, Solomon B, Brooks BP, Gerber LH, Turner ML, Domingo DL, Hart TC, Graf J, Reynolds JC, Gropman A, Yanovski JA, Gerhard-Herman M, Collins FS, Nabel EG, Cannon RO, Gahl WA & Introne WJ (2008) Phenotype and Course of Hutchinson–Gilford Progeria Syndrome. *N. Engl. J. Med.* 358, 592–604.

Miano JM (2003) Serum response factor: Toggling between disparate programs of gene expression. *J. Mol. Cell. Cardiol.* 35, 577–593.

Mitchell GF, Hwang SJ, Vasan RS, Larson MG, Pencina MJ, Hamburg NM, Vita JA, Levy D & Benjamin EJ (2010) Arterial stiffness and cardiovascular events: the Framingham Heart Study. *Circulation* 121, 505–511.

Mithieux SM & Weiss AS (2005) Elastin. In *Advances in protein chemistry*. pp.437–461.

Monnerat G, Evaristo GPC, Evaristo JAM, dos Santos CGM, Carneiro G, Maciel L, Carvalho VO, Nogueira FCS, Domont GB & Campos de Carvalho AC (2019) Metabolomic profiling suggests systemic signatures of premature aging induced by Hutchinson–Gilford progeria syndrome. *Metabolomics* 15.

Moon HJ, Finney J, Xu L, Moore D, Welch DR & Mure M (2013) MCF-7 cells expressing nuclear associated lysyl oxidase-like 2 (LOXL2) exhibit an epithelial-to-Mesenchymal transition (EMT) phenotype and are highly invasive in Vitro. *J. Biol. Chem.* 288, 30000–30008.

Morgan KG (1990) The role of calcium in the control of vascular tone as assessed by the Ca2+ indicator aequorin. *Cardiovasc. Drugs Ther.* 4, 1355–1362.

Mottram PM, Haluska BA, Leano R, Carlier S, Case C & Marwick TH (2005) Relation of arterial stiffness to diastolic dysfunction in hypertensive heart disease. *Heart* 91, 1551–1556.

Murtada S-I, Kawamura Y, Caulk AW, Ahmadzadeh H, Mikush N, Zimmerman K, Kavanagh D, Weiss D, Latorre M, Zhuang ZW, Shadel GS, Braddock DT & Humphrey JD (2020) Paradoxical aortic stiffening and subsequent cardiac dysfunction in Hutchinson–Gilford progeria syndrome. *J. R. Soc. Interface* 17, 20200066.

Navarro CL, Cadiñanos J, De Sandre-Giovannoli A, Bernard R, Courrier S, Boccaccio I, Boyer A, Kleijer WJ, Wagner A, Giuliano F, Beemer FA, Freije JM, Cau P, Hennekam RCM, López-Otín C, Badens C & Lévy N (2005) Loss of ZMPSTE24 (FACE-1) causes autosomal recessive restrictive dermopathy and accumulation of Lamin A precursors. *Hum. Mol. Genet.* 14, 1503–1513.

Navarro CL, De Sandre-Giovannoli A, Bernard R, Boccaccio I, Boyer A, Geneviève D, Hadj-Rabia S, Gaudy-Marqueste C, Smitt HS, Vabres P, Faivre L, Verloes A, Van Essen T, Flori E, Hennekam R, Beemer FA, Laurent N, Le Merrer M, Cau P & Lévy N (2004) Lamin A and ZMPSTE24 (FACE-1) defects cause nuclear disorganization and identify restrictive dermopathy as a lethal neonatal laminopathy. *Hum. Mol. Genet.* 13, 2493–2503.

Nilsson M, Adamo H, Bergh A, Halin Bergström S & Kim Y (2016) Inhibition of Lysyl Oxidase and Lysyl Oxidase-Like Enzymes Has Tumour-Promoting and Tumour-Suppressing Roles in Experimental Prostate Cancer. *Sci. Rep.* 6, 19608.

Nissan X, Blondel S, Navarro C, Maury Y, Denis C, Girard M, Martinat C, De Sandre-Giovannoli A, Levy N & Peschanski M (2012) Unique preservation of neural cells in hutchinson- gilford progeria syndrome is due to the expression of the neural-specific miR-9 microRNA. *Cell Rep.* 2, 1–9.

Noblesse E, Cenizo V, Bouez C, Borel A, Gleyzal C, Peyrol S, Jacob MP, Sommer P & Damour O (2004) Lysyl oxidase-like and lysyl oxidase are present in the dermis and epidermis of a skin equivalent and in human skin and are associated to elastic fibers. *J. Invest. Dermatol.* 122, 621–630.

O'Callaghan CJ & Williams B (2000) Mechanical Strain–Induced Extracellular Matrix Production by Human Vascular Smooth Muscle Cells. *Hypertension* 36.

Olive M, Harten I, Mitchell R, Beers JK, Djabali K, Cao K, Erdos MR, Blair C, Funke B, Smoot L, Gerhard-Herman M, Machan JT, Kutys R, Virmani R, Collins FS, Wight TN, Nabel EG & Gordon LB (2010) Cardiovascular Pathology in Hutchinson-Gilford Progeria: Correlation With the Vascular Pathology of Aging. *Arterioscler. Thromb. Vasc. Biol.* 30.

Osmanagic-Myers S, Kiss A, Manakanatas C, Hamza O, Sedlmayer F, Szabo PL, Fischer I, Fichtinger P, Podesser BK, Eriksson M & Foisner R (2018) Endothelial progerin expression causes cardiovascular pathology through an impaired mechanoresponse. *J. Clin. Invest.* 129, 531–545.

Osorio FG, Navarro CL, Cadinanos J, Lopez-Mejia IC, Quiros PM, Bartoli C, Rivera J, Tazi J, Guzman G, Varela I, Depetris D, de Carlos F, Cobo J, Andres V, De Sandre-Giovannoli A, Freije JMP, Levy N & Lopez-Otin C (2011) Splicing-Directed Therapy in a New Mouse Model of Human Accelerated Aging. *Sci. Transl. Med.* 3, 106ra107-106ra107.

Owens GK, Kumar MS & Wamhoff BR (2004) Molecular regulation of vascular smooth muscle cell differentiation in development and disease. *Physiol. Rev.* 84, 767–801.

Pacheco LM, Gomez LA, Dias J, Ziebarth NM, Howard GA & Schiller PC (2014) Progerin expression disrupts critical adult stem cell functions involved in tissue repair. *Aging (Albany. NY).* 6, 1049–1063.

Pegoraro G, Kubben N, Wickert U, Göhler H, Hoffmann K & Misteli T (2009) Ageing-related chromatin defects through loss of the NURD complex. *Nat. Cell Biol.* 11, 1261–1267.

Pellegrini C, Columbaro M, Capanni C, D'Apice MR, Cavallo C, Murdocca M, Lattanzi G & Squarzoni S (2015) All-trans retinoic acid and rapamycin normalize Hutchinson

Gilford progeria fibroblast phenotype. *Oncotarget* 6, 29914–29928.

Pendás AM, Zhou Z, Cadiñanos J, Freije JMP, Wang J, Hultenby K, Astudillo A, Wernerson A, Rodríguez F, Tryggvason K & López-Otín C (2002) Defective prelamin A processing and muscular and adipocyte alterations in Zmpste24 metalloproteinase-deficient mice. *Nat. Genet.* 31, 94–99.

Petersen E, Wågberg F & Ängquist KA (2002) Serum concentrations of elastin-derived peptides in patients with specific manifestations of atherosclerotic disease. *Eur. J. Vasc. Endovasc. Surg.* 24, 440–444.

Prakash A, Gordon LB, Kleinman ME, Gurary EB, Massaro J, D'Agostino R, Kieran MW, Gerhard-Herman M & Smoot L (2018) Cardiac Abnormalities in Patients With Hutchinson-Gilford Progeria Syndrome. *JAMA Cardiol.* 3, 326.

Prockop DJ & Kivirikko KI (1995) Collagens: molecular biology, diseases, and potentials for therapy. *Annu Rev Biochem* 64, 403–434.

Rensen SSM, Doevendans PAFM & van Eys GJJM (2007) Regulation and characteristics of vascular smooth muscle cell phenotypic diversity. *Neth. Heart J.* 15, 100–8.

Reusch HP, Chan G, Ives HE & Nemenoff RA (1997) Activation of JNK/SAPK and ERK by mechanical strain in vascular smooth muscle cells depends on extracellular matrix composition. *Biochem. Biophys. Res. Commun.* 237, 239–244.

Reusch P, Wagdy H, Reusch R, Wilson E & Ives HE (1996) Mechanical strain increases smooth muscle and decreases nonmuscle myosin expression in rat vascular smooth muscle cells. *Circ. Res.* 79, 1046–1053.

Ricard-Blum S (2011) The Collagen Family. *Cold Spring Harb. Perspect. Biol.* 3, 1–19.

Ringvold HC & Khalil RA (2017) Protein Kinase C as Regulator of Vascular Smooth

Muscle Function and Potential Target in Vascular Disorders. In *Advances in Pharmacology*. Academic Press Inc., pp.203–301.

Rork JF, Huang JT, Gordon LB, Kleinman M, Kieran MW & Liang MG (2014) Initial cutaneous manifestations of hutchinson-gilford progeria syndrome. *Pediatr. Dermatol.* 31, 196–202.

Rzucidlo EM, Martin KA & Powell RJ (2007) Regulation of vascular smooth muscle cell differentiation. *J. Vasc. Surg.* 45, A25–A32.

De Sandre-Giovannoli A, Bernard R, Cau P, Navarro C, Amiel J, Boccaccio I, Lyonnet S, Stewart CL, Munnich A, Le Merrer M & Lévy N (2003) Lamin A truncation in Hutchinson-Gilford progeria. *Science (80-.).* 300, 2055.

Santiago-Fernández O, Osorio FG, Quesada V, Rodríguez F, Basso S, Maeso D, Rolas L, Barkaway A, Nourshargh S, Folgueras AR, Freije JMP & López-Otín C (2019) Development of a CRISPR/Cas9-based therapy for Hutchinson–Gilford progeria syndrome. *Nat. Med.* 25, 423–426.

Saxena S & Kumar S (2020) Pharmacotherapy to gene editing: potential therapeutic approaches for Hutchinson–Gilford progeria syndrome. *GeroScience* 42, 467–494.

Scaffidi P & Misteli T (2006) Lamin A-Dependent Nuclear Defects in Human Aging. *Science (80-.).* 312, 1059–1063.

Sharma-Bhandari A, Park SH, Kim JY, Oh J & Kim Y (2015) Lysyl oxidase modulates the osteoblast differentiation of primary mouse calvaria cells. *Int. J. Mol. Med.* 36, 1664–1670.

Shaw LM & Olsen BR (1991) FACIT collagens: diverse molecular bridges in extracellular matrices. *Trends Biochem. Sci.* 16, 191–194.

Shumaker DK, Dechat T, Kohlmaier A, Adam SA, Bozovsky MR, Erdos MR, Eriksson M,

Goldman AE, Khuon S, Collins FS, Jenuwein T & Goldman RD (2006) Mutant nuclear lamin A leads to progressive alterations of epigenetic control in premature aging. *Proc. Natl. Acad. Sci. U. S. A.* 103, 8703–8708.

Sinha JK, Ghosh S & Raghunath M (2014) Progeria: A rare genetic premature ageing disorder. *Indian J. Med. Res.* 139, 667–674.

Somlyo A V., Khromov AS, Webb MR, Ferenczi MA, Trentham DR, He ZH, Sheng S, Shao Z & Somlyo AP (2004) Smooth muscle myosin: Regulation and properties. In *Philosophical Transactions of the Royal Society B: Biological Sciences*. Royal Society, pp.1921–1930.

van Steensel B & Belmont AS (2017) Lamina-Associated Domains: Links with Chromosome Architecture, Heterochromatin, and Gene Repression. *Cell* 169, 780–791.

Steppan J, Wang H, Bergman Y, Rauer MJ, Tan S, Jandu S, Nandakumar K, Barreto-Ortiz S, Cole RN, Boronina TN, Zhu W, Halushka MK, An SS, Berkowitz DE & Santhanam L (2019) Lysyl oxidase-like 2 depletion is protective in age-associated vascular stiffening. *Am. J. Physiol. Circ. Physiol.* 317, H49–H59.

Szamosi T, Szollár J, Meggyesi V, Wilhelm O, Bodánszky H & Mátyus J (1984) Serum cholesterol and triglyceride levels in progeria as a model of ageing. *Mech. Ageing Dev.* 28, 243–248.

Szasz T & Webb RC (2017) Rho-Mancing to Sensitize Calcium Signaling for Contraction in the Vasculature: Role of Rho Kinase. In *Advances in Pharmacology*. Academic Press Inc., pp.303–322.

Tonino P, Simon M & Craig R (2002) Mass determination of native smooth muscle myosin filaments by scanning transmission electron microscopy. *J. Mol. Biol.* 318,

999–1007.

Torres S, Garcia-Palmero I, Herrera M, Bartolomé RA, Peña C, Fernandez-Aceñero MJ, Padilla G, Peláez-García A, Lopez-Lucendo M, Rodriguez-Merlo R, García De Herreros A, Bonilla F & Ignacio Casal J (2015) LOXL2 is highly expressed in cancer-associated fibroblasts and associates to poor colon cancer survival. *Clin. Cancer Res.* 21, 4892–4902.

Toth JI, Yang SH, Qiao X, Beigneux AP, Gelb MH, Moulson CL, Miner JH, Young SG & Fong LG (2005) Blocking protein farnesyltransferase improves nuclear shape in fibroblasts from humans with progeroid syndromes. *Proc. Natl. Acad. Sci. U. S. A.* 102, 12873–12878.

Trackman PC (2016) Lysyl Oxidase Isoforms and Potential Therapeutic Opportunities for Fibrosis and Cancer. *Expert Opin. Ther. Targets* 20, 935–945.

Tsamis A, Krawiec JT & Vorp DA (2013) Elastin and collagen fibre microstructure of the human aorta in ageing and disease: a review. *J. R. Soc. Interface* 10, 20121004.

Uitto J, Christiano AM, Kahari VM, Bashir MM & Rosenbloom J (1991) Molecular biology and pathology of human elastin. In *Biochemical Society Transactions*. Biochem Soc Trans, pp.824–829.

Ullrich NJ & Gordon LB (2015) Hutchinson-Gilford progeria syndrome. In *Handbook of Clinical Neurology*. Elsevier B.V., pp.249–264.

Varela I, Pereira S, Ugalde AP, Navarro CL, Suárez MF, Cau P, Cadiñanos J, Osorio FG, Foray N, Cobo J, De Carlos F, Lévy N, Freije JMP & López-Otín C (2008) Combined treatment with statins and aminobisphosphonates extends longevity in a mouse model of human premature aging. *Nat. Med.* 14, 767–772.

Varga R, Eriksson M, Erdos MR, Olive M, Harten I, Kolodgie F, Capell BC, Cheng J,

Faddah D, Perkins S, Avallone H, San H, Qu X, Ganesh S, Gordon LB, Virmani R, Wight TN, Nabel EG & Collins FS (2006) Progressive vascular smooth muscle cell defects in a mouse model of Hutchinson–Gilford progeria syndrome.

Verstraeten VLRM, Ji JY, Cummings KS, Lee RT & Lammerding J (2008) Increased mechanosensitivity and nuclear stiffness in Hutchinson-Gilford progeria cells: effects of farnesyltransferase inhibitors. *Aging Cell* 7, 383–93.

Villa-Bellosta R, Rivera-Torres J, Osorio FG, Acín-Pérez R, Enriquez JA, López-Otín C, Andrés V, Sandre-Giovannoli A De, Bernard R, Cau P, Navarro C, et al. (2013) Defective extracellular pyrophosphate metabolism promotes vascular calcification in a mouse model of Hutchinson-Gilford progeria syndrome that is ameliorated on pyrophosphate treatment. *Circulation* 127, 2442–51.

Vrhovski B & Weiss AS (1998) Biochemistry of tropoelastin. *Eur. J. Biochem.* 258, 1–18.

Wagenseil JE & Mecham RP (2012) Elastin in large artery stiffness and hypertension. *J. Cardiovasc. Transl. Res.* 5, 264–73.

Wagenseil JE & Mecham RP (2009) Vascular extracellular matrix and arterial mechanics. *Physiol. Rev.* 89, 957–89.

Wang Z, Wang D-Z, Pipes GCT & Olson EN (2003) Myocardin is a master regulator of smooth muscle gene expression. *Proc. Natl. Acad. Sci. U. S. A.* 100, 7129–34.

Webb RC (2003) Smooth muscle contraction and relaxation. In *American Journal of Physiology - Advances in Physiology Education*. American Physiological Society, pp.201–206.

Xu J & Shi G-P (2014) Vascular wall extracellular matrix proteins and vascular diseases. *Biochim. Biophys. Acta* 1842, 2106–2119.

Yamauchi M & Sricholpech M (2012) Lysine post-translational modifications of collagen.

Essays Biochem. 52, 113–133.

Yang SH, Andres DA, Spielmann HP, Young SG & Fong LG (2008) Progerin elicits disease phenotypes of progeria in mice whether or not it is farnesylated. *J. Clin. Invest.* 118, 3291–3300.

Yang SH, Bergo MO, Toth JI, Qiao X, Hu Y, Sandoval S, Meta M, Bendale P, Gelb MH, Young SG & Fong LG (2005) Blocking protein farnesyltransferase improves nuclear blebbing in mouse fibroblasts with a targeted Hutchinson-Gilford progeria syndrome mutation. *Proc. Natl. Acad. Sci. U. S. A.* 102, 10291–10296.

Yang SH, Chang SY, Ren S, Wang Y, Andres DA, Spielmann HP, Fong LG & Young SG (2011) Absence of progeria-like disease phenotypes in knock-in mice expressing a non-farnesylated version of progerin. *Hum. Mol. Genet.* 20, 436–444.

Yang SH, Meta M, Qiao X, Frost D, Bauch J, Coffinier C, Majumdar S, Bergo MO, Young SG & Fong LG (2006) A farnesyltransferase inhibitor improves disease phenotypes in mice with a Hutchinson-Gilford progeria syndrome mutation. *J. Clin. Invest.* 116, 2115–2121.

Zaghini A, Sarli G, Barboni C, Sanapo M, Pellegrino V, Diana A, Linta N, Rambaldi J, D'Apice MR, Murdocca M, Baleani M, Baruffaldi F, Fognani R, Mecca R, Festa A, Papparella S, Paciello O, Prisco F, Capanni C, Loi M, Schena E, Lattanzi G & Squarzoni S (2020) Long term breeding of the Lmna G609G progeric mouse: Characterization of homozygous and heterozygous models. *Exp. Gerontol.* 130, 110784.

Zhang C (2009) MicroRNA-145 in vascular smooth muscle cell biology: A new therapeutic target for vascular disease. *Cell Cycle* 8, 3469–3473.

Zhu Y, Qu J, He L, Zhang F, Zhou Z, Yang S & Zhou Y (2019) Calcium in Vascular

Smooth Muscle Cell Elasticity and Adhesion: Novel Insights Into the Mechanism of Action. *Front. Physiol.* 10, 852.

Chapter 2: Arterial stiffness and cardiac dysfunction in Hutchinson-Gilford Progeria Syndrome corrected by inhibition of Lysyl Oxidase

Ryan von Kleeck[1,2], Emilia Roberts[1,3], Paola Castagnino[1,3], Kyle Bruun[1], Sonja A. Brankovic[1,2], Elizabeth A. Hawthorne[1], Tina Xu[1], John W. Tobias[4], and Richard K. Assoian[1-3]

[1]Department of Systems Pharmacology and Translational Therapeutics, [2]Center for Engineering MechanoBiology, [3]Institute of Translational Medicine and Therapeutics, and [4]Penn Genomic Analysis Core and University of Pennsylvania, Philadelphia PA 19104

Research adapted from published work:

Ryan von Kleeck, Emilia Roberts, Paola Castagnino, Kyle Bruun, Sonja Brankovic, Elizabeth A Hawthorne, Tina Xu, John W Tobias, Richard K Assoian

Life Science Alliance Mar 2021, 4 (5) e202000997; DOI: 10.26508/lsa.202000997

2.1 Abstract

Arterial stiffening and cardiac dysfunction are hallmarks of premature aging in Hutchinson-Gilford Progeria Syndrome (HGPS), but the molecular regulators remain unknown. Here, we show that the LaminA^{G609G} mouse model of HGPS recapitulates the premature arterial stiffening and early diastolic dysfunction seen in human HGPS. Lysyl oxidase (LOX) is upregulated in the arteries of these mice, and treatment with the LOX inhibitor, β-aminopropionitrile, improves arterial mechanics and cardiac function. Genome-wide and mechanistic analysis revealed reduced expression of the LOX-regulator, miR-145, in HGPS arteries, and forced expression of miR-145 restores normal LOX gene expression in HGPS smooth muscle cells. LOX abundance is also increased in the carotid arteries of aged wild-type mice, but its spatial expression differs from HGPS and its upregulation is independent of changes in miR-145 abundance. Our results show that miR145 is selectively misregulated in HGPS and that the consequent upregulation of LOX is causal for premature arterial stiffening and cardiac dysfunction.

2.2 Introduction

Hutchinson-Gilford Progeria Syndrome (HGPS) is a rare genetic disease of premature aging. HGPS is caused by an autosomal dominant mutation in *LMNA*, the gene encoding Lamin A (Gonzalo et al. 2016; Capell et al. 2007). The mutation is "silent" (LaminA^{G608G}) but leads to a defect in biosynthetic processing of the Lamin A precursor and results in a truncated, farnesylated version of Lamin A called Progerin, that is defective in its localization within the nucleus (Gonzalo et al. 2016; Capell et al. 2007). Children with HGPS typically die in their teenage years as a consequence of cardiovascular disease (atherosclerosis, myocardial infarction, heart failure, and/or stroke) (Gonzalo et al. 2016; Capell et al. 2007). These cardiovascular consequences occur in the absence of high cholesterol or triglycerides (Gordon et al. 2005), suggesting that cholesterol-independent risk factors must be at play.

Intriguingly, the arteries of HGPS patients are abnormally stiff (Gerhard-Herman et al. 2011), and arterial stiffness is a cholesterol-independent risk factor for cardiovascular disease (Mitchell et al. 2010). Increased arterial stiffness is also a hallmark of normal aging and increases substantially after the age of 50 in healthy males and females (Mitchell et al. 2007). However, the arterial stiffness in HGPS children resembles that of ~60 year-old individuals (Gerhard-Herman et al. 2011), indicating a striking acceleration of arterial stiffening. Pathologically stiff arteries increase load on the heart (Safar 2010; Laurent & Boutouyrie 2015), which can then have systemic consequences and correlates with cardiac abnormalities such as left ventricular hypertrophy and diastolic dysfunction (Mottram et al. 2005; Kim et al. 2017). Consistent

with these relationships, left ventricular hypertrophy and, particularly, diastolic dysfunction are also observed in HGPS children (Prakash et al. 2018).

The composition of the extracellular matrix (ECM) plays a critical role in arterial stiffness (Cox & Erler 2011). The stiffness of the major arteries relies on a balance of elastin and collagen fibers (Humphrey et al. 2014), which maintains a proper response to blood pressure. Elastin allows for recoil at lower load and dampens cyclic loading from the beating heart while fibrillar collagens contribute to the strain-stiffening property of arteries at high load (Kohn et al. 2015). Arteries express three main fibrillar collagens, with collagen-I>collagen-III>collagen-V in abundance (Hulmes 2008; Prockop & Kivirikko 1995). Increased collagen deposition as well as elastin fragmentation has been observed in the arteries of HGPS children at autopsy (Olive et al. 2010; Merideth et al. 2008) and in aged arteries (Kohn et al. 2015; Tsamis et al. 2013).

In addition to increases in fibrillar collagens, the mechanical properties of tissues are regulated by matrix remodeling enzymes (Freitas-Rodríguez et al. 2017; Lampi & Reinhart-King 2018), especially Lysyl Oxidase (LOX) and its family members (LOXL1, LOXL2, LOXL3 and LOXL4) (Yamauchi & Sricholpech 2012; Nilsson et al. 2016; Steppan et al. 2019). These enzymes covalently cross-link newly synthesized collagen and elastin fibers to enhance their stability and tensile strength (Tsamis et al. 2013; Baker et al. 2013; Herchenhan et al. 2015), and LOX overexpression is commonly seen in stiffness-related pathologies (Desmoulière et al. 1997; Kagan 1994). However, since elastin biosynthesis ends early in life (Tsamis et al. 2013; Wagenseil & Mecham 2012; Davidson et al. 1986; Mithieux & Weiss 2005; Kelleher et al. 2004), LOX-mediated crosslinking is thought to target newly synthesized collagens in normal aging and promote arterial stiffening.

Since HGPS is a very rare genetic disease (Gerhard-Herman et al. 2011; Olive et al. 2010) the number of HGPS patients is very small and the detailed analysis of early and potentially causal events in the pathogenesis of HGPS must rely heavily on animal models. Osorio et al. (Osorio et al. 2011) developed a knock-in mouse (hereafter called HGPS mouse) that models the human disease by expressing murine Progerin ($Lmna^{G609G/G609G}$) at the endogenous *Lmna* locus. These mice display many traits of the human disease including premature death. Arterial stiffening, left ventricular diastolic dysfunction, and an increase in the expression of several collagens, including collagen-III, IV, and V is also apparent in these mice near the end of their lifespan (del Campo et al. 2019; Murtada et al. 2020). Whether these changes are primary or secondary effects of progerin expression is not known.

In this chapter, I have examined arterial mechanics, cardiac function, and molecular mechanism in young HGPS mice (2-months of age, before the onset of morbidity) in an effort to identify early and potentially causal events in disease progression. We report that arterial stiffening in HGPS is strikingly premature and associated with diastolic dysfunction. Arterial LOX is strongly upregulated in these young mice, and systemic LOX inhibition improves arterial mechanics and cardiac function. Genome-wide profiling and cell-based mechanistic analysis indicates that a pathologic misregulation of miR-145 in HGPS is a critical and selective determinant of elevated LOX expression.

2.3 Results

Premature arterial stiffening in HGPS mice. I began my studies of arterial stiffening in HGPS by comparing mechanics and ECM remodeling in the arteries of WT mice versus the Progerin-expressing HGPS mouse. I focused on the carotid artery, a prominent site of atherosclerotic lesion formation, as its occlusion is thought to be responsible for induction of stroke in HGPS children (Gerhard-Herman et al. 2011). Freshly isolated carotid arteries were stretched below, at, and above their *in vivo* lengths at constant pressure to provide insight into axial arterial stress (Fig. 2.01A1, left). The artery was also stretched to its *in vivo* length (referred to as the In Vivo Stretch; IVS), and then pressurized incrementally to provide insight into circumferential vessel mechanics (Fig. 2.01A2, right). Changes in outer diameter, wall thickness, and inner radius were used to generate axial and circumferential stress-stretch relationships, in which axial and circumferential stiffness is represented as the stress the artery experiences for a defined increase in stretch. These stress-stretch data were also used to derive the axial and circumferential tangent modulus (vs. stretch), an additional way to estimate arterial stiffness.

Brankovic et al. (2019) recently used these analyses to examine the mechanical and geometric properties of carotid arteries of C57BL/6 mice aged from 2-24 months; the results showed decreases in IVS as well as increased axial and circumferential arterial stiffness with age, beginning at 12-months and becoming even more evident by 24 months (Brankovic et al. 2019). Therefore, young (2-month) HGPS mice and 24-month WT mice were compared to understand how arterial mechanics are affected early

in HGPS and how they compare to the changes that occur in normal aging. Additionally, use of the Progerin-expressing HGPS mouse allowed me to analyze sex differences in arterial biomechanics that have not been attainable given the small numbers of HGPS girls and boys.

Changes in outer diameter, inner radius, and wall thickness with pressure (Fig. 2.02A-F) were measured and used to establish stress-stretch relationships in carotid arteries from 2-month WT and HPGS mice. The circumferential stress-stretch (Fig. 2.01B and D) and tangent modulus (Fig. 2.03B and D) curves of young HGPS and aged WT mice were left-shifted for both sexes indicating increased circumferential stiffness. Axially, the IVS was reduced in HGPS male and female mice, but the magnitude was less than that seen in old WT mice of either sex (Table 1). The axial stress-stretch (Fig. 2.01C and E) and tangent modulus (Fig. 2.03A and C) curves suggested that axial stiffening can occur early in HGPS but may be less prominent than circumferential stiffening, particularly in the males. Collectively, these data indicate that arterial stiffening in HGPS mice is premature as it is in the human syndrome, but the early effect is anisotropic, especially in males, an insight that has not been obtainable by pulse-wave velocity studies of HGPS children (Gerhard-Herman et al. 2011).

Osorio et al. (2011) have reported that heterozygous HGPS mice begin to display a delayed decline in weight at around 8-months of age with an average survival of approximately 240 days. Changes in carotid artery outer diameter, inner radius, and wall thickness with pressure were analyzed in 2- and 9- month male heterozygous HGPS ($LMNA^{+/G609G}$) mice (Fig. 2.04A-C). Interestingly, 2-month male heterozygous HGPS mice displayed similar circumferential stress-stretch relationships as 2-month male WT mice but the circumferential stiffening effect was observed by 9-months of age (compare

Figs. 2.01 and 2.04D). However, heterozygous HGPS mice also displayed a significant decrease in IVS (Table 2) and increase in axial arterial stiffness at 9 months (Fig. 2.04E), effects that were not seen in the 2-month male homozygous mice (Table 1 and Fig. 2.01). This suggests that a single copy of progerin also produces increased arterial stiffening and that the effect is delayed relative to the homozygous male mice. However, it is important to note at this 9-month timepoint it is difficult to tease out the contribution of arterial stiffening from aging versus progerin expression. Further comparisons of arterial mechanics in WT mice at 9-months may be an interesting matter for future study,

Although reduced smooth muscle cell (SMC) number has been reported in the ascending aorta of HGPS children at autopsy (Hamczyk & Andrés 2019), histological analysis of 2-month WT and HGPS carotid arteries showed similar cellularity (Fig. 2.05A) and numbers of SMC nuclei in the medial layer of young mouse carotids (Fig. 2.05B). We observed a small increase in the abundance of the senescence marker $p16^{INK4A}$ in the carotid medial layer of 2-month HGPS mice (Fig. 2.05C-D), but other markers of late HGPS vascular lesions including increases in calcium content (Merideth et al. 2008; Olive et al. 2010), apoptotic cells, and changes in elastin integrity were not seen in the HGPS carotid arteries at this early time-point (Figs. 2.05E-F and 2.06A-C). Collectively, these results indicate that arterial stiffening is a very early event in the progression of HGPS and that our experimental conditions have the potential to identify initiating events before the onset of gross HGPS arterial pathology.

Canonical upregulation of fibrillar collagens is lacking in early HGPS. Tissue remodeling and stiffening often involves increased amounts of fibrillar collagens and/or elastin fragmentation. Collagen-I is the major strain-stiffening component of the arterial ECM,

but an immunostaining analysis of carotid sections was unable to detect statistically significant increases in collagen-I in either the medial or adventitial layers of 2-month male HGPS carotid arteries as compared to age- and sex-matched WT controls (Figs. 2.07A-B and 2.08A-B). Of the minor fibrillar collagens, these young HGPS carotid arteries showed a statistically significant but small increase in medial collagen-III and no change in the abundance of collagen-V (Figs. 2.07A-B and 2.08). Second harmonic generation (SHG) imaging was performed collecting both forward and backward scatter in order to capture collagen structure at multiple distances within the sample and detect fibers at different optical alignments (Williams et al. 2005). SHG showed that fibrillar collagen was much more abundant in the adventitia than the media for all samples. I saw no dramatic changes in SHG signals in the media layer of 2-month WT and HGPS carotid arteries. (Fig. 2.09). Thus, the SHG results indicated that collagen structure was similar in the carotid arteries of 2-month male WT and HGPS mice. Higher resolution analysis by Transmission Electron Microscopy (TEM; Fig. 2.10A) did allow for a more detailed analysis of collagen between the two genotypes (Fig. 2.10B-C). Similar to observations in humans (Greenberg 1986), TEM revealed that collagen in the medial layer of both WT and HGPS mouse carotid arteries was restricted to the elastin folds (Fig. 2.10A). While the area of collagen within these folds was significantly greater in HGPS, the magnitude of the effect was small (Fig. 2.10B-C).

Upregulation of Lysyl Oxidase is an early event in HGPS and causal for premature arterial stiffening. In contrast to the results with collagens, immunostaining readily detected a pronounced increase in abundance of LOX in the medial layer of carotid arteries from 2-month HGPS mice as compared to age-matched WT mice (Fig. 2.07C-

D). To determine the onset of this LOX upregulation in HGPS, we examined LOX abundance in 1-month mice. Although medial LOX levels were slightly increased in 1-month HGPS mice, the effect was not significant and much less pronounced than at 2 months (Fig. 2.07C-D). Adventitial LOX abundance was not affected by age or genotype (Fig 2.07C-D).

To determine if the minimal increase in abundance of LOX in 1-month HGPS mice correlated with changes in arterial stiffening, pressure-outer diameter, inner radius, and wall thickness measurements (Fig. 2.11A-C) were used to generate circumferential and axial stress-stretch (Fig. 2.11D-E) and tangent modulus (Fig. 2.11F-G) curves for these very young WT and HGPS mice. The pronounced genotype differences in the circumferential stress-stretch relationship (compare Fig. 2.01 and 2.11E) and tangent modulus curves (Fig. 2.11G) were much attenuated at 1 month. Axial arterial mechanics in 1-month HGPS carotid arteries, as judged by the IVS (Table 3) and stress-stretch and tangent modulus curves (Fig. 2.11D and F), were similar to the WT controls. Thus, the molecular analysis (Fig. 2.07C-D) and functional testing (Fig. 2.01 and 2.11) are in agreement and indicate that the time-dependent increase in medial LOX abundance in HGPS mice begins between 1-2 months of age and is coincident with the onset of acute arterial stiffening.

HGPS mice were treated with the highly selective LOX enzymatic inhibitor, β-aminopropionitrile (BAPN) (Finney et al. 2014; Tang et al. 1983; Jung et al. 2003; Kim et al. 2003; Lee & Kim 2006; Rodriguez et al. 2010) to determine the role of lysyl oxidase activity in the early arterial stiffening of HGPS. BAPN was administered between 1 and 2-months of age, when the levels of medial LOX are increasing (Fig. 2.07C-D). The BAPN concentration and injection regime used was previously shown to be effective in

altering fibrillar collagen structure and reducing arterial stiffness in vivo (Kothapalli et al. 2012). Furthermore, SHG imaging revealed a reduction in SHG signal in the adventitial layer of BAPN-treated HGPS carotid arteries, confirming that our dosing regimen was sufficient to reduce fibrillar collagen structure (Fig. 2.12). However, the area of collagen within the medial elastin folds of carotid arteries was similar with or without BAPN treatment as was the expression of arterial LOX (Fig. 2.13A-D).

Biaxial inflation-extension tests examined the effect of LOX inhibition on arterial mechanics of the HGPS carotid arteries. Pressure-outer diameter, inner radius and wall thickness measurements (Fig. 2.14A-C) were used to generate circumferential and axial stress-stretch curves (Fig. 2.15A-B), and these (together with the corresponding tangent modulus graphs; Fig. 2.14D-E) showed that BAPN reduced circumferential stiffness of the HGPS carotid arteries without comparable effect on the WT controls (Figs. 2.15A-B and 2.14D). In fact, the circumferential stretch of BAPN-treated HGPS mice showed no statistical difference from those of WT mice treated with PBS (Fig. 2.15A and 2.14D). The IVS was not affected by BAPN (Table 4), but curiously, the axial stress-stretch curves showed small but opposing effects in HGPS and WT mice (Fig. 2.15B and 2.14E). Collectively, the elevated expression of LOX coincident with premature circumferential arterial stiffening and the correction of this defect by BAPN indicates that early LOX induction plays an important causal role in the premature circumferential arterial stiffening of HPGS.

In addition to arterial stiffness, HGPS patients display cardiac abnormalities, particularly diastolic dysfunction, which may increase the risk for death (Prakash et al. 2018; Halley et al. 2011). As diastolic dysfunction has been positively correlated with arterial stiffness (Mottram et al. 2005; Kim et al. 2017), we asked if the BAPN-mediated

reduction in circumferential arterial stiffness of HGPS mice was also associated with improved diastolic function. HGPS mice were treated with vehicle or BAPN using conditions shown in Figs. 2.15A-B. Echocardiography was performed to measure E (mitral peak velocity of early filling) and E' (early diastolic mitral annular velocity) (Fig. 2.16A-B). We then determined (E/E') as a measure of diastolic dysfunction. E/E' was improved in the BAPN-treated HGPS mice and similar to that of age-and sex-matched WT mice (Fig. 2.15C). Although less common, left ventricular hypertrophy has been detected in HGPS children, mostly as they age (Prakash et al. 2018). Consistent with these studies, the left ventricular mass index (LVMI), a marker of LV hypertrophy, trended lower in the BAPN-treated HGPS mice. (Fig. 2.15D) Systolic, diastolic, and pulse pressures were not affected by BAPN (Fig. 2.16C-E).

To determine if BAPN treatment improved HGPS mouse lifespan, BAPN was administered to WT and HGPS mixed-sex mice starting at 1-month of age and continued until the mice became moribund. We observed no changes in survival of HGPS mice treated with BAPN (Fig. 2.17A). This could be a result of BAPN's toxic metabolite effects, as chronic administration of BAPN has well-demonstrated toxicity (Bachhuber et al. 1955; Levene 1985). However, BAPN administration did not significantly reduce WT or HGPS mouse weights in comparison to vehicle-treated mice (Fig. 2.17B). Alternatively, reducing arterial stiffness through BAPN administration may not improve lifespan because C57BL/6 mice are highly resistant to dying from cardiovascular disease (Oppi et al. 2019; von Scheidt et al. 2017). Future studies may want to explore the potential success for combination therapies (e.g. farnesyl transferase inhibitors with use of less toxic LOX inhibitors.

To determine if the morphologic and molecular characteristics of the HGPS carotid extended to other large arteries, the analyses shown in Figs. 2.05 and 2.07 were repeated in 2-month WT and HGPS aortas. Indeed, results in the aortas were similar to those seen in the carotid arteries with regard to overall morphology, SMC number, p16 expression, calcification, and apoptosis (Fig. 2.18A-F). I also found that these 2-month WT and HGPS mice had similar expression levels of collagen-I, -III and -V protein (Fig. 2.19A-B) and mRNAs (Fig. 2.19C-D) in the aortic media and adventitia, results that again resembled those seen in the carotid. The only exceptions were the modest increases in p16 and collagen-III, which were statistically significant in the HGPS carotid media but not in the aortic media (Fig. 2.18C and 2.19B, respectively). Importantly, the notably increased medial abundance of LOX in the HGPS carotid artery was also seen in the HGPS aorta (Fig. 2.20A-B and C-D). Additionally, the relatively larger aortic mass allowed us to demonstrate that the increased abundance of arterial LOX protein in HGPS was accompanied by increased LOX enzymatic activity (Fig. 2.20E).

Reduced expression of miR-145 underlies the misregulation of arterial LOX in HGPS SMCS. We used isolated aortas and primary aortic smooth muscle cells from age-matched WT and HGPS mice to explore the molecular mechanism responsible for upregulation of arterial LOX. We first found that the increased abundance of LOX protein we observed in the arterial media of 2-month HGPS mice was accompanied by an increase in medial LOX mRNA (Fig. 2.20F-G). As in the carotid, this upregulation was minimally detected in younger (1-month) HPGS mice (Fig. 2.21A.) We then extended the mRNA analysis to all of the LOX family members: LOXL4 mRNA was increased significantly in 2-month HGPS aortic media and adventitia (Fig. 2.20F-G), but a

comparison of delta-Ct values revealed that arterial expression of LOXL4 is very low relative to the LOX isoform (Fig. 2.21B). Continued mechanistic analysis therefore focused on regulation of the LOX isoform in vascular smooth muscle cells.

To identify molecular mechanism(s) upstream of LOX gene expression in HGPS, we performed a genome-wide analysis of descending aortas from 2-month WT and HGPS mice in addition to 24-month WT mice. A principal component analysis showed clustering amongst the replicates and separation between the experimental conditions (Fig. 2.22A). Using a 1.5x fold change and an adjusted p-value of <0.001 as cut-offs, we identified nearly 4,000 differentially expressed genes (DEGs) between 2-month WT and HGPS aortas, and a gene ontology analysis identified "extracellular matrix" among the most differentially expressed gene categories (Fig. 2.22B). We then used Ingenuity Pathway Analysis (IPA) to identify 852 regulators predicted to be either activated or inhibited based on the entire set of DEGs (Fig. 2.23A and Table 5). Within this list of 852, we focused on the 139 categorized as transcription regulators (which includes both transcription factors and epigenetic modifiers) and 10 categorized as microRNAs (miRs) (Fig. 2.23A-B).

The set of 139 activated or inhibited transcription regulators identified from genome-wide analysis was compared to the IPA list of 29 transcription regulators reported to be upstream of LOX (Fig. 2.23B; left). This analysis identified 8 candidate transcription regulators of LOX (Fig. 2.23B and Table 6) that were either activated or inhibited in HGPS. However, none of these were strong candidates for LOX mRNA regulation either because their predicted activation/inhibition state did not match with the upregulation of LOX mRNA in HGPS or because their reported transcriptional effects

were inconsistent with the selective upregulation of the LOX isoform we detected in HGPS (Fig. 2.20F-G and Table 6).

We then examined the 10 upstream microRNA (miR) regulators identified by IPA (Fig. 2.23B; right). All of these miRs were predicted to have an inhibited activation state (Table 5), but an analysis of LOX-targeting miRs with TargetScan indicated that only one of them, miR-145, had a highly conserved target sequence in the 3' UTR of LOX (Fig. 2.23C). The miR-145 target sequence is also absent from the LOX family members that are not strongly upregulated in HGPS. RT-qPCR extended the IPA prediction of a reduced miR-145 signature and showed that miR-145 levels are downregulated in the medial layer of 2-month HGPS aortas (Fig. 2.23D) but not in the adventitial layer (Fig. 2.23E), which (as with the protein; refer to Fig. 2.20A-B) expressed lower levels of LOX. This downregulation of medial miR-145 may be specific to the HGPS vasculature as it was not detected in two other SMC-containing tissues, intestine and bladder (Fig. 2.21C-D). The levels of miR-145 were also similar in the aortas of 1-month WT and HGPS mice (Fig. 2.21A), consistent with the absence of strongly upregulated LOX gene expression (Fig. 2.21) or arterial stiffening (Fig. 2.11) at this early 1-month time-point.

We were able to extend our results to isolated aortic SMCs. Primary SMCs from HGPS mice also displayed reduced miR-145 transcript levels (Fig. 2.24A). Moreover, ectopic expression of miR-145 in primary WT and HGPS aortic SMCs reduced the level of LOX mRNA, and the elevated expression of LOX mRNA seen in HGPS SMCs became similar to that of the WT controls (Fig. 2.24B). While these results do not exclude a possible role for aberrant transcriptional control of LOX in HGPS, they strongly support miR-145 downregulation as an important and causal regulator of arterial LOX abundance in HGPS.

As HGPS is associated with reduced expression of WT Lamin A as well as expression of progerin (see Introduction), we depleted Lamin A from WT SMCs with siRNAs and asked if reduced Lamin A abundance would be sufficient to generate the miR-145/LOX relationship seen in HGPS. Distinct Lamin A siRNAs effectively reduced Lamin A protein levels (Fig. 2.24C) but did not significantly alter the expression levels of LOX protein (Fig. 2.24C), LOX mRNA (Fig. 2.24D), or miR-145 (Fig. 2.24D). We conclude that a Progerin-mediated gain-of-function in HGPS mice is responsible for the downregulation of miR-145 and the consequent increase of LOX gene expression in HGPS.

Finally, we used TargetScan to identify several other putative miR-145 targets within the DEGs of 2-month WT and HGPS aortas (Fig. 2.25A). We selected 3 of those genes based on fold changes that were greater or equal to that of LOX and then examined changes in their mRNA levels in isolated SMCs with and without ectopic miR-145 expression. None showed the strong regulation by miR-145 seen with LOX. (Fig. 2.25B). Thus, arterial LOX mRNA appears to be a particularly strong miR-145 target in HGPS.

Distinct regulation of the ECM, Lysyl Oxidase and miR-145 in HGPS and normal aging. As many parallels have been drawn between HGPS and normal aging, we evaluated levels of the fibrillar collagens, LOX, and miR-145 in aged (24-month) WT mice (Fig. 2.26). The carotid arteries of the aged WT mice showed only small changes in medial collagen III and collagen-V (Fig. 2.26A-B). However, aged WT mice showed a statistically significant increase in adventitial collagen-I (Fig. 2.26A-B); this was not seen in HGPS (refer to Fig. 2.07). LOX protein increased with time in both the carotid medial

and adventitial layers during normal aging (Fig. 2.26C-D), whereas it was mostly limited to the carotid media in HGPS (refer to Fig. 2.07C-D). Unexpectedly, our RNASeq analysis indicated that LOX mRNA abundance was minimally altered in the aortas of 2- versus 24-month WT mice (Fig. 2.22C), and RT-qCPR showed that this change was not significant (Fig 2.26E). Similarly, arterial miR-145 levels were not decreased in aged WT mice (Fig. 2.26F). These data indicate that arterial LOX upregulation in normal aging is mechanistically distinct from that seen in HGPS. Thus, the downregulation of miR-145 and consequent steady-state increase in LOX mRNA and protein we describe in HGPS are disease-specific effects.

2.4 Discussion

We show here that the carotid arteries of HGPS mice stiffen prematurely and that this stiffening is preferentially circumferential, particularly in males. Although the expression of several arterial collagens is elevated in old HGPS mice (del Campo et al. 2019), our results show that the initiation of arterial stiffening in HGPS is much more closely associated with increased medial LOX expression. Importantly, pharmacologic intervention with the pan-LOX inhibitor, BAPN, improved arterial mechanics of HPGS mice, thereby establishing LOX upregulation as an underlying and causal mechanism in the early arterial stiffening of HGPS.

While we did not see pronounced increases in arterial fibrillar collagens early in HGPS, TEM revealed a slight increase in collagen area within the medial elastin folds of HGPS arteries. As adventitial collagen abundance was similar in WT and HGPS mice, the medial collagen in these folds may be the target of the elevated medial LOX in

HGPS. Indeed, previous studies have reported that the medial layer contributes more toward circumferential stiffening while the adventitial layer contributes more to axial mechanics (Kohn et al. 2015). Since the expression of collagen genes can increase with ECM stiffness (Kothapalli et al. 2012), the LOX-mediated increase in arterial stiffness described in our studies here with very young HGPS mice may also contribute to the eventual induction of other SMC collagens as seen when HGPS mice are aged (del Campo et al. 2019).

In addition to reducing arterial stiffness, BAPN administration also improved diastolic function in HGPS mice. Diastolic dysfunction is a prominent cardiac abnormality in both HGPS children (Prakash et al. 2018) and HGPS animal models (Osmanagic-Myers et al. 2018; Dorado et al. 2019; Murtada et al. 2020). Although the basis of diastolic dysfunction is multi-faceted, it has been correlated with increased arterial stiffness (Mottram et al. 2005; Kim et al. 2017). Thus, the reduction in arterial stiffness by BAPN may be causal for the observed improvement in diastolic function. However, it is not yet clear if our systemic administration of BAPN is affecting diastolic dysfunction indirectly through its effects on arterial stiffness, or directly through effects on LOX activity in the heart. A comparative analysis of BAPN effects on arterial versus cardiac (cardiomyocyte and cardiac fibroblast) LOX abundance and enzymatic activity, as well as the consequences of BAPN treatment for the arterial and cardiac ECMs, will be required to address this issue.

Genome-wide analysis predicted that the elevated expression of LOX in HGPS is linked causally to an abnormal downregulation of miR-145 in vascular SMCs. Others have shown that miR-145 is one of the most highly expressed microRNAs in rodent carotid arteries, where it is largely restricted to the SMCs (Cheng et al. 2009; Zhang

2009). miR-145 is thought to play a critical role in vascular smooth muscle function and a protective role preventing fibrotic ECM synthesis (Zhao et al. 2015). In addition, Faccini and colleagues (Faccini et al. 2017) identified reduced circulating levels of miR-145 as a diagnostic biomarker for coronary artery disease. Our results extend those findings to HGPS, which shows reduced aortic miR-145 abundance relative to age-matched WT arteries and isolated smooth muscle cells.

In addition to the bioinformatic prediction, a connection between miR-145 and LOX mRNA abundance has been described experimentally. We have previously reported that overexpression of miR-145 reduced LOX mRNA levels in WT SMCs (Kothapalli et al. 2012). Additionally, the same study showed that a miR-145 antagomir counteracted the suppression of LOX mRNA seen in WT SMCs having elevated miR-145. The work described here extends these studies by demonstrating that enforced expression of miR-145 restores near-normal LOX mRNA levels to HGPS SMCs. Collectively, these results strongly suggest a causal connection between the decreased expression of miR-145 and the increased expression of LOX in HGPS. A reporter assay showing that miR-145 can regulate mRNA abundance through the LOX 3'UTR would further support this connection.

Reduced expression of WT Lamin A failed to regulate miR-145 or LOX mRNA, indicating that misregulation of miR-145 and LOX in HGPS reflects a gain-of-function from progerin expression. However, how progerin may be eliciting these effects is cause for further study. As it has recently been appreciated that Lamin A and the nuclear lamina play an important role in mediating transfer of information from the cytoplasm to the nucleus, the altered nuclear structure due the presence of progerin in HGPS may hinder or promote transfer of this information across the nuclear boundary, leading to

deregulated gene expression (Kelley et al. 2011; Wilson 2018). Additionally, progerin may have a more direct effect on miR-145 expression, as recent studies have shown that HGPS nuclei have a dramatically altered epigenetic signature which can lead to improper gene silencing or activation (Arancio et al. 2014; Köhler et al. 2020). Altered LOX and miR-145 expression in HGPS could also be a secondary effect of long-term progerin expression, perhaps with progerin-expressing SMCs secreting altered chemokines to promote vascular remodeling in HGPS.

As progerin has been detected in aged tissues, cells, and atherosclerotic lesions (Scaffidi & Misteli 2006; Olive et al. 2010; McClintock et al. 2007), there has been significant interest in the idea that progerin-like splicing may contribute to phenotypes of natural aging in addition to driving early aging in HGPS. Indeed, both 2-month HGPS and 24-month WT carotid arteries display increased expression of medial LOX and increased circumferential stiffness. However, the axial mechanics of 2-month male HGPS carotid arteries are mostly intact, while 24-month male WT carotids display clear axial stiffening. This distinction implies that in addition to the common effect of increased LOX abundance, there must also be inherent differences between the early arterial stiffening in HGPS and the late arterial stiffening of normal aging. Interestingly, this distinction in the directionality of arterial stiffening is lost as HGPS progresses; HGPS mice much nearer to the end of their life display axial stiffening (Murtada et al. 2020).

Others have recently reported increased LOX and LOXL2 in old (20-22 month) versus young (3-4 month) aortas of WT mice (Steppan et al. 2019). This work complements our findings of increased LOX expression in HGPS carotid arteries, and the joint findings support the idea that increased LOX activity with age is likely to be a general feature of large artery stiffening. However, in our work, LOX, rather than LOXL2,

is the major upregulated arterial LOX family member. We also identified upregulated levels of LOXL4 mRNA in HGPS. As BAPN is an inhibitor of all LOX isoforms, we cannot exclude a potential role for LOXL4 in arterial stiffening. However, LOXL4 expression levels were much lower than the LOX isoform.

Our immunofluorescence analysis shows that LOX is induced in both the arterial medial and adventitial layers with natural aging whereas its induction is largely restricted to the media in HGPS. Finally, unlike HGPS, the levels of miR-145 are not strongly reduced in aged WT mice. The preferential expression of miR-145 by arterial SMCs (Cheng et al. 2009; Zhang 2009) could explain why we see a selective effect on medial rather than adventitial LOX in HGPS. Thus, while an increase in overall LOX activity is a common feature of arterial stiffening in both natural aging and HGPS, the uncoupling of LOX expression from miR-145, the distinct spatial expression patterns of arterial LOX, and the differences in directional arterial stiffening distinguish natural aging and HGPS. Although we show that LOX levels are not increased in other SMC-containing tissues in HGPS mice (i.e., bladder and intestine), it would be of interest to evaluate LOX and miR-145 expression levels in non-SMC containing tissues such as the skin, which also displays abnormalities in HGPS (Gonzalo et al. 2016).

Administration of sodium nitrate to HGPS mice (del Campo et al. 2019) and administration of Lonafarnib, a farnesyltransferase inhibitor, to HGPS children reduce arterial stiffness (Gordon et al. 2012; Gordon et al. 2018). Furthermore, the reduction in arterial stiffness by lonafarnib was associated with an increased lifespan of HGPS children (Gordon et al. 2018). These studies did not distinguish between effects on axial versus circumferential mechanics, nor are the mechanisms by which nitrate and lonafarnib reduce arterial stiffness fully clear. Nevertheless, these studies and this report

collectively indicate that decreasing arterial stiffness could lessen the burden of cardiovascular disease in HGPS. Our results further indicate that targeting circumferential arterial mechanics, potentially though LOX inhibition, may be an important consideration in the development of mechanically inspired therapeutics for HGPS.

2.5 Methods

Mice and artery isolation. WT C57BL/6 mice were purchased from Jackson Labs and aged to 24-months. $LMNA^{G609G/+}$ mice on the C57/BL6 background were generously provided Dr. Carlos Lopez-Otin (Universidad de Oviedo, Oviedo, Spain). Mice were genotyped by ear clipping and DNA was isolated using Puregene Core Kit A (Qiagen 1042601) according to manufacturer's instructions. DNA was amplified using the following primers (at a final concentration of 0.5µm): Forward: AAGGGGCTGGGAGGACAGAG; and Reverse: AGCATGCCATAGGGTGGAAGGA using the following PCR protocol: 95°C for 60s, [95°C for 30s, 64°C for 30s, 72°C for 30s]x35, 72°C for 120s to generate bands of 100bp for WT and 240bp for LMNAG609G. Mice were fed a chow diet ad libitum. For experiments including HGPS arteries or cells, WT littermate controls were obtained from LMNAG609G/+ matings. At the appropriate age, the mice were sacrificed by CO_2 asphyxiation, the left carotid artery was immediately removed, stripped of most fat, and used for pressure myography as outlined below. The remaining arteries were perfused in situ with PBS. The right carotid artery was then removed, cleaned in PBS and fixed in either Prefer for paraffin-embedding or TEM fixative (see below). The descending aorta was isolated from the end of the aortic arch to the diaphragm, cleaned as above, and used either for the preparation of RNA (for RT-qPCR and genome-wide analysis) or protein for immunoblotting (see below and Methods)**.** Animal protocols were approved by the University of Pennsylvania Institutional Animal Care and Use Committee. All experiments were performed on male mice unless otherwise specified in the legends.

Biaxial extension-inflation tests using a pressure myograph. Arterial mechanics were determined on a DMT 114P pressure myography with force transducer largely as described (Brankovic et al. 2019). Freshly isolated carotid arteries from WT and HGPS mice (with a mean age of 31 ± 1 days for 1-month mice, 64 ± 6 days for 2-month mice, and 726 ± 9 days for 24-month mice) were secured to 380 μm (outer diameter) cannulas using silk sutures; blood was cleared, and any remaining fat was removed. Once mounted, the arteries were visualized by light microscopy, and the unloaded/unpressurized arterial wall thickness and inner radius was measured at the axial length where the artery transitioned from being bent to straight. Arteries were brought to a stretch of 1.7 and pressurized to 100 mm Hg for 15 min with HBSS. The arteries were then preconditioned by cyclic pressurization three times from 0–140 mmHg in 1-min increments. Unloaded (unstretched and unpressurized) vessel wall thickness and outer diameter were measured in multiple sections after preconditioning and averaged for post-test data analysis.

In vivo stretch (IVS) was determined using force-length tests as described (Brankovic et al. 2019; Ferruzzi et al. 2013). Briefly, the carotid arteries were axially stretched in 10% increments at three constant pressures (90, 120, and 140 mmHg). Equilibrium force was recorded for each stretch and pressure, and the intersection of the three force-stretch curves was defined as the IVS. Loaded inner radius and wall thickness were determined from pressure-outer diameter tests with samples at their IVS and pressurized in 10-mm Hg (30-sec) steps from 0–140 mm Hg before returning the artery to 0 mm Hg (Brankovic et al. 2019). This test was performed three times, and the mean of three stress-stretch curves was taken. We confirmed the validity of our IVS

determinations by measuring axial force through the circumferential tests, and we excluded samples where axial force varied from the mean by >25% with pressure. Stress-stretch relationships were also analyzed by deriving the tangent modulus. See Methods for further details of data analysis.

Transmission Electron Microscopy (TEM) analysis of collagen structure. Carotid arteries for TEM were fixed overnight at 4^{o}C in 0.1M sodium cacodylate buffer, pH7.4 containing 2.5% glutaraldehyde and 2.0% paraformaldehyde. After subsequent buffer washes, the samples were post-fixed in 2.0% osmium tetroxide for 1 hour at room temperature and rinsed in water prior to *en bloc* staining with 2% uranyl acetate. Briefly, after dehydration through a graded ethanol series, the tissue was infiltrated and embedded in EMbed-812 (Electron Microscopy Sciences, Fort Washington, PA). Thin cross sections were stained with uranyl acetate and lead citrate and examined with a JEOL 1010 electron microscope fitted with a Hamamatsu digital camera and AMT Advantage image capture software. Images of artery cross sections were taken at increasing magnification; collagen abundance was evaluated as described in Methods.

In vivo treatment with BAPN. Mixed sex WT and HGPS mice (a mean age of 35 ± 2 days old) were injected peritoneally with BAPN (Sigma A3134; 333 mg/kg) or an equal volume of vehicle (PBS). BAPN was dissolved in PBS and injected in a volume of 0.2 ml per day until the mice reached 2-months of age (a mean of 24 ± 2 days of injections). No dramatic alterations in mouse behavior, no changes in appearance, and no weight loss were observed during the injection period. At approximately 2-months of age (a mean of 60 ± 2 days old), the mice were sacrificed, carotid arteries were isolated, and unloaded

wall thickness and inner radii were determined. The samples were then analyzed by pressure myography as described above. For the echocardiography and invasive hemodynamics experiments, male mice were analyzed between 64-75 days of age immediately after a 30-day treatment with BAPN (333 mg/kg as described; (Kothapalli et al. 2012)). Echo and hemodynamics performed by the UPenn Cardiovascular Phenotyping Core. See Methods for additional echocardiography methods.

In vivo BAPN survival study. Mice were IP injected daily starting from 30 days of age with 200ul of solution 50mg/ml Beta-aminopropionitrile (Sigma Aldrich A3134) in PBS. Solution was sterile filtered and injected into mice using 26Gx8/3 syringe (0.45mmx10mm; BD syringe 309625). Vehicle-treated mice were given 200ul of sterile filtered PBS by IP injection. Food and water were replenished weekly, and cages changed bi-weekly. Mice were weighed once a week with progeria mice showing a decline in weight as the study progressed. Injections were continued until progeria mice began to display signs of morbidity, which was uncontrolled shivering and lethargic activity. No dramatic changes in WT mice were observed either with vehicle or BAPN injections. After all progeria mice in the study had died, injections of BAPN and vehicle were continued in WT mice for two additional weeks before euthanasia. After sacrificing mice, all portions of the aorta were collected, heart, and carotids.

Genome-wide sequencing and analysis: Descending aortas containing the intimal, medial and adventitial layers were isolated from six 2-month male WT, six 24-month WT mice, and six HGPS mice, and RNA was extracted using the RNeasy Plus Micro kit

(Qiagen 74034). The high-throughput library was prepared using the truSeq stranded total RNA (ribo-Zero) kit (Illumina 20037135). Paired end sequencing was performed on a HiSeq4000 Sequencing System (Illumina) and generated 14-30 million reads/sample.

Raw sequence files were mapped to the genome with using salmon (https://combine-lab.github.io/salmon/) against the mouse transcripts described in genecode (version M23, built on the mouse genome GRCm38.p6, https://www.gencodegenes.org). Transcript counts were summarized to the gene level using tximport (https://bioconductor.org/packages/release/bioc/html/tximport.html), and normalized and tested for differential expression using DESeq2 (https://bioconductor.org/packages/release/bioc/html/DESeq2.html). Sequence files can be found under GEO ascension number GSE165409. The normalized values for the 300 genes with the highest variance across all samples were imported into Partek Genomics Suite (v7, Partek, Inc., St. Louis, MO) for principal component analysis.

DEGs having a 1.5x fold change and adjusted p-values of <0.001 were subjected to gene ontology analysis (GO cellular component) using DAVID (https://david.ncifcrf.gov/home.jsp) and a core analysis with Ingenuity Pathway Analysis (IPA). Default settings were used for all other core analysis parameters. The core analysis included the prioritization of upstream regulators based on enrichment of a regulator's target gene set in the set of DEGs. For each regulator, IPA tested the directionality of each of the genes in the overlap to infer an activation or inactivation of the regulator (Z-score). We defined putative upstream regulators of DEGs as those having Z-scores >1.75 (activated) or <-1.75 (inhibited). This set of upstream regulators

was then filtered to identify those classified by IPA as either transcription regulators (including transcription factors and epigenetic regulators) or microRNAs (miRs).

The list of transcription regulators categorized by IPA as either being in an activated or inhibited state (positive or negative Z-scores, respectively) was compared to the transcriptional regulators of LOX present in the IPA database. The overlapping gene set was individually examined to determine if its proposed activation or inhibition state correctly corresponded to the experimental upregulation of LOX we observed in HGPS. We also checked for the specificity of upstream regulator effect on the LOX gene. These comparisons allowed us to assess the appropriateness of the IPA-proposed transcription regulator relationship. The list of 10 miRs identified by IPA were all categorized as being in an inhibited activation state in HGPS (negative Z-scores). The entire miR list was therefore compared to the list of miRs targeting mouse LOX as determined by TargetScan (www.targetscan.org).

Statistical Analysis. Statistical analysis was performed using Prism software (GraphPad). For the pressure myography experiments, differences in inner radius, wall thickness, axial stress and circumferential stretch at pressure-matched points were compared by age, genotype, or response to BAPN across the entire curves and analyzed by two-way ANOVA relative to the relevant 2-month WT control. For other mouse experiments and for all studies with isolated cells, ANOVAs were used for multiple comparisons, and two-tailed Mann-Whitney tests were used to compare two datasets. Statistical significance for all graphs is demarcated by *($p<0.05$), **($p<0.01$), ***($p<0.001$). Box plots show Tukey whiskers.

Carotid artery and aorta immunostaining and histologic analysis. Isolated arteries were fixed after excision in Prefer (Anatech #414), embedded in paraffin, and 5-µm cross sections were stained. Paraffin-embedded sections (5 µm) of freshly isolated carotid arteries or descending aortas were deparaffinized and hydrated before antigen unmasking (Vector Labs, H3300). Carotid or aortic cross sections were washed in PBS three times before blocking with 2% BSA in PBS for 15 min, incubated overnight at 4°C with antibodies directed to $p16^{INK4A}$ (Proteintech, 10883-1-AP; 1:50 dilution), collagen-I (Southern Biotech, 1310-01; 1:400 dilution), collagen-III (Proteintech, 22734-1-AP; 1:400 dilution), collagen-V (Abcam, ab7046; 1:250 dilution), and LOX (Santa-Cruz, sc32409 selective for the LOX isoform; 1:50 dilution). Replicate sections were incubated in parallel with isotype-matched control antibodies. All samples were washed three time with PBS before incubation with a 1:100 dilution of Alexa 594-conjugated isotype-matched secondary antibody (Lifetech donkey anti-goat A11058 or Invitrogen Goat anti-rabbit A11012) for two hours at room temperature. Sections were then washed three times in PBS followed by addition of Dapi (1:1000 dilution in PBS). Slides were briefly washed in PBS and then water before mounting with SlowFade Gold (Thermo, S36936). Results were visualized with a Nikon Eclipse 80i microscope with a QI-Click Qimaging camera. Carotid arteries were imaged at 20x magnification.

Images were quantified using ImageJ. The media of each section was traced using the polygon drawing tool, and its raw integrated intensity was divided by the area of the outlined media to obtain relative fluorescence intensity. The procedure was then repeated for the adventitial layer. Relative fluorescence intensity values were then plotted relative to the mean fluorescence intensity value of the corresponding WT control. Fluorescent intensity values were passed through a Grubbs' test. Background

intensity, as determined from the isotype-matched control antibodies, was negligible (see Fig. 2.10). Results are presented as box plots with Tukey whiskers.

Staining with Hematoxylin (Fisher, SH30-500D) and Eosin (Fisher, SE22-500D) was performed using standard procedures. Apoptosis was determined by immunostaining for cleaved caspase-3 (Cell Signaling Technologies SignalStain Apoptosis IHC Detection kit, #12692S) according to manufactures instructions with tumor xenograft sections as positive controls. To determine calcium deposition, deparaffinized and hydrated sections were incubated with a 5% solution of Alizarin Red S (Sigma, A5533) pH 4.2 for 30 minutes, with calcified bone tissue as positive control. Arterial elastin layers were visualized by autofluorescence using a cyan filter on a Nikon Eclipse 80i Fluorescence microscope.

Carotid artery second harmonic generation imaging. Paraffin-embedded carotid artery cross-sections were de-paraffinized in xylene (20 minutes) and hydrated in decreasing concentrations of ethanol (100%, 95%, 75%, 50%), following by a 5 min wash in deionized water. Slides were stored in water until ready for imaging. SHG imaging was performed on a Leica SP8 multiphoton microscope, using an immersion lens, keeping the carotid cross-sections hydrated in water. Forward and backward SHG signals were collected to capture collagens at multiple distances within the sample and detect fibers at different optical alignments.

Quantification of collagen within elastin folds. TEM images of vehicle (PBS)-treated or untreated WT and HGPS carotid arteries were taken at 7500 x magnification to visualize

the elastin folds (Fig 2.10; A1). The folds were defined as areas where the elastin invaginates, creating a roughly parabolic shape (Fig. 2.10; A2). Using the polygon Selection Tool in ImageJ, an area was defined by continuously tracing along the two sides of the parabolic shape; that region was then enclosed by connecting the two apexes with a straight line (Fig. 2.10; A3). This area was added to the ROI Manager to calculate total area of the elastin fold. To calculate the area within the fold containing collagen, the Paintbrush Tool was used to manually black-out areas containing collagen fibers (Fig. 2.10; A4). The painted area was isolated with the Threshold Tool (Fig. 2.10; A5) and added to the ROI manager (Fig. 2.10; A6). The ratio of collagen/total areas was defined as percent collagen in the elastin fold.

RT-qPCR of mRNAs and miRs. Descending aortas from 2-month WT and HGPS mice were isolated and stripped of adventitia. The adventitial and remaining medial/intimal (referred to as medial tissue in the text) tissues were stored separately in RNAlater (Qiagen) at -80^{o}C for subsequent analysis. To strip adventitia from the aorta, a cleaned isolated aorta was incubated in 1 mg/ml Type 2 collagenase (Worthington Biochem, LS004174) in Hanks Balanced Salt Solution (Lifetech, 14170-112) for 10 minutes at 37^{o}C. The adventitial layer was carefully peeled off before storing the aorta (intimal/medial and adventitial layers separately) in RNAlater. Total RNA was isolated with the RNeasy Fibrous Tissue Mini Kit (Qiagen) according to manufacturer's instructions and using 0.3 ml buffer RLT per aorta. Reverse transcription reactions contained 200-500 ng of total RNA. RNA was extracted from cultures of primary SMCs with TRIzol reagent (Thermofisher 15596026) according to manufacturer’s instruction.

microRNA was reverse transcribed from total RNA using the TaqMan microRNA reverse transcription kit (ABI 4366596). Ten to fifteen percent of the cDNA was subjected to qPCR with the following primer-probe sets from Applied Biosystems: Col1a1 (Mm00801666_g1), Col3a1 (Mm00802300_m1), Col5a1 (Mm00489299_m1); LOX (Mm00495386_m1), LOXL1 (Mm01145738_m1), LOXL2 (Mm00804740), LOXL3 (Mm01184865_m1), LOXL4 (Mm00446385), has-miR-145 (TM: 002278), SnoRNA202 (TM:001232). The primer-probe set for 18S rRNA has been described (Klein et al. 2007). qPCR samples were analyzed in duplicates. Levels of each tested transcript were normalized to 18S rRNA (for mRNA) or SnoRNA202 (for miRNA), and changes in RNA abundance were calculated using the ddCT method.

Immunoblotting. Intact descending aortas (consisting of the adventitia, media and intima) that had been stored in RNAlater (Thermo-Fisher) were chopped into small pieces and sonicated in lysis buffer (50mM Tris-HCl pH8, 250mM NaCl, 2mM EDTA, 1%NP40) containing protease inhibitors (Cell Signaling Technologies 5872S). Lysates were centrifuged for 5 min (4^{o}C, 15,000 rpm), and the supernatants were diluted into SDS sample buffer (final concentration of 2% SDS, 10% glycerol, 50mM Tris pH 6.8, 0.01% Bromphenol blue, 1% β-mercaptoethanol) and analyzed by immunoblotting after SDS-PAGE. Approximately 20-30 μg protein was fractionated per sample on an 8% polyacrylamide gel. Lamin A (protein tech 10298), and Focal Adhesion Kinase (BD Transduction Labs 610088), and Lysyl Oxidase (abcam ab31238) antibodies were used at a 1:300 dilution.

Lysyl Oxidase Activity Assay. Intact descending aortas were isolated, flash frozen in liquid nitrogen and stored at -80oC prior to the analysis of LOX activity. Thawed aortas were chopped into small pieces and sonicated in 0.2ml PBS three times for 15-20 seconds each and stored immediately on ice. Lysates were centrifuged at 14,000 x g for 5 min, and 50 µl of each supernatant was analyzed using the Abcam Lysyl oxidase activity assay kit (ab112139) according to manufacturer's instructions. Samples were run in technical duplicates. Relative fluorescent intensity values were normalized to the total protein concentration of each lysate as determined using BioRad protein concentration reagent (Biorad 5000006).

Myograph data analysis. Measurements of intraluminal pressure, force, and outer diameter were converted into stress-stretch curves using equations 1–4 where *l* and *L*=loaded and unloaded vessel lengths, respectively (µm), a_i and A_i=loaded and unloaded inner radii, respectively (µm), a_o and A_o=loaded and unloaded outer radii, respectively (µm), *h* and *H* = loaded and unloaded vessel wall thickness, respectively (µm), *P*= intraluminal pressure (mm Hg), and f_T=axial force (nN). Vessel wall thickness was calculated in the post-test analysis as described (Brankovic et al. 2019) with the standard assumption that the sample was incompressible.

Equation 1: Axial stretch $(\lambda_z)=\frac{l}{L}$

Equation 2: Axial stress $(\sigma_z)=\frac{Pa^2\pi + f_T}{\pi h(2a + h)}$

Equation 3: Circumferential stretch $(\lambda_\theta)=\frac{a + h/2}{A + H/2}$

Equation 4: Circumferential stress $(\sigma_\theta) = \frac{Pai}{h}$

Axial stress-stretch curves show means ± SD. Circumferential stress-stretch curves as well as inner radius and wall thickness results were determined from triplicate determinations per sample and are therefore presented as means ± SE.

To estimate tissue stiffness, axial and unloaded circumferential stresses and stretches for each tested vessel were fit to an exponential function ($y=a^{bx}$) using Matlab (R2020a, Curve Fitting Tool). The derivative of each vessels exponential fit was then used to plot the tangent modulus as a function of stretch for each individual vessel. Tangent modulus values were passed through the Grubbs' test and one mouse was eliminated as an outlier. These results were then averaged and plotted as the tangent modulus graphs. The adjusted R2 values identified in MatLab for each fit were assessed to be greater than 0.95 in order to be included in the mean tangent modulus curves.

Echocardiography. Ultrasound examination of the left ventricle was performed using a Fujifilm VisualSonics Ultrasound System (VisualSonics Inc, Toronto, ON, Canada) and using MS400 (18-38 MHZ) transducer. Mice were lightly anesthetized with an i.p. injection of 0.005 ml/g of 2% Avertin (2,2,2-Tribromoethanol, Sigma-Aldrich, St. Louis, MO). Hair was removed from the anterior chest using chemical hair remover (Nair), and the animals were placed on a warming pad in a left lateral decubitus position to maintain normothermia (37°C), monitored by a rectal thermometer. Ultrasound gel was applied to

the chest. Care was taken to maintain adequate contact while avoiding excessive pressure on the chest. Left ventricular (LV) systolic function: Two-dimensional long-axis, short-axis M-Mode images were obtained. LV diastolic function: Transmitral inflow pattern and tissue Doppler were obtained in modified 4 chamber apical view. After completion of the imaging studies, mice were allowed to recover from anesthesia and returned to their cages. M Mode Images were analyzed for LV structure and function related parameters and Pulse wave and tissue Doppler images were analyzed for diastolic function related parameters using Vevo Lab software (Visual Sonics Inc, Toronto, ON, Canada).

Aortic Catheterization. Closed-chest cardiac catheterization was performed under isoflurane (1.5-4%) by ligating the right carotid artery and advancing a 1F Millar catheter (SPR-1000) into the ascending aorta, where it was secured. Measurements were taken using Millar MPVS Ultra and ADInstruments LabChart for approximately 5 minutes after catheter insertion. The temperature of the animal was maintained between 36.5-37.5 degrees Celsius.

Cell culture, viral infection and RNAi. Primary mouse SMCs were isolated from the descending aortas of 2-month old WT and HGPS male mice and prepared by explant culture as described (Cuff et al. 2001). SMCs were cultured in growth medium [1:1 Dulbecco's modified Eagle's medium (DMEM)/Ham's F-12 supplemented with 2mM L-glutamine and 20mM HEPES, pH7.4] with 20% FBS. Cells were passaged at near confluence with trypsin/EDTA and used between passages 2-4. Near confluent, asynchronous SMCs were infected with adenoviruses encoding LacZ (control) or miR-

145 (AdmiRa-has-miR-145-5p; ABM #mh0185) at a MOI of 600 in growth medium and incubated overnight. The cells were incubated for 72 hours in fresh growth medium before sample collection. Infection efficiency of the miR-145 adenovirus was ~70% as determined by expression of co-transcribed GFP. siRNA-mediated knock-down of Lamin A in near-confluent WT SMCs was performed using Lipofectamine RNAiMAX Transfection Reagent (Thermofisher #13778100) in OPTI-MEM with final siRNA concentrations of 150 nM (Thermofisher siRNA ID #s69252, #s69253, #s69254). A non-specific siRNA (Ambion 4390843) was used as control. After 4 hours of siRNA transfection, cells were switched to fresh growth medium. Total RNA or protein was collected 72 hours after transfection using TRIzol reagent (for RNA analysis) or immunoblotting lysis buffer (see above), respectively.

2.6 Acknowledgements

We thank Dr. Carlos Lopez-Otín for the generous gift of the LMNA^{G609G} mouse line and the Electron Microscopy Research Laboratory at the University of Pennsylvania for preparing arterial tissue for TEM, the Next Generation Sequencing Core at University of Pennsylvania for performing the RNASeq, and the Mouse Cardiovascular Phenotyping Core at University of Pennsylvania for mouse echocardiography. Myography experiments were performed in collaboration with Sonja Brankovic and Emilia Roberts. The TEM analysis was performed by Kyle Bruun. The bioinformatic analysis was performed with John Tobias. BAPN administration was assisted by Elizabeth Hawthorne and Tina Xu. Lamin A knockdown analysis was assisted by Paola Castagnino.

This work was supported by NIH grants AG047373 and AG062140, the Progeria Research Foundation, and the Center for MechanoBiology, a National Science Foundation Science and Technology Center under grant agreement CMMI: 15-48571. RvK was supported by NIH grants T32-GM008076 and F31-HL142160.

2.7 Figures

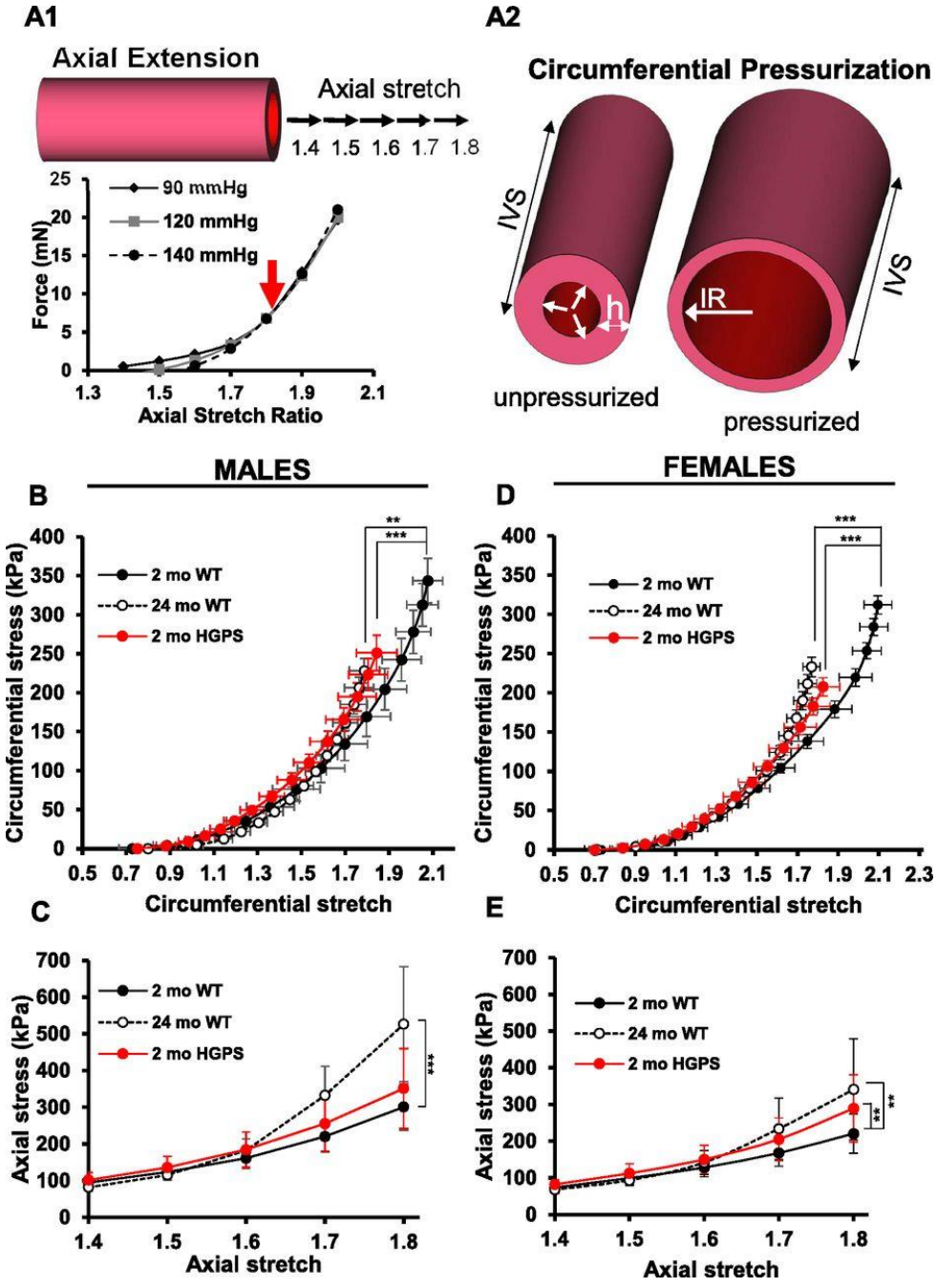
A1
Axial Extension
Axial stretch
1.4 1.5 1.6 1.7 1.8
90 mmHg
120 mmHg
140 mmHg
Force (mN)
Axial Stretch Ratio
A2
Circumferential Pressurization
IVS
IR
h
unpressurized
pressurized
MALES
FEMALES
B
D
2 mo WT
24 mo WT
2 mo HGPS
Circumferential stress (kPa)
Circumferential stretch
C
E
Axial stress (kPa)
Axial stretch

Fig. 2.01. **Mechanical properties of isolated carotid arteries display premature circumferential stiffening in HGPS male and female mice.** Carotid arteries from male (panel B-C) and female (panel D-E) 2-month (n=7 per sex) and 24-month (n=5 per sex) WT and 2-month HGPS (n=6 per sex) mice were analyzed by pressure myography. **(A1)** Arteries are axially stretched at multiple pressures, and the intersection point of the stretch-force curves defines the “in vivo stretch” (IVS). The graph displays a representative axial stretch-force curve for a 2-month WT mouse carotid artery (red arrow shows the IVS). **(A2)** Arteries are brought to their individual IVS and pressurized. White arrows indicate circumferential deformation with pressure (IR=inner radius, h=wall thickness). **(B,D)** Circumferential stretch-stress curves for male and female mice, respectively. Each data point corresponds to the circumferential stress and stretch at increments of 10mmHg starting from 0 to 140mmHg. **(C,E)** Axial stretch-stress curves, determined at 90mmHg, for male and female mice, respectively. Results in panels B and D show means ± SE and results in panel C and E show means ± SD. Statistical significance in all panels was determined by two-way ANOVA in comparison to 2-month WT mice. Myographic experiments were performed in collaboration with Sonja Brankovic (University of Pennsylvania).

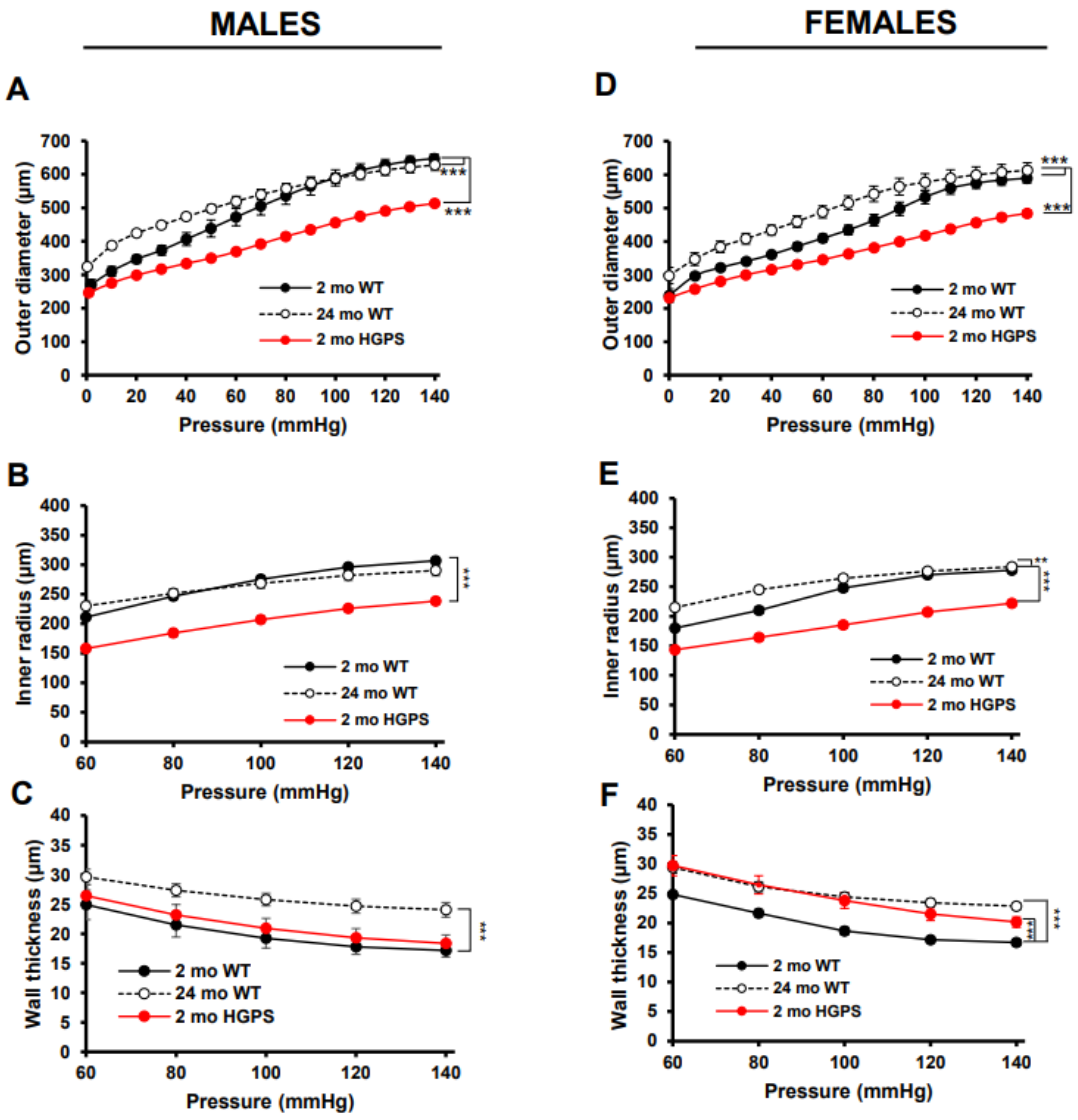

Fig. 2.02. Biaxial inflation-extension tests and biomechanical properties of WT and HGPS carotid arteries. Changes in outer diameter **(A,D)**, inner radius **(B,E)** and wall thickness **(C,F)** with pressure for the male **(A-C)** and female **(D-F)** mice in Figure 2.01. Results show mean ± SE. Statistical significance was determined by 2-way ANOVA relative to the 2-mo WT arteries.

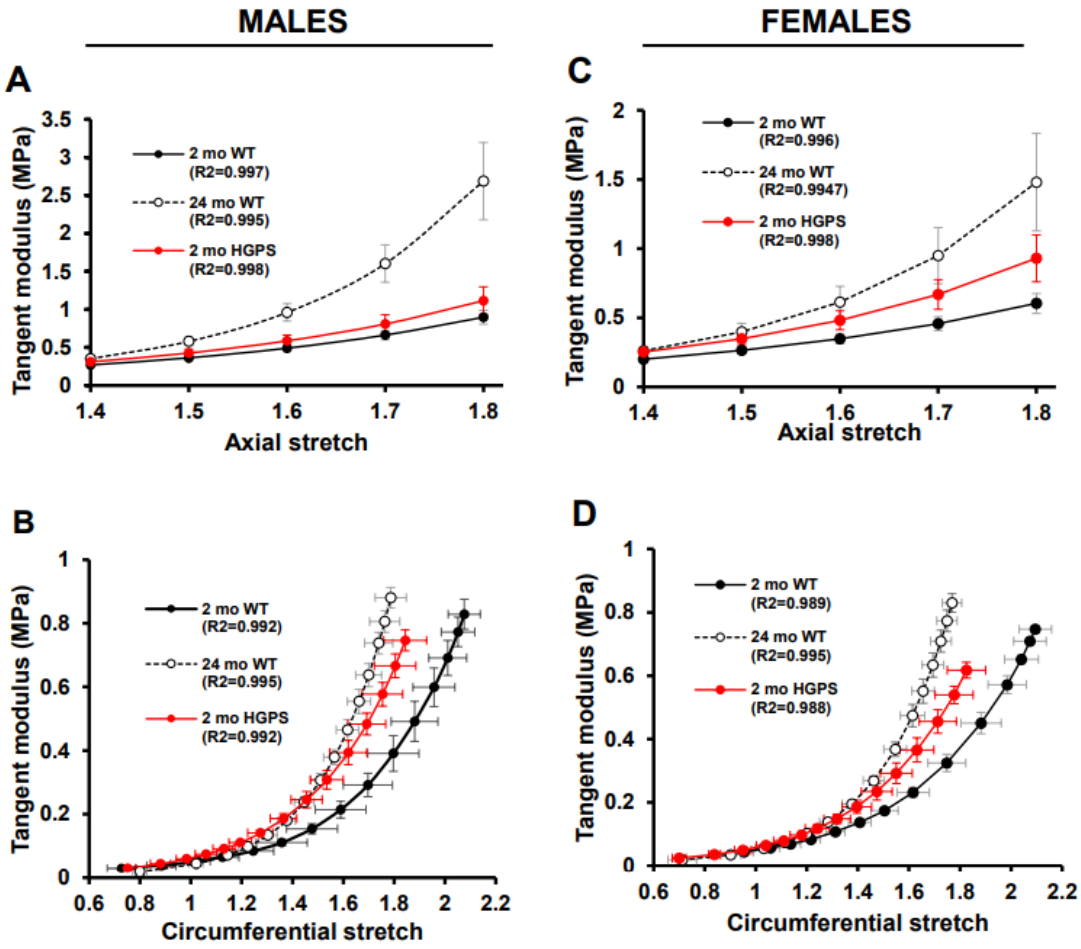

Fig. 2.03. Stiffness estimates by tangent modulus. Derived axial **(A** and **C)** and circumferential **(B** and **D)** tangent modulus versus stretch plots of the carotid arteries from male **(A-B)** and female **(C-D)** WT and HGPS mice shown in Figure 2.01.

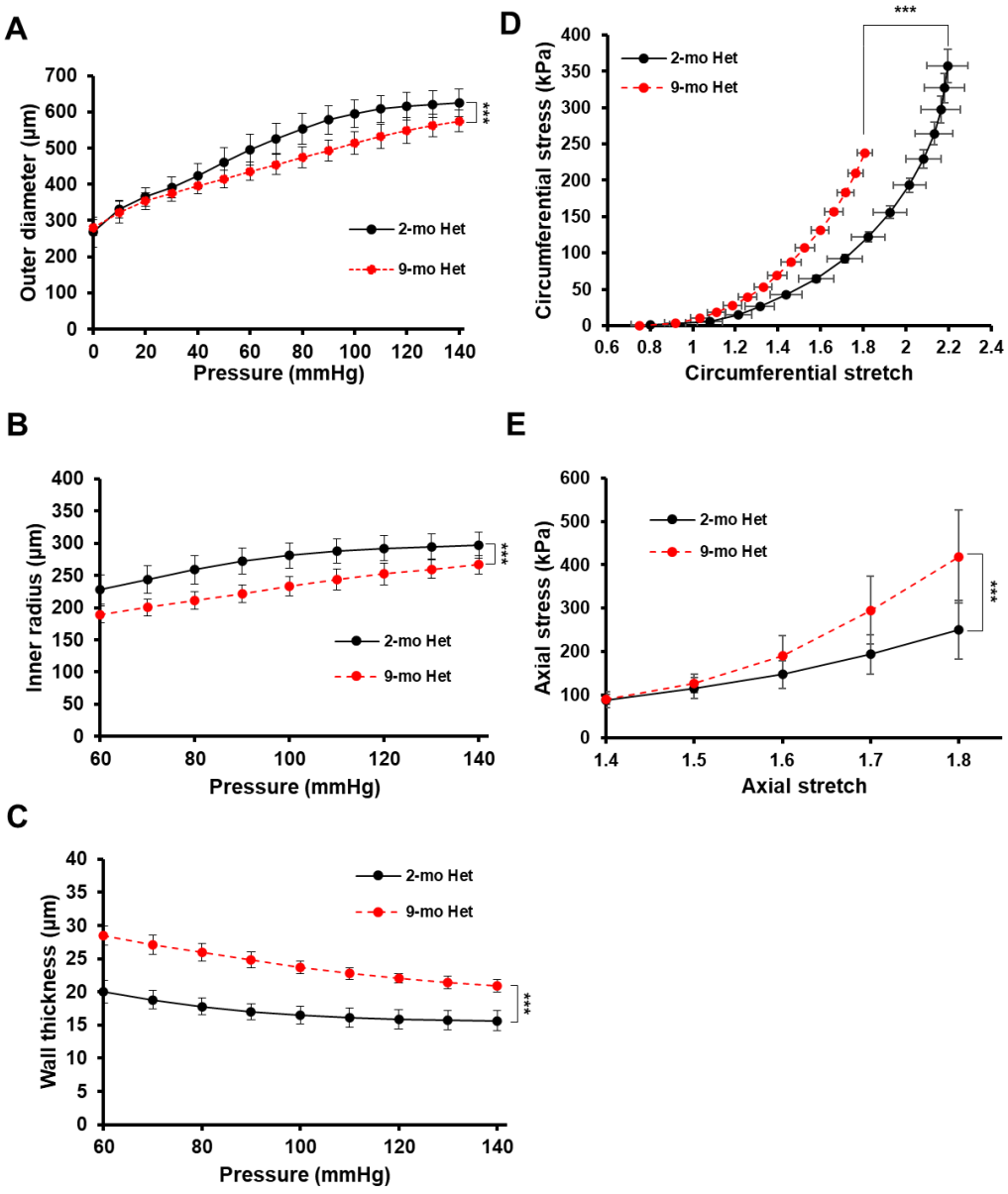

Fig. 2.04. Pressure myography characterization of male 2-mo (n=6) and 9-mo (n=5) LMNA$^{+/G609G}$ (heterozygous; Het) mice. Changes in **(A)** outer diameter, **(B)** inner radius, **(C)** wall thickness with pressure. Results in A-C show means ± SD. **(D)** Circumferential stress-stretch curves. Results show mean ± SE. **(E)** Axial stress-stretch

curves performed at 90mmHg. Results show mean ± SD. Statistical significance in A-E was determined by two-way ANOVA. Myograph analysis was performed in collaboration with Sonja Brankovic.

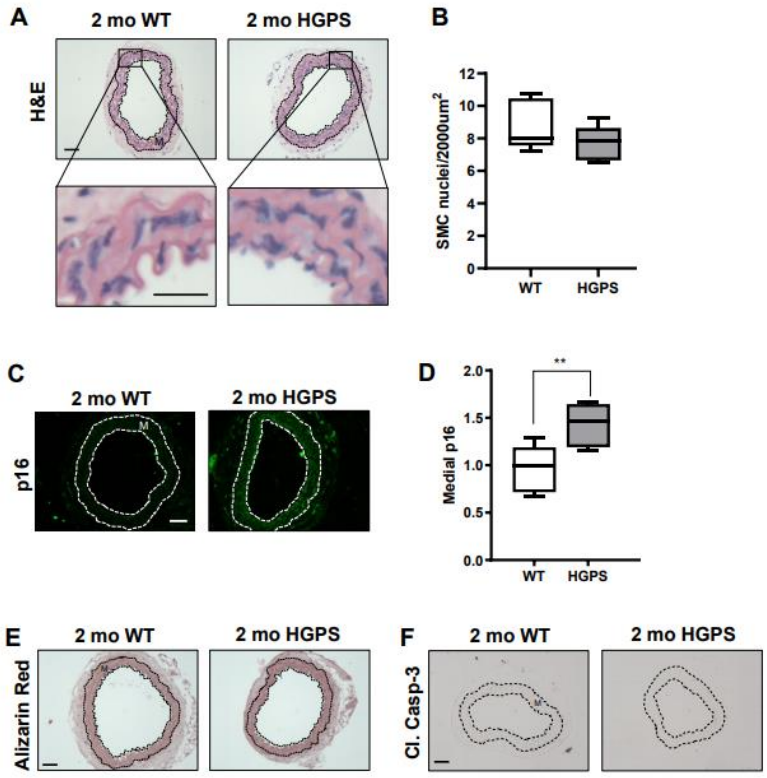

Fig. 2.05. Carotid arteries from 2-month WT and HGPS mice display similar histology. (A-B) Carotid artery cross sections from 2-month WT and HGPS mice were stained with H&E (scale bar = 50 µm and inset bar = 25 µm), and the number of medial smooth muscle cell (SMC) nuclei was quantified from H&E images (n=7-10 carotids per genotype with 3 sections analyzed per mouse). **(C-D)** Carotid cross sections were immunostained for the senescence marker, p16INK4A, and the level of medial p16INK4A was normalized to the mean signal intensity of carotid sections from 2-month WT mice; (n=6-10 per genotype). Scale bar = 50 µm. Statistical significance in B and D was determined by Mann-Whitney tests. **(E)** Carotid cross sections were stained with Alizarin Red (n=5 per genotype) and **(F)** immunostained for cleaved caspase-3 (n=5 per

genotype). Scale bars in E and F = 50 µm. The arterial media (M) is outlined with dashed lines.

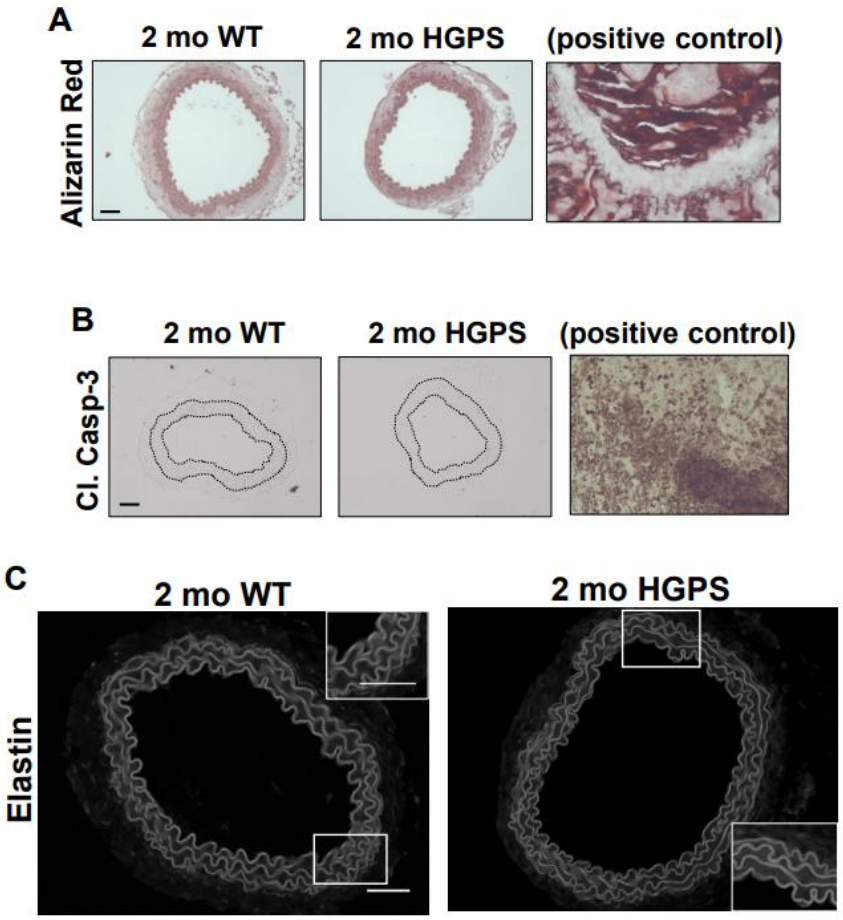

Fig. 2.06. Positive controls for morphologic analyses and evaluation of elastic laminae of in WT and HPGS carotid arteries. (A-B) The images presented in Fig. 2E-F are reproduced here with corresponding positive controls, bone and tumor tissue, respectively. **(C)** Representative elastin autofluorescence images of 2-mo WT and HGPS carotid artery cross sections (n=7-9 per genotype). Scale bar = 50 µm.

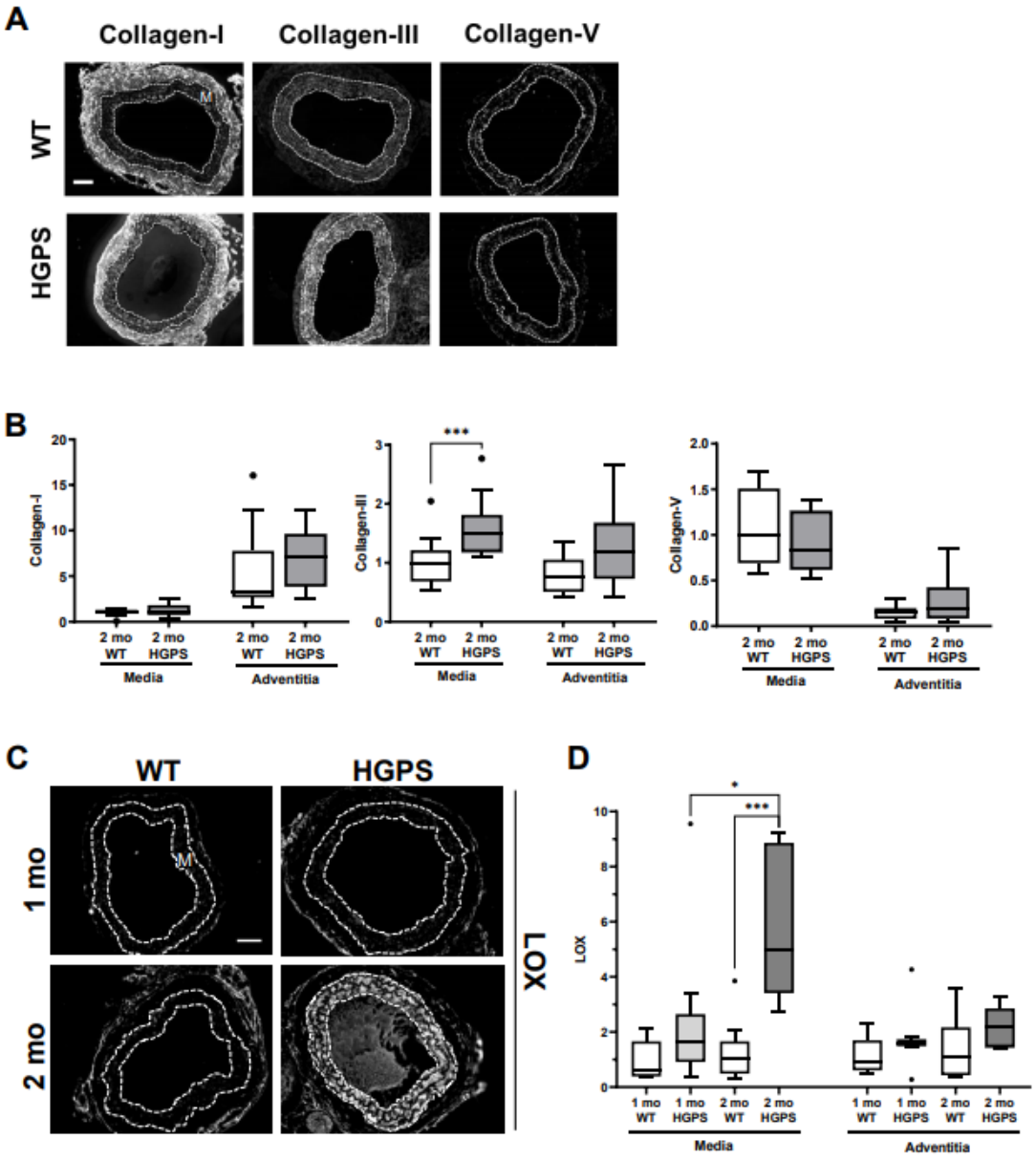

Fig. 2.07. HGPS carotid arteries display alterations in abundance of fibrillar collagens and Lysyl Oxidase (LOX). (A) Representative images of carotid artery cross sections from 2-month WT and HGPS mice immunostained for collagen-I (n=11-12), -III (n=13-15), and -V (n=9-10); scale bar = 50 μm. **(B)** Collagen signal intensities from the

immunostained sections were quantified, and results were normalized to the mean signal intensity in the 2-month WT media. **(C)** Representative images of LOX immunostaining of carotid artery sections from 1- and 2-month WT and HGPS mice (n=7-9 mice per age and genotype). Scale bar = 50 μm. **(D)** LOX signal intensities from the medial and adventitial layers were quantified, and the results were normalized to the mean signal intensity of the 1-month WT medial layer. Statistical significance in B and D was determined by Mann-Whitney tests. The arterial media (M) is outlined with dashed lines.

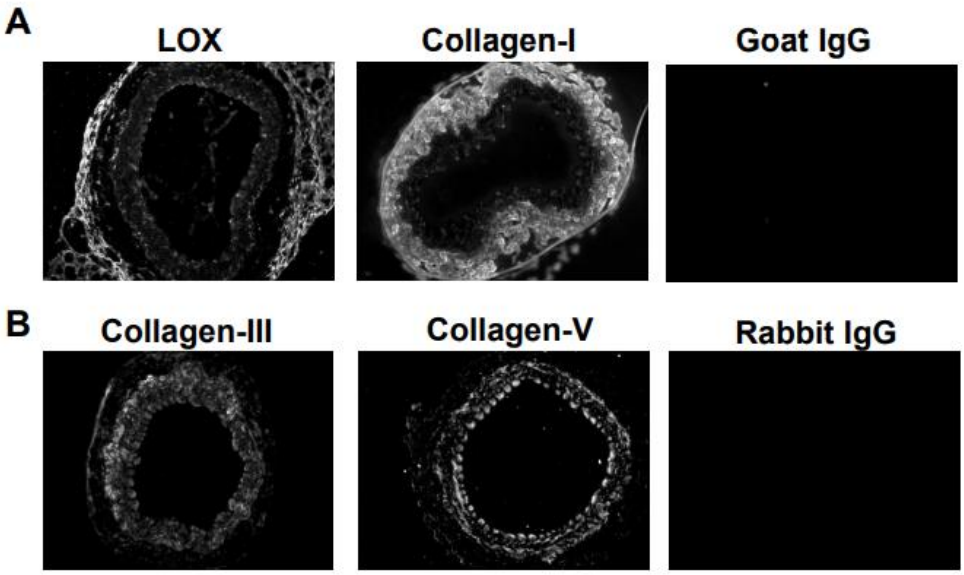

Fig. 2.08. Immunostaining controls for WT and HGPS carotid arteries. Representative images of background signals for carotid artery cross sections incubated with targeted versus isotype-matched (negative control) primary antibodies from **(A)** goat (LOX and COL1) or **(B)** rabbit (COL3 and COL5).

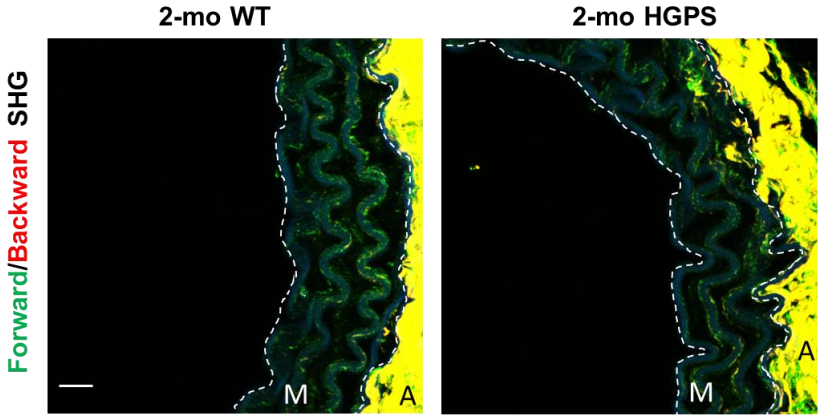

Fig. 2.09. Forward and backward second harmonic generation (SHG) imaging of carotid artery cross sections. Carotid artery cross sections of 2-mo WT and HGPS mice were imaged by second harmonic generation (n=4 mice per genotype). Representative images are shown. Media layer is denoted by “M” and outlined in white dashed lines. The adventitia layer is noted by “A.” Scale bar 10μm.

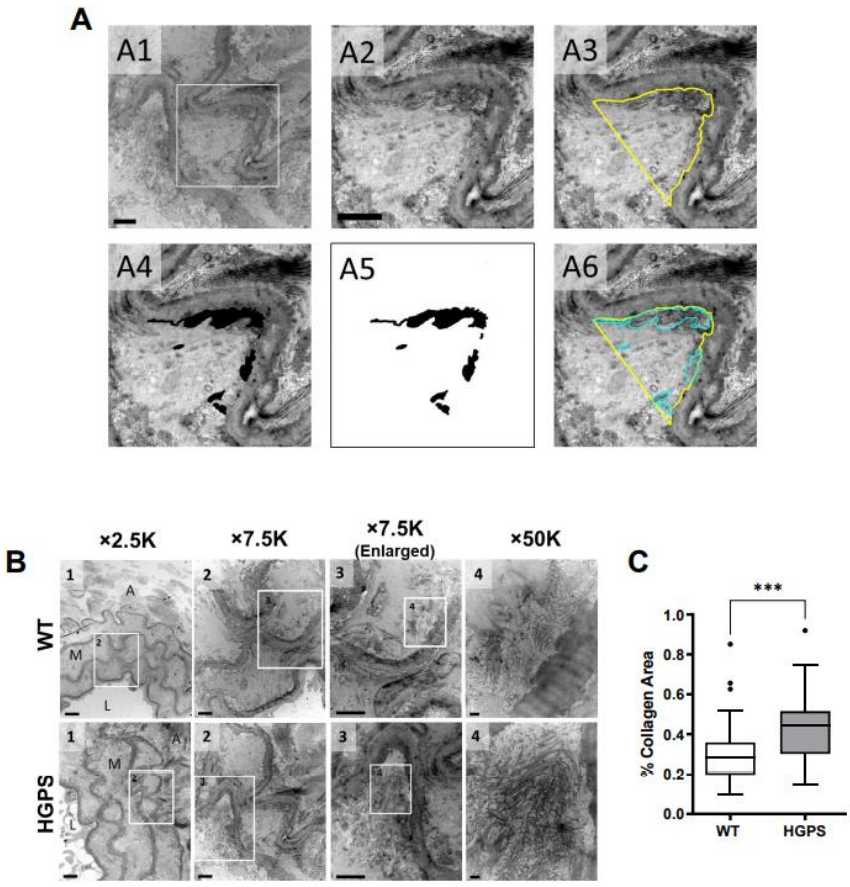

Fig. 2.10. Quantification of collagen abundance in elastin folds. (A) Representative transmission electron microscopy (TEM) images from a mouse carotid artery cross section processed in ImageJ to quantify the area of collagen within an elastin fold. The boxed region in image A1 is shown in images A2-A6. Scale bar = 2 µm. See Methods for details. **(B)** Carotid arteries from 2-mo WT and HGPS mice were sectioned and imaged by TEM. Representative images are shown at the indicated magnification. Numbers in each image correspond to the boxed ROI in the preceding image. In image

1, the lumen (L), media (M), and adventitia (A) of the artery are noted (scale bar = 6 μm). Image 2 shows multiple elastin folds, and image 3 shows a 2-fold enlargement of an individual fold used to quantify collagen area as described in Methods (scale bar = 2 μm). In image 4, individual collagen fibrils within the elastin fold are readily distinguishable (scale bar = 200 nm). **(C)** Collagen area in elastin folds of WT and HGPS carotid arteries was quantified as described in methods (n=6 mice per genotype, 60 elastin folds per genotype). Mouse numbers in C were accrued from vehicle-injected and uninjected mice. Statistical significance was determined by Mann-Whitney test. TEM performed by Kyle Bruun (University of Pennsylvania).

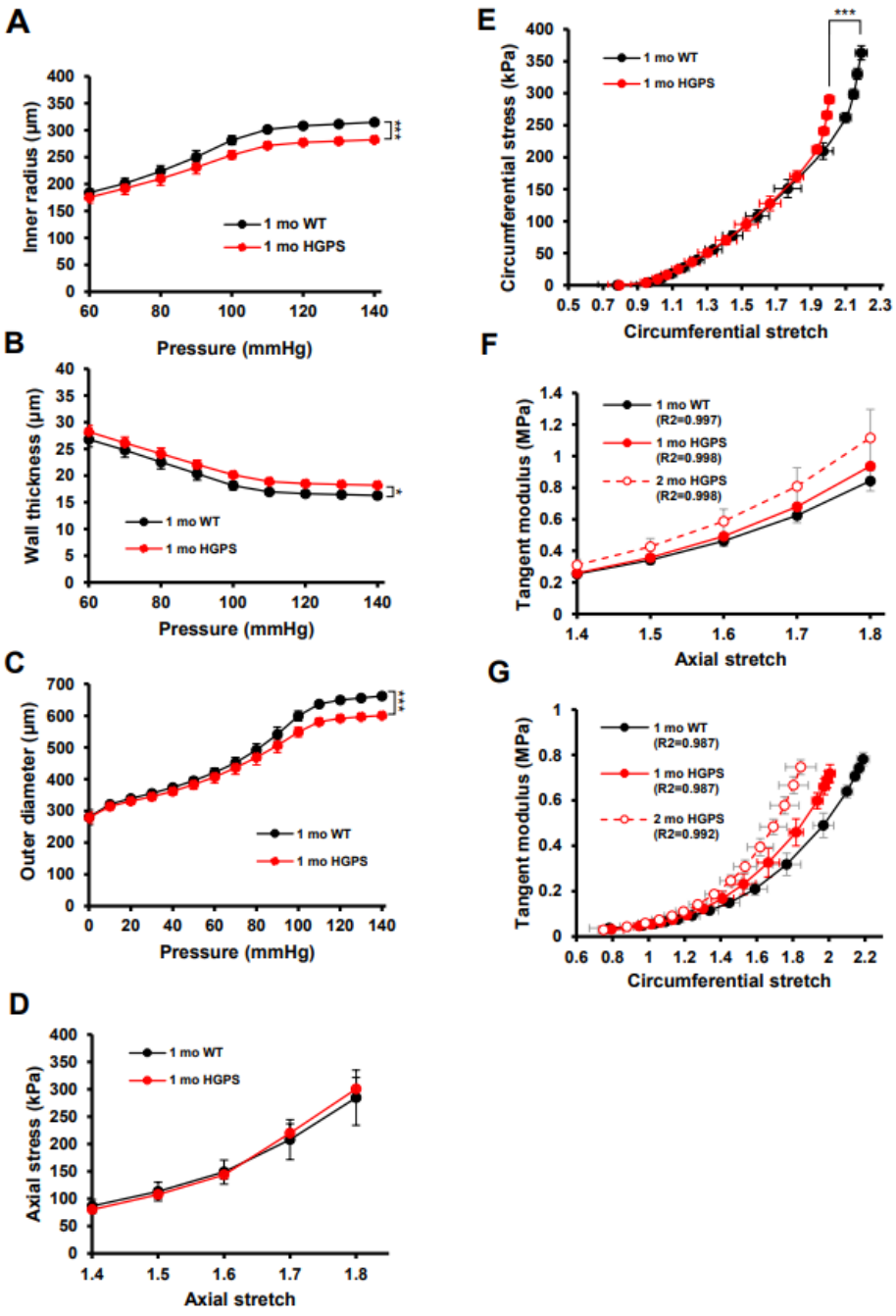

Fig. 2.11. Mechanical properties of 1-month WT and HGPS carotid arteries. Carotid arteries from mixed sex 1-mo WT (n=5) and HGPS (n=5) mice were analyzed by pressure myography. **(A-C)** Changes in inner radius, wall thickness, and outer diameter

with pressure. Results show mean ± SE. **(D)** Axial stress-stretch curves performed at 80mmHg. Results show mean ± SD. **(E)** Circumferential stress-stretch curves. Results show mean ± SE. Statistical significance in A-E was determined by two-way ANOVA. **(F-G)** Derived axial and circumferential tangent modulus versus stretch plots. Male 2-mo HGPS tangent curves were reproduced from Figure 2.03 for reference (dashed red line). Myographic experiments were performed in collaboration with Emilia Roberts (University of Pennsylvania).

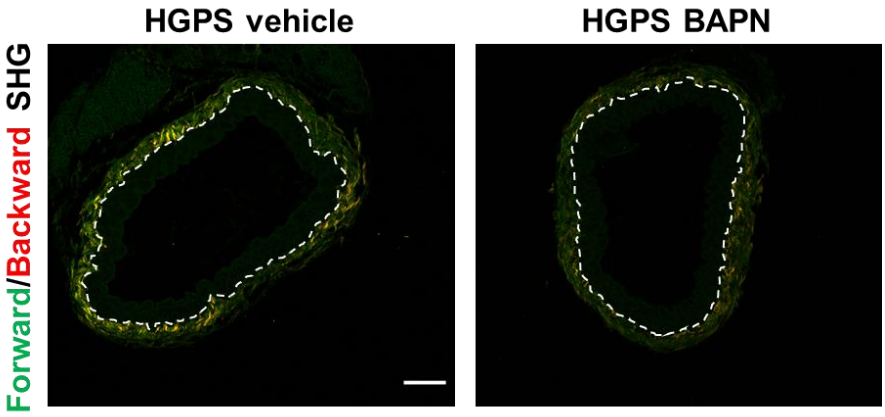

Fig. 2.12. BAPN treatment reduces second harmonic generation (SHG) signal of carotid artery adventitia. Mixed-sex HGPS mice were treated with daily IP injections of PBS (vehicle) or BAPN for approximately 30 days starting at 1-month (see methods for additional details). Carotid artery cross sections were then imaged by second harmonic generation (n=4 mice per treatment group). Representative images are shown. The external elastic lamina is outlined in white dashed lines. Scale bar 50μm.

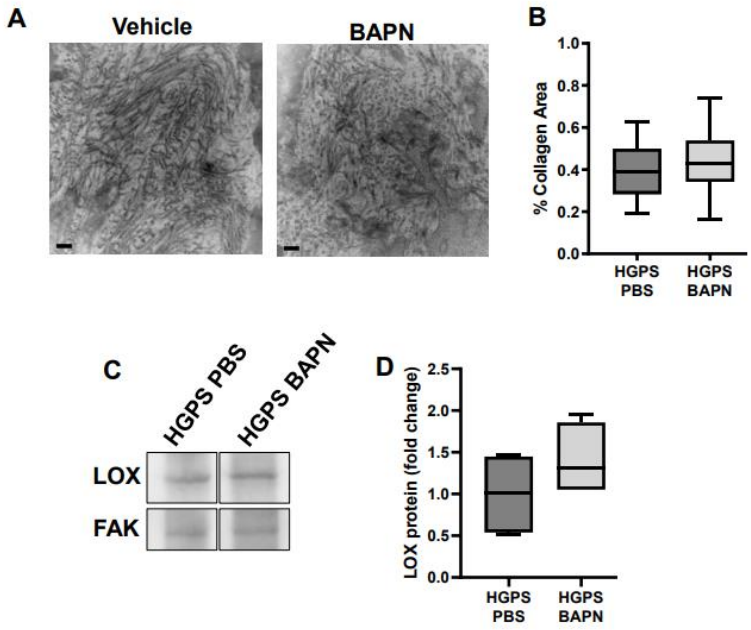

Fig. 2.13. Collagen and LOX abundance in PBS and BAPN-treated mice. (A) Representative TEM images (50,000x magnification) of cross sections from 2-mo HGPS carotid arteries that had been treated with vehicle (PBS) or BAPN as described in Materials and Methods. Scale bar = 200 nm. **(B)** Quantification of collagen area within the elastin folds as described in Methods and Fig. 2.10 (n=3-4 mice per treatment with 10 elastin folds analyzed per mouse). **(C-D)** Aorta lysates, prepared from 2-mo HGPS mice treated with PBS or BAPN, were analyzed by western blotting and probed for LOX and Focal Adhesion Kinase (FAK, loading control). **(C)** Representative western blot; white spaces indicate removal of extraneous data. **(D)** Quantification of LOX signal intensities, normalized to the loading control, in HGPS mice treated with PBS (n=4) or BAPN (n=4). TEM experiments were performed in collaboration with Kyle Bruun.

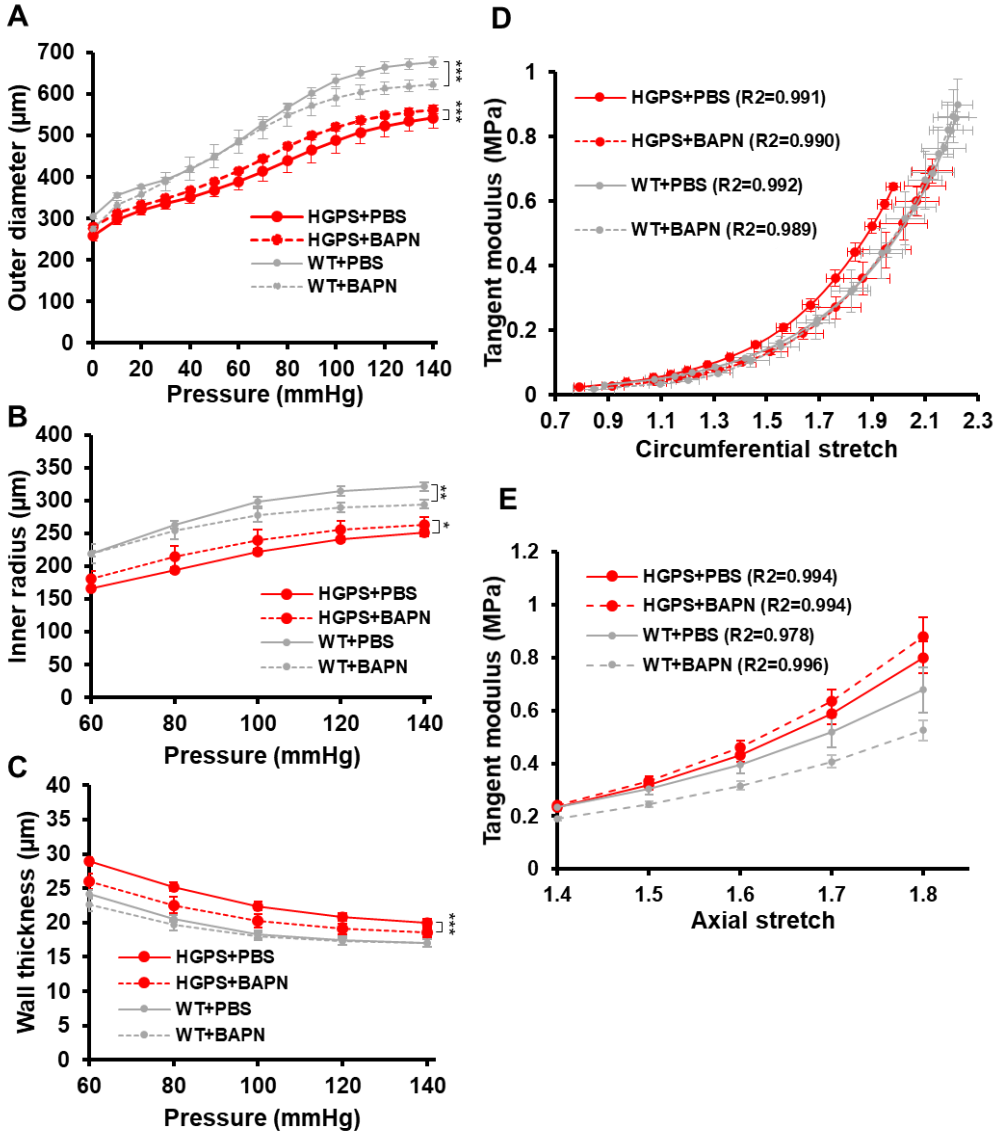

Fig. 2.14. Effect of BAPN on carotid artery geometry and tangent modulus in mixed sex WT and HGPS mice. (A-C) Changes in outer diameter, inner radius, and wall thickness with pressure for the PBS- and BAPN-treated HGPS and WT mice shown in Figure 2.15. Results show mean ± SE. Statistical significance was determined by 2-

way ANOVA relative to the vehicle treated arteries. **(D-E)** Derived circumferential and axial tangent modulus versus stretch plots. Myography experiments were performed in collaboration with Emilia Roberts. Elizabeth Hawthorne assisted with BAPN injections.

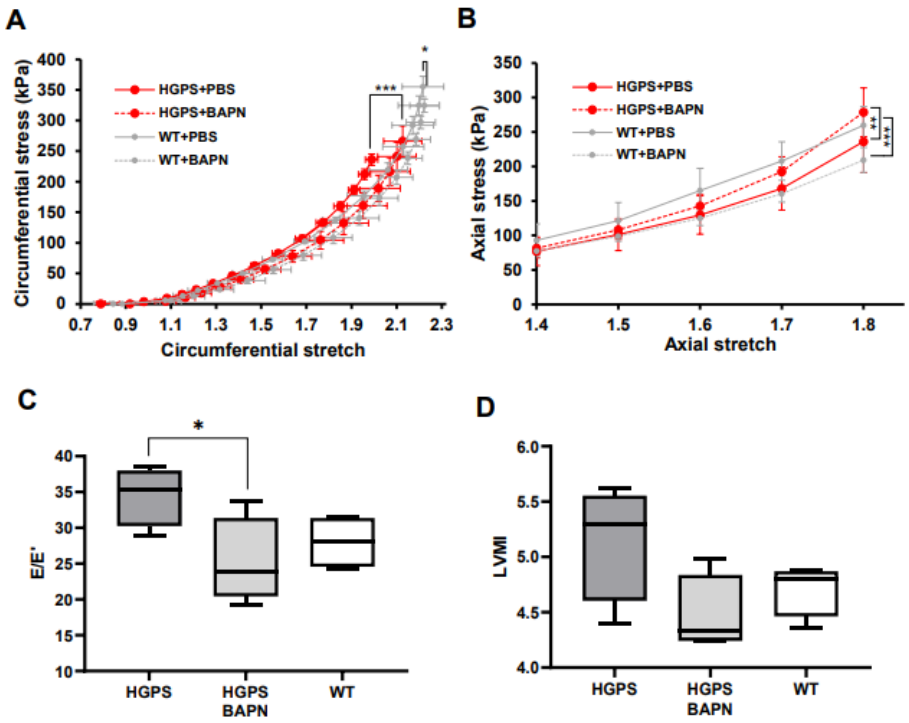

Fig. 2.15. Elevated Lysyl Oxidase expression is linked to premature arterial stiffening and diastolic dysfunction in HGPS mice. Mixed sex WT and HGPS mice aged to 1-month were treated with β-aminopropionitrile, BAPN (WT n=5, HGPS n=6) or PBS (WT n=6, HGPS n=7) for approximately 30 days followed by pressure myography of isolated carotid arteries. **(A-B)** Circumferential and axial stretch-stress curves, respectively, of WT and HGPS mice treated with PBS or BAPN. Results in panels A display means ± SE, and results in panel B display means ± SD. Statistical significance for the myographic analysis was determined by two-way ANOVA. **(C-D)** Echocardiography measurements of **(C)** the E/E' ratio and **(D)** the left ventricular mass index (LVMI, left ventricular mass to body weight ratio) of 64-75 day old HGPS mice (n=4), 65-75 day old HGPS mice treated with BAPN (n=4), and 66-75 day WT mice

(n=4). Mouse numbers in C-D were accrued from vehicle-injected and uninjected mice, and statistical significance was determined by Mann- Whitney tests.

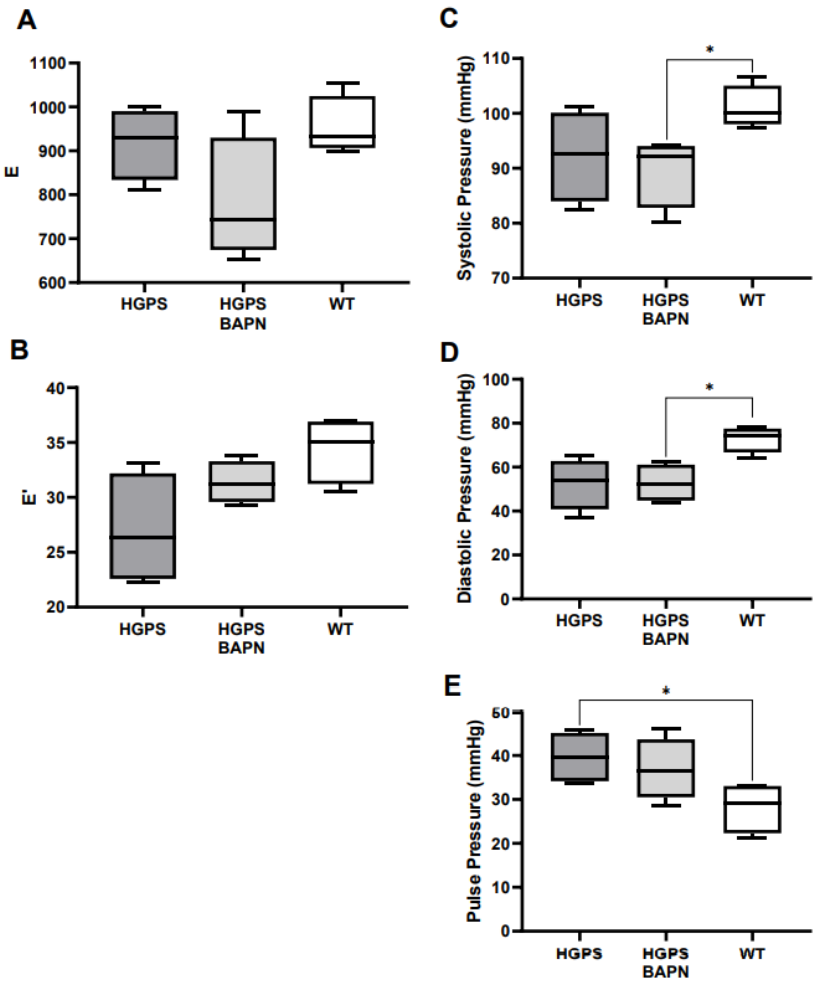

Fig. 2.16. Effect of BAPN on diastolic function and aortic hemodynamics in HGPS mice. Diastolic function and pressures of the mice used in Figs. 2.15C-D. **(A-B)** E and E' as determined by echocardiography. **(C)** Systolic pressure, **(D)** diastolic pressure, and **(E)** pulse pressure. Statistical significance was determined by Mann-Whitney test.

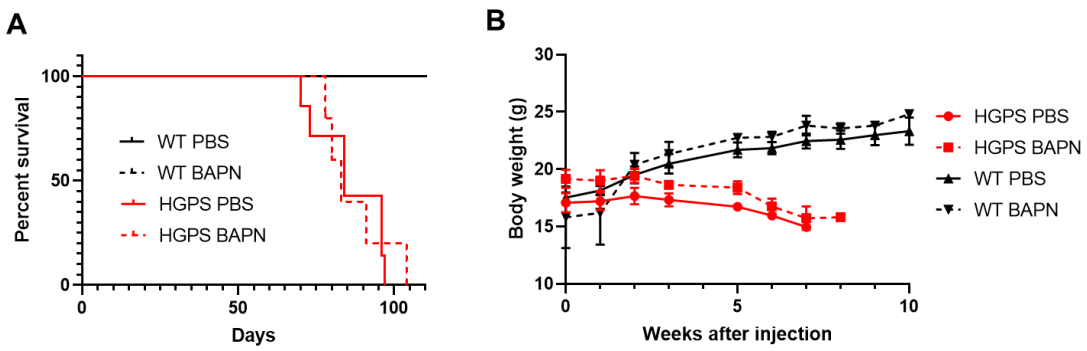

Fig. 2.17. Daily BAPN administration does not prolong HGPS mouse lifespan. 1-month WT and HGPS mixed-sex mice were injected daily with PBS (WT n=5; HGPS n=6) or BAPN (WT n=3; HGPS n=5) until moribund as described in methods. **(A)** Kaplan-Meier curve displaying percent survival of mice treated with PBS or BAPN. No statistical changes in survival of HGPS mice after BAPN administration was observed by Gehan-Breslow-Wilcoxon test. **(B)** Weekly bodyweight measurements of WT and HGPS mice starting at the time of initial injection of PBS or BAPN (~1-month of age) until euthanasia. No significance in weight change was observed between PBS or BAPN treatment in WT or HGPS mice as determined by 2-way ANOVA with Holm-Sidak post-tests comparing weight each week.

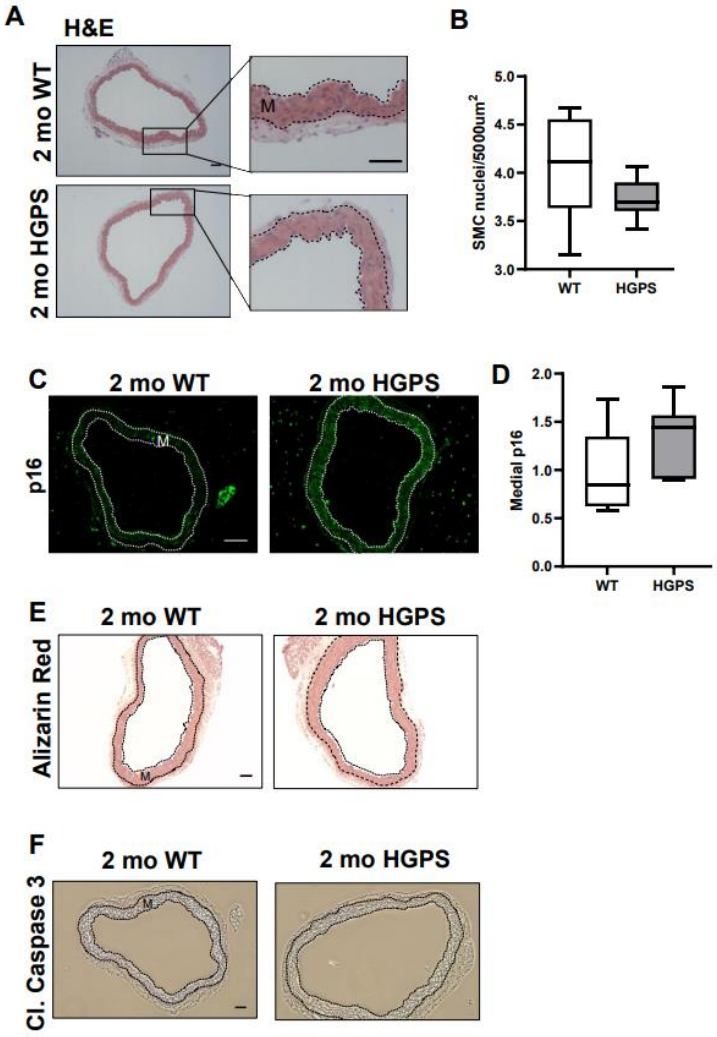

Fig. 2.18. Characterization of 2-mo WT and HGPS aortas. (A-B) WT and HGPS aortic cross sections were characterized for overall morphology and SMC number by H&E staining. The number of SMC nuclei was quantified (n=7 mice per genotype, 3 sections per mouse). **(C-D)** 2-mo WT and HGPS aorta were immunostained with anti-p16 (n=7), and signal intensity in the medial layer (dashed lines) was quantified and normalized to 2-mo WT. **(E)** Calcification was assessed by alizarin red staining (n=4), with bone tissue

used as a positive control as in Fig. 2.06. Scale bar in panels A-E=100 mm. **(F)** Apoptotic cells were assessed in WT and HGPS aortas by staining for cleaved caspase-3 (scale bar=50 mm, n=4) with tumor tissue used as positive control as in Fig. 2.06. Medial layer is outlined in dashed lines and marked with “M”.

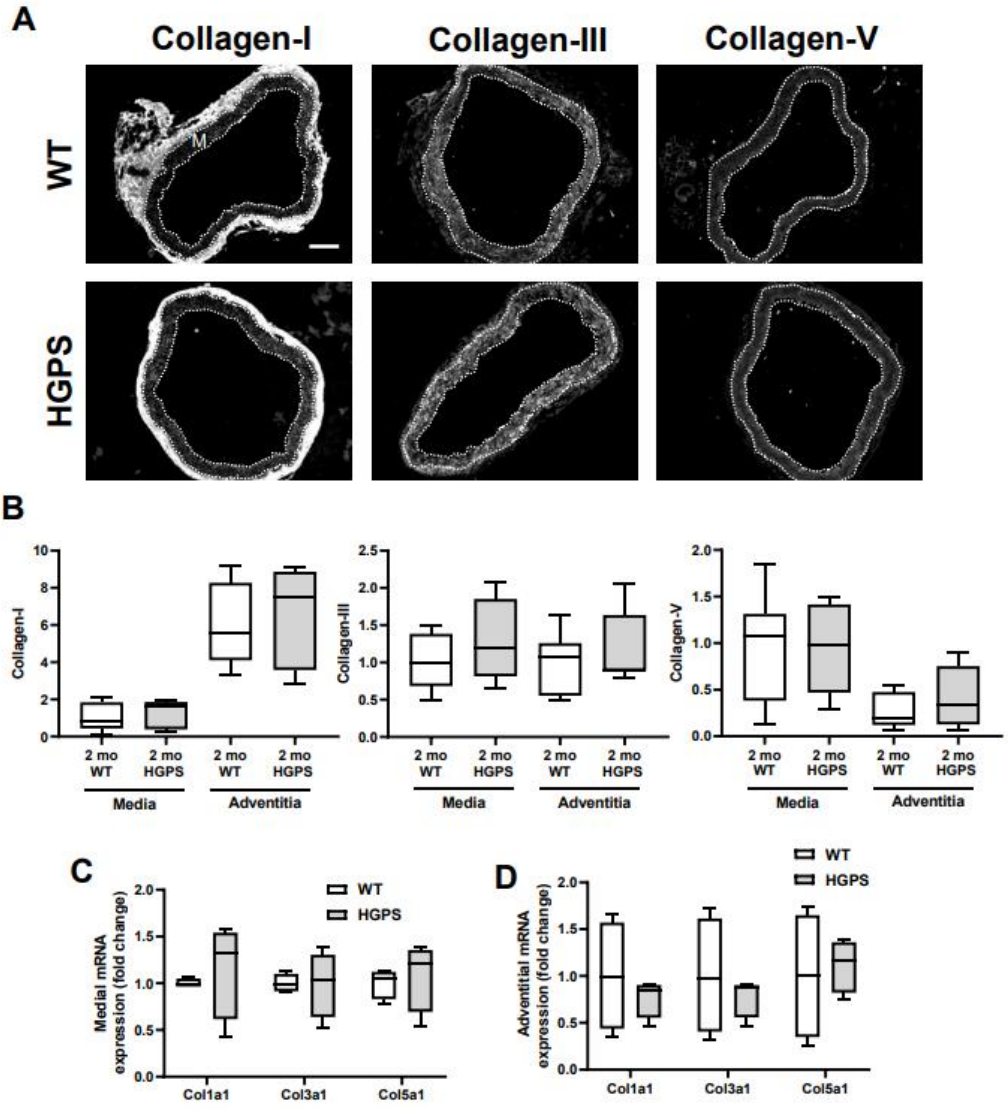

Fig. 2.19. Collagen immunostaining and transcript levels in 2-month WT and HGPS aortas. (A) Representative images of collagens-I, -III, -V immunostaining in 2-mo WT (n=7) and HGPS (n=7) aortic cross sections. Scale bar 100 mm. Medial layer is outlined in dashed lines and marked with “M”. **(B)** Quantification of immunostaining with results presented as fold change in fluorescent signal intensity for the medial and adventitial

layers normalized to the mean intensity of the 2-mo WT media. Statistical significance between genotypes was evaluated by Mann-Whitney test. **(C-D)** Col1a1, Col3a1, and Col5a1 transcript levels in aortic **(C)** media layer (n=4 per genotype) or **(D)** adventitia layer (n=4 per genotype).

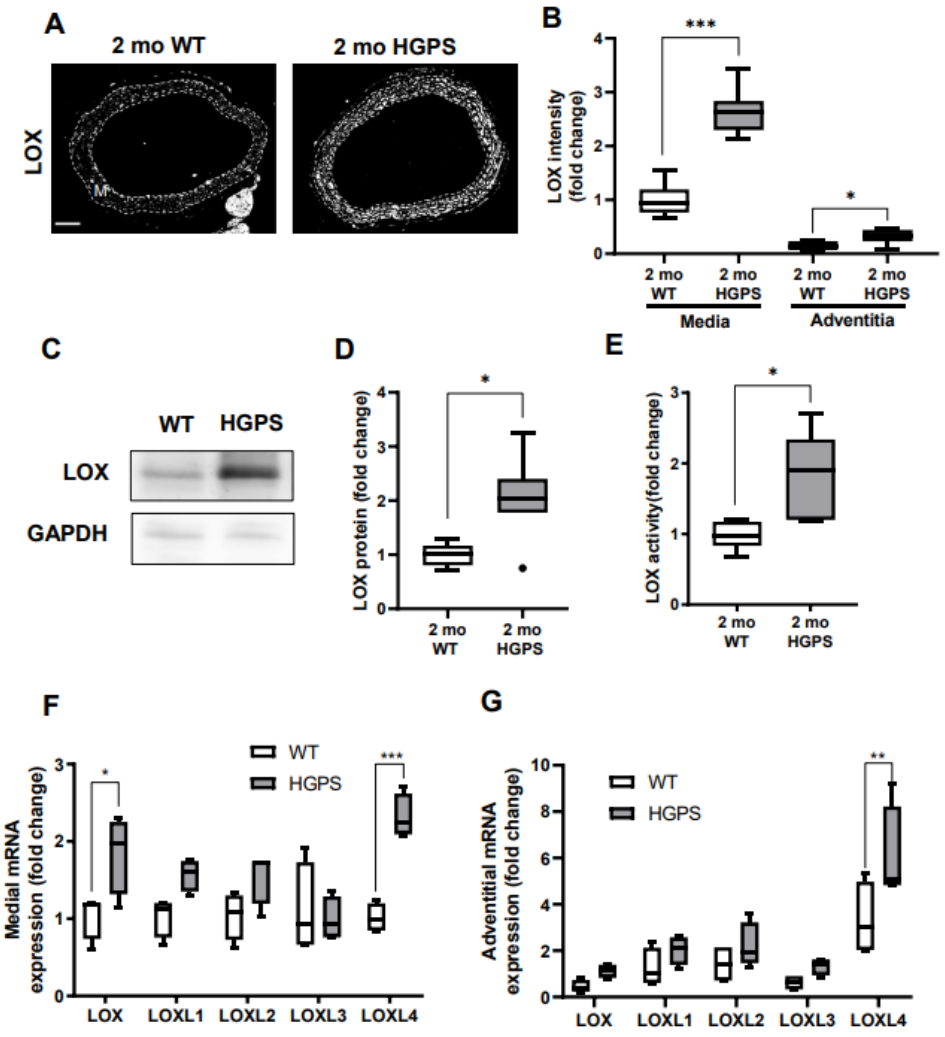

Fig. 2.20. HGPS aortas display increased Lysyl Oxidase (LOX) abundance and activity. (A) Representative images of 2-month WT (n=8) and HGPS (n=7) aortic sections immunostained for LOX; scale bar = 100 μm. The arterial media (M) is outlined with dashed lines. **(B)** LOX signal intensities from the immunostained sections were quantified, and results were normalized to the mean signal intensity of the 2-month WT

medial layer. **(C)** Representative immunoblot of aortic lysate from 2-month WT and HGPS mice, and **(D)** quantification of immunoblots (n=6-7 per genotype). **(E)** LOX activity in 2-month WT and HGPS aortic tissue (n=5 per genotype). Statistical significance in A-E was determined by Mann-Whitney tests between genotypes. **(F)** mRNA expression levels of LOX family isoforms in adventitia-free 2-month WT and HGPS aortas and **(G)** 2-month WT and HGPS aortic adventitial tissue were quantified by RT-qPCR (n=4 independent experiments, with 2 aortas pooled per experiment). Transcript levels were normalized to 2-month WT medial layer values. Statistical significance was determined by two-way ANOVA followed by Holm-Sidak post-tests.

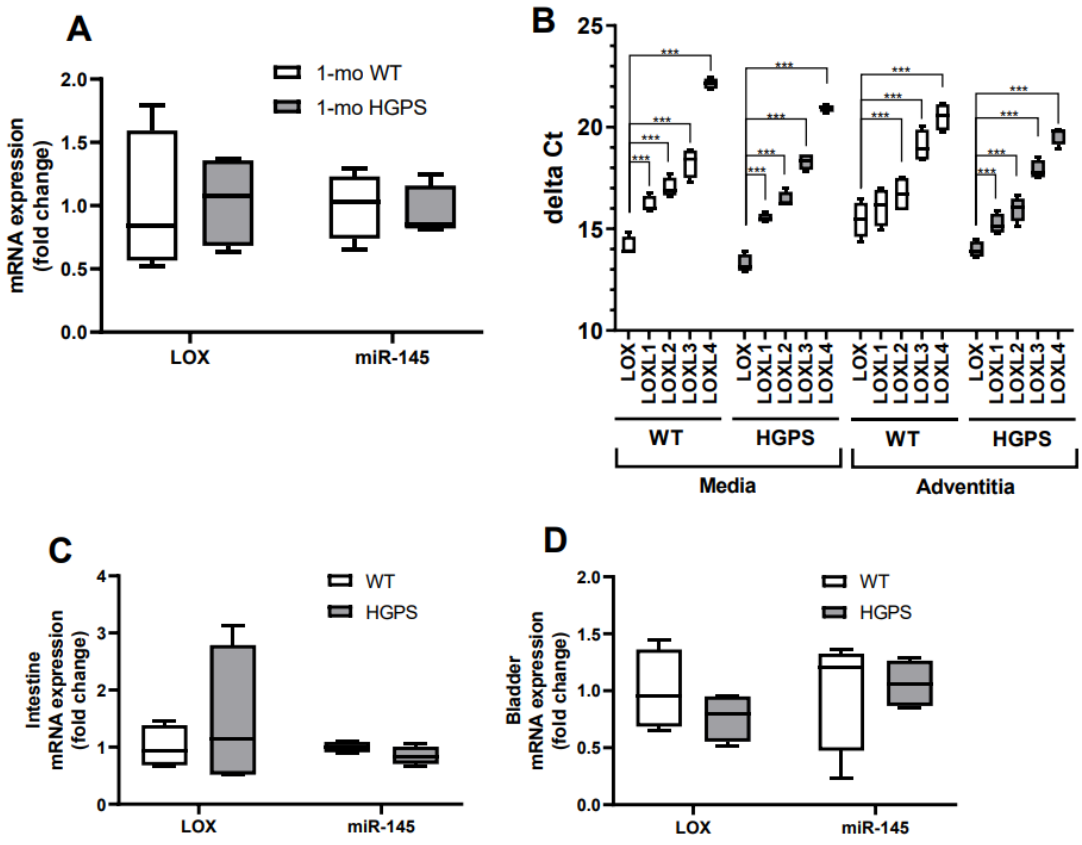

Fig. 2.21. LOX and miR-145 transcript abundance. (A) LOX and miR-145 transcript levels in 1-month male WT and HGPS mice (n=4 per genotype). Statistical significance was determined by Mann-Whitney tests. **(B)** Relative abundance of the LOX family members in the medial and adventitial layers of 2-month WT and HGPS aorta was quantified by RT-qPCR. Results show delta-Ct values plotted as Tukey plots (n=4 mice per genotype). Statistical significance was determined by Two-way ANOVA using LOX as a reference; results of the individual Holm-Sidak post-tests are shown. **(C-D)** LOX

and miR-145 transcript levels in intestine (n=4 per genotype) and bladder (n=4 per genotype) of 2-mo male WT and HGPS mice.

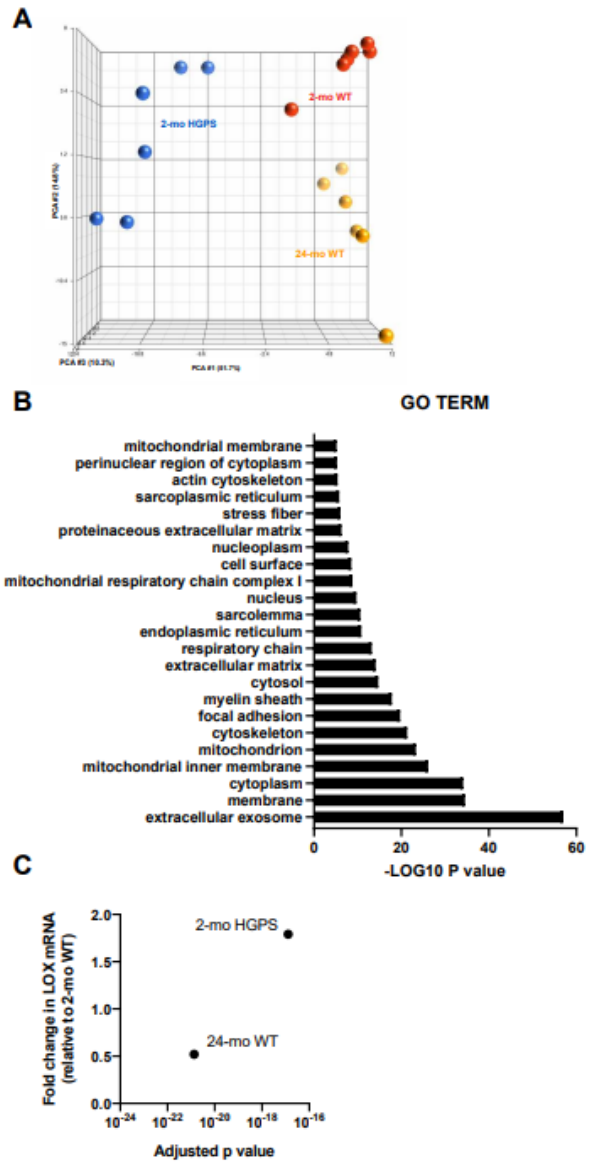

Fig. 2.22. Initial characterizations of the genome-wide analysis. (A) Principal component analysis of RNASeq data performed in Partek Genomics Suite. **(B)** Gene ontology (GO) cellular component analysis performed in DAVID as described in Materials and Methods. GO Terms with greater than a -LOG10(P value) of 5 are shown.

(C) Fold changes and adjusted p-values for LOX mRNA in the DEGs of aortas from 2-mo HGPS and 24-mo WT mice as normalized to 2-mo WT mice.

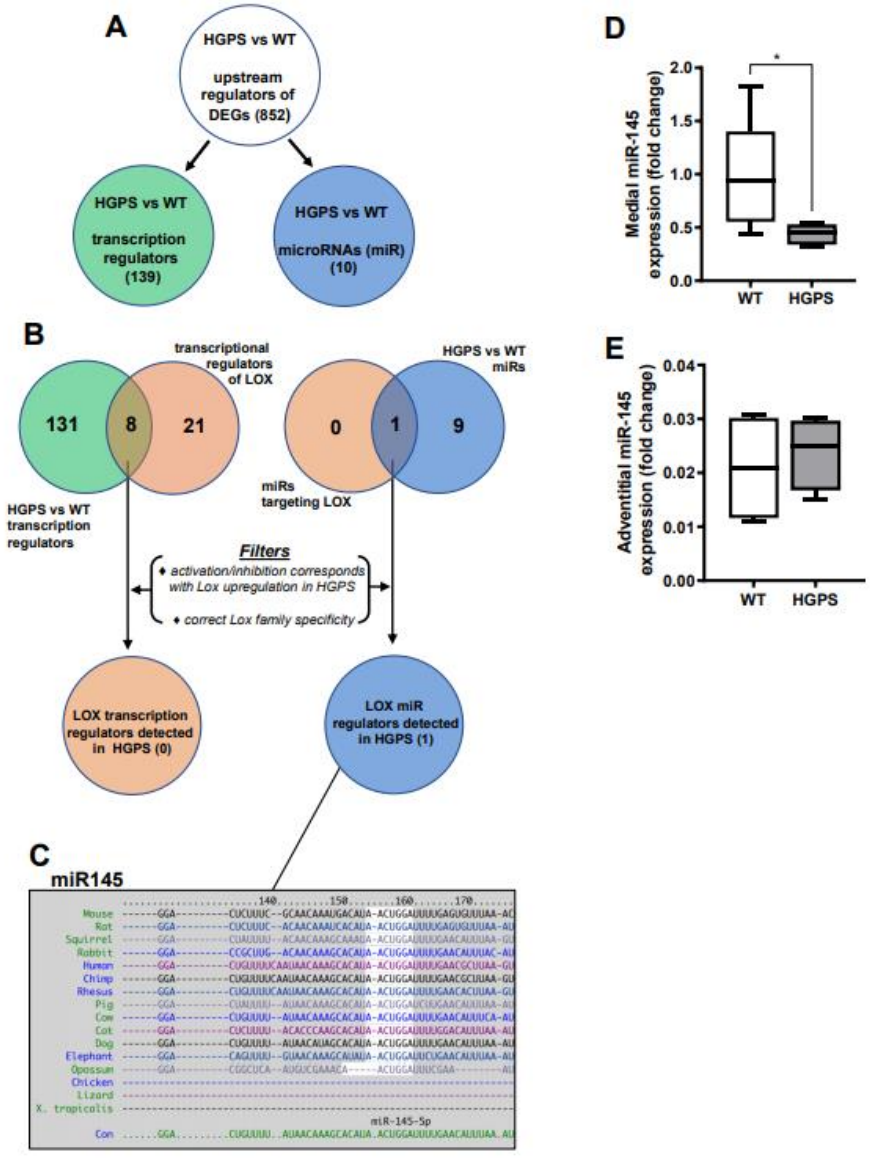

Fig. 2.23. HGPS aortic tissues show reduced miR-145 transcript levels. RNA-sequencing analysis was performed (see Materials and Methods) on cleaned aortas from 2-month WT and HGPS mice (n=6 per genotype) to identify potential upstream

regulators of LOX. **(A)** The number of activation or inhibition signatures in the HGPS vs. WT aortas was inferred from an Ingenuity pathway (IPA) core analysis of differentially expressed genes (DEGs), and the list of total activation/inhibition signatures (top) was subdivided into transcription regulators and microRNAs. **(B)** Venn diagram identifying the number of activation/inhibition signatures in HGPS categorized as either transcription regulators (left, green) or microRNAs (right, blue) were compared to known transcriptional or microRNA regulators of LOX identified from IPA (beige). The likelihood of the 8 transcription regulators and 1 miR accounting for LOX upregulation in HGPS was then considered individually using the criteria shown ("Filters"). **(C)** TargetScan depiction of the conserved 3'UTR miR-145-5p target sequence in LOX. **(D)** miR-145 transcript levels from the medial layer (n=6) and **(E)** adventitial layer (n=4) of 2-month WT and HGPS mice. miR-145 transcript levels were normalized to WT-media values**.** Statistical significance was determined by Mann-Whitney tests.

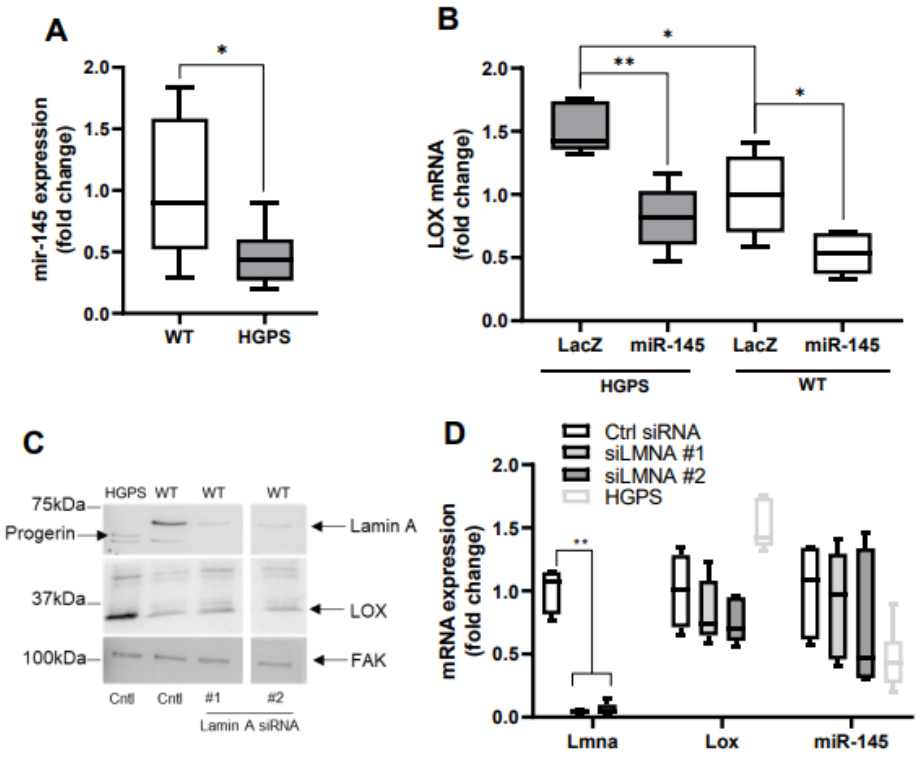

Fig. 2.24. Ectopic expression of miR-145 reduces Lysyl Oxidase (LOX) mRNA in primary HGPS vascular smooth muscle cells (SMCs) and *Lmna* knockdown does not recapitulate the HGPS phenotype. (A) miR-145 transcript levels in isolated WT and HGPS SMCs as determined by RT-qPCR (n=8 per genotype). Statistical significance was determined by a Mann-Whitney test. **(B)** LOX mRNA levels in WT and HGPS SMCs infected with adenoviruses encoding LacZ (control) or miR-145 determined by RT-qPCR and normalized to the WT LacZ control (n=5). Statistical significance was determined by Mann-Whitney tests. **(C)** WT SMCs were transfected with a control siRNA or two different siRNAs targeting LMNA; lysates were analyzed by western blotting and

probed for Lamin A, LOX, and FAK (loading control) (n=3). HGPS SMCs were included as reference. White spaces indicate removal of extraneous data. **(D)** LMNA mRNA was knocked-down in WT SMCs using two distinct siRNAs, and transcript levels of Lmna, Lox, and miR-145 were analyzed by RT-qPCR and normalized to the Ctrl siRNA treatment (n=5). Statistical significance was determined by two-way ANOVA with Holm-Sidak post-tests. The light grey bars in the Tukey plots show HGPS references for miR-145 and LOX and are reproduced from Figure 2.24A and B, respectively.

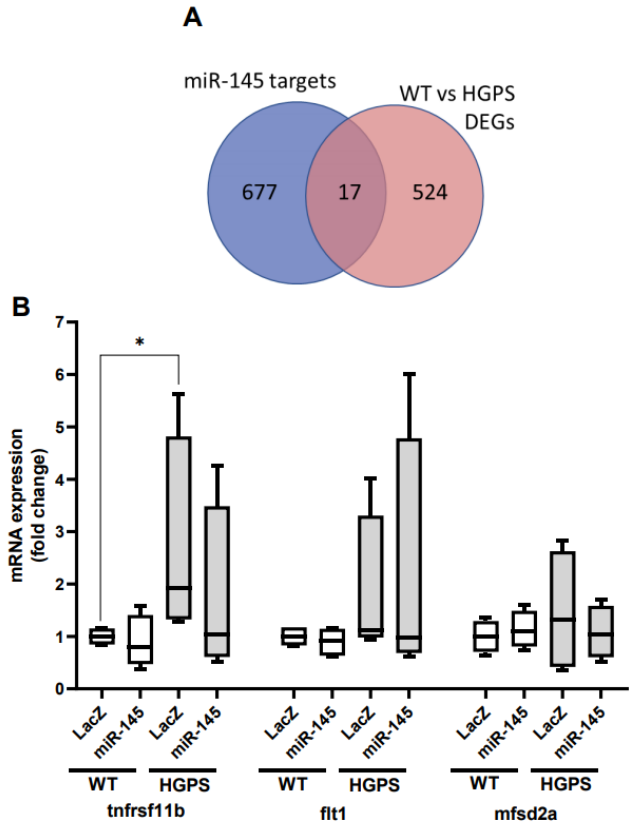

Fig. 2.25. Additional differentially expressed miR-145 target genes in HGPS. (A) The list of miR-145-5p predicted transcripts with conserved sites in the mouse genome, as determined by TargetScan (www.targetscan.org), were compared to the differentially expressed genes in the aortas of 2-mo HGPS vs. WT mice using a log2 fold change $\geq$ 0.8 and an adjusted p-value of <0.0001 as cut-offs. **(B)** Primary aortic smooth muscle cells from 2-mo WT and HGPS mice were infected with an adenovirus encoding LacZ (control) or miR-145. After 72 hours, RNA was isolated and analyzed by RT-qPCR (n=4) for three of the putative miR-145 target genes from panel A, which were selected based on their similar or greater induction than LOX mRNA in HGPS aortas.

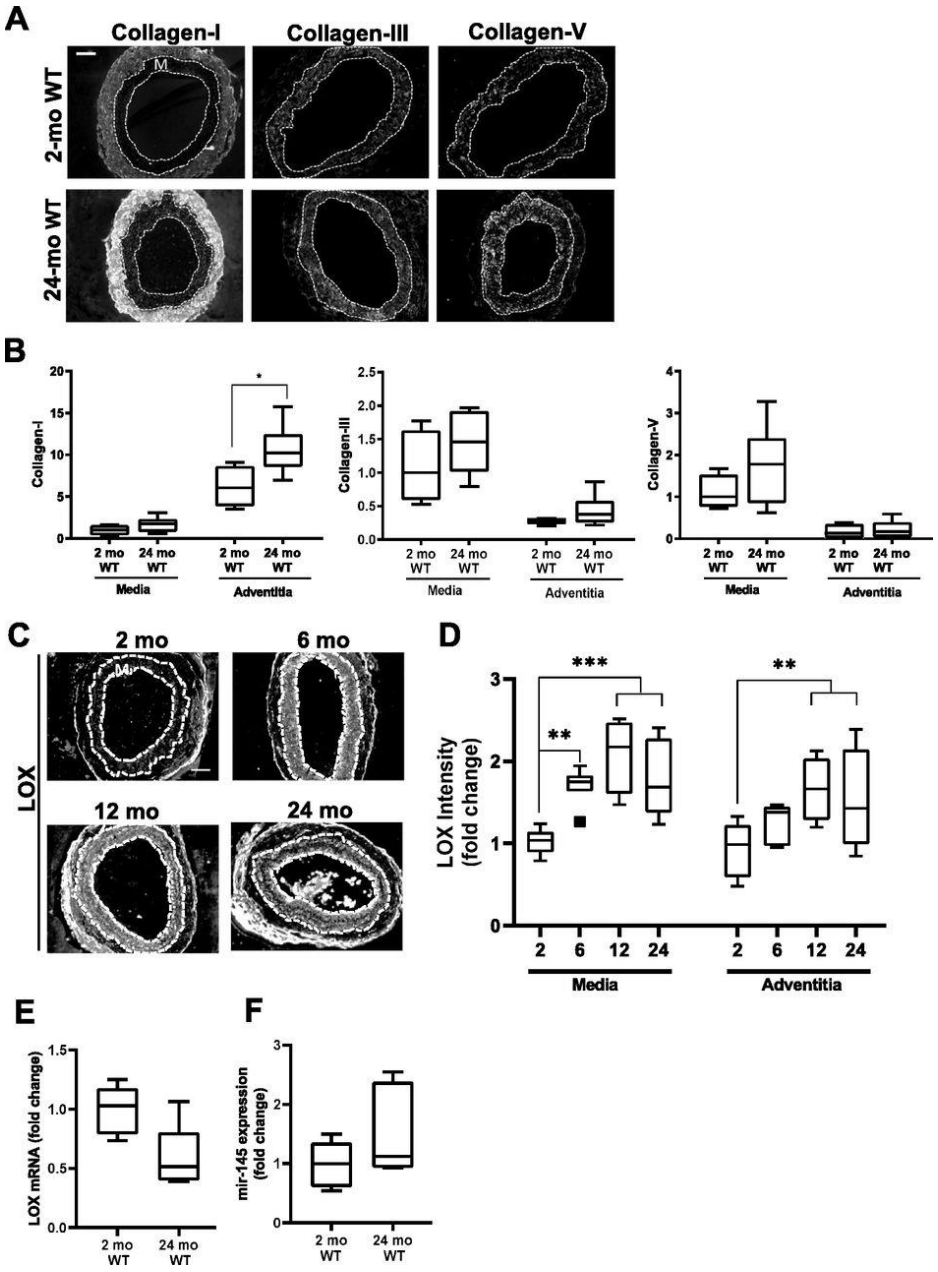

Fig. 2.26. Differential mechanisms drive overexpression of Lysyl Oxidase (LOX) in normal aging. C57BL/6 (WT) mice were aged from 2 to 24 months. **(A)** Representative images of collagen-I, -III, -V immunostaining in carotid artery sections of 2- and 24-

month WT mice (n=4-7 mice per age group). **(B)** Collagen signal intensities in the medial and adventitial layers of the immunostained carotid cross sections were quantified, and results were normalized to the mean of the 2-month WT medial layer for each collagen. Statistical significance was determined by Mann-Whitney tests between ages. **(C)** Representative images of LOX immunostaining of carotid artery cross sections from 2-month (n=8), 6-month (n=7), 12-month (n=4), and 24-month (n=9) WT mice. **(D)** LOX signal intensities were quantified from the immunostained sections, and results were normalized to the mean signal intensity of the 2-month WT medial layer. Statistical significance was determined by one-way ANOVA relative to the 2-month mice followed by Holm-Sidak post-tests. **(E)** LOX mRNA (n=5 per age) and **(F)** miR-145 expression levels (n=6 per age) in 2- and 24-month WT aorta determined by RT-qPCR and normalized to 2-month WT. Statistical significance was determined using Mann-Whitney tests. In carotid cross section images, the arterial media (M) is outlined with dashed lines; scale bar = 50 μm.

2.8 Tables

Table 1. In Vivo Stretch (IVS) values for WT and HGPS mice. Significance was determined by Mann-Whitney test in comparison to the IVS of 2-month WT mice. NS; not significant.

Genotype	Age	Sex	IVS (mean)	IVS (SD)	n	p (relative to 2-mo WT)
WT	2 mo	M	1.85	0.04	13	reference
WT	24 mo	M	1.72	0.05	5	***
HGPS	2 mo	M	1.79	0.10	9	NS
WT	2 mo	F	1.88	0.07	7	reference
WT	24 mo	F	1.74	0.04	5	*
HGPS	2 mo	F	1.79	0.07	10	*

Table 2. In Vivo Stretch (IVS) values for heterozygous 2-month and 9-month and HGPS mice. Significance was determined by Mann-Whitney test.

Age	IVS (mean)	IVS (SD)	n	p
2-mo	1.94	0.07	6	reference
9-mo	1.77	0.04	5	**

Table 3. In Vivo Stretch (IVS) values for mixed sex, 1-month WT and HGPS mice. Significance was determined by Mann-Whitney test. NS; not significant.

Genotype	IVS (mean)	IVS (SD)	n	p
WT	1.83	0.02	5	reference
HGPS	1.8	0.03	5	NS

Table 4. In Vivo Stretch (IVS) values for mixed sex, 2-month WT and HGPS mice treated with vehicle or BAPN. Significance was determined by Mann-Whitney test. NS; not significant.

Genotype	BAPN	IVS (mean)	IVS (SD)	n	p (relative to untreated mice)
WT		1.85	0.05	6	reference
WT	✓	1.84	0.06	5	NS
HGPS		1.73	0.07	7	reference
HGPS	✓	1.74	0.05	6	NS

Table 5. Candidate upstream regulators in HGPS as identified by IPA. The list of 852 upstream regulators that are activated or inhibited in the aortas of 2-month old male HGPS mice relative to 2-month old male WT littermates using a Z-score cutoff of > +1.75 (activated) or < -1.75 (inhibited).

Upstream Regulator	Molecule Type	Activation z-score
poly rI:rC-RNA	biologic drug	5.411
vancomycin	biologic drug	3.348
enterotoxin B	biologic drug	2.724
oblimersen	biologic drug	2.538
aldesleukin	biologic drug	2
isotretinoin	biologic drug	1.867
ceruletide	biologic drug	1.759
beta-estradiol	chemical - endogenous mammalian	5.241
palmitic acid	chemical - endogenous mammalian	4.009
hydrogen peroxide	chemical - endogenous mammalian	3.923
tretinoin	chemical - endogenous mammalian	3.791
inosine	chemical - endogenous mammalian	3.719
fatty acid	chemical - endogenous mammalian	3.615
cholesterol	chemical - endogenous mammalian	3.539
D-fructose	chemical - endogenous mammalian	3.419
homocysteine	chemical - endogenous mammalian	3.145
aldosterone	chemical - endogenous mammalian	3.122
ethanol	chemical - endogenous mammalian	3.052
Ca2+	chemical - endogenous mammalian	2.747
linoleic acid	chemical - endogenous mammalian	2.615
2-arachidonoylglycerol	chemical - endogenous mammalian	2.574
lysophosphatidylinositol	chemical - endogenous mammalian	2.53
carbohydrate	chemical - endogenous mammalian	2.449
acetyl-L-carnitine	chemical - endogenous mammalian	2.414
cyclic AMP	chemical - endogenous mammalian	2.386
sucrose	chemical - endogenous mammalian	2.335
L-triiodothyronine	chemical - endogenous	2.268

	mammalian	
dihydrotestosterone	chemical - endogenous mammalian	2.263
diacylglycerol	chemical - endogenous mammalian	2.236
oxysterol	chemical - endogenous mammalian	2.236
advanced glycation end-products	chemical - endogenous mammalian	2.219
ursodeoxycholic acid	chemical - endogenous mammalian	2.209
fluoride	chemical - endogenous mammalian	2.2
DL-fructose	chemical - endogenous mammalian	2.183
heparin	chemical - endogenous mammalian	2.131
prostaglandin E2	chemical - endogenous mammalian	2.082
uric acid	chemical - endogenous mammalian	2.041
hyaluronic acid	chemical - endogenous mammalian	2.015
manganese	chemical - endogenous mammalian	1.982
8,9-epoxyeicosatrienoic acid	chemical - endogenous mammalian	1.982
lactic acid	chemical - endogenous mammalian	1.98
beta-glycerophosphoric acid	chemical - endogenous mammalian	1.964
acetone	chemical - endogenous mammalian	1.951
norepinephrine	chemical - endogenous mammalian	1.947
anandamide	chemical - endogenous mammalian	1.929
epinephrine	chemical - endogenous mammalian	1.91
platelet activating factor	chemical - endogenous mammalian	1.785
chenodeoxycholic acid	chemical - endogenous mammalian	1.756
oleic acid	chemical - endogenous mammalian	1.755
L-methionine	chemical - endogenous mammalian	-1.786
sterol	chemical - endogenous mammalian	-1.84
lipid	chemical - endogenous mammalian	-2
levodopa	chemical - endogenous mammalian	-2.083
beta-carotene	chemical - endogenous mammalian	-2.331
estriol	chemical - endogenous mammalian	-2.53
choline	chemical - endogenous mammalian	-2.599
salmonella minnesota R595 lipopolysaccharides	chemical - endogenous non-mammal	3.97
E. coli serotype 0127B8 lipopolysaccharide	chemical - endogenous non-mammal	3.873

tunicamycin	chemical - endogenous non-mammal	3.722
E. coli B5 lipopolysaccharide	chemical - endogenous non-mammal	3.611
guanidinopropionic acid	chemical - endogenous non-mammal	3.439
5-O-mycolyl-beta-araf-(1->2)-5-O-mycolyl-alpha-araf-(1->1')-glycer	chemical - endogenous non-mammal	2.84
lipoteichoic acid	chemical - endogenous non-mammal	2.587
hemozoin	chemical - endogenous non-mammal	2.533
E. coli lipopolysaccharide	chemical - endogenous non-mammal	2.316
peptidoglycan	chemical - endogenous non-mammal	2.133
brefeldin A	chemical - endogenous non-mammal	2.13
linalool	chemical - endogenous non-mammal	2
diallyl trisulfide	chemical - endogenous non-mammal	1.982
N-acetylmuramyl-L-alanyl-D-isoglutamine	chemical - endogenous non-mammal	1.977
baicalin	chemical - endogenous non-mammal	1.912
pregna-4,17-diene-3,16-dione	chemical - endogenous non-mammal	-1.982
largazole	chemical - endogenous non-mammal	-2
SP600125	chemical - kinase inhibitor	-1.84
Go6983	chemical - kinase inhibitor	-1.982
JAK inhibitor I	chemical - kinase inhibitor	-1.982
KN 93	chemical - kinase inhibitor	-1.982
H-7	chemical - kinase inhibitor	-1.982
wortmannin	chemical - kinase inhibitor	-2.374
tyrphostin AG 1478	chemical - kinase inhibitor	-2.465
bisindolylmaleimide I	chemical - kinase inhibitor	-2.536
calphostin C	chemical - kinase inhibitor	-2.647
AG490	chemical - kinase inhibitor	-2.709
Bay 11-7082	chemical - kinase inhibitor	-2.71
H89	chemical - kinase inhibitor	-2.725
Go 6976	chemical - kinase inhibitor	-2.736
Ro31-8220	chemical - kinase inhibitor	-3.077
PD98059	chemical - kinase inhibitor	-4.259
LY294002	chemical - kinase inhibitor	-4.51
U0126	chemical - kinase inhibitor	-4.629
SB203580	chemical - kinase inhibitor	-4.908
cardiotoxin	chemical - other	3.9
phorbol esters	chemical - other	1.918
2-amino-5-phosphonovaleric acid	chemical - other	1.763

lactacystin	chemical - protease inhibitor	3.077
proteasome inhibitor PSI	chemical - protease inhibitor	1.754
TAPI-1	chemical - protease inhibitor	-2
tosylphenylalanyl chloromethyl ketone	chemical - protease inhibitor	-2.213
lipopolysaccharide	chemical drug	7.159
rosiglitazone	chemical drug	5.827
cisplatin	chemical drug	4.858
tetradecanoylphorbol acetate	chemical drug	4.817
CpG oligonucleotide	chemical drug	4.475
bleomycin	chemical drug	4.375
bezafibrate	chemical drug	4.357
acetaminophen	chemical drug	3.75
clofibrate	chemical drug	3.705
AGN194204	chemical drug	3.569
imiquimod	chemical drug	3.548
GW501516	chemical drug	3.465
indomethacin	chemical drug	3.411
gentamicin	chemical drug	3.394
fenofibrate	chemical drug	3.325
PLX5622	chemical drug	3.162
cytarabine	chemical drug	3.091
triamterene	chemical drug	3.08
paclitaxel	chemical drug	3.079
5-azacytidine	chemical drug	3.033
resiquimod	chemical drug	3.026
trovafloxacin	chemical drug	3
CL 316243	chemical drug	2.974
phenylbutazone	chemical drug	2.949
alitretinoin	chemical drug	2.911
gemfibrozil	chemical drug	2.853
allopurinol	chemical drug	2.846
troglitazone	chemical drug	2.817
pioglitazone	chemical drug	2.753
cephaloridine	chemical drug	2.735
deferoxamine	chemical drug	2.683
lomustine	chemical drug	2.673
gentamicin C	chemical drug	2.668
mibolerone	chemical drug	2.592
fluticasone propionate	chemical drug	2.566
ciprofibrate	chemical drug	2.549

diethylstilbestrol	chemical drug	2.53
daidzein	chemical drug	2.53
isoproterenol	chemical drug	2.524
1-(carboxymethylthio)tetradecane	chemical drug	2.425
tosedostat	chemical drug	2.408
ribavirin	chemical drug	2.408
hydroxyurea	chemical drug	2.405
clopidogrel	chemical drug	2.4
doxifluridine	chemical drug	2.384
arsenic trioxide	chemical drug	2.319
methotrexate	chemical drug	2.311
NO 1886	chemical drug	2.236
idarubicin	chemical drug	2.236
methylprednisolone	chemical drug	2.233
raloxifene	chemical drug	2.232
GW7647	chemical drug	2.219
WR 1065	chemical drug	2.208
docetaxel	chemical drug	2.205
vitamin K3	chemical drug	2.176
deoxycorticosterone acetate	chemical drug	2.174
phenacetin	chemical drug	2.157
vinblastine	chemical drug	2.156
nelfinavir	chemical drug	2.121
cocaine	chemical drug	2.04
bardoxolone	chemical drug	2.025
glucocorticoid	chemical drug	2.008
genistein	chemical drug	2.001
meldonium	chemical drug	2
hyperforin	chemical drug	2
chloropromazine	chemical drug	1.982
ABT-737	chemical drug	1.982
calcium chloride	chemical drug	1.96
mitomycin C	chemical drug	1.949
camptothecin	chemical drug	1.944
streptozocin	chemical drug	1.943
amitriptyline	chemical drug	1.941
progestin	chemical drug	1.941
nitrofurantoin	chemical drug	1.846
phenobarbital	chemical drug	1.754
valsartan	chemical drug	-1.896

fingolimod	chemical drug	-1.901
fulvestrant	chemical drug	-1.927
roscovitine	chemical drug	-1.937
midostaurin	chemical drug	-1.96
prednisolone	chemical drug	-1.963
edaravone	chemical drug	-1.982
ramipril	chemical drug	-1.982
chelerythrine	chemical drug	-2
nilotinib	chemical drug	-2
zinc	chemical drug	-2.01
thalidomide	chemical drug	-2.219
oleoyl-estrone	chemical drug	-2.224
everolimus	chemical drug	-2.364
alpha-tocopherol	chemical drug	-2.393
spironolactone	chemical drug	-2.42
halofuginone	chemical drug	-2.433
silibinin	chemical drug	-2.439
tanespimycin	chemical drug	-2.655
minocycline	chemical drug	-2.749
flutamide	chemical drug	-2.779
medroxyprogesterone acetate	chemical drug	-2.865
calcitriol	chemical drug	-2.916
alvocidib	chemical drug	-2.939
vitamin E	chemical drug	-2.94
ST1926	chemical drug	-3
N-acetyl-L-cysteine	chemical drug	-3.78
sirolimus	chemical drug	-4.472
metribolone	chemical reagent	6.102
trinitrobenzenesulfonic acid	chemical reagent	3.767
1,2-dithiol-3-thione	chemical reagent	3.282
2-bromoethylamine	chemical reagent	3.217
fenamic acid	chemical reagent	3.05
(5-(4-N-methyl-N(2-pyridyl)amino)ethoxy)benzyl thiazolidine-2,4-dion	chemical reagent	2.621
Ni2+	chemical reagent	2.621
LG100268	chemical reagent	2.596
CpG ODN 1826	chemical reagent	2.584
CpG ODN 2395	chemical reagent	2.433
CpG ODN 2006	chemical reagent	2.417
ionomycin	chemical reagent	2.399
3M-002	chemical reagent	2.383

calcimycin	chemical reagent	2.266
CpG ODN 2216	chemical reagent	2.219
azetidyl-2-carboxylic acid	chemical reagent	2.2
Pam3-Cys-Ser-Lys4	chemical reagent	2.175
TO-901317	chemical reagent	2.11
gamma-secretase inhibitor XX	chemical reagent	2
ST3-Hel2A-2	chemical reagent	2
5,8,11,14-eicosatetraynoic acid	chemical reagent	2
MALP-2s	chemical reagent	2
DPP-23	chemical reagent	1.982
15-E2-isoketal modified phosphatidylethanolamine	chemical reagent	1.98
SR1078	chemical reagent	1.972
N-acetylsphingosine	chemical reagent	1.793
puromycin aminonucleoside	chemical reagent	1.765
sodium orthovanadate	chemical reagent	1.761
NS-398	chemical reagent	-1.794
U73122	chemical reagent	-1.96
cycloheximide	chemical reagent	-1.995
JNJ-39933673	chemical reagent	-2
sea cucumber body wall meal	chemical reagent	-2
poloxamer	chemical reagent	-2.166
diphenyleneiodonium	chemical reagent	-2.216
pyrrolidine dithiocarbamate	chemical reagent	-2.251
pifithrin alpha	chemical reagent	-2.401
GW9662	chemical reagent	-3.03
torin1	chemical reagent	-4.841
mono-(2-ethylhexyl)phthalate	chemical toxicant	6.472
pirinixic acid	chemical toxicant	5.924
E. coli B4 lipopolysaccharide	chemical toxicant	4.744
forskolin	chemical toxicant	3.531
lipid A	chemical toxicant	3.44
thioacetamide	chemical toxicant	3.398
chrysotile asbestos	chemical toxicant	3.078
hexachlorobenzene	chemical toxicant	3.023
cigarette smoke	chemical toxicant	2.945
isobutylmethylxanthine	chemical toxicant	2.709
ethionine	chemical toxicant	2.53
cadmium	chemical toxicant	2.478
methylnitronitrosoguanidine	chemical toxicant	2.388
6-hydroxydopamine	chemical toxicant	2.364

1,4-bis[2-(3,5-dichloropyridyloxy)]benzene	chemical toxicant	2.319
thapsigargin	chemical toxicant	2.274
pristane	chemical toxicant	2.219
methyl methanesulfonate	chemical toxicant	2.189
bucladesine	chemical toxicant	2.185
cadmium chloride	chemical toxicant	2.167
diethylmaleate	chemical toxicant	2.158
3-methylcholanthrene	chemical toxicant	2.116
1-methyl-4-phenyl-1,2,3,6-tetrahydropyridine	chemical toxicant	2.028
monocrotaline	chemical toxicant	2.016
4-nitroquinoline-1-oxide	chemical toxicant	2
triadimefon	chemical toxicant	2
1-methyl-4-phenylpyridinium	chemical toxicant	1.945
reactive oxygen species	chemical toxicant	1.828
Salmonella enterica serotype abortus equi lipopolysaccharide	chemical toxicant	1.824
mercuric chloride	chemical toxicant	1.819
GW 4064	chemical toxicant	1.768
4-tert-octylphenol	chemical toxicant	1.753
Sn50 peptide	chemical toxicant	-1.891
rottlerin	chemical toxicant	-2.147
CD3	complex	4.886
PDGF BB	complex	4.568
LDL	complex	4.47
CG	complex	4.213
PI3K (complex)	complex	4.159
Ige	complex	4.018
NFkB (complex)	complex	4.004
T3-TR-RXR	complex	2.359
Lh	complex	2.304
Collagen type IV	complex	2.236
MAC	complex	2.2
Calcineurin protein(s)	complex	2.136
Pka	complex	2.014
IL23	complex	1.961
MTORC1	complex	1.819
BCR (complex)	complex	1.807
histone deacetylase	complex	-2
CSF2	cytokine	6.388
IFNG	cytokine	5.357
IL5	cytokine	5.216

IL6	cytokine	4.702
SPP1	cytokine	4.637
CSF1	cytokine	4.412
IL1B	cytokine	4.349
TNF	cytokine	4.151
IL13	cytokine	4.011
IL17A	cytokine	3.85
IL4	cytokine	3.816
IFNA2	cytokine	3.794
IL15	cytokine	3.515
IL3	cytokine	3.466
IL1A	cytokine	3.294
TNFSF11	cytokine	3.234
CCL5	cytokine	3.215
IFNB1	cytokine	3.099
OSM	cytokine	3.048
IL21	cytokine	3.047
LIF	cytokine	2.953
IL2	cytokine	2.94
CD40LG	cytokine	2.897
IL33	cytokine	2.873
C5	cytokine	2.846
IL18	cytokine	2.65
IL17F	cytokine	2.425
IFNL1	cytokine	2.415
IL24	cytokine	2.243
IFNE	cytokine	2.219
IFNA1/IFNA13	cytokine	2.209
IL10	cytokine	2.133
TNFSF12	cytokine	2.099
FLT3LG	cytokine	2.057
IL7	cytokine	2.043
Ccl6	cytokine	2
IFNK	cytokine	2
FASLG	cytokine	1.982
CCL11	cytokine	1.97
IL9	cytokine	1.954
TSLP	cytokine	1.941
EPO	cytokine	1.929
IFNA4	cytokine	1.912

PRL	cytokine	1.891
CCL2	cytokine	1.808
MIF	cytokine	1.755
IL1RN	cytokine	-1.997
TGM2	enzyme	4.181
CD38	enzyme	3.594
PNPLA2	enzyme	3.37
FASN	enzyme	2.924
HRAS	enzyme	2.813
PTGS2	enzyme	2.795
CYP2E1	enzyme	2.765
FN1	enzyme	2.509
KRAS	enzyme	2.505
TRAF6	enzyme	2.425
NSUN6	enzyme	2.309
FMO3	enzyme	2.236
ACSS2	enzyme	2.236
CGAS	enzyme	2.224
SAT1	enzyme	2.2
DGAT1	enzyme	2.186
PIN1	enzyme	2.135
CPT1C	enzyme	1.987
LDHB	enzyme	1.982
PRPF19	enzyme	1.982
PARP2	enzyme	1.98
PLCE1	enzyme	1.964
DDX58	enzyme	1.816
RACK1	enzyme	-1.953
ST8SIA1	enzyme	-1.97
TREX1	enzyme	-1.98
SURF1	enzyme	-1.982
EHHADH	enzyme	-2
PLA2G6	enzyme	-2
PNPT1	enzyme	-2.137
RNF31	enzyme	-2.143
SUV39H1	enzyme	-2.2
SCD	enzyme	-2.206
SIRT6	enzyme	-2.213
DNASE2	enzyme	-2.216
CBLB	enzyme	-2.219

ENPP2	enzyme	-2.236
PCYT2	enzyme	-2.236
SSB	enzyme	-2.236
DICER1	enzyme	-2.241
CBS/CBSL	enzyme	-2.425
SPTLC2	enzyme	-2.425
B4GALNT1	enzyme	-2.433
ADA	enzyme	-2.589
CYB5R4	enzyme	-2.622
CAT	enzyme	-2.896
FBXW7	enzyme	-2.905
ALDH2	enzyme	-2.985
ACOX1	enzyme	-3.002
NRAS	enzyme	-3.52
PTGER2	G-protein coupled receptor	3.147
C5AR1	G-protein coupled receptor	2.963
CASR	G-protein coupled receptor	2.834
F2R	G-protein coupled receptor	2.785
FZD9	G-protein coupled receptor	2.619
FFAR3	G-protein coupled receptor	2.376
ADRB3	G-protein coupled receptor	2.191
VIPR1	G-protein coupled receptor	1.987
CCR5	G-protein coupled receptor	1.837
HCAR2	G-protein coupled receptor	-2
SMO	G-protein coupled receptor	-2.232
ACKR2	G-protein coupled receptor	-3.118
Ifnar	group	4.021
Mek	group	3.919
ERK	group	3.915
IFN Beta	group	3.786
P38 MAPK	group	3.643
Interferon alpha	group	3.609
Vegf	group	3.18
ERK1/2	group	3.1
Jnk	group	3.091
Ifn	group	3.052
E2f	group	2.933
cytokine	group	2.869
CD3 group	group	2.767
IL1	group	2.702

Srebp	group	2.646
caspase	group	2.607
MAP2K1/2	group	2.578
Nfat (family)	group	2.517
IFN type 1	group	2.406
Creb	group	2.229
Insulin	group	2.227
IL12 (family)	group	2.189
JAK1/2	group	2.121
Tlr	group	2.029
Gsk3	group	2
elastase	group	1.98
Fgf	group	1.98
Pka catalytic subunit	group	1.954
IFN alpha/beta	group	1.947
SRC (family)	group	1.941
STAT5a/b	group	1.804
ADRB	group	-1.878
DNA-methyltransferase	group	-1.973
Sod	group	-2
Pde4	group	-2.186
estrogen receptor	group	-2.266
Calmodulin	group	-2.333
Rb	group	-2.728
EGLN	group	-3.461
N-cor	group	-3.486
EGF	growth factor	4.298
VEGFA	growth factor	4.09
IGF1	growth factor	4.07
ANGPT2	growth factor	3.59
TGFB1	growth factor	3.473
AREG	growth factor	3.267
AGT	growth factor	3.21
FGF2	growth factor	3.162
NRG1	growth factor	3.034
FGF7	growth factor	2.923
PGF	growth factor	2.382
NGF	growth factor	2.371
FGF10	growth factor	2.333
TGFA	growth factor	2.27

GHRL	growth factor	2.138
FGF21	growth factor	1.871
HGF	growth factor	1.771
NRG4	growth factor	-2.207
CCN5	growth factor	-2.53
TRPV4	ion channel	2.227
KCNJ11	ion channel	1.982
CLCN5	ion channel	-1.944
INSR	kinase	5.205
CHUK	kinase	4.501
STK11	kinase	3.693
PIK3R1	kinase	3.587
IKBKB	kinase	3.523
CAB39L	kinase	3.308
IKBKG	kinase	3.281
MTOR	kinase	3.25
JAK1	kinase	3.228
RAF1	kinase	3.228
AKT1	kinase	3.086
EIF2AK2	kinase	2.961
ERBB2	kinase	2.948
JAK2	kinase	2.943
PRKCD	kinase	2.916
MAPK14	kinase	2.785
SRC	kinase	2.653
EGFR	kinase	2.642
MAP3K7	kinase	2.578
EIF2AK4	kinase	2.575
NTRK2	kinase	2.517
IKBKE	kinase	2.507
MAPKAPK2	kinase	2.465
FGFR1	kinase	2.457
PIM1	kinase	2.393
CHEK2	kinase	2.392
MAP2K3	kinase	2.366
MAPK9	kinase	2.298
MET	kinase	2.289
RIPK2	kinase	2.265
TNK1	kinase	2.219
MAP3K1	kinase	2.191

CSF1R	kinase	2.173
MAPK8	kinase	2.132
Brd4	kinase	2.121
PRKD1	kinase	2.08
BRD4	kinase	2.038
PRKCA	kinase	2.025
PRKAR2B	kinase	2
RIPK1	kinase	1.982
ILK	kinase	1.976
ROCK2	kinase	1.964
MAP3K14	kinase	1.964
DDR1	kinase	1.953
IRAK4	kinase	1.939
PIK3CA	kinase	1.904
ROR1	kinase	1.89
EFNA2	kinase	1.89
PLK1	kinase	-1.953
Sik1	kinase	-1.969
SIK1/SIK1B	kinase	-1.98
ERBB4	kinase	-1.997
GNE	kinase	-2
PCK1	kinase	-2.414
CDK19	kinase	-2.706
TRIB3	kinase	-2.778
MAP4K4	kinase	-5.009
PPARG	ligand-dependent nuclear receptor	5.312
PPARA	ligand-dependent nuclear receptor	4.129
ESRRA	ligand-dependent nuclear receptor	3.94
PPARD	ligand-dependent nuclear receptor	3.469
NR1I3	ligand-dependent nuclear receptor	2.734
ESR1	ligand-dependent nuclear receptor	2.56
RORA	ligand-dependent nuclear receptor	2.514
NR1I2	ligand-dependent nuclear receptor	1.918
NR3C2	ligand-dependent nuclear receptor	1.907
THRA	ligand-dependent nuclear receptor	-2.102
NR0B2	ligand-dependent nuclear receptor	-2.277
NR4A1	ligand-dependent nuclear receptor	-2.6
miR-124-3p (and other miRNAs w/seed AAGGCAC)	mature microRNA	-1.777
miR-217-5p (and other miRNAs w/seed ACUGCAU)	mature microRNA	-2
miR-27a-3p (and other miRNAs w/seed UCACAGU)	mature microRNA	-2.005

miR-155-5p (miRNAs w/seed UAAUGCU)	mature microRNA	-2.079
miR-199a-3p (and other miRNAs w/seed CAGUAGU)	mature microRNA	-2.213
miR-24-3p (and other miRNAs w/seed GGCUCAG)	mature microRNA	-2.408
mir-145	microRNA	-1.799
mir-33	microRNA	-2.414
let-7	microRNA	-2.925
mir-21	microRNA	-3.595
ELAVL1	other	4.795
MYD88	other	4.55
TICAM1	other	4.027
TMEM173	other	3.32
RETNLB	other	3.297
CCNC	other	3.267
RETN	other	3.123
PCGEM1	other	3.105
SCAP	other	3.089
Hbb-b2	other	3
CD44	other	2.938
HRG	other	2.828
SELPLG	other	2.828
Firre	other	2.828
RABL6	other	2.668
BID	other	2.646
C2CD5	other	2.619
C1QA	other	2.58
THBS4	other	2.578
APP	other	2.564
Ins1	other	2.521
TRAF3IP2	other	2.457
NKX2-2-AS1	other	2.449
TRADD	other	2.449
EWSR1	other	2.449
FST	other	2.446
TP53COR1	other	2.425
METRNL	other	2.401
THBS1	other	2.401
TAC1	other	2.361
PEBP1	other	2.335
CAMP	other	2.329
SAMSN1	other	2.309

S100A9	other	2.245
ACTB	other	2.236
HNF1A-AS1	other	2.219
ADM2	other	2.216
Trp53cor1	other	2.207
ERFE	other	2.2
LINC00963	other	2.176
GAST	other	2.173
MYOC	other	2.157
LLGL2	other	2.121
MEDAG	other	2
SH3TC2	other	2
PAF1	other	2
ORMDL3	other	1.994
PNN	other	1.982
TG	other	1.981
LGALS3	other	1.975
LAMA5	other	1.964
TERF2IP	other	1.964
ASXL2	other	1.89
EFNA1	other	1.89
LIN9	other	1.834
RPTOR	other	1.795
MAVS	other	1.795
NOD2	other	1.767
SFTPD	other	-1.824
TSC2	other	-1.838
HOTAIR	other	-1.872
TOPBP1	other	-1.924
RBL2	other	-1.937
NREP	other	-1.954
SPINT2	other	-1.964
SLPI	other	-1.964
RBM5	other	-1.964
MGP	other	-1.982
BCL2L12	other	-2
SCGB3A2	other	-2
UBD	other	-2
FANCC	other	-2
CORT	other	-2

PLIN5	other	-2.109
TNIP1	other	-2.195
PECAM1	other	-2.2
SELENOS	other	-2.2
TUG1	other	-2.224
ZNF106	other	-2.333
CIDEC	other	-2.36
INSIG2	other	-2.391
ANXA2	other	-2.425
1810019D21Rik	other	-2.5
GAS2L3	other	-2.63
Bvht	other	-2.668
FLCN	other	-2.711
Irgm1	other	-3.487
VCAN	other	-3.789
SOCS1	other	-4.111
RICTOR	other	-4.741
INSIG1	other	-4.746
USP22	peptidase	3.742
CFB	peptidase	2.789
F2	peptidase	2.766
SENP1	peptidase	2.607
PLG	peptidase	2.185
MBTPS1	peptidase	2
MMP1	peptidase	1.97
MMP2	peptidase	1.782
ADAM17	peptidase	1.762
PSEN1	peptidase	-1.818
USP18	peptidase	-1.982
ZMPSTE24	peptidase	-2.377
PSMB11	peptidase	-2.858
NCSTN	peptidase	-3.45
CLPP	peptidase	-5.648
PPP2CA	phosphatase	2.236
PDCD1	phosphatase	-1.89
PPP1R15B	phosphatase	-1.964
NT5E	phosphatase	-2
PON1	phosphatase	-2
PTPN6	phosphatase	-2.534
PTPN11	phosphatase	-2.559

Ptprd	phosphatase	-2.646
PPARGC1A	transcription regulator	5.108
ATF4	transcription regulator	4.757
SREBF1	transcription regulator	4.571
CEBPA	transcription regulator	4.327
STAT1	transcription regulator	4.302
PPARGC1B	transcription regulator	4.052
CEBPB	transcription regulator	3.967
HIF1A	transcription regulator	3.892
MITF	transcription regulator	3.889
IRF3	transcription regulator	3.888
IFI16	transcription regulator	3.73
MED1	transcription regulator	3.723
IRF7	transcription regulator	3.65
JUN	transcription regulator	3.618
SREBF2	transcription regulator	3.545
NFKBIA	transcription regulator	3.531
FOXM1	transcription regulator	3.46
NFKB1	transcription regulator	3.412
MYC	transcription regulator	3.4
FOXO1	transcription regulator	3.362
RELA	transcription regulator	3.34
EGR1	transcription regulator	3.337
NFE2L2	transcription regulator	3.302
KLF15	transcription regulator	3.217
REL	transcription regulator	3.177
SPIB	transcription regulator	3.13
MTPN	transcription regulator	3.096
Esrra	transcription regulator	3.049
STAT3	transcription regulator	3.029
CREB1	transcription regulator	3.025
MLXIPL	transcription regulator	2.949
NCOA2	transcription regulator	2.91
GATA4	transcription regulator	2.899
CTNNB1	transcription regulator	2.811
STAT4	transcription regulator	2.75
ATF6	transcription regulator	2.687
SP3	transcription regulator	2.678
TP63	transcription regulator	2.624
YBX1	transcription regulator	2.621

NFYA	transcription regulator	2.598
SMYD1	transcription regulator	2.588
MLX	transcription regulator	2.577
IRF5	transcription regulator	2.558
EBF1	transcription regulator	2.554
E2F3	transcription regulator	2.534
TFAM	transcription regulator	2.53
CCND1	transcription regulator	2.497
DDIT3	transcription regulator	2.487
FOXF2	transcription regulator	2.434
IRF1	transcription regulator	2.389
STAT2	transcription regulator	2.386
ETS1	transcription regulator	2.375
ECSIT	transcription regulator	2.372
TFE3	transcription regulator	2.35
SP1	transcription regulator	2.281
XBP1	transcription regulator	2.273
IRF8	transcription regulator	2.258
HIRA	transcription regulator	2.236
FOS	transcription regulator	2.23
PLAGL1	transcription regulator	2.216
NRF1	transcription regulator	2.212
SPI1	transcription regulator	2.211
CARM1	transcription regulator	2.204
SRA1	transcription regulator	2.2
NCOA3	transcription regulator	2.197
TWIST2	transcription regulator	2.19
USF2	transcription regulator	2.18
ELK1	transcription regulator	2.16
HDAC5	transcription regulator	2.157
SMAD2	transcription regulator	2.149
ARNT2	transcription regulator	2.121
MEN1	transcription regulator	2.057
MYBL2	transcription regulator	1.998
PITX2	transcription regulator	1.997
FOXL2	transcription regulator	1.988
MED14	transcription regulator	1.987
CEBPE	transcription regulator	1.982
SIM1	transcription regulator	1.976
CRTC1	transcription regulator	1.969

HUWE1	transcription regulator	1.963
PHF1	transcription regulator	1.96
VDR	transcription regulator	1.958
MAF	transcription regulator	1.951
WDR5	transcription regulator	1.944
HEY1	transcription regulator	1.941
HEY2	transcription regulator	1.94
ASCL1	transcription regulator	1.912
ELL2	transcription regulator	1.89
LHX1	transcription regulator	1.89
MAFB	transcription regulator	1.841
HNF4A	transcription regulator	1.837
HDAC4	transcription regulator	1.83
H2AX	transcription regulator	1.802
FOSL1	transcription regulator	1.786
KLF11	transcription regulator	1.777
HAND2	transcription regulator	1.765
MYCN	transcription regulator	1.763
NFAT5	transcription regulator	1.755
MDM4	transcription regulator	-1.763
CTCF	transcription regulator	-1.803
ID1	transcription regulator	-1.837
ASXL1	transcription regulator	-1.89
HOXA3	transcription regulator	-1.912
ZNF281	transcription regulator	-1.914
DNAJB6	transcription regulator	-1.945
ZBTB16	transcription regulator	-1.948
NOTCH4	transcription regulator	-1.951
MXI1	transcription regulator	-1.969
FHL2	transcription regulator	-1.976
MAML1	transcription regulator	-1.98
HOXA11	transcription regulator	-1.982
HAND1	transcription regulator	-1.982
MRTFB	transcription regulator	-1.985
PIAS1	transcription regulator	-1.986
Cux1	transcription regulator	-2
IKZF2	transcription regulator	-2
HES3	transcription regulator	-2
ONECUT1	transcription regulator	-2
HNF1B	transcription regulator	-2.034

CBL	transcription regulator	-2.056
KDM5B	transcription regulator	-2.144
FOXA1	transcription regulator	-2.165
SERTAD2	transcription regulator	-2.177
FOXA3	transcription regulator	-2.202
CREBZF	transcription regulator	-2.207
SP110	transcription regulator	-2.309
TFAP2C	transcription regulator	-2.414
SRSF2	transcription regulator	-2.433
GLIS2	transcription regulator	-2.449
MED13	transcription regulator	-2.496
SMAD7	transcription regulator	-2.517
TAF4	transcription regulator	-2.6
MRTFA	transcription regulator	-2.689
SIRT1	transcription regulator	-2.728
NRIP1	transcription regulator	-2.853
TRPS1	transcription regulator	-2.874
RBL1	transcription regulator	-3.12
ZFP36	transcription regulator	-3.617
SRF	transcription regulator	-3.887
KDM5A	transcription regulator	-4.134
EIF2S1	translation regulator	3.302
EIF4E	translation regulator	2.89
RPL22	translation regulator	-2.425
CD28	transmembrane receptor	4.805
TLR7	transmembrane receptor	4.58
TLR3	transmembrane receptor	4.231
IFNAR1	transmembrane receptor	3.906
TLR4	transmembrane receptor	3.697
TLR9	transmembrane receptor	3.575
CD36	transmembrane receptor	2.575
CD40	transmembrane receptor	2.491
CD2	transmembrane receptor	2.449
PLA2R1	transmembrane receptor	2.415
OLR1	transmembrane receptor	2.396
TLR8	transmembrane receptor	2.191
SEMA7A	transmembrane receptor	2.121
LTBR	transmembrane receptor	2.121
EDNRA	transmembrane receptor	2
Klra7 (includes others)	transmembrane receptor	1.982

IFNGR1	transmembrane receptor	1.982
ITGA5	transmembrane receptor	1.98
NCR2	transmembrane receptor	1.98
IL6R	transmembrane receptor	1.978
IL17RA	transmembrane receptor	1.964
ICOS	transmembrane receptor	1.944
LGR5	transmembrane receptor	1.937
CD14	transmembrane receptor	1.931
ITGA6	transmembrane receptor	1.925
TNFRSF9	transmembrane receptor	1.912
F3	transmembrane receptor	1.908
IGF1R	transmembrane receptor	1.892
IL11RA	transmembrane receptor	1.876
TYROBP	transmembrane receptor	1.782
NGFR	transmembrane receptor	-1.972
IL27RA	transmembrane receptor	-1.982
SFRP1	transmembrane receptor	-3
IL10RA	transmembrane receptor	-3.156
UCP1	transporter	4.317
Hbb-b1	transporter	3.881
HBA1/HBA2	transporter	3.207
SYVN1	transporter	3
ALB	transporter	2.621
SLC29A1	transporter	2.433
SLC5A5	transporter	2
BAX	transporter	1.961
FABP1	transporter	-1.89
SCARB1	transporter	-1.949
SLC30A7	transporter	-1.982
STAR	transporter	-2
HBB	transporter	-2
APOA1	transporter	-2.183
SFTPA1	transporter	-2.221
ABCC8	transporter	-2.224
ABCB4	transporter	-2.228
COMMD1	transporter	-2.449
TFRC	transporter	-2.478
APOE	transporter	-5.113

Table 6. Candidate transcription regulators of LOX gene expression in HGPS. The eight transcription regulators identified by IPA that are upstream of LOX and either activated or inhibited in HGPS. The table also shows the basis for their exclusion using the filters identified in Fig. 2.22B and the corresponding citations in the IPA database.

Transcription Regulator	
DDIT3	negative regulator of LOX (Engström et al. 2006) but activated in HGPS
Fos	positive regulator of LOX (Johnston et al. 2000) but inhibited in HGPS
Myc	negative regulator of LOX (O'Connell et al. 2003) but activated in HGPS
TFAP2C	transcriptional activator of LOXL2 as well as LOX (Bogachek et al. 2014)
FOXM1	transcriptional activator of LOXL2 as well as LOX (Park et al. 2011)
HIF1A	transcriptional activator of LOXL2 as well as LOX (Schietke et al. 2010; Elvidge et al. 2006; Wang et al. 2005)
STAT3	effect on LOX is in coordination with HIF-1A (Pawlus et al. 2014)
KLF11	inconsistent effects of KLF11 on LOX gene expression (Mathison et al. 2013)

2.9 References

Arancio W, Pizzolanti G, Genovese SI, Pitrone M & Giordano C (2014) Epigenetic involvement in Hutchinson-Gilford progeria syndrome: a mini-review. *Gerontology* 60, 197–203.

Bachhuber TE, Lalich JJ, Angevine DM, Schilling ED & Strong FM (1955) Lathyrus Factor Activity of Beta-Aminopropionitrile and Related Compounds. *Exp. Biol. Med.* 89, 294–297.

Baker A-M, Bird D, Lang G, Cox TR & Erler JT (2013) Lysyl oxidase enzymatic function increases stiffness to drive colorectal cancer progression through FAK. *Oncogene* 32, 1863–1868.

Bogachek M V., Chen Y, Kulak M V., Woodfield GW, Cyr AR, Park JM, Spanheimer PM, Li Y, Li T & Weigel RJ (2014) Sumoylation pathway is required to maintain the basal breast cancer subtype. *Cancer Cell* 25, 748–761.

Brankovic S, Hawthorne EA, Yu X, Zhang Y & Assoian RK (2019) MMP12 preferentially attenuates axial stiffening of aging arteries. *J. Biomech. Eng.*

del Campo L, Sánchez-López A, Salaices M, von Kleeck RA, Expósito E, González-Gómez C, Cussó L, Guzmán-Martínez G, Ruiz-Cabello J, Desco M, Assoian RK, Briones AM & Andrés V (2019) Vascular smooth muscle cell-specific progerin expression in a mouse model of Hutchinson–Gilford progeria syndrome promotes arterial stiffness: Therapeutic effect of dietary nitrite. *Aging Cell*, e12936.

Capell BC, Collins FS & Nabel EG (2007) Mechanisms of cardiovascular disease in accelerated aging syndromes. *Circ. Res.* 101, 13–26.

Cheng Y, Liu X, Yang J, Lin Y, Xu DZ, Lu Q, Deitch EA, Huo Y, Delphin ES & Zhang C (2009) MicroRNA-145, a novel smooth muscle cell phenotypic marker and modulator, controls vascular neointimal lesion formation. *Circ. Res.* 105, 158–166.

Cox TR & Erler JT (2011) Remodeling and homeostasis of the extracellular matrix: implications for fibrotic diseases and cancer. *Dis. Model. Mech.* 4, 165–78.

Cuff CA, Kothapalli D, Azonobi I, Chun S, Zhang Y, Belkin R, Yeh C, Secreto A, Assoian RK, Rader DJ & Puré E (2001) The adhesion receptor CD44 promotes atherosclerosis by mediating inflammatory cell recruitment and vascular cell activation. *J. Clin. Invest.* 108, 1031–1040.

Davidson JM, Hill KE & Alford JL (1986) Developmental changes in collagen and elastin biosynthesis in the porcine aorta. *Dev. Biol.* 118, 103–11.

Desmoulière A, Darby I, Costa AM, Raccurt M, Tuchweber B, Sommer P & Gabbiani G (1997) Extracellular matrix deposition, lysyl oxidase expression, and myofibroblastic differentiation during the initial stages of cholestatic fibrosis in the rat. *Lab. Invest.* 76, 765–78.

Dorado B, Pløen GG, Barettino A, Macías A, Gonzalo P, Andrés-Manzano MJ, González-Gómez C, Galán-Arriola C, Alfonso JM, Lobo M, López-Martín GJ, Molina A, Sánchez-Sánchez R, Gadea J, Sánchez-González J, Liu Y, Callesen H, Filgueiras-Rama D, Ibáñez B, Sørensen CB & Andrés V (2019) Generation and characterization of a novel knockin minipig model of Hutchinson-Gilford progeria syndrome. *Cell Discov.* 5, 1–15.

Elvidge GP, Glenny L, Appelhoff RJ, Ratcliffe PJ, Ragoussis J & Gleadle JM (2006) Concordant regulation of gene expression by hypoxia and 2-oxoglutarate-dependent dioxygenase inhibition: The role of HIF-1α, HIF-2α, and other pathways.

J. Biol. Chem. 281, 15215–15226.

Engström K, Willén H, Kåbjörn-Gustafsson C, Andersson C, Olsson M, Göransson M, Järnum S, Olofsson A, Warnhammar E & Åman P (2006) The myxoid/round cell liposarcoma fusion oncogene FUS-DDIT3 and the normal DDIT3 induce a liposarcoma phenotype in transfected human fibrosarcoma cells. *Am. J. Pathol.* 168, 1642–1653.

Faccini J, Ruidavets JB, Cordelier P, Martins F, Maoret JJ, Bongard V, Ferrières J, Roncalli J, Elbaz M & Vindis C (2017) Circulating MIR-155, MIR-145 and let-7c as diagnostic biomarkers of the coronary artery disease. *Sci. Rep.* 7, 1–10.

Ferruzzi J, Bersi MR & Humphrey JD (2013) Biomechanical Phenotyping of Central Arteries in Health and Disease: Advantages of and Methods for Murine Models. *Ann. Biomed. Eng.* 41, 1311–1330.

Finney J, Moon HJ, Ronnebaum T, Lantz M & Mure M (2014) Human copper-dependent amine oxidases. *Arch. Biochem. Biophys.* 546, 19–32.

Freitas-Rodríguez S, Folgueras AR & López-Otín C (2017) The role of matrix metalloproteinases in aging: Tissue remodeling and beyond. *Biochim. Biophys. Acta - Mol. Cell Res.* 1864, 2015–2025.

Gerhard-Herman M, Smoot LB, Wake N, Kieran MW, Kleinman ME, Miller DT, Schwartzman A, Giobbie-Hurder A, Neuberg D & Gordon LB (2011) Mechanisms of Premature Vascular Aging in Children With Hutchinson-Gilford Progeria Syndrome. *Hypertension* 59.

Gonzalo S, Kreienkamp R & Askjaer P (2016) Hutchinson-Gilford Progeria Syndrome: A premature aging disease caused by LMNA gene mutations. *Ageing Res. Rev.*

Gordon LB, Harten IA, Patti ME & Lichtenstein AH (2005) Reduced adiponectin and HDL

cholesterol without elevated C-reactive protein: Clues to the biology of premature atherosclerosis in Hutchinson-Gilford Progeria Syndrome. *J. Pediatr.* 146, 336–341.

Gordon LB, Kleinman ME, Miller DT, Neuberg DS, Giobbie-Hurder A, Gerhard-Herman M, Smoot LB, Gordon CM, Cleveland R, Snyder BD, Fligor B, Bishop WR, Statkevich P, Regen A, Sonis A, Riley S, Ploski C, Correia A, Quinn N, Ullrich NJ, Nazarian A, Liang MG, Huh SY, Schwartzman A & Kieran MW (2012) Clinical trial of a farnesyltransferase inhibitor in children with Hutchinson-Gilford progeria syndrome. *Proc. Natl. Acad. Sci. U. S. A.* 109, 16666–71.

Gordon LB, Shappell H, Massaro J, D'Agostino RB, Brazier J, Campbell SE, Kleinman ME & Kieran MW (2018) Association of Lonafarnib Treatment vs No Treatment With Mortality Rate in Patients With Hutchinson-Gilford Progeria Syndrome. *JAMA* 319, 1687.

Greenberg SR (1986) The association of medial collagenous tissue with atheroma formation in the aging human aorta as revealed by a special technique. *Histol. Histopathol.* 1, 323–6.

Halley CM, Houghtaling PL, Khalil MK, Thomas JD & Jaber WA (2011) Mortality rate in patients with diastolic dysfunction and normal systolic function. *Arch. Intern. Med.* 171, 1082–1087.

Hamczyk MR & Andrés V (2019) Vascular smooth muscle cell loss underpins the accelerated atherosclerosis in Hutchinson-Gilford progeria syndrome. *Nucleus* 10, 48–54.

Herchenhan A, Uhlenbrock F, Eliasson P, Weis M, Eyre D, Kadler KE, Magnusson SP & Kjaer M (2015) Lysyl Oxidase Activity Is Required for Ordered Collagen Fibrillogenesis by Tendon Cells. *J. Biol. Chem.* 290, 16440–16450.

Hulmes DJS (2008) Collagen diversity, synthesis and assembly. In *Collagen: Structure and Mechanics*. Springer US, pp.15–47.

Humphrey JD, Dufresne ER & Schwartz MA (2014) Mechanotransduction and extracellular matrix homeostasis. *Nat. Rev. Mol. Cell Biol.* 15, 802–812.

Johnston IMP, Spence HJ, Winnie JN, McGarry L, Vass JK, Meagher L, Stapleton G & Ozanne BW (2000) Regulation of a multigenic invasion programme by the transcription factor, AP-1: Re-expression of a down-regulated gene, TSC-36, inhibits invasion. *Oncogene* 19, 5348–5358.

Jung ST, Kim MS, Seo JY, Kim HC & Kim Y (2003) Purification of enzymatically active human lysyl oxidase and lysyl oxidase-like protein from Escherichia coli inclusion bodies. *Protein Expr. Purif.* 31, 240–6.

Kagan HM (1994) Lysyl Oxidase: Mechanism, Regulation and Relationship to Liver Fibrosis. *Pathol. - Res. Pract.* 190, 910–919.

Kelleher CM, McLean SE & Mecham RP (2004) Vascular Extracellular Matrix and Aortic Development. *Curr. Top. Dev. Biol.* 62, 153–188.

Kelley JB, Datta S, Snow CJ, Chatterjee M, Ni L, Spencer A, Yang C-S, Cubenas-Potts C, Matunis MJ & Paschal BM (2011) The Defective Nuclear Lamina in Hutchinson-Gilford Progeria Syndrome Disrupts the Nucleocytoplasmic Ran Gradient and Inhibits Nuclear Localization of Ubc9. *Mol. Cell. Biol.* 31, 3378–3395.

Kim HL, Lim WH, Seo J Bin, Chung WY, Kim SH, Kim MA & Zo JH (2017) Association between arterial stiffness and left ventricular diastolic function in relation to gender and age. *Med. (United States)* 96.

Kim MS, Kim S-S, Jung ST, Park J-Y, Yoo H-W, Ko J, Csiszar K, Choi S-Y & Kim Y (2003) Expression and Purification of Enzymatically Active Forms of the Human

Lysyl Oxidase-like Protein 4. *J. Biol. Chem.* 278, 52071–52074.

Klein EA, Yung Y, Castagnino P, Kothapalli D & Assoian RK (2007) Cell Adhesion, Cellular Tension, and Cell Cycle Control. *Methods Enzymol.* 426, 155–175.

Köhler F, Bormann F, Raddatz G, Gutekunst J, Corless S, Musch T, Lonsdorf AS, Erhardt S, Lyko F & Rodríguez-Paredes M (2020) Epigenetic deregulation of lamina-associated domains in Hutchinson-Gilford progeria syndrome. *Genome Med.* 12, 46.

Kohn JC, Lampi MC & Reinhart-King CA (2015) Age-related vascular stiffening: causes and consequences. *Front. Genet.* 06, 112.

Kothapalli D, Liu S-L, Bae YH, Monslow J, Xu T, Hawthorne EA, Byfield FJ, Castagnino P, Rao S, Rader DJ, Puré E, Phillips MC, Lund-Katz S, Janmey PA & Assoian RK (2012) Cardiovascular Protection by ApoE and ApoE-HDL Linked to Suppression of ECM Gene Expression and Arterial Stiffening. *Cell Rep.* 2, 1259–1271.

Lampi MC & Reinhart-King CA (2018) Targeting extracellular matrix stiffness to attenuate disease: From molecular mechanisms to clinical trials. *Sci. Transl. Med.* 10, eaao0475.

Laurent S & Boutouyrie P (2015) The Structural Factor of Hypertension. *Circ. Res.* 116, 1007–1021.

Lee J-E & Kim Y (2006) A Tissue-specific Variant of the Human Lysyl Oxidase-like Protein 3 (LOXL3) Functions as an Amine Oxidase with Substrate Specificity. *J. Biol. Chem.* 281, 37282–37290.

Levene CI (1985) POSSIBILITIES FOR THE THERAPEUTIC CONTROL OF FIBROSIS. *Br. J. Dermatol.* 112, 363–371.

Mathison A, Grzenda A, Lomberk G, Velez G, Buttar N, Tietz P, Hendrickson H, Liebl A,

Xiong YY, Gores G, Fernandez-Zapico M, LaRusso NF, Faubion W, Shah VH & Urrutia R (2013) Role for Krüppel-Like Transcription Factor 11 in Mesenchymal Cell Function and Fibrosis. *PLoS One* 8.

McClintock D, Ratner D, Lokuge M, Owens DM, Gordon LB, Collins FS & Djabali K (2007) The Mutant Form of Lamin A that Causes Hutchinson-Gilford Progeria Is a Biomarker of Cellular Aging in Human Skin A. Lewin, ed. *PLoS One* 2, e1269.

Merideth MA, Gordon LB, Clauss S, Sachdev V, Smith ACM, Perry MB, Brewer CC, Zalewski C, Kim HJ, Solomon B, Brooks BP, Gerber LH, Turner ML, Domingo DL, Hart TC, Graf J, Reynolds JC, Gropman A, Yanovski JA, Gerhard-Herman M, Collins FS, Nabel EG, Cannon RO, Gahl WA & Introne WJ (2008) Phenotype and Course of Hutchinson–Gilford Progeria Syndrome. *N. Engl. J. Med.* 358, 592–604.

Mitchell GF, Guo C-Y, Benjamin EJ, Larson MG, Keyes MJ, Vita JA, Vasan RS & Levy D (2007) Cross-Sectional Correlates of Increased Aortic Stiffness in the Community. *Circulation* 115, 2628–2636.

Mitchell GF, Hwang SJ, Vasan RS, Larson MG, Pencina MJ, Hamburg NM, Vita JA, Levy D & Benjamin EJ (2010) Arterial stiffness and cardiovascular events: the Framingham Heart Study. *Circulation* 121, 505–511.

Mithieux SM & Weiss AS (2005) Elastin. In *Advances in protein chemistry*. pp.437–461.

Mottram PM, Haluska BA, Leano R, Carlier S, Case C & Marwick TH (2005) Relation of arterial stiffness to diastolic dysfunction in hypertensive heart disease. *Heart* 91, 1551–1556.

Murtada S-I, Kawamura Y, Caulk AW, Ahmadzadeh H, Mikush N, Zimmerman K, Kavanagh D, Weiss D, Latorre M, Zhuang ZW, Shadel GS, Braddock DT & Humphrey JD (2020) Paradoxical aortic stiffening and subsequent cardiac

dysfunction in Hutchinson–Gilford progeria syndrome. *J. R. Soc. Interface* 17, 20200066.

Nilsson M, Adamo H, Bergh A, Halin Bergström S & Kim Y (2016) Inhibition of Lysyl Oxidase and Lysyl Oxidase-Like Enzymes Has Tumour-Promoting and Tumour-Suppressing Roles in Experimental Prostate Cancer. *Sci. Rep.* 6, 19608.

O'Connell BC, Cheung AF, Simkevich CP, Tam W, Ren X, Mateyak MK & Sedivy JM (2003) A large scale genetic analysis of c-Myc-regulated gene expression patterns. *J. Biol. Chem.* 278, 12563–12573.

Olive M, Harten I, Mitchell R, Beers JK, Djabali K, Cao K, Erdos MR, Blair C, Funke B, Smoot L, Gerhard-Herman M, Machan JT, Kutys R, Virmani R, Collins FS, Wight TN, Nabel EG & Gordon LB (2010) Cardiovascular Pathology in Hutchinson-Gilford Progeria: Correlation With the Vascular Pathology of Aging. *Arterioscler. Thromb. Vasc. Biol.* 30.

Oppi S, Lüscher TF & Stein S (2019) Mouse Models for Atherosclerosis Research—Which Is My Line? *Front. Cardiovasc. Med.* 6, 46.

Osmanagic-Myers S, Kiss A, Manakanatas C, Hamza O, Sedlmayer F, Szabo PL, Fischer I, Fichtinger P, Podesser BK, Eriksson M & Foisner R (2018) Endothelial progerin expression causes cardiovascular pathology through an impaired mechanoresponse. *J. Clin. Invest.* 129, 531–545.

Osorio FG, Navarro CL, Cadiñanos J, López-Mejía IC, Quirós PM, Bartoli C, Rivera J, Tazi J, Guzmán G, Varela I, Depetris D, de Carlos F, Cobo J, Andrés V, De Sandre-Giovannoli A, Freije JMP, Lévy N & López-Otín C (2011) Splicing-directed therapy in a new mouse model of human accelerated aging. *Sci. Transl. Med.* 3, 106ra107.

Park HJ, Gusarova G, Wang Z, Carr JR, Li J, Kim KH, Qiu J, Park YD, Williamson PR, Hay N, Tyner AL, Lau LF, Costa RH & Raychaudhuri P (2011) Deregulation of FoxM1b leads to tumour metastasis. *EMBO Mol. Med.* 3, 21–34.

Pawlus MR, Wang L & Hu CJ (2014) STAT3 and HIF1α cooperatively activate HIF1 target genes in MDA-MB-231 and RCC4 cells. *Oncogene* 33, 1670–1679.

Prakash A, Gordon LB, Kleinman ME, Gurary EB, Massaro J, D'Agostino R, Kieran MW, Gerhard-Herman M & Smoot L (2018) Cardiac abnormalities in patients with hutchinson-gilford progeria syndrome. *JAMA Cardiol.* 3, 326–334.

Prockop DJ & Kivirikko KI (1995) Collagens: molecular biology, diseases, and potentials for therapy. *Annu Rev Biochem* 64, 403–434.

Rodriguez HM, Vaysberg M, Mikels A, McCauley S, Velayo AC, Garcia C & Smith V (2010) Modulation of lysyl oxidase-like 2 enzymatic activity by an allosteric antibody inhibitor. *J. Biol. Chem.* 285, 20964–74.

Safar ME (2010) Arterial aging—hemodynamic changes and therapeutic options. *Nat. Rev. Cardiol.* 7, 442–449.

Scaffidi P & Misteli T (2006) Lamin A-Dependent Nuclear Defects in Human Aging. *Science (80-.).* 312.

von Scheidt M, Zhao Y, Kurt Z, Pan C, Zeng L, Yang X, Schunkert H & Lusis AJ (2017) Applications and Limitations of Mouse Models for Understanding Human Atherosclerosis. *Cell Metab.* 25, 248–261.

Schietke R, Warnecke C, Wacker I, Schödel J, Mole DR, Campean V, Amann K, Goppelt-Struebe M, Behrens J, Eckardt KU & Wiesener MS (2010) The lysyl oxidases LOX and LOXL2 are necessary and sufficient to repress E-cadherin in Hypoxia: Insights into cellular transformation processes mediated by HIF-1. *J. Biol.*

Chem. 285, 6658–6669.

Steppan J, Wang H, Bergman Y, Rauer MJ, Tan S, Jandu S, Nandakumar K, Barreto-Ortiz S, Cole RN, Boronina TN, Zhu W, Halushka MK, An SS, Berkowitz DE & Santhanam L (2019) Lysyl oxidase-like 2 depletion is protective in age-associated vascular stiffening. *Am. J. Physiol. Circ. Physiol.* 317, H49–H59.

Tang SS, Trackman PC & Kagan HM (1983) Reaction of aortic lysyl oxidase with beta-aminopropionitrile. *J. Biol. Chem.* 258, 4331–8.

Tsamis A, Krawiec JT & Vorp DA (2013) Elastin and collagen fibre microstructure of the human aorta in ageing and disease: a review. *J. R. Soc. Interface* 10, 20121004.

Wagenseil JE & Mecham RP (2012) Elastin in large artery stiffness and hypertension. *J. Cardiovasc. Transl. Res.* 5, 264–73.

Wang V, Davis DA, Haque M, Huang LE & Yarchoan R (2005) Differential gene up-regulation by hypoxia-inducible factor-1α and hypoxia-inducible factor-2α in HEK293T cells. *Cancer Res.* 65, 3299–3306.

Williams RM, Zipfel WR & Webb WW (2005) Interpreting second-harmonic generation images of collagen I fibrils. *Biophys. J.* 88, 1377–1386.

Wilson KL (2018) Nuclear import pathway key to rescuing dominant progerin phenotypes. *Sci. Signal.* 11, 9448.

Yamauchi M & Sricholpech M (2012) Lysine post-translational modifications of collagen. *Essays Biochem.* 52, 113–133.

Zhang C (2009) MicroRNA-145 in vascular smooth muscle cell biology: A new therapeutic target for vascular disease. *Cell Cycle* 8, 3469–3473.

Zhao N, Koenig SN, Trask AJ, Lin CH, Hans CP, Garg V & Lilly B (2015) MicroRNA miR145 regulates TGFBR2 expression and matrix synthesis in vascular smooth

muscle cells. *Circ. Res.* 116, 23–34.

Chapter 3: Decreased vascular smooth muscle contractility in Hutchinson-Gilford Progeria Syndrome linked to defective smooth muscle myosin heavy chain expression

Ryan von Kleeck[1,2], Paola Castagnino[1,3], Emilia Roberts[1,3], Shefali Talwar[1,2], Giovanni Ferrari[4], and Richard K Assoian[1,2,3]

[1]Department of Systems Pharmacology and Translational Therapeutics, [2]Center for Engineering MechanoBiology, and [3]Institute of Translational Medicine and Therapeutics at University of Pennsylvania, Philadelphia PA 19104. [4]Departments of Surgery and Biomedical Engineering, Columbia University, New York, NY 10032

Research adapted from submitted work:

Ryan von Kleeck, Paola Castagnino, Emilia Roberts, Shefali Talwar, Giovanni Ferrari, and Richard K Assoian. Scientific Reports (2021). *In press.*

3.1 Abstract

Children with Hutchinson-Gilford Progeria Syndrome (HGPS) suffer from multiple cardiovascular pathologies due to the expression of progerin, a mutant form of the nuclear envelope protein Lamin A. Progerin expression has a dramatic effect on arterial smooth muscle cells (SMCs) and results in decreased viability and increased arterial stiffness. However, very little is known about how progerin affects SMC contractility. Here, we studied the LaminA$^{G609G/G609G}$ mouse model of HGPS and found reduced arterial contractility at an early age that correlates with a decrease in smooth muscle myosin heavy chain (SM-MHC) mRNA and protein expression. Traction force microscopy on isolated SMCs from these mice revealed reduced force generation compared to wild-type controls; this effect was phenocopied by depletion of SM-MHC in WT SMCs and overcome by ectopic expression of SM-MHC in HGPS SMCs. Arterial SM-MHC levels are also reduced with age in wild-type mice and humans, suggesting a common defect in arterial contractility in HGPS and normal aging.

3.2 Introduction

Hutchinson-Gilford Progeria Syndrome (HGPS) is a rare premature aging disease. The “classical” form of HGPS is caused by a point mutation (c. 1824C>T; pG608G) in the *LMNA* gene (Lamin A)(Gonzalo et al. 2016). This mutation causes the expression of progerin, a mutant form of the nuclear envelope protein Lamin A that has a 50 amino acid deletion and retains a farnesylated C-terminus (Gonzalo et al. 2016; Capell et al. 2007). Others have shown that progerin can alter nuclear lamina structure to cause nuclear blebbing, altered nuclear import and export, and dynamic epigenetic changes (Gonzalo et al. 2016; Kelley et al. 2011; Arancio et al. 2014; Dahl et al. 2006). Children with HGPS begin to display clinical symptoms about two years after birth, including loss of hair, thin and aged skin, and growth retardation – characteristics of normally aged individuals (Gonzalo et al. 2016; Merideth et al. 2008). Cardiovascular complications, including arterial fibrosis, generation of severe atherosclerotic lesions, and the death of arterial smooth muscle cells (SMCs), are hallmarks of the disease, and HGPS children typically die from heart attacks or strokes (Gerhard-Herman et al. 2011; Olive et al. 2010; Stehbens et al. 2001; Brassard et al. 2016; Varga et al. 2006). Vascular SMCs normally populate the medial layer of arteries, but at autopsy, HGPS patients display very few medial SMCs, and their arteries are instead filled with a collagen-dense matrix (Varga et al. 2006; Stehbens et al. 2001).

One of the main functions of vascular SMCs is to regulate blood flow to target organs by modulating arterial tone and peripheral resistance. Vascular tone is regulated by periodic contraction and dilation of the arteries (Brozovich et al. 2016). Similar to

other muscle cells, the major contractile components in SMCs consists of actin and myosin (Webb 2003; Hathaway et al. 1991). However, a smooth muscle-specific myosin heavy chain (SM-MHC, encoded by the *Myh11* gene) and smooth muscle alpha-actin (SMA, encoded by the *Acta2* gene) exist in SMCs, and these play important roles in SMC contractility (Martin et al. 2007; Lehman & Morgan 2012; Webb 2003; Hathaway et al. 1991).

The *Myh11* gene is alternatively spliced into four SM-MHC isoforms, and these allow for the prolonged tonic contraction of SMCs (Babu et al. 2000). Additionally, SMCs contain other cell-specific contractile proteins such as transgelin (gene *Tagln*), an actin cross-linking protein, and calponin (gene *Cnn1*) that can regulate ATPase activity of myosin in smooth muscle (Carmichael et al. 1994; Shanahan et al. 1993; Zhang et al. 2001). The inability to properly regulate vascular tone through contraction and dilation may lead to impaired blood flow to target tissues (Brozovich et al. 2016; Reho et al. 2014).

As HGPS is a rare disease, animal models are used to understand the pathology caused by progerin expression, especially when looking for early events that are not amenable to analysis at autopsy. The $Lmna^{G609G/G609G}$ mouse model (hereafter referred to as HGPS mice) has been commonly used since it contains the equivalent point mutation seen in the classical HGPS human syndrome at the mouse *Lmna* locus (Osorio et al. 2011). This mouse model recapitulates many of the cardiovascular complications seen in the human syndrome including arterial fibrosis and stiffening as well as the progressive loss of aortic SMCs as these mice approach the end of their lifespan (Osorio et al. 2011; Murtada et al. 2020; del Campo et al. 2019). Studies in HGPS mice have also observed decreased arterial vasoconstriction, although these studies were

performed on arteries isolated from older HGPS mice (approx.100 and 140 days) that had the expected loss of SMCs at 140 days (Murtada et al. 2020; del Campo et al. 2020). Thus, whether reduced arterial contractility is an early event in HGPS remains unclear.

In this work, we analyzed arterial gene expression and contractility in young (2-month) HPGS mice, before SMC loss is detectable (von Kleeck et al. 2021), with the goal of identifying potentially causal events in HPGS pathogenesis. We found a reduced abundance of SM-MHC mRNA and protein that was associated with impaired arterial contraction in isolated HGPS carotid arteries and reduced force generation in isolated HGPS SMCs. Moreover, RNAi-mediated downregulation of SM-MHC reduced traction forces in WT SMCs while enforced expression of SM-MHC increased traction force in HGPS SMCs. Interestingly, reduced SM-MHC abundance is also a characteristic of normal arterial aging, both in WT mice and in humans. Impaired arterial SMC contractility may be a common feature of premature and normal aging.

3.3 Results

Reduced smooth muscle myosin heavy chain and contractility early in HGPS. To better understand the effects of progerin expression on SMC function, I interrogated our recent genome-wide transcriptome analysis of isolated descending aortas from 2-month-old WT and HGPS mice (von Kleeck et al. 2021). I chose to focus on mice at 2-months of age as, aside from stunted growth, these young mice do not show overt features of the syndrome. In particular, the arteries of 2-month HGPS mice have yet to show SMC loss or apoptosis (von Kleeck et al. 2021). KEGG pathway analysis (Kanehisa 2019) of the differentially expressed genes in these HGPS vs. WT aortas indicated that several pathways associated with contractility were altered early in HGPS including vascular smooth muscle contraction, focal adhesions, and ECM-receptor interactions (Fig. 3.01a, Fig. 3.02a-b).

To extend the results of the KEGG analysis, I performed RT-qPCR on 2-month WT and HGPS aortas and evaluated the expression of several SMC contractile genes (Fig. 3.01b). The mRNA level of *Myh11*, the gene encoding SM-MHC, was significantly decreased while levels of other contractility-regulating genes (*Acta2, Tagln, and Cnn1)* mRNA were not significantly altered (Fig. 3.01B). SM-MHC has multiple isoforms (Babu et al. 2000; Martin et al. 2007), and I found that all the *Myh11* mRNA isoforms present in the aorta were decreased in HGPS (Fig. 3.01c). Additionally, immunoblotting (Fig. 3.01d-e) and immunostaining (Fig. 3.01f-g) of 2-month WT and HGPS aortas showed decreased abundance of SM-MHC protein while SMA protein was minimally affected.

I then expanded our analysis to the carotid artery and found similar results to what we observed in the aorta: HGPS carotid arteries showed a preferential decrease in the level of SM-MHC protein as determined by immunostaining (Fig. 3.03a-b) and a decrease in *Myh11* mRNA as determined by RT-qPCR (Fig. 3.03c). The reduced expression of SM-MHC led us to reason that arterial contractility might be defective in HGPS arteries, even at early ages when the number of arterial SMCs is still similar to WT (von Kleeck et al. 2021). To test this hypothesis, we measured how 2-month WT and HGPS carotid arteries respond to KCl, a canonical vasoconstrictor dependent on SM-MHC for its effect (Hathaway et al. 1991). Contractility was measured on a pressure myograph so that results could be obtained at physiological arterial pressure and stretch(Ferruzzi et al. 2013; Amin et al. 2012). Indeed, carotid artery vasoconstriction to KCl was reduced in HGPS (Fig. 3.03d), supporting the idea that decreased vasoconstriction is an early event in HGPS and even precedes the loss of SMCs from large arteries. As I have previously reported increased arterial stiffness at this timepoint, I treated WT and HGPS mice with lysyl oxidase inhibitor β-aminopropionitrile at a dosing regimen shown to reduce arterial stiffness (von Kleeck et al. 2021) and evaluated if decreasing vessel stiffness restored contractility to HGPS carotids. The results showed that reducing arterial stiffness had no significant effect on vessel contractility of HGPS mice (Fig. 3.03e).

To get a general idea of when arterial SM-MHC is downregulated in HGPS, I assessed *Myh11* transcript levels in isolated aortas of 1-, 2-, and 3-month HGPS mice (Fig. 3.04a). In comparison to 1-month HGPS aortas, *Myh11* mRNA was significantly downregulated in 2-month HGPS aortas and remained downregulated through 3-months. Surprisingly, *Acta2* transcript levels did not significantly change throughout the 1

to 3-month period (Fig. 3.04a). I also evaluated *Myh11* transcript levels in other SMC-containing tissues and found that the downregulation of SM-MHC was specific to the vascular smooth muscle cells of the aorta (Fig. 3.04b), as bladder and intestine did not display a reduction in transcript levels.

Reduced SM-MHC is causal for traction force defects in HGPS SMCs. To determine if the reduced arterial contractility observed in HGPS carotids was associated with defective vascular SMC force generation, I isolated primary aortic SMCs from 2-month WT and HGPS mice. First, we evaluated SM-MHC and SMA abundance in isolated SMCs and observed a preferential reduction in SM-MHC levels in HGPS, consistent with our observations *in vivo* (Fig. 3.05a-b). Although smooth muscle myosins are thought to be the major force generating myosin in SMCs, non-muscle myosins IIA and IIB (NMII2A and NMIIB) are also present and are believed to perform a house-keeping function (Eddinger & Meer 2007). The abundance of these non-muscle myosins trended lower in HGPS SMCs although not to the same extent as SM-MHC (Fig. 3.05a-b).

We next performed traction force microscopy on primary WT and HGPS SMCs. HGPS SMCs presented with decreased cell area (Fig. 3.05c) and force generation compared to WT (Fig. 3.05d-e; column 1 vs 2), suggesting an important role for SM-MHC in contractility. We then assessed the contribution of non-muscle myosins to HGPS cell force generation by treating WT and HGPS SMCs with blebbistatin, a myosin-ATPase inhibitor (Fig. 3.05d-e). We used a low concentration of blebbistatin expected to inhibit non-muscle myosins but not SM-MHC (Limouze et al. 2004). This low dose treatment decreased cell area and decreased traction force in HGPS SMCs to very low levels (Fig. 3.05c-d; column 2 vs 4). Low dose blebbistatin treatment also reduced cell

area and traction force in WT SMCs (Fig. 3.05c-d; columns 1 vs 3), but the remaining traction force in WT SMCs remained much higher than in the blebbistatin-treated HGPS cells, (Fig. 3.05d; columns 3 vs 4) as would be expected given the higher level of SM-MHC in WT SMCs. Note that the magnitude of the blebbistatin effect on decreasing mean traction force was similar in WT and HGPS SMCs (~70 and 75%, respectively) despite their difference in SM-MHC abundance. This finding supports the notion that our low dose blebbistatin treatment was preferentially targeting the non-muscle myosins and not smooth muscle myosin as reported (Limouze et al. 2004) (also see Discussion). The data in Fig. 3.05 therefore indicate that defective expression of SM-MHC in HGPS SMCs correlates with reduced cell traction force and that HGPS SMCs maintain a basal level of force generation through the action of non-muscle myosins.

As decreased cellular contractility is associated with changes to the actin cytoskeleton, I evaluated stress fibers in WT and HGPS SMCs (Fig. 3.06a). However, I found that average actin intensity across the cell as visualized by phalloidin stain was not reduced and even slightly higher in HGPS SMCs (Fig. 3.06b). As progerin expression is shown to disrupt nucleoskeletal connections (Chang et al. 2019; Booth et al. 2015), I also evaluated actin intensity over the nucleus but saw no change in comparison to WT SMCs (Fig. 3.06c). Thus, the basal amount of force generated by the non-muscle myosins (see above), working together with the low amounts of SM-MHC, appears sufficient to support the stress fiber formation seen in these cultured HGPS SMCs, at least when the cells are cultured on a rigid substratum.

I then treated WT SMCs with two distinct siRNAs targeting *Myh11* (Fig. 3.07a-b) and found that each siRNA resulted in a significant reduction in cell area (Fig. 3.07c) and a ~70% reduction in mean traction force (Fig. 3.07d-e), which was similar to the ~80%

reduction we observed in HGPS SMCs as compared to WT (Fig. 3.05d; columns 1 vs. 2). Thus, deliberate reduction of SM-MHC in WT SMCs phenocopied the reduced traction force seen in HGPS SMCs. Conversely, adenoviral enforced expression of SM-MHC (Fig. 3.08a-b) increased cell area (Fig. 3.08c) and traction force in HGPS SMCs (Fig. 3.08d-e). I do note that traction forces in the HPGS SMCs infected with adeno-*Myh11* were not quite increased to the levels seen in WT SMCs (see Discussion). Interestingly, knockdown of Lmna did not reproduce the decreased Myh11 or Acta2 mRNA seen in HGPS (Fig. 3.09), indicating that the effect is likely due to progerin expression rather than reduced Lmna levels. Nevertheless, the results collectively indicate that defective SM-MHC expression in HGPS SMCs is causally related to the defect in SMC force generation.

Reduced SM-MHC in aging aortas of WT mice and humans. Many parallels have been drawn between HGPS and natural aging, especially in regard to age-associated cardiovascular pathology (Brassard et al. 2016; Gonzalo et al. 2016; Olive et al. 2010). As reduced arterial contractility has also been observed with age (Wheeler et al. 2015; Seawright et al. 2018), I asked if this reduction in contractility was associated with a preferential decrease in SM-MHC. Indeed, immunofluorescence staining of carotid artery cross sections from 2- and 24-month WT mice revealed a decrease in SM-MHC staining in the aged WT mice and a smaller difference in the levels of SMA (Fig. 3.10a-b), which was associated in a decrease in carotid contractility in 24-month WT mice in response to KCl (Fig. 3.10c). Moreover, I found a similar reduction in SM-MHC levels in ascending aorta and aortic root sections from relatively young (age = 35-49 years) versus older (age = 77-81 years) humans whereas SMA abundance was minimally changed (Fig.

3.10d-e). Thus, reduced SM-MHC expression, and a consequent effect on arterial contraction, may be a common event in both HGPS and the natural aging process.

3.4 Discussion

Medial SMCs play a major role in arterial vasoconstriction, which is essential for regulation of vascular tone and blood flow to target tissues (Brozovich et al. 2016; Reho et al. 2014). As SMC death is a hallmark of HGPS, it is not surprising that reduced arterial contractility has been observed in late HGPS, when arteries are deficient in their number of SMCs (Stehbens et al. 2001; Murtada et al. 2020; Osorio et al. 2011). However, we show here that reduced contractility in HGPS begins before the onset of many clinical phenotypes of the syndrome and prior to the loss of SMCs. Thus, reduced vasoconstriction is one of the earliest cardiovascular defects in HGPS, at least in mice, and not merely a secondary consequence of SMC death or increased arterial stiffness. We also show that these young HGPS arteries are defective for expression of SM-MHC and that arteries of aged WT mice and humans also display reduced SM-MHC abundance. Additionally, this decrease in SM-MHC was specific to the vascular SMC population as SMCs in bladder and intestinal tissue did not display the defect. Thus, the defective expression of SM-MHC in the arteries of young HGPS mice foreshadows the pathophysiology of normal arterial aging.

By using primary SMCs in culture, I was able to link the decreased abundance of SM-MHC to decreased cell area and defective force generation. My initial experiments used pharmacologic inhibition of myosin II with blebbistatin and were based on Limouze et al. (Limouze et al. 2004), which demonstrated that the blebbistatin IC50 for smooth

muscle myosins is >10-fold greater than that of the non-muscle myosins (80 versus 2-5 μM). Thus, we reasoned that use of 15 μM blebbistatin should be selective for the non-muscle myosins, which are expressed at similar levels in both WT and HGPS SMCs. Though the IC50 difference was smaller, a similar result has also been reported Zhang et al. (Zhang et al. 2017). We acknowledge that both of these studies examined blebbistatin effects on purified proteins and that the blebbistatin IC50's for different myosins may differ in cells. Nevertheless, if 15 μM blebbistatin were also inhibiting smooth muscle myosin, one would not expect to see the similar effect of blebbistatin on mean traction force that we observed in WT versus HGPS SMCs (given their large difference in the amount of SM-MHC). The fact that treating HGPS SMCs with blebbistatin further decreased traction force suggests that non-muscle myosins provide basal force generation for HGPS SMCs. I postulate that the action of non-muscle myosins is why cultured HGPS SMCs display no overt defects in stress fiber formation.

Further analysis used RNAi and ectopic expression to assess the effect of SM-MHC on traction force. Reducing SM-MHC levels in WT SMCs with RNAi produced a similar percent reduction in traction force as observed in HGPS SMCs. Additionally, restoration of SM-MHC levels in HGPS through adenoviral overexpression partially rescued SMC force generation. This incomplete effect could be due to a multifaceted regulation of SMC contractility that relies on regulatory proteins and signaling pathways aside from smooth muscle myosin and actin (Hathaway et al. 1991; Webb 2003). Indeed, KEGG pathway (Kanehisa 2019) evaluation of our genome-wide transcriptome analysis (GEO ascension number GSE165409) revealed slight decreases in genes such as *Myl9*, the smooth muscle myosin regulatory light chain, and *Mlck1*, smooth muscle myosin light chain kinase (Fig. 3.02b). Although not reduced to the extent of SM-MHC

(Myh11), the combined contributions of other gene products such as these may be required to restore WT levels of contractility to HGPS SMCs.

Even though we have reported decreased force generation in isolated SMCs, arterial contractility at a tissue level can depend on multiple factors from the external environment (Hathaway et al. 1991; Webb 2003). For example, the composition and stiffness of the extracellular matrix can dictate the ability of smooth muscle to contract (Ahmed & Warren 2018; Sazonova et al. 2015), and the arteries of HGPS mice are much stiffer than WT (del Campo et al. 2019; Murtada et al. 2020; von Kleeck et al. 2021). However, reducing arterial stiffness through administration of BAPN did not restore arterial contractility to HGPS arteries. Additionally, work done by del Campo et al. (del Campo et al. 2020), albeit in older (14 weeks) HGPS mice, found that collagen disruption by collagenase in aorta did not restore the contractile response of arteries in response to KCl. Collectively, these findings suggest that although the ECM is stiffer in HGPS arteries, it may not play as much of a role in regulating vasoconstriction as altered SMC force generation. Additionally, arterial contractility *in vivo* relies on complex signaling of agonist-receptor interactions (Webb 2003; Hathaway et al. 1991). It is possible that in addition to reduced contractile machinery, cells in HGPS arteries are producing altered amounts of circulating factors essential for regulating vasoconstriction and vasodilation.

How progerin affects SM-MHC mRNA levels remains to be clearly defined. Research suggests that incorporation of progerin into the nuclear lamina can change the nuclear architecture, making nuclei stiffer and blebbed (Booth et al. 2015; Verstraeten et al. 2008). This effect could potentially interfere with the nuclear translocation of transcription factors essential for contractile gene transcription. Additionally, cell

contractility is tightly tied to mechanotransduction, or the sensing of the mechanical properties of the microenvironment (Martino et al. 2018). As transmission of mechanical stimuli from the microenvironment to the nucleus depends on the nuclear lamina and LINC (linker of nucleoskeleton and cytoskeleton) complex (Martino et al. 2018), the altered nuclear lamina in HGPS may impair mechanotransduction (Chang et al. 2019; Booth et al. 2015).

Many phenotypic similarities exist between HGPS and normal aging, and it has been reported that some aged tissues show low levels of progerin expression (Scaffidi & Misteli 2006; Olive et al. 2010; McClintock et al. 2007; Rodriguez et al. 2009). We show that SM-MHC levels are also decreased in aging mouse and human arteries. It remains to be determined if the molecular mechanisms underlying reduced SM-MHC abundance in HGPS and normal arterial aging are common or distinct. Nevertheless, if reduced levels of SM-MHC leads to diminished arterial contraction and blood flow, then this phenotype of defective SM-MHC mRNA and protein abundance in early HGPS may provide important insight into complications arising from reduced blood flow in normal aging (Dinenno et al. 1999; Dinenno et al. 2001).

3.5 Methods

Mice and artery isolations. For aging experiments, WT C57BL/6 mice were purchased from Jackson Labs and aged up to 24-months. $LMNA^{G609G/+}$ mice on the C57/BL6 background were generously provided Dr. Carlos Lopez-Otin (Universidad de Oviedo, Oviedo, Spain)(Osorio et al. 2011). Mice were genotyped using the following primers: Forward: AAGGGGCTGGGAGGACAGAG; and Reverse:

AGCATGCCATAGGGTGGAAGGA. Mice were fed a chow diet *ad libitum*. For experiments including HGPS arteries or cells, WT littermate controls were obtained from $LMNA^{G609G/+}$ matings.

Unless noted otherwise, arteries were perfused with PBS in situ through the left ventricle, the left and right carotids were isolated, and the descending aorta was isolated from the end of the aortic arch to the diaphragm. The isolated arteries were cleaned of excess fat and stored in RNAlater for RT-qPCR or genome-wide analysis, flash frozen and stored at -80ºC for protein analysis, or fixed in Prefer (Anatech #414) for embedding and sectioning. Animal protocols were approved by the University of Pennsylvania Institutional Animal Care and Use Committee, and animal experiments followed the recommended ARRIVE guidelines. Experiments were performed on male mice unless otherwise specified in the legends.

Human artery sections. Human aortic root or ascending aorta sections from both men and women were obtained from patients undergoing aortic valve/root replacement and/or ascending aortic repair/replacement at Columbia University Irving Medical Center under IRB Protocol # AAAR6796 with informed consent from all subjects. Specimens were fixed in 10% formalin for 24 h and embedded in paraffin. Cross sections (5-μm) were prepared. Two cohorts of samples (young and old) were generated based on age (35-49 years and 77-81 years, respectively). Results from aortic root and ascending aorta were combined for data analysis.

Genome-wide transcript analysis. Our previously described genome-wide analysis of differentially expressed genes in 2-month WT versus HGPS mice(von Kleeck et al.

2021) (GEO ascension number GSE165409) was subjected to KEGG pathway analysis(Kanehisa 2019) using gprofiler (https://biit.cs.ut.ee/gprofiler/gost). The cutoffs used were >0.5 $\log_2$ or <-0.5 $\log_2$ fold change and an adjusted p-value of < 0.0001.

Carotid artery contractility analysis. Carotid artery contractility was measured using a DMT 114P pressure myograph. Dissected left carotid arteries were cleaned of excess fat, secured at both ends to 380-µm diameter steel cannulas in the myograph chamber using four silk sutures (Teleflex Medical, 104-S), and maintained in 5 ml of Hanks Balanced Salt Solution with calcium. The closed system was checked for leaks by pressurizing the vessel at 30 mm Hg using HBSS. The system was then returned to 0 mm Hg, and un-stretched vessel length (UVL) was determined as the minimum distance between the cannulas where the artery was no longer bent.

Mounted vessels were preconditioned by stretching them axially to 1.15 times their UVL at 40 mm Hg for 15 min and then 1.3 times their UVL at 60 mm Hg for 15 min. The preconditioned vessels were brought to their in-vivo stretch (IVS) based on the values we recently reported(von Kleeck et al. 2021) and pressurized to 100 mm Hg. Increasing concentrations of KCl (10^{-4} M to 10^{-1} M in Hanks Balanced Salt Solution with calcium; 5 ml) were added to the vessel chamber sequentially at 10-min intervals or once the constriction plateau had been reached. Each new KCl solution was added after removing the prior KCl solution. Outer diameters were recorded in real time at each drug concentration using an inline tracking camera (Imaging Source) and MYOVIEW software.

Cell culture, viral infection, and RNAi. Primary mouse SMCs were isolated from the descending aortas of 2-month WT and HGPS male mice and prepared by explant culture as described(Cuff et al. 2001). SMCs were cultured in growth medium [1:1 Dulbecco's modified Eagle's medium (DMEM)/Ham's F-12 supplemented with 2 mM L-

glutamine and 20 mM HEPES, pH7.4] with 20% FBS. Cells were passaged at near confluence with trypsin/EDTA and used between passages 4-6. Near confluent, asynchronous SMCs were infected with adenoviruses encoding LacZ (control) and *Myh11* (Vigene Biosciences VH802236). Adenoviruses were amplified using standard procedures, added to WT or HGPS SMCs in growth medium at a MOI of 800, and incubated overnight. The infected cells were washed and incubated for 72 h in fresh growth medium before subsequent analysis.

siRNA-mediated knock down of SM-MHC in near-confluent WT SMCs was performed using Lipofectamine RNAiMAX Transfection Reagent (Thermofisher #13778100) in OPTI-MEM with two distinct siRNAs (Ambion s70252 and s70253) at a final siRNA concentration of 150 nM. A non-specific siRNA (Ambion 4390843) was used as control. After 4 h of siRNA transfection, cells were switched to fresh growth medium. Protein or traction force analysis was performed 72 h after transfection.

Traction Force Microscopy (TFM). Polyacrylamide hydrogels with a Young's modulus of 20-25 kPa were prepared as described(Shutova et al. 2017) with 0.2 µm diameter fluorescent microspheres (F8810; Invitrogen, 1% vol/vol) added to the polyacrylamide solution before polymerization. Hydrogels were coated with 10 µg/ml bovine fibronectin (EMD-341631) as described(Klein et al. 2007). After three 10-min PBS washes, hydrogels were incubated with cell growth medium for 30 min. Cells were sparsely plated on the hydrogels (~1000 cells/cm^2) and incubated for 24 h before imaging. Fluorescence images of cells and embedded beads were captured at 20X magnification using a Zeiss Axio Observer 7 inverted microscope with Zeiss Axiocam 503 color CCD camera in an environmental chamber at 37^{o}C and 5% CO_2. The cells were visualized

with Lysosensor Green DND-189 (Invitrogen L7535, 1:1000), added immediately before imaging. Image sequences were taken for live cells and beads. A solution of 10% SDS (Invitrogen; 5% of media volume) was then added to the culture medium and incubated for 10 min before image sequences were taken a second time. Data analysis was performed largely as described(Shutova et al. 2017) using freely available plug-ins for ImageJ (Tseng et al.(Tseng et al. 2012); adapted from Dembo and Wang(Dembo & Wang 1999)). For Fourier transform traction cytometry, the Poisson's ratio of the polyacrylamide gel was assumed to be 0.45 and a regularization parameter of 10^{-9} was used. Traction force vector maps were analyzed using a custom script in MATLAB (Mathworks) to determine mean traction stress generated by each cell and total force exerted per cell. Cell area was determined from the corresponding images of green fluorescence in ImageJ. For cells genetically modified with siRNA or adenoviral infection, cells were transfected or infected as described above, incubated in fresh media for 48 h, and plated on hydrogels for an additional 24 h before being imaged for TFM. For blebbistatin treated cells, SMCs were incubated with 15 μM blebbistatin or vehicle (an equivalent dilution of DMSO) in growth media for 30 min prior to traction force microscopy analysis. Results shown for the TFM experiments were accrued from 2-3 independent experiments. As variability in traction forces between experiments may arise from batch-to-batch differences in hydrogels or primary SMCs, relevant controls were included as reference in each experiment. Similarly, comparisons between experiments were based on percent changes in mean traction force per cell rather than changes in Newtons.

RT-qPCR. Descending aortas or carotid arteries were isolated and cleaned from 2-month WT and HGPS mice. Cleaned tissues were stored in RNAlater (Qiagen) at -80^{o}C for subsequent analysis. Total RNA was isolated with the RNeasy Fibrous Tissue Mini Kit (Qiagen) according to manufacturer's instructions. For carotid analyses, left and right carotids were combined for each mouse. For RT-qPCR of cultured SMCs, RNA was extracted using TriZol reagent (Thermofisher 15596026) according to manufacturer's instructions. Reverse transcription reactions contained 200-500 ng of total RNA. Ten to fifteen percent of the cDNA was subjected to RT-qPCR. Samples were run in technical duplicates on an ABI Prism 7000 sequence detection system or ABI Quantstudio 3 with the following primer-probe sets from ThermoFisher:. Tagln: Mm00441661_g1, Myh11: Mm00443013_m1, Acta2: Mm00725412_s1, Cnn1: Mm00487032_m1. For the RT-qPCR of Myh11 isoforms, custom primer-probe (FAM-labeled) sets were from ThermoFisher: SM-A isoform: Forward CCACAAGGGCAAGAAAGACA, Reverse TTCTTGACGGTTTTCGCATT, Probe CAGCATCACGGGGGAGCTG. SM-B isoform: Forward GTGGCATCCTCCCACAAG, Reverse GGATTGGGTTTGCCTGTAGA, Probe CGCAAGGTCCATCTTTTGCCTAC. SM1 isoform: Forward CTTCGCCCAAGTGACTTTTT, Reverse AAGTGACCATGGGTGCAAAT, Probe AACACTGCTCCCAGAGCGAGC. SM2 isoform: Forward ACGCCCTCAAGAGCAAACT, Reverse GCCCTTCTGGAAGGAACAA, Probe CCCCACAGGAAACTTCGCAGT. Samples from each mouse were accrued, and the final RT-qPCR reactions were performed at one time. Results from each experiment were analyzed using the ddCt method and normalized to the mean of the respective control.

Immunoblotting. For tissue immunoblotting, isolated aortas were thawed, chopped into small pieces and sonicated in lysis buffer (50 mM Tris-HCl pH 8, 250 mM NaCl, 2 mM EDTA, 1% NP-40) containing protease inhibitors (Cell Signaling Technologies 5872S). Lysates were centrifuged for 5 min (4°C, 15,000 x *g*). The supernatants were collected and quantified with the Bio-Rad Protein Assay (Catalog #5000006) with a BSA standard. Similar amounts (~25μg) of each sample were diluted into SDS sample buffer (final concentration of 50 mM Tris pH 6.8, 2% SDS, 10% glycerol, 0.01% Bromophenol blue, and 1% β-mercaptoethanol), fractionated on 7.5% SDS polyacrylamide gels, and electrophoretically transferred to nitrocellulose. For immunoblotting of cell lysates, isolated WT and HGPS SMCs were plated at confluence in 60-mm culture dishes for 24 h. Cytoplasmic fractions were collected using NE-PER nuclear cytoplasmic extraction kit (Thermo 79933). For cell experiments using siRNA transfection or adenoviral infection, cells were lysed directly in SDS sample buffer after a 72-h incubation with the siRNA or adenovirus.

Incubations with primary antibodies were performed overnight at 4°C with rocking in TBST (Tris-buffered saline with 0.1% Tween 20) with 5% milk or 2% BSA. Incubation with secondary antibodies were performed for 2 h at room temperature in the same TBST buffer as the primary antibody. The antibodies used were non-muscle myosin 2A: Abcam Ab55456 (1:2000), non-muscle myosin 2B: Cell Signaling 3404 (1:2000), smooth muscle actin: Sigma F3777 (1:1000), smooth muscle myosin heavy chain: Protein Tech 21404-1-AP (1:300), glyceraldehyde-3-phosphate dehydrogenase (GAPDH): Invitrogen MA5-15738 (1:500), focal adhesion kinase: BD Transduction labs 610088 (1:300), and α-tubulin: Santa Cruz SC-8035 (1:300). Bound antibodies were visualized by enhanced

chemiluminescence. Blots were stripped and re-probed using Restore Western Blot Stripping Buffer (Thermo 21059).

Immunoblots were quantified in ImageJ relative to one of three loading controls (FAK, α-tubulin, or GAPDH) depending upon the molecular masses of additional probed proteins to minimize stripping and reprobing of blots; see Fig. 3.11 for validation of loading controls. Immunoblot quantification normalized HGPS or Myh11 siRNA signal intensities to the mean signal intensity of the respective WT control, which was set to 1.0 for each blot in order to combine data from multiple experiments. A Grubbs' test was used to justify exclusion of an outlier.

Tissue Immunostaining. For mouse tissue immunostaining, 2- or 24-month WT and 2-month HGPS male mouse right carotid arteries or descending aortas were perfused with PBS, excised, cleaned to remove excess fat, and fixed in Prefer (Anatech #414). Carotids and aortas were embedded in paraffin, and 5-μm cross sections were prepared. Paraffin sections from mouse and human arteries were deparaffinized and hydrated before antigen unmasking (Vector Labs, H3300) for 25 min at ~100^{o}C). Carotid or aortic cross sections were washed in PBS three times before blocking with 2% BSA in PBS for 15 min, incubated overnight at 4^{o}C with antibodies directed to smooth muscle myosin heavy chain (Protein Tech 21404-1-AP, diluted 1:200 in PBS) or smooth muscle actin (FITC-conjugated; Sigma F3777, diluted 1:300 in PBS). Replicate sections were incubated in parallel with isotype-matched control antibodies. All samples were washed three time with PBS before incubation with a 1:100 dilution of Alexa 594-conjugated isotype-matched secondary antibody (Invitrogen goat anti-rabbit A11012) for two h at room temperature. Sections were then washed three times in PBS followed by addition

of Dapi (1:500 dilution in PBS). Slides were briefly washed in PBS and then water before mounting with SlowFade Gold (Thermo, S36936). Results were visualized with a Nikon Eclipse 80i microscope with a QI-Click Qimaging camera. Carotid arteries were imaged at 20x magnification and pseudo-colored green (SM-MHC) or red (SMA). Samples from each mouse were accrued, and the final immunostainings were performed at one time.

Images were quantified using ImageJ. The media of each section was traced using the polygon drawing tool, and its raw integrated density was divided by the area of the outlined media to obtain relative fluorescence intensity. Background intensity, as determined from the isotype-matched control antibodies, was negligible. Relative fluorescence intensity values were plotted relative to the mean fluorescence intensity value of the corresponding control for each experiment. A Grubbs' test was used to justify exclusion of an outlier.

Cell immunostaining. For cell immunostaining, SMCs were plated on 12mm coverslips and incubated overnight before fixation with 3.7 % formaldehyde+ 1% Triton-X for Paxillin and Phalloidin staining for 20 min. Following fixation, cells were incubated in permeabilization buffer (0.4% Triton-X-100, 2% BSA, and 50 mM NH_4Cl in PBS) for 2 h at room temperature. Three quick PBS washes were performed followed before addition of primary antibody to paxillin (BD Transduction Labs 610052, 1:50) diluted in blocking buffer (0.3% Triton-X-100, 2% BSA in PBS) overnight at 4^{o}C. Three 10 min PBS washes were performed followed by the addition of secondary antibody (Invitrogen A21202) and phalloidin stain (Invitrogen A12381, 1:100) for 2 h at room temperature. Coverslips were washed three times in PBS and dipped in water before mounting with SlowFade Gold

(Thermo, S36936). Results were visualized with a Nikon Eclipse 80i microscope with a QI-Click Qimaging camera. Pictures were taken at 40x magnification.

Average phalloidin intensity in the cell and over the nucleus was calculated using detailed methods published by Zonderland et al. (2019). Cell area measurement were determined during traction force microscopy experiments as described below.

Statistical Analysis. Statistical analysis was conducted using Prism software (GraphPad) with tests based on the method of data collection and quantification (see Supplemental Methods). Statistical significance for immunostaining, TFM, AFM, and RT-qPCR was determined using 2-tailed Mann-Whitney tests unless testing for significance in a particular direction. Significance in immunoblot results was determined by Wilcoxon signed rank test. Significance of the myography vasoconstriction experiments was determined by two-way ANOVA, and statistical differences due to genotype are shown in the figure.

3.6 Acknowledgments

We thank Dr. Carlos Lopez-Otín for the generous gift of the LMNA^{G609G} mouse line and the Cell and Developmental Biology Microscopy Core at University of Pennsylvania for use of microscopes for traction force experiments. The MATLAB script used to analyze traction force data was generously provided by Robert Mauck (University of Pennsylvania). Emilia Roberts assisted in performing arterial contractility experiments using the pressure myograph. Paola Castagnino assisted in experimental design, troubleshooting, and project direction. Shefali Tawlar helped in teaching and performing some traction force microscopy experiments.

This work was supported by NIH grant AG062140, the Progeria Research Foundation, and the Center for MechanoBiology, a National Science Foundation Science and Technology Center under grant agreement CMMI: 15-48571. RvK was supported by NIH grants T32-GM008076 and F31-HL142160. GF was supported by NIH grant HL122805.

3.7 Figures

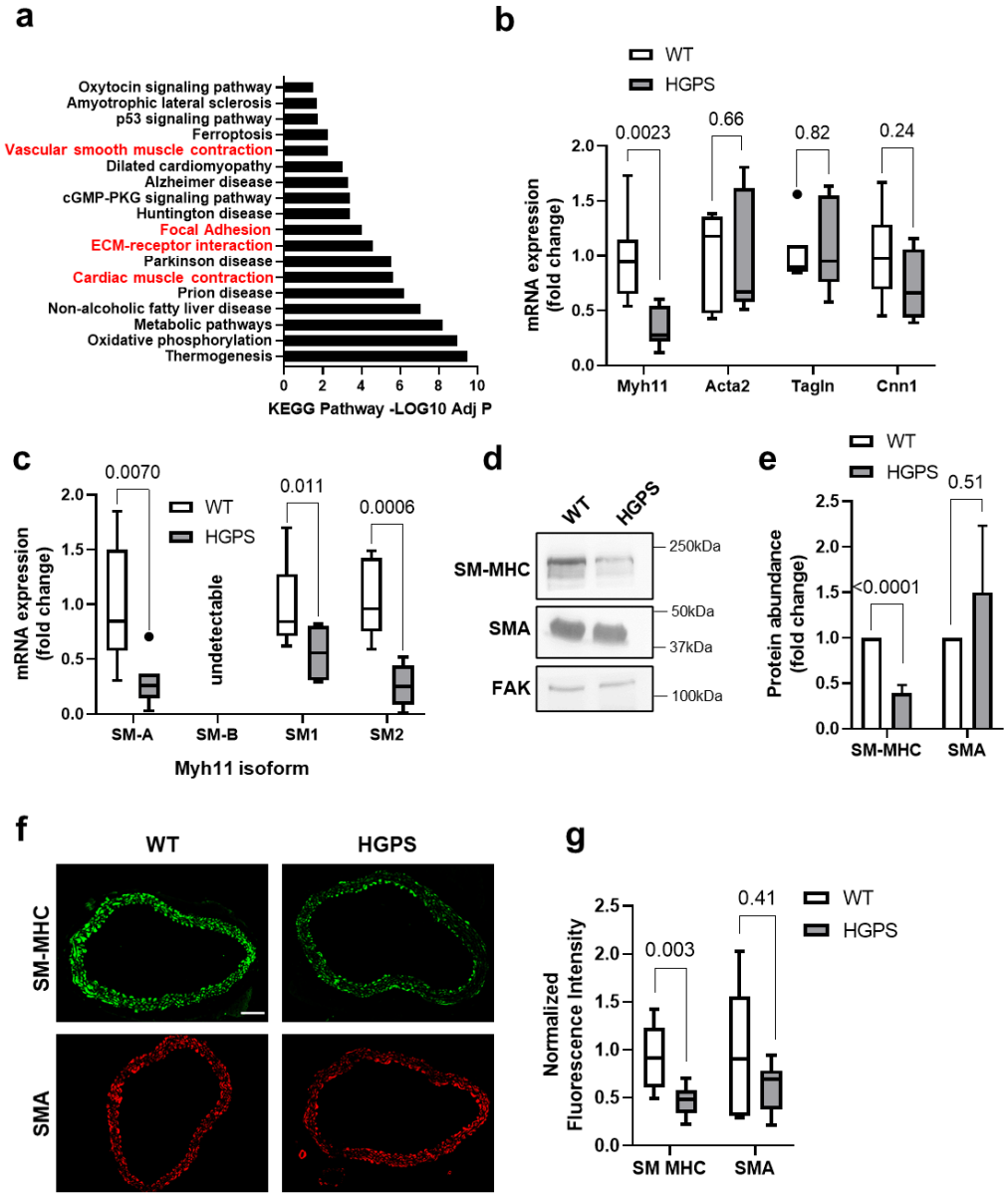

Figure 3.01. Reduced smooth muscle myosin heavy chain abundance in HGPS aortas. (a) KEGG pathway analysis was performed on the differentially expressed genes from 2-month WT versus HGPS descending aortas (n=6 per genotype). KEGG

pathways with p-adjusted values < 0.05 are shown. **(b)** Descending aortas were isolated from 2-month WT and HGPS mice (n=5-7 per genotype). SMC contractility gene transcript levels were assessed by RT-qPCR and plotted relative to the WT control. **(c)** Smooth muscle myosin heavy chain isoform transcript expression was assessed by RT-qPCR in 2-month WT and HGPS descending aortas (n=7 per genotype) and plotted relative to the WT control. **(d)** Representative images of SM-MHC and SMA protein levels determined from 2-month WT and HGPS descending aortas by immunoblotting. Focal Adhesion Kinase (FAK) is shown as the loading control. Black boxes around the immunoblots indicate cropping for removal of extraneous space. **(e)** Quantification of immunoblotting results normalized for loading and plotted relative to the WT control. Results show mean ± SE (n=7 per genotype). **(f)** Representative images of 2-month WT (n=7) and HGPS (n=9) descending aorta cross sections immunostained for SM-MHC and SMA; scale bar=50 μm. **(g)** Quantification of aortic immunostaining with results plotted relative to the WT controls. Results in b, c and g are shown as box plots with Tukey whiskers. Significance in panels b, c and g was determined by Mann-Whitney tests. Significance in panel e was determined by Wilcoxon signed rank test.

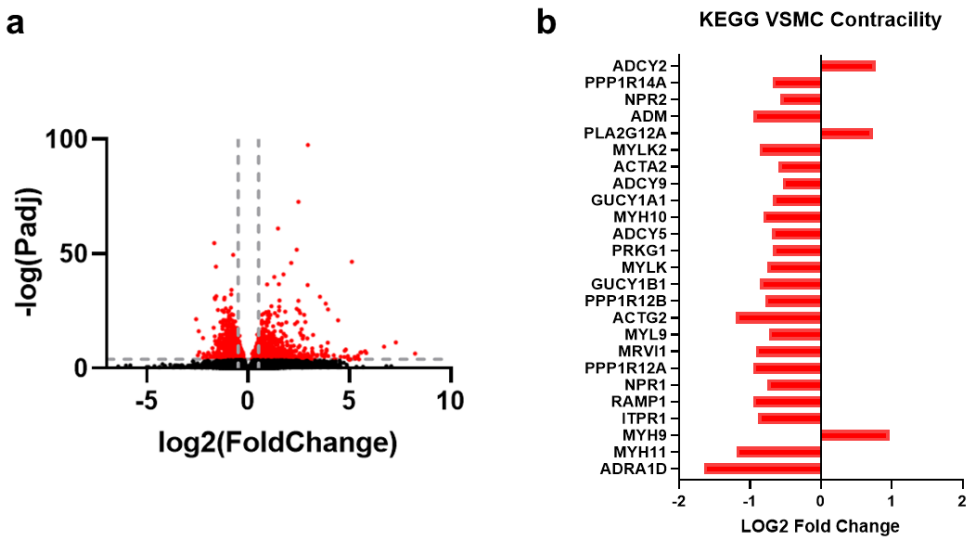

Figure 3.02. Additional analysis of genome-wide transcriptome profiling. (a) Volcano plot displaying differentially expressed genes from genome wide transcriptome analysis of 2-month WT and HGPS aortas (n=6 per genotype). Red dots display genes that met the cutoffs of >0.5 log_2 or <-0.5 log_2 fold change and an adjusted p-value of < 0.0001. **(b)** Genes within the cutoffs were subjected to KEGG pathway analysis (see Fig. 3.01a), and log_2 fold change values for genes within the vascular smooth muscle (VSMC) contractility pathway are shown.

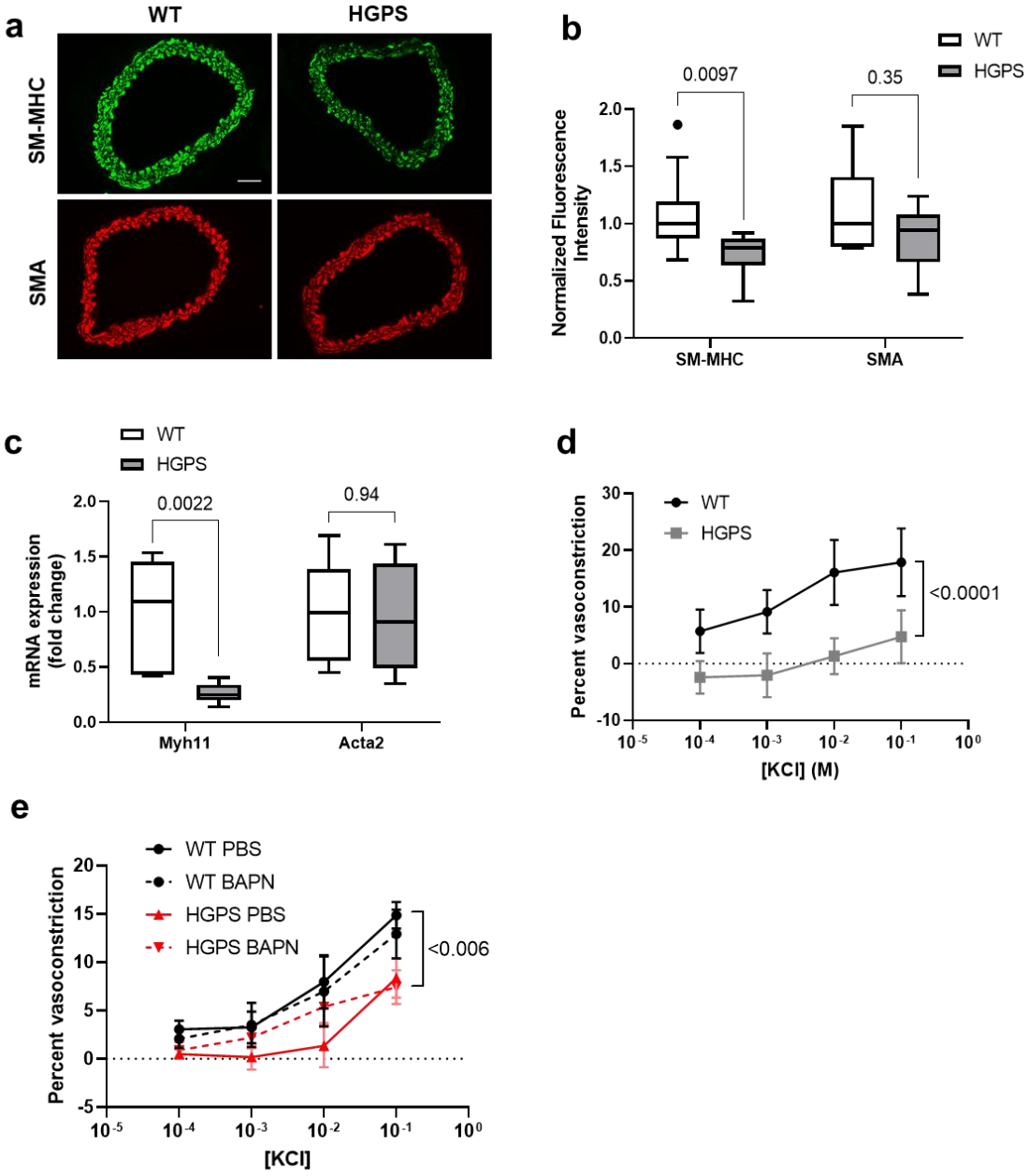

Figure 3.03. Reduced smooth muscle myosin heavy chain and decreased contractility in HGPS carotid arteries. (a) Representative images of 2-month WT (n=10) and HGPS (n=7) carotid artery cross sections immunostained for SM-MHC and

SMA; scale bar=50 μm. **(b)** Quantification of carotid artery immunostaining with results plotted relative to the WT controls. **(c)** Carotid arteries from 2-month WT and HGPS mice (n=6 per genotype) were isolated, and *Myh11* and *Acta2* mRNA transcript levels were determined by RT-qPCR. Results are plotted relative to the WT controls. Results in b and c are plotted as box plots with Tukey whiskers, and significance was determined by Mann-Whitney tests. **(d)** Mixed sex 2-month WT (n=7) and HGPS (n=5) carotid arteries were mounted on a pressure myograph and pressurized to 90 mm Hg. Percent vasoconstriction was measured in response to increasing concentrations of KCl. Significance in panel d was determined by two-way ANOVA, and results show mean ± SD. **(e)** WT and HGPS mice were subjected to daily PBS (WT n=6; HGPS n=7) or BAPN (WT n=4; HGPS n=6) injections starting at ~1-month of age (see Ch. 2 methods). Injections were continued until ~2-months of age and carotid arteries were isolated and subjected to vasoconstriction analysis as described in panel d. Plot shows mean ± SE, and significant was determined by 2-way ANOVA evaluating changes between treatment groups. Significance between WT PBS and HGPS BAPN mice are reported in the figure.

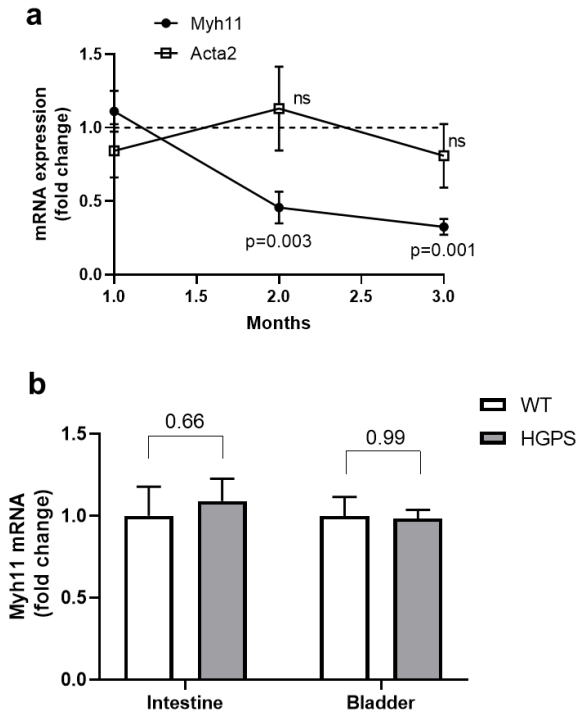

Figure 3.04. Myh11 transcript decreases over time in HGPS Aorta. (a) Descending aortas were isolated from 1-month, 2-month, and 3-month WT and HGPS mice and Myh11 and Acta2 transcript levels were evaluated by RT-qPCR (n=4 per genotype). HGPS transcript levels were normalized to respective age-matched WT levels (WT represented by dashed white line). Plots show mean fold change ± SE. Significance determined by ANOVA with Dunnett post-tests comparing each point to its respective levels in the 1-month HGPS aorta. **(b)** Myh11 transcript levels were evaluated in intestine (n=5 per genotype) and bladder (n=3 per genotype) by RT-qPCR in 2-month WT and HGPS mice. HGPS transcript levels were normalized to WT. Results show mean ± SE. Statistical significance determined by Mann-Whitney.

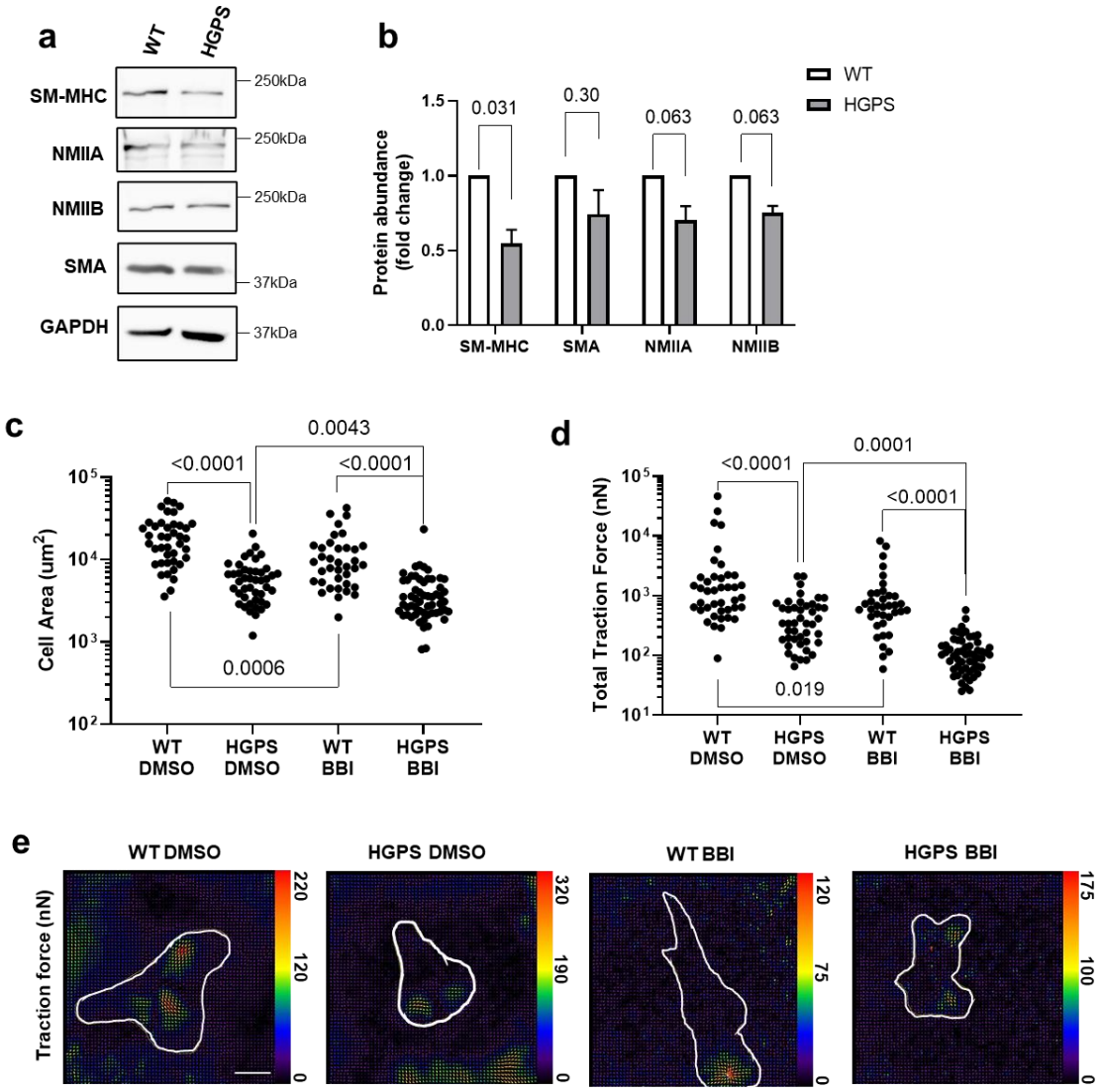

Figure 3.05. Decreased myosin abundance and traction force in isolated HGPS aortic vascular smooth muscle cells. (a) Representative images of cytosolic lysates from cultured SMCs immunoblotted for SM-MHC, non-muscle myosin II A and B (NMIIA and NMIIB, respectively), and SMA. GAPDH is shown as the loading control. Black boxes around the immunoblots indicate cropping for removal of extraneous space. Blots were stripped and re-probed when evaluating the abundance of multiple myosins and

SMA. **(b)** Quantification of immunoblotting results normalized for loading and plotted relative to the WT control**.** Results show mean ± SE (n=5-7). Significance was determined by Wilcoxon signed rank test. **(c-e)** Cultured SMCs were incubated on polyacrylamide hydrogels for 24 h. Cells were treated with vehicle (DMSO) or 15 μM blebbistatin (BBI) for 30 min prior to traction force analysis. **(c)** Cell area and **(d)** total traction force plots (n=37-57 cells) are shown, and each dot represents the total traction force of a single cell. Significance was determined by Mann-Whitney tests, and results are displayed as scatter plots. **(e)** Representative traction force images of cells analyzed in panel d. Cell areas are outlined in white, and traction force scale bars (in nanonewtons) are displayed to the right of each respective image. Optical scale bar=50 μm.

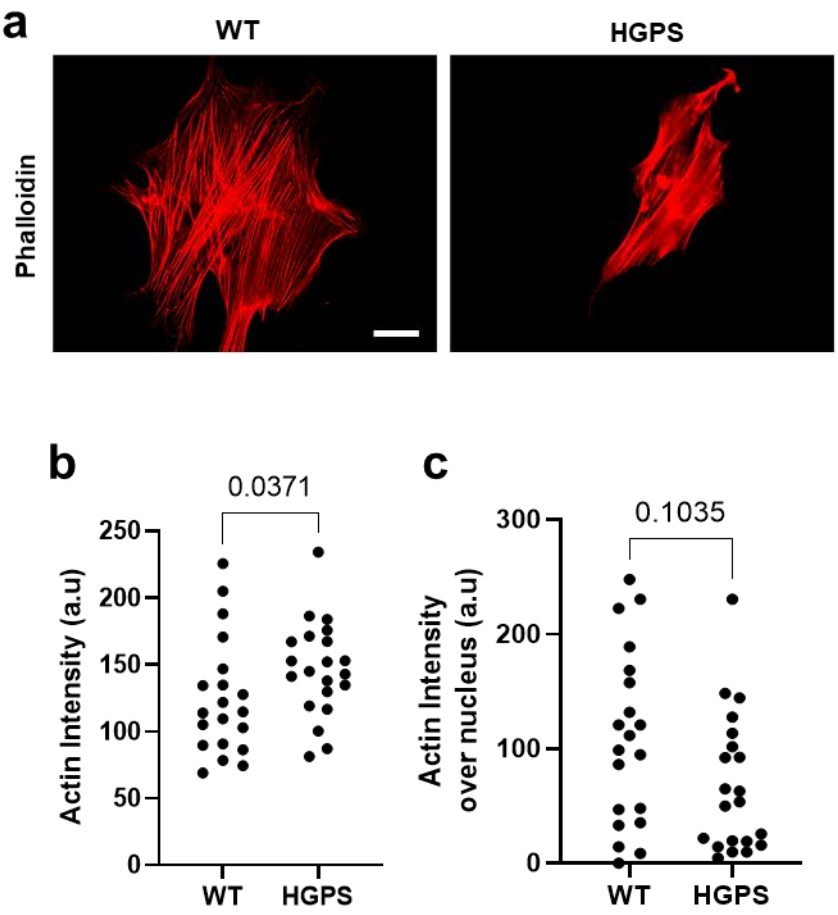

Figure 3.06. WT and HGPS SMCs display similar F-Actin. (a) WT and HGPS primary SMCs cultured on glass coverslips were stained with phalloidin to visualize F-actin. Scale bar 50 μm. **(b)** Average actin intensity across the cell and **(c)** Actin intensity over the nucleus was quantified. Data in panels B-C are accrued from 2 individual experiments quantifying 10-12 cells per genotype per experiment. Statistical testing was done by Mann-Whitney test.

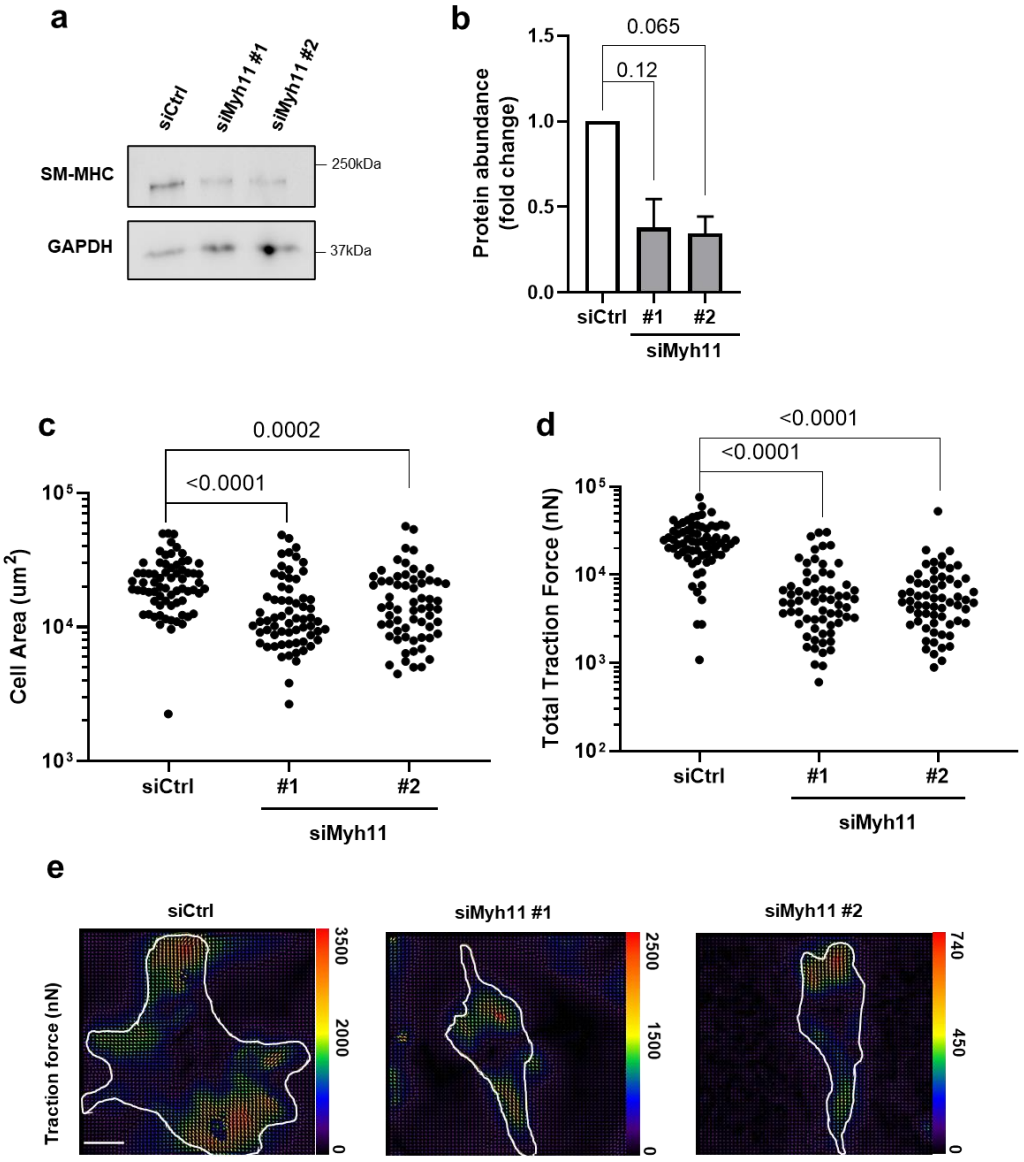

Figure 3.07. Knock down of SM-MHC reduces force generation in WT SMCs. Aortic SMCS isolated from 2-month WT mice were incubated with a control siRNA (siCtrl) or two distinct siRNAs targeting Myh11. **(a)** Representative images of lysates from the transfected cells immunoblotted for SM-MHC and GAPDH (loading control). Black boxes around the immunoblots indicate cropping for the removal of extraneous space. **(b)**

Quantification of immunoblotting results normalized for loading and plotted relative to the siCtrl control**.** Results show mean ± SE (n=4-5). Significance was determined by Wilcoxon signed rank test. **(c)** Cell area and **(d) t**otal traction force plots of siCtrl- or siMyh11-treated SMCs (n=63-69 cells). Each dot represents the total traction force of a single cell. Significance was determined by Mann-Whitney tests. **(e)** Representative traction force images of cells analyzed in panel d. Cell areas are outlined in white, and traction force scale bars (in nanonewtons) is displayed to the right of each respective image. Optical scale bar=50 μm.

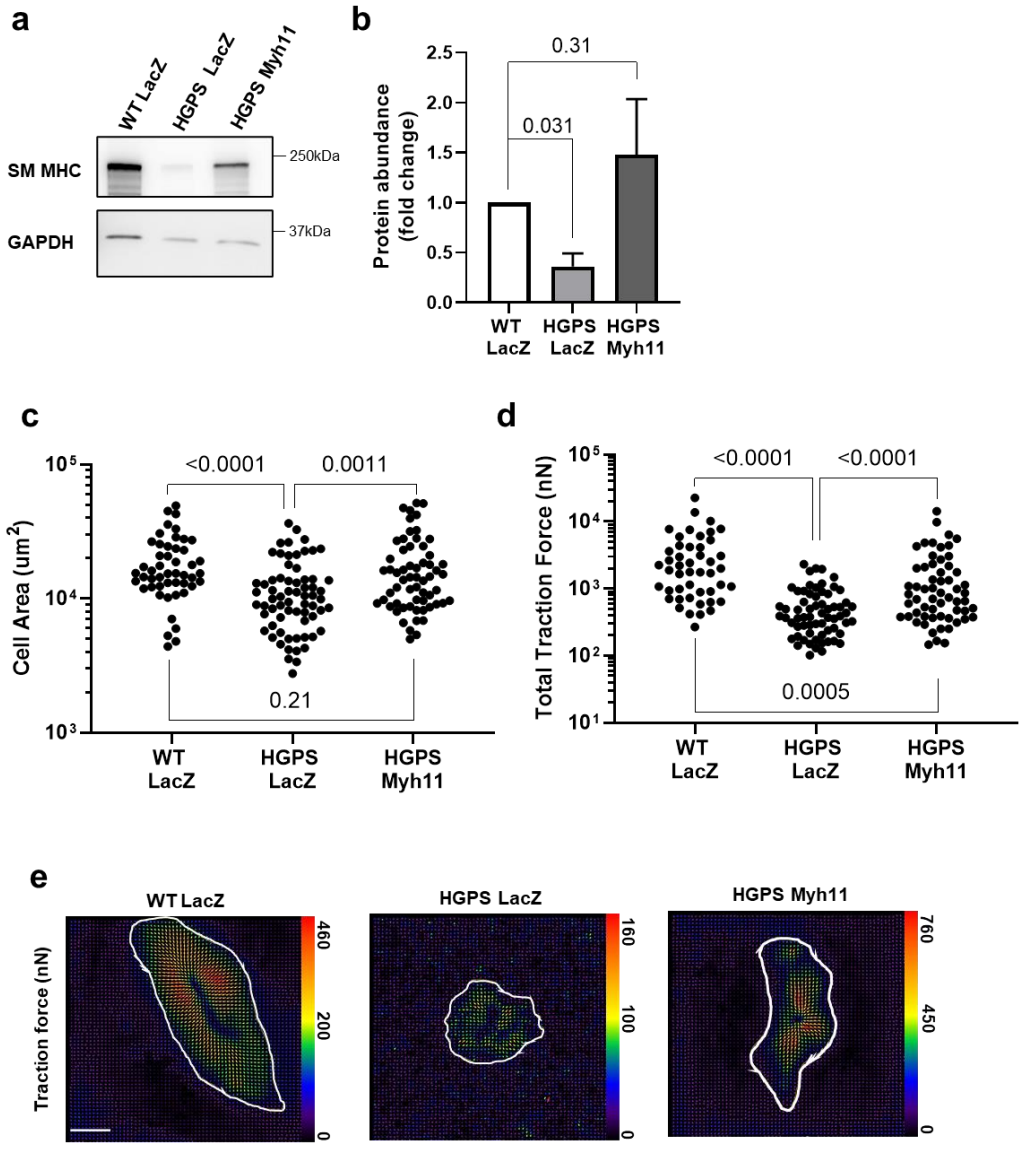

Figure 3.08. Smooth muscle myosin heavy chain overexpression restores contractility in isolated HGPS smooth muscle cells. Aortic SMCs isolated from 2-month WT and HGPS mice were incubated with adenovirus encoding LacZ (control) or *Myh11* for 72 h. **(a)** Representative images of lysates from the infected cells immunoblotted for SM-MHC and GAPDH (loading control). Black boxes around the

immunoblots indicate cropping for the removal of extraneous space. **(b)** Quantification of immunoblotting results normalized for loading and plotted relative to the WT LacZ control**.** Results show mean ± SE (n=6). Significance was determined by Wilcoxon signed rank test. **(c)** Cell area and **(d)** total traction force plots of primary WT and HGPS aortic SMCs incubated with an adenovirus encoding LacZ or *Myh11* (n=47-65 cells). Each dot represents the total traction force of a single cell. Significance was determined by Mann-Whitney tests. **(e)** Representative traction force images of cells analyzed in panel d. Cell areas are outlined in white, and traction force scale bars (in nanonewtons) are displayed to the right of each respective image. Optical scale bar=50 μm.

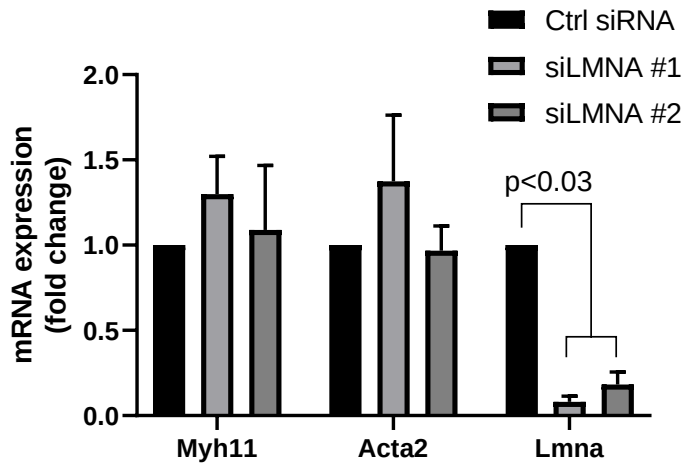

Figure 3.09. Acute LMNA knockdown does not reduce smooth muscle myosin heavy chain or smooth muscle actin mRNA. LMNA mRNA was knocked-down in WT SMCs using two distinct siRNAs as previously described in Figure 2.24, and transcript levels of Lmna, Myh11, and Acta2 were analyzed by RT-qPCR and normalized to the Ctrl siRNA treatment (n=3). Statistical significance was determined by two-way ANOVA with Holm-Sidak post-tests.

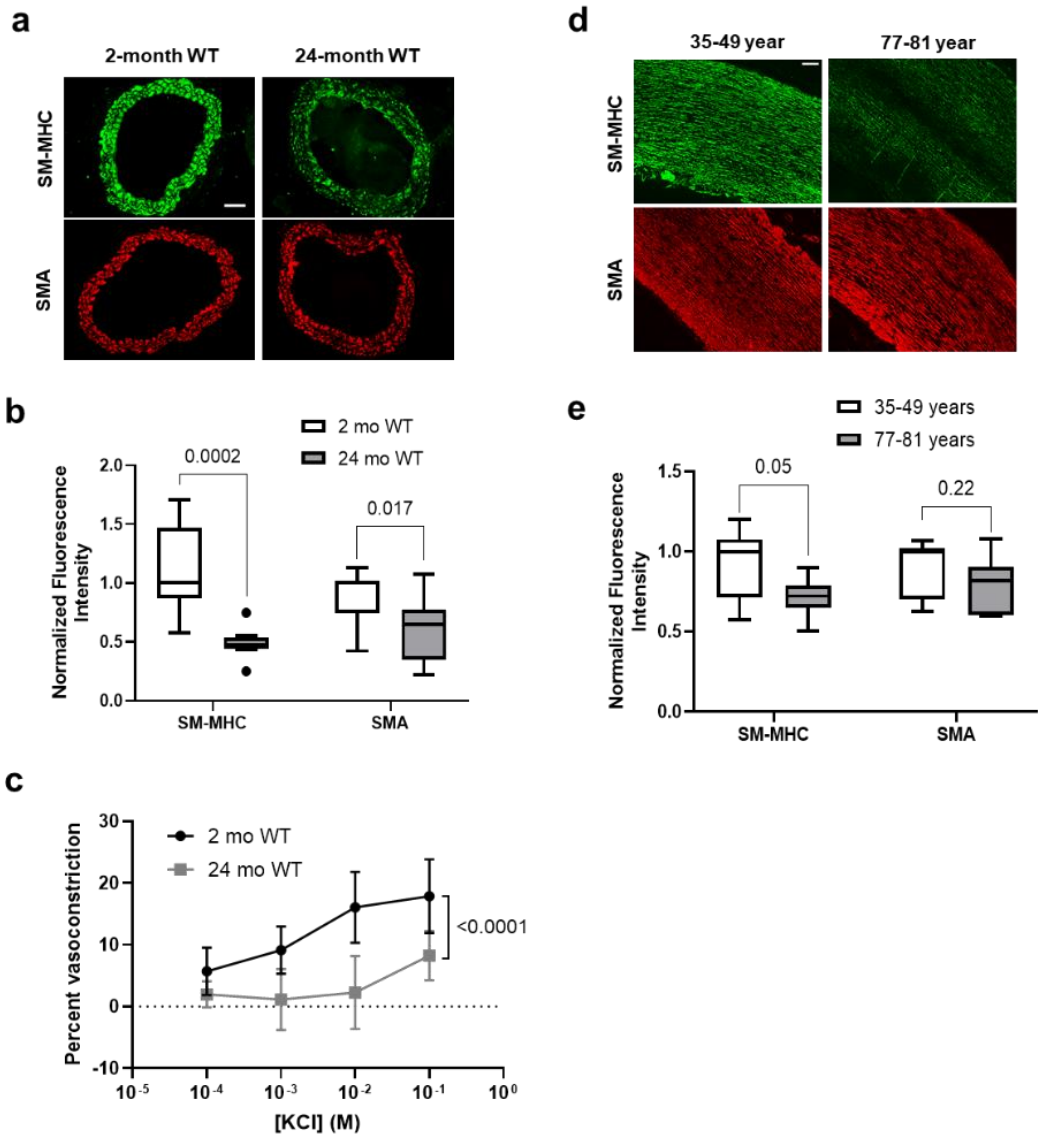

Figure 3.10. Decreased smooth muscle myosin heavy chain in aged mouse and human arteries. (a) Representative images of 2-month (n=7) and 24-month (n=9-10) WT mice carotid artery cross sections immunostained for SM-MHC and SMA; scale bar=50 μm. **(b)** Quantification of carotid artery immunostaining with results plotted relative to the WT controls. **(c)** Mixed sex 2-month WT (n=7, reproduced from Fig. 3.03d)

and 24-month WT (n=6) carotid arteries were mounted on a pressure myograph and pressurized to 90 mm Hg. Percent vasoconstriction was measured in response to increasing concentrations of KCl. Significance in panel c was determined by two-way ANOVA, and results show mean ± SD. **(d)** Representative images of human ascending aorta and aortic root cross sections of young (35-49 years, n=6-7) and old (77-81 years, n=7) immunostained for SM-MHC and SMA; scale bar=200 μm. **(e)** Quantification of immunostaining of ascending aorta and aortic root sections with results plotted relative to the young cohort. Results in b and e show box plots with Tukey whiskers. Significance was determined by 1-tail Mann-Whitney tests.

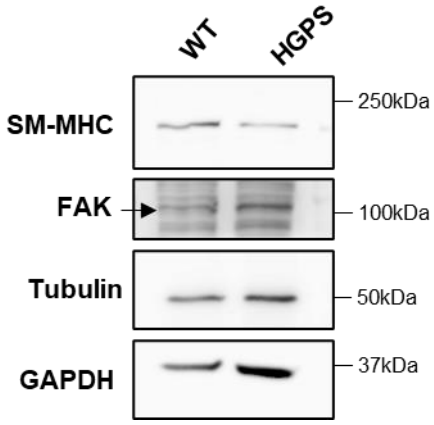

Figure 3.11. Validation of loading controls. WT and HGPS SMC lysates were immunoblotted for SM-MHC and three loading controls; Focal Adhesion Kinase (FAK), α–Tubulin, and GAPDH. Results are representative of several independent experiments probing for multiple loading controls.

3.8 References

Ahmed S & Warren DT (2018) Vascular smooth muscle cell contractile function and mechanotransduction. *Vessel Plus* 2, 36.

Amin M, Le VP & Wagenseil JE (2012) Mechanical Testing of Mouse Carotid Arteries: from Newborn to Adult. *J. Vis. Exp.*

Arancio W, Pizzolanti G, Genovese SI, Pitrone M & Giordano C (2014) Epigenetic involvement in Hutchinson-Gilford progeria syndrome: a mini-review. *Gerontology* 60, 197–203.

Babu GJ, Warshaw DM & Periasamy M (2000) Smooth muscle myosin heavy chain isoforms and their role in muscle physiology. *Microsc. Res. Tech.* 50, 532–540.

Booth EA, Spagnol ST, Alcoser TA & Dahl KN (2015) Nuclear stiffening and chromatin softening with progerin expression leads to an attenuated nuclear response to force. *Soft Matter* 11, 6412–8.

Brassard JA, Fekete N, Garnier A & Hoesli CA (2016) Hutchinson–Gilford progeria syndrome as a model for vascular aging. *Biogerontology* 17, 129–145.

Brozovich F V., Nicholson CJ, Degen C V., Gao YZ, Aggarwal M & Morgan KG (2016) Mechanisms of vascular smooth muscle contraction and the basis for pharmacologic treatment of smooth muscle disorders. *Pharmacol. Rev.* 68, 476–532.

del Campo L, Sánchez-López A, González-Gómez C, Andrés-Manzano MJ, Dorado B & Andrés V (2020) Vascular Smooth Muscle Cell-Specific Progerin Expression Provokes Contractile Impairment in a Mouse Model of Hutchinson-Gilford Progeria

Syndrome that Is Ameliorated by Nitrite Treatment. *Cells* 9, 656.

del Campo L, Sánchez-López A, Salaices M, von Kleeck RA, Expósito E, González-Gómez C, Cussó L, Guzmán-Martínez G, Ruiz-Cabello J, Desco M, Assoian RK, Briones AM & Andrés V (2019) Vascular smooth muscle cell-specific progerin expression in a mouse model of Hutchinson–Gilford progeria syndrome promotes arterial stiffness: Therapeutic effect of dietary nitrite. *Aging Cell*, e12936.

Capell BC, Collins FS & Nabel EG (2007) Mechanisms of cardiovascular disease in accelerated aging syndromes. *Circ. Res.* 101, 13–26.

Carmichael JD, Winder SJ, Walsh MP & Kargacin GJ (1994) Calponin and smooth muscle regulation. In *Canadian Journal of Physiology and Pharmacology*. Canadian Science Publishing, pp.1415–1419.

Chang W, Wang Y, Gant Luxton GW, Östlund C, Worman HJ & Gundersen GG (2019) Imbalanced nucleocytoskeletal connections create common polarity defects in progeria and physiological aging. *Proc. Natl. Acad. Sci. U. S. A.* 116, 3578–3583.

Cuff CA, Kothapalli D, Azonobi I, Chun S, Zhang Y, Belkin R, Yeh C, Secreto A, Assoian RK, Rader DJ & Puré E (2001) The adhesion receptor CD44 promotes atherosclerosis by mediating inflammatory cell recruitment and vascular cell activation. *J. Clin. Invest.* 108, 1031–1040.

Dahl KN, Scaffidi P, Islam MF, Yodh AG, Wilson KL & Misteli T (2006) Distinct structural and mechanical properties of the nuclear lamina in Hutchinson-Gilford progeria syndrome. *Proc. Natl. Acad. Sci. U. S. A.* 103, 10271–6.

Dembo M & Wang YL (1999) Stresses at the cell-to-substrate interface during locomotion of fibroblasts. *Biophys. J.* 76, 2307–2316.

Dinenno FA, Jones PP, Seals DR & Tanaka H (1999) Limb blood flow and vascular

conductance are reduced with age in healthy humans: Relation to elevations in sympathetic nerve activity and declines in oxygen demand. *Circulation* 100, 164–170.

Dinenno FA, Seals DR, Desouza CA & Tanaka H (2001) Age-related decreases in basal limb blood flow in humans: Time course, determinants and habitual exercise effects. *J. Physiol.* 531, 573–579.

Eddinger TJ & Meer DP (2007) Myosin II isoforms in smooth muscle: Heterogeneity and function. *Am. J. Physiol. - Cell Physiol.* 293, 493–508.

Ferruzzi J, Bersi MR & Humphrey JD (2013) Biomechanical Phenotyping of Central Arteries in Health and Disease: Advantages of and Methods for Murine Models. *Ann. Biomed. Eng.* 41, 1311–1330.

Gerhard-Herman M, Smoot LB, Wake N, Kieran MW, Kleinman ME, Miller DT, Schwartzman A, Giobbie-Hurder A, Neuberg D & Gordon LB (2011) Mechanisms of Premature Vascular Aging in Children With Hutchinson-Gilford Progeria Syndrome. *Hypertension* 59.

Gonzalo S, Kreienkamp R & Askjaer P (2016) Hutchinson-Gilford Progeria Syndrome: A premature aging disease caused by LMNA gene mutations. *Ageing Res. Rev.*

Hathaway DR, March KL, Lash JA, Adam LP & Wilensky RL (1991) Vascular smooth muscle. A review of the molecular basis of contractility. *Circulation* 83, 382–90.

Kanehisa M (2019) Toward understanding the origin and evolution of cellular organisms. *Protein Sci.* 28, 1947–1951.

Kelley JB, Datta S, Snow CJ, Chatterjee M, Ni L, Spencer A, Yang C-S, Cubenas-Potts C, Matunis MJ & Paschal BM (2011) The Defective Nuclear Lamina in Hutchinson-Gilford Progeria Syndrome Disrupts the Nucleocytoplasmic Ran Gradient and

Inhibits Nuclear Localization of Ubc9. *Mol. Cell. Biol.* 31, 3378–3395.

von Kleeck R, Roberts E, Castagnino P, Bruun K, Brankovic SA, Hawthorne EA, Xu T, Tobias JW & Assoian RK (2021) Arterial stiffness and cardiac dysfunction in Hutchinson–Gilford Progeria Syndrome corrected by inhibition of lysyl oxidase. *Life Sci. Alliance* 4, e202000997.

Klein EA, Yung Y, Castagnino P, Kothapalli D & Assoian RK (2007) Cell Adhesion, Cellular Tension, and Cell Cycle Control. In *Methods in enzymology*. pp.155–175.

Lehman W & Morgan KG (2012) Structure and dynamics of the actin-based smooth muscle contractile and cytoskeletal apparatus. *J. Muscle Res. Cell Motil.* 33, 461–469.

Limouze J, Straight AF, Mitchison T & Sellers JR (2004) Specificity of blebbistatin, an inhibitor of myosin II. *J. Muscle Res. Cell Motil.* 25, 337–341.

Martin AF, Bhatti S, Pyne-Geithman GJ, Farjah M, Manaves V, Walker L, Franks R, Strauch AR & Paul RJ (2007) Expression and function of COOH-terminal myosin heavy chain isoforms in mouse smooth muscle. *Am. J. Physiol. Physiol.* 293, C238–C245.

Martino F, Perestrelo AR, Vinarský V, Pagliari S & Forte G (2018) Cellular mechanotransduction: From tension to function. *Front. Physiol.* 9, 824.

McClintock D, Ratner D, Lokuge M, Owens DM, Gordon LB, Collins FS & Djabali K (2007) The Mutant Form of Lamin A that Causes Hutchinson-Gilford Progeria Is a Biomarker of Cellular Aging in Human Skin A. Lewin, ed. *PLoS One* 2, e1269.

Merideth MA, Gordon LB, Clauss S, Sachdev V, Smith ACM, Perry MB, Brewer CC, Zalewski C, Kim HJ, Solomon B, Brooks BP, Gerber LH, Turner ML, Domingo DL, Hart TC, Graf J, Reynolds JC, Gropman A, Yanovski JA, Gerhard-Herman M,

Collins FS, Nabel EG, Cannon RO, Gahl WA & Introne WJ (2008) Phenotype and Course of Hutchinson–Gilford Progeria Syndrome. *N. Engl. J. Med.* 358, 592–604.

Murtada S-I, Kawamura Y, Caulk AW, Ahmadzadeh H, Mikush N, Zimmerman K, Kavanagh D, Weiss D, Latorre M, Zhuang ZW, Shadel GS, Braddock DT & Humphrey JD (2020) Paradoxical aortic stiffening and subsequent cardiac dysfunction in Hutchinson–Gilford progeria syndrome. *J. R. Soc. Interface* 17, 20200066.

Olive M, Harten I, Mitchell R, Beers JK, Djabali K, Cao K, Erdos MR, Blair C, Funke B, Smoot L, Gerhard-Herman M, Machan JT, Kutys R, Virmani R, Collins FS, Wight TN, Nabel EG & Gordon LB (2010) Cardiovascular Pathology in Hutchinson-Gilford Progeria: Correlation With the Vascular Pathology of Aging. *Arterioscler. Thromb. Vasc. Biol.* 30.

Osorio FG, Navarro CL, Cadiñanos J, López-Mejía IC, Quirós PM, Bartoli C, Rivera J, Tazi J, Guzmán G, Varela I, Depetris D, de Carlos F, Cobo J, Andrés V, De Sandre-Giovannoli A, Freije JMP, Lévy N & López-Otín C (2011) Splicing-directed therapy in a new mouse model of human accelerated aging. *Sci. Transl. Med.* 3, 106ra107.

Reho JJ, Zheng X & Fisher SA (2014) Smooth muscle contractile diversity in the control of regional circulations. *Am. J. Physiol. - Hear. Circ. Physiol.* 306, H163.

Rodriguez S, Coppedè F, Sagelius H & Eriksson M (2009) Increased expression of the Hutchinson-Gilford progeria syndrome truncated lamin A transcript during cell aging. *Eur. J. Hum. Genet.* 17, 928–937.

Sazonova O V., Isenberg BC, Herrmann J, Lee KL, Purwada A, Valentine AD, Buczek-Thomas JA, Wong JY & Nugent MA (2015) Extracellular matrix presentation

modulates vascular smooth muscle cell mechanotransduction. *Matrix Biol.* 41, 36–43.

Scaffidi P & Misteli T (2006) Lamin A-Dependent Nuclear Defects in Human Aging. *Science (80-.).* 312.

Seawright JW, Sreenivasappa H, Gibbs HC, Padgham S, Shin SY, Chaponnier C, Yeh AT, Trzeciakowski JP, Woodman CR & Trache A (2018) Vascular Smooth Muscle Contractile Function Declines With Age in Skeletal Muscle Feed Arteries. *Front. Physiol.* 9.

Shanahan CM, Weissberg PL & Metcalfe JC (1993) Isolation of gene markers of differentiated and proliferating vascular smooth muscle cells. *Circ. Res.* 73, 193–204.

Shutova MS, Asokan SB, Talwar S, Assoian RK, Bear JE & Svitkina TM (2017) Self-sorting of nonmuscle myosins IIA and IIB polarizes the cytoskeleton and modulates cell motility. *J. Cell Biol.* 216, 2877–2889.

Stehbens WE, Delahunt B, Shozawa T & Gilbert-Barness E (2001) Smooth muscle cell depletion and collagen types in progeric arteries. *Cardiovasc. Pathol.* 10, 133–136.

Tseng Q, Duchemin-Pelletier E, Deshiere A, Balland M, Guilloud H, Filhol O & Theńy M (2012) Spatial organization of the extracellular matrix regulates cell-cell junction positioning. *Proc. Natl. Acad. Sci. U. S. A.* 109, 1506–1511.

Varga R, Eriksson M, Erdos MR, Olive M, Harten I, Kolodgie F, Capell BC, Cheng J, Faddah D, Perkins S, Avallone H, San H, Qu X, Ganesh S, Gordon LB, Virmani R, Wight TN, Nabel EG & Collins FS (2006) Progressive vascular smooth muscle cell defects in a mouse model of Hutchinson–Gilford progeria syndrome.

Verstraeten VLRM, Ji JY, Cummings KS, Lee RT & Lammerding J (2008) Increased

mechanosensitivity and nuclear stiffness in Hutchinson-Gilford progeria cells: effects of farnesyltransferase inhibitors. *Aging Cell* 7, 383–93.

Webb RC (2003) Smooth muscle contraction and relaxation. In *American Journal of Physiology - Advances in Physiology Education*. American Physiological Society, pp.201–206.

Wheeler JB, Mukherjee R, Stroud RE, Jones JA & Ikonomidis JS (2015) Relation of murine thoracic aortic structural and cellular changes with aging to passive and active mechanical properties. *J. Am. Heart Assoc.* 4, e001744.

Zhang H-M, Ji H-H, Ni T, Ma R-N, Wang A & Li X (2017) Characterization of Blebbistatin Inhibition of Smooth Muscle Myosin and Nonmuscle Myosin-2. *Biochemistry* 56, 4235–4243.

Zhang JCL, Kim S, Helmke BP, Yu WW, Du KL, Lu MM, Strobeck M, Yu Q-C & Parmacek MS (2001) Analysis of SM22α-Deficient Mice Reveals Unanticipated Insights into Smooth Muscle Cell Differentiation and Function. *Mol. Cell. Biol.* 21, 1336–1344.

Zonderland J, Wieringa P & Moroni L (2019) A quantitative method to analyse F-actin distribution in cells. *MethodsX* 6, 2562–2569.

Chapter 4: Direct effects of progerin on smooth muscle cell contractility

4.1 Introduction

Hutchinson-Gilford Progeria Syndrome (HGPS) is an ultra-rare premature aging disease that affects around 1 in 4-8 million births (Sinha et al. 2014). At around a year after birth, HGPS children present with progressive clinical signs of aging such as loss of hair, thinning of the skin, stiff joints, and severely stunted growth (Saxena & Kumar 2020). HGPS is also characterized by arterial dysfunction including a dramatic loss of smooth muscle cells (SMCs) from the large arteries, a severely fibrotic arterial environment, and prominent atherosclerotic lesions (Merideth et al. 2008; Saxena & Kumar 2020). Ultimately, HGPS children die in their early teen years due to heart attack and stroke.

The classical form of HGPS is a result of a single nucleotide point mutation to the Lamin A gene, leading to altered splicing and production of a mutant form of Lamin A termed progerin (De Sandre-Giovannoli et al. 2003; Eriksson et al. 2003; Goldman et al. 2004). Compared to normal Lamin A, progerin lacks 50 amino acids near the C-terminus and remains permanently farnesylated, which leads to improper incorporation into the inner nuclear membrane and formation of an altered nuclear lamina network (Hamczyk et al. 2018; Saxena & Kumar 2020).

Lamin A, one of the major elements of the nuclear lamina, is a critical component for mechanotransduction signaling. Mechanical feedback such as actomyosin contraction from the cytoskeleton is transmitted to the nucleus through the Linker of Nucleoskeleton and Cytoskeleton (LINC) complex. The LINC complex connects to the actin cytoskeleton and intermediate filaments through Nesprin proteins which cross the

outer nuclear membrane. Nesprins connect to SUN proteins in the nuclear envelope, and SUN proteins connect to the nuclear lamina meshwork on the inner nuclear membrane (Dahl et al. 2008; Dahl & Kalinowski 2011; Crisp et al. 2006; Martino et al. 2018). The disrupted nuclear lamina due to the presence of progerin has been associated with altered mechanotransduction (Dahl et al. 2006; Verstraeten et al. 2008; Chen et al. 2014). The SMC population is constantly responding to mechanical stimuli, whether it be feedback from the stiffness of the extracellular matrix (ECM), or the cyclic stretching of the arteries due to blood flow from the heart. In particular, Kim et al. (2018) showed that progerin-expressing SMCs showed increased cell death in response to repetitive biaxial stretching, and forced disruption of the LINC complex reduced SMC death *in vivo* (Kim et al. 2018).

SMCs comprise the media layer of the large elastic arteries where they regulate blood flow by tonic vasoconstriction or dilation (Webb 2003; Hathaway et al. 1991). SMCs can undergo phenotypic modulation, existing along a spectrum from a differentiated “contractile state” to a more dedifferentiated “synthetic state” (Owens et al. 2004; Davis-Dusenbery et al. 2011). Contractile SMCs have high expression of smooth muscle contractile machinery, such as smooth muscle myosins, smooth muscle actin, calponin, and transgelin. Upon stimuli such as arterial injury, SMCs can dedifferentiate to a more synthetic state where they downregulate expression of key contractile genes and become migratory, proliferative, and remodel the ECM to promote wound healing (Hao et al. 2003; Owens et al. 2004; Rensen et al. 2007a). However, in some diseases such as atherosclerosis, phenotypic switching can lead to an aberrant population of synthetic SMCs, leading to arterial stenosis (Hao et al. 2003; Grootaert & Bennett 2021).

Phenotypic switching is regulated in part by mechanotransduction in SMCs. Mechanical strain increased accumulation of ECM proteins and produced a proliferative response in SMCs (Lee et al. 2001; Wang et al. 2018). In other work, hypertensive pressure stimulated phenotypic switching to a more synthetic state, altering actin organization and cell structure (Onoue et al. 2008; Sit et al. 2020). Our lab has recently reported that ECM stiffness promotes emergence of both contractile and synthetic SMCs from a "null" precursor population that possesses neither contractile nor synthetic characteristics; this emergence is regulated by stiffness-stimulated activation of Rac and Rho GTPases (Talwar et al. 2021). Taken together, these studies suggest that disrupted mechanotransduction, as observed in HGPS SMCs, may lead to altered SMC gene expression and disrupted modulation of phenotypic state. Interestingly, I previously reported that HGPS SMCs display defective force generation and present with down-regulation of SMC contractility markers, in particular SM-MHC (see Chapter 3). As reduced contractility is a key hallmark of a more synthetic SMC, my results raise the possibility that HGPS SMCs exist in an altered phenotypic state.

The phenotypic state of SMCs is largely regulated by cis-acting elements in DNA termed CArG boxes ($CC(AT)_6GG$) in the promoters of contractile genes, which allow binding of Serum Response Factor (SRF) and myocardin-related transcription factors (MRTFs) to promote contractile gene expression (Kim et al. 1997; Li et al. 1996; Mack & Owens 1999). Transcriptional repressors, such as Kruppel like factor 4 (KLF4), or activators, such as MRTF-A, also known as MKL1/MAL, are critical for balancing phenotypic state. Indeed, studies show that MRTF-A can induce contractile gene expression and promote SMC differentiation as a transcriptional activator of SRF (Jeon et al. 2008; Du et al. 2004). Interestingly, MRTF-A localization is mechanosensitive. In

unstimulated cells, MRTF-A is sequestered in the cytoplasm through binding to G-Actin through its RPEL motifs which flank a nuclear localization signal (Guettler et al. 2008). Upon actin polymerization, the G-actin pool is depleted, and the exposed nuclear localization signal allows MRTF-A to enter the nucleus and modulate gene expression. Ho et al. (2013) showed that Lamin A-deficient fibroblasts had decreased actin polymerization and consequently reduced nuclear import of MRTF-A (Ho et al. 2013). Surprisingly, they corelated defective MRTF-A signaling with altered localization of emerin, an inner-nuclear membrane protein that caps the pointed end of actin filaments and promotes actin polymerization *in vitro*. Interestingly, Osmanagic-Myers et al. (2018) have shown that progerin expression in endothelial cells also mislocalizes emerin protein, and MRTF-A is sequestered at the nuclear periphery (Osmanagic-Myers et al. 2018). Oddly, this sequestration was associated with increased MRTF-A gene transcription.

In this chapter, I show that acute progerin expression in WT SMCs recapitulates the decreased SM-MHC but not the increased LOX or decreased miR-145 abundance observed in HGPS. I provide preliminary evidence indicating HGPS SMCs from the widely used $LMNA^{G609G/G609G}$ HGPS mouse model (Osorio et al. 2011) present with decreased MRTF-A nuclear localization and that this defect can be recapitulated by ectopic expression of progerin in WT SMCs. Furthermore, I show that knockdown of MRTF-A decreases contractile gene expression in WT SMCs and discuss the similarities and differences between the MRTF-A-dependent contractile gene profile and that of HGPS SMCs. These findings suggest that altered nuclear localization of MRTF-A in HGPS SMCs could contribute to the decline in contractile function observed in isolated HGPS cells and arteries and that progerin may be promoting a more synthetic-like state

in HGPS SMCs. However, additional complimentary and follow-up experiments are needed to support this hypothesis and are expanded upon in the Discussion section.

4.2 Results

Acute Progerin expression reduces SMMHC and traction force in WT SMCs. As previous experiments displaying reduced SM-MHC, reduced force generation, and increased LOX abundance (reported in Chapters 2 and 3) were conducted in HGPS SMCs which have chronic progerin expression, I wanted to determine whether acute progerin expression in WT SMCs would recapitulate our observations. Overexpression of GFP-tagged progerin in WT SMCs did not recapitulate the decreased miR-145 and increased LOX abundance observed in HGPS SMCs (Fig. 4.01a-b). However, acute progerin expression did selectively reduce SM-MHC protein and *Myh11* mRNA levels in comparison to SMA protein and *Acta2* mRNA (Fig. 4.01c-e). This reduction in SM-MHC was accompanied by a reduction in cell area and decreased traction force in progerin overexpressing cells (Fig. 4.01f-h).

HGPS aorta display a reduced MRTF-A target-gene signature. I postulated that the reduced force generation and contractile gene expression of HGPS SMCs may be due to HGPS SMCs existing in a more synthetic state. I interrogated our transcriptome-wide analysis of WT and HGPS aortas for significantly altered contractile and synthetic markers (Rensen et al. 2007b; Owens et al. 2004; Beamish et al. 2010; Long et al. 2008; Miano 2003; Rzucidlo et al. 2007) and found that key contractile SMC markers were downregulated (Fig. 4.02a, green) while synthetic SMC markers tended to be

upregulated (Fig. 4.02a, red). Canonical regulation of contractile gene expression in SMCs relies on the delicate balance of transcriptional activators, such as MRTF-A, or repressors, such as KLF4, to modulate SRF activity (Fig. 4.02b). I used Ingenuity Pathway Analysis (IPA) on our previously reported genome-wide sequencing of 2-month WT and HGPS aorta (von Kleeck et al. 2021) to predict activation or inhibition of upstream regulators of genes associated with SMC differentiation. This analysis identified MRTF-A and KLF4 based upon enriched target gene sets from nearly 4,000 differentially expressed genes. IPA predicted a slightly reduced target gene signature for KLF4, which would not explain the decreased contractile gene expression I observed in HGPS aortas (Fig. 4.02c, also see Chapter 3). In contrast, the MRTF-A target-gene signature, and consequently SRF signature, was highly reduced (Fig. 4.02c). As many SMC contractile genes are regulated by MRTF-A (see Introduction), this finding was consistent with the idea that reduced MRTF-A signaling could account for the decreased force generation observed in HGPS SMCs (Chapter 3).

Reduced nuclear-cytoplasmic ratios of MRTF-A in HGPS SMCs. MRTF-A protein levels were similar in lysates of 2-month WT and HGPS aorta (Fig. 4.03a-b), consistent with many studies showing that MRTF-A activity is regulated by cytoplasmic-nuclear translocation (see Introduction). Indeed, I observed that isolated HGPS SMCs had a significantly reduced nuclear-cytoplasmic ratio of MRTF-A as compared to WT controls (Fig. 4.03c-d). To determine if reduced nuclear MRTF-A in HGPS was a direct consequence of progerin, I expressed GFP-tagged progerin in WT SMCs and observed MRTF-A distribution. I saw that progerin-expressing cells (Fig. 4.03e, white arrows),

displayed more diffuse MRTF-A in comparison to cells lacking progerin or WT SMCs cells expressing GFP.

MRTF-A knockdown reduces contractile gene expression. MRTF-A is a positive regulator of many contractile genes expressed in SMCs and one report indicates that it also regulates LOX levels in mammary epithelial cells (Gurbuz et al. 2014). I used siRNA-mediated knockdown of MRTF-A in primary WT SMCs to determine if reduced MRTF-A would recapitulate the increased *Lox* and preferential reduction in *Myh11* transcript levels seen in HGPS SMCs. As opposed to Gurbuz et al. (2014), I found that knockdown of MRTF-A did not change *Lox* or miR-145 transcript levels (Fig. 4.04a) to a similar extent of what was observed in HGPS SMCs (Fig. 4.04b). Intriguingly, I have noted that HGPS aorta display a more selective reduction in smooth muscle myosin heavy chain (SM-MHC, gene *Myh11*) as opposed to other contractile genes such as alpha-smooth muscle actin (SMA, gene *Acta2*), calponin (gene *Cnn1*), or transgelin (gene *Tagln*). I found that knockdown of MRTF-A by three separate siRNAs did produce a more pronounced reduction in *Myh11* transcript than *Acta2* (although both transcripts were significantly reduced, Fig. 4.04c), similar to what was observed in HGPS SMCs (Fig. 4.04d). However, MRTF-A knockdown also produced a pronounced decrease in *Cnn1* which was not observed in HGPS aorta (Fig. 4.04e).

4.3 Discussion

In this work in progress, I show that the acute progerin expression recapitulates the decrease in SM-MHC observed in HGPS but progerin does not have a direct effect

on the miR-145-LOX pathway. Furthermore, a bioinformatically-predicted decrease in MRTF-A signaling *in vivo* correlates with a decrease in nuclear-cytoplasmic abundance of MRTF-A in isolated HGPS SMCs. Acute progerin expression in WT SMCs recapitulates the altered nuclear localization of MRTF-A seen in HGPS SMCs. Additionally, knockdown of MRTF-A decreased contractile gene expression in WT SMCs, albeit MRTF-A knockdown appears to reduce many contractile genes in addition to *Myh11*. More studies will be needed to compare the contractile gene profile in MRTF-A knockdown cells and HGPS SMCs. Moreover, direct DNA-binding studies through chromatin immunoprecipitation will be needed to confirm that this decreased nuclear abundance correlates with reduced MRTF-A association with SRF promoter elements of these contractility genes.

Intriguingly, acute expression of progerin revealed that the altered miR-145-LOX signaling in HGPS is not a direct effect of progerin. This suggests that cell-extrinsic factors contribute to the high LOX expression observed in HGPS arteries. As composition of the extracellular matrix can have direct effects on gene expression and cell signaling, it may be that altered matrix deposition by HGPS SMCs is driving the decreased miR-145 and consequent increase in LOX expression. Alternatively, it may be that increased LOX abundance is a consequence of long-term rather than acute progerin expression, and a time course to understand how gene expression changes with extended progerin expression in WT SMCs will aid our understanding. However, acute progerin expression did have a direct effect on reducing SM-MHC abundance and decreasing traction force in HGPS SMCs. Follow-up studies to understand how progerin may be altering the epigenetic landscape of SMCs will help to determine why progerin

has a more selective effect on decreasing SM-MHC as opposed to other contractile genes.

Future experiments will determine how progerin is causing altered nuclear MRTF-A localization. HGPS cells expressing a MRTF-A construct lacking RPEL actin-binding motifs could be used to determine if the altered nuclear localization of MRTF-A is due to altered actin dynamics or due to defective nuclear import independent of actin. Intriguingly, both altered actin dynamics such as altered nuclear F-actin formation (Takahashi et al. 2020; Mu et al. 2020) and deregulated nuclear import (Kelley et al. 2011) have been reported in HGPS fibroblasts. I have previously reported that HGPS SMCs show no overt changes in stress fiber abundance or organization as visualized with phalloidin stain (see Chapter 3). However, fluorescence recovery after photobleaching (FRAP) experiments to study actin polymerization dynamics in HGPS SMCs could be useful in determining if HGPS SMCs have lowered actin polymerization rates, which may explain the reduced nuclear MRTF-A. Further experimentation to examine emerin localization could be used to determine if HGPS SMCs also present with altered emerin distribution as previously reported in HGPS endothelial cells and Lamin A knockout fibroblasts (Ho et al. 2013; Osmanagic-Myers et al. 2018). Better understanding MRTF-A localization could highlight the similarities between how progerin alters signaling in multiple cell types.

Increased ECM production and decreased contractility are observed in HGPS mouse arteries and cells (del Campo et al. 2019; del Campo et al. 2020; Chapter 2-3). Thus, I hypothesize that HGPS SMCs exist in a more dedifferentiated, synthetic state. This idea is further supported by a more synthetic like gene profile from unbiased transcriptome-wide analysis of HGPS aortas and my observation of reduced size of

HGPS SMCs, as dedifferentiated SMCs are smaller than differentiated ones (Talwar et al. 2021, Chapter 3). My observations support the idea that progerin expression may be promoting a more synthetic-like gene program in HGPS SMCs in part through altering MRTF-A nuclear localization. Intriguingly, knockdown of MRTF-A produced a significant reduction in all contractile genes analyzed (*Myh11, Acta2, Cnn1, Tagln*), albeit to different extents. However, in HGPS arteries I observed a much more striking decrease in *Myh11* than other contractile genes (see chapter 3). It would be worthwhile to survey a larger array of contractile genes in both HGPS SMCs and in MRTF-A knockdown SMCs to get a better understanding of potential overlaps in the contractile gene signatures. It could be that additional altered signaling pathways complement the effect of reduced MRTF-A translocation to generate the selective profile of contractile gene expression seen in HGPS.

4.4 Methods

Mice and artery isolation. LMNA$^{G609G/+}$ mice on the C57/BL6 background were generously provided Dr. Carlos Lopez-Otin (Universidad de Oviedo, Oviedo, Spain). Mice were genotyped using the following primers: Forward: AAGGGGCTGGGAGGACAGAG; and Reverse: AGCATGCCATAGGGTGGAAGGA, with band sizes of 100bp for WT and 240bp for LMNA^{G609G}. Mice were fed a chow diet *ad libitum*. For HGPS mouse experiments, WT littermate controls were obtained from LMNA$^{G609G/+}$ matings. Arteries were perfused with PBS in situ through the left ventricle, and the descending aorta was isolated from the end of the aortic arch to the diaphragm. The isolated aorta was cleaned of excess fat and flash frozen and stored at -80C for protein analysis. Animal protocols were approved by the University of Pennsylvania Institutional Animal Care and Use Committee.

Genome-wide transcript analysis. I used our previously described genome-wide analysis of differentially expressed genes in 2-month WT versus HGPS mouse aortas to interrogate pathway activation or inhibition (von Kleeck et al. 2021) (GEO ascension number GSE165409). Differentially expressed genes having a 1.5x fold change and adjusted p-values of <0.001 were subjected to a core analysis with Ingenuity Pathway Analysis (IPA). Default settings were used for all other core analysis parameters. The core analysis included the prioritization of upstream regulators based on enrichment of a regulator's target gene set in the set of differentially expressed genes. For each regulator, IPA tested the directionality of each of the genes in the overlap to infer an

activation or inactivation of the regulator (Z-score). We defined putative upstream regulators of DEGs as those having Z-scores >1.75 (activated) or <-1.75 (inhibited).

Cell culture and RNAi. Primary mouse SMCs were isolated from the descending aortas of 2-month WT and HGPS male mice and prepared by explant culture as described (Cuff et al. 2001). SMCs were cultured in growth medium [1:1] Dulbecco's modified Eagle's medium (DMEM)/Ham's F-12 supplemented with 2 mM L-glutamine and 20 mM HEPES, pH7.4] with 20% FBS. Cells were passaged at near confluence with trypsin/EDTA and used between passages 4-6.

siRNA-mediated knock-down of MRTF-A in near-confluent WT SMCs was performed using Lipofectamine RNAiMAX Transfection Reagent (Thermofisher #13778100) in OPTI-MEM with a final siRNA concentration of 300 nM (Origene 223701). A non-specific siRNA was used as control (included from Origene). After 4-hours of siRNA transfection, cells were switched to fresh growth medium. RT-qPCR analysis was performed 72-hours after transfection.

GFP-Progerin Adenovirus. pBABE-GFP-Progerin (Addgene 17663) was cloned into pENTR/D-TOPO by PCR (Invitrogen K2400-20). The resultant GFP-progerin entry vector was gel-purified (Qiagen 28104) then cloned into the pAd/CMV/V5-DEST Gateway vector (Invitrogen V493-20). Protocols were followed in accordance with manufacturer's instructions. The Gateway vector was then transfected into 293A cells, which were collected ~10 days after transfection when lytic plaques were visible. Crude lysate from transfected 293A cells were used to transduce additional 293A cells and titer the virus. For SMC experiments, GFP-Progerin adenovirus was used at 300-500 moi.

Virus was incubated in fresh media on SMCs for 16 hours, after which the media was replaced with fresh growth media and incubated for an additional 56 hours (a total of 72 hours).

Immunostaining and nuclear-cytoplasmic quantification. WT and HGPS primary aortic SMCs were plated on glass coverslips in fresh growth medium for 24 hours at ~60% confluency before fixation in 3.7% formaldehyde in PBS for 1hr at room temperature. Coverslips were blocked and permeabilized for 2 hours in PBS containing 0.4% Triton X-100, 2% BSA and 50 mM NH_4Cl at room temperature. Coverslips were rinsed with PBS and primary antibody (MRTF-A: Protein Tech #21166-1-AP, 1:50 dilution) diluted in blocking buffer (PBS containing 0.4% Triton X-100, 2% BSA) was added to the coverslips and incubated at 4^{o}C overnight. Coverslips were washed in blocking buffer three times for 10 minutes each before addition of secondary antibody (Alexafluor-488 chicken anti-Rabbit Santa Cruz #A21441, 1:100; in addition to DAPI stain, 1:300) in blocking buffer for 2 hours at room temperature. Coverslips were washed three times for 10 minutes each in blocking buffer, rinsed in PBS, then dipped in water, and mounted using SlowFade Gold anti-fade agent (Thermofisher #P36930). Fluorescent images were acquired on a Nikon Eclipse inverted phase contrast microscope and captured on the QI Click Qimaging camera using QCapture Suite Plus software.

Nuclear-cytoplasmic ratios of MRTF-A were calculated using ImageJ. The nuclear boundary was traced using DAPI stain, and the tracing was added to the region of interest (ROI) manager. This nuclear tracing was then overlayed on the MRTF-A stain images, and mean pixel intensity of MRTF-A in the nucleus was recorded (mean pixel intensity = raw integrated density/area). Then, using long-exposures of MRTF-A staining

to mark cell boundary, the entire cell area was traced, and total MRTF-A raw integrated density was recorded for the entire cell. The nuclear raw integrated density of MRTF-A was then subtracted from the total cell raw integrated density to get the cytoplasmic raw integrated density of MRTF-A. The cytoplasmic raw integrated density was then divided by the cytoplasmic area (total cell area – nuclear area) to get the mean pixel intensity of MRTF-A in the cytoplasm. Nuclear-cytoplasmic ratios are the mean pixel intensity of MRTF-A in the nucleus divided by the mean pixel intensity of MRTF-A in the cytoplasm.

RT-qPCR of mRNAs. RNA was extracted from cultures of primary SMCs with TRIzol reagent (Thermofisher 15596026) according to manufacturer's instruction. Ten to fifteen percent of the cDNA was subjected to qPCR with the following primer-probe sets from Applied Biosystems: MRTF-A: Mm00461840_m1, Myh11: Mm00443013_m1, Acta2: Mm00725412_s1, Tagln: Mm00441661_g1, Cnn1: Mm00487032_m1, Lox (Mm00495386_m1), has-miR-145 (TM: 002278), SnoRNA202 (TM:001232). The primer-probe set for 18S rRNA has been described (Klein et al. 2007). qPCR samples were analyzed in duplicates. Levels of each tested transcript were normalized to 18S rRNA, and changes in RNA abundance were calculated using the ddCT method.

Immunoblotting. For tissue immunoblotting, isolated aortas were thawed, chopped into small pieces and sonicated (using a Virtis Virsonic 475 cell disruptor) in ~150 µl lysis buffer (50 mM Tris-HCl pH 8, 250 mM NaCl, 2 mM EDTA, 1% NP-40) containing protease inhibitors (Cell Signaling Technologies 5872S). Lysates were centrifuged for 5 minutes (4^{o}C, 15,000 x *g*), and the supernatants were diluted into SDS sample buffer (final concentration of 50mM Tris pH 6.8, 2% SDS, 10% glycerol, 0.01% Bromophenol

blue) with 1% β-mercaptoethanol. The samples (20-30 µg) were fractionated on 7.5% SDS polyacrylamide gels and electrophoretically transferred to nitrocellulose. Incubations with primary antibodies were performed overnight at 4^{o}C with rocking in TBST (Tris-buffered saline with 0.1% Tween 20) with 5% milk or 2% BSA. Incubation with secondary antibodies were performed for 2-hours at room temperature in the same TBST-buffer as the primary antibody. The antibodies used were: MRTF-A: Protein Tech #21166-1-AP, 1:50 dilution; GAPDH: thermofisher MA5-15738, 1:400 dilution; ECL anti-mouse IgG HRP: GE healthcare 3143, 1:500. Bound antibodies were visualized by enhanced chemiluminescence and quantified on a GE ImageQuant LAS4000.

Statistical Analysis. Statistical analysis was performed using Prism software (GraphPad), and statistical tests are defined in respective figure legends. Mann-Whitney tests or One-sample t-tests were used for comparison between two groups and two-way ANOVA was used for testing of significance throughout multiple groups.

4.6 Figures

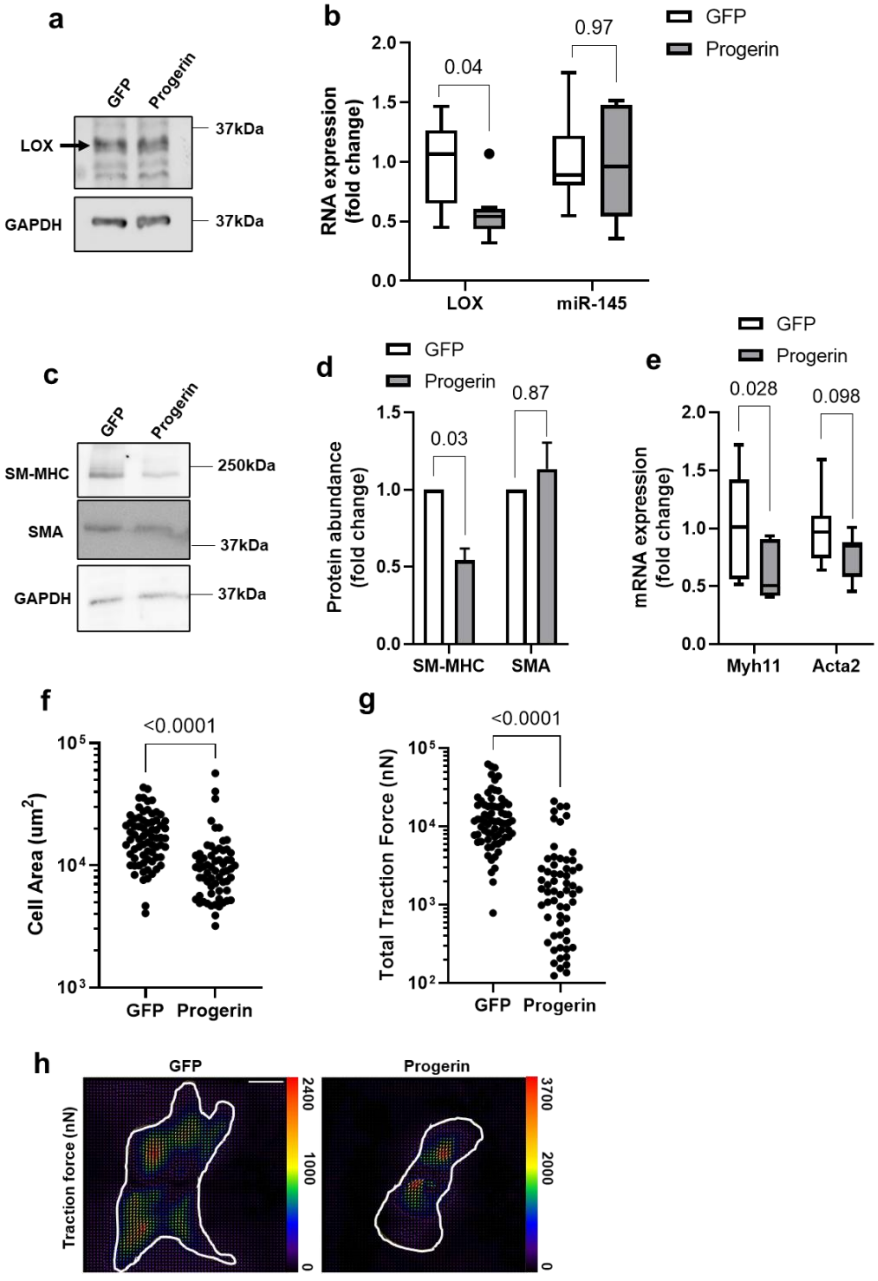

Figure 4.01. Progerin expression in WT SMCs reduces SM-MHC and force generation. Vascular SMCs isolated from 2-month WT mouse aorta were incubated

with adenovirus encoding GFP (control) or GFP-Progerin (Progerin) for 72-hours. **(A)** LOX abundance was evaluated by immunoblot from lysates of primary WT aortic SMCs incubated with adenovirus encoding GFP or GFP-Progerin. Black boxes around the immunoblots indicate cropping for removal of extraneous space (n=2). **(B)** *Lox* and miR-145 transcript levels were evaluated by RT-qPCR in primary WT aortic SMCs incubated with adenovirus encoding GFP or GFP-Progerin (n=6-8). Results displayed as box plots with Tukey bars. **(C-D)** SM-MHC (n=6) and SMA (n=4) protein abundance was evaluated by immunoblot from lysates of primary WT aortic SMCs incubated with adenovirus encoding GFP or GFP-Progerin. Results are quantified in panel D and results show mean ± SE. **(E)** *Myh11* and *Acta2* mRNA levels were evaluated by RT-qPCR in primary WT aortic SMCs incubated with adenovirus encoding GFP or GFP-Progerin (n=7-8). Results displayed as box plots with Tukey bars. **(F)** Cell area and **(G)** Total traction force plots of primary WT aortic SMCs incubated with adenovirus encoding GFP or GFP-Progerin (n=60-70 cells). **(H)** Representative traction force images of cells treated as described in panels F-G. Cell areas are outlined in white and traction force scale bars (in nanonewtons) are displayed to the right of each respective image. Optical scale bar = 50 mm. Significance in panel B, E, F, and G was determined by Mann-Whitney tests. Significance in panel D was determined by Wilcoxon signed rank test.

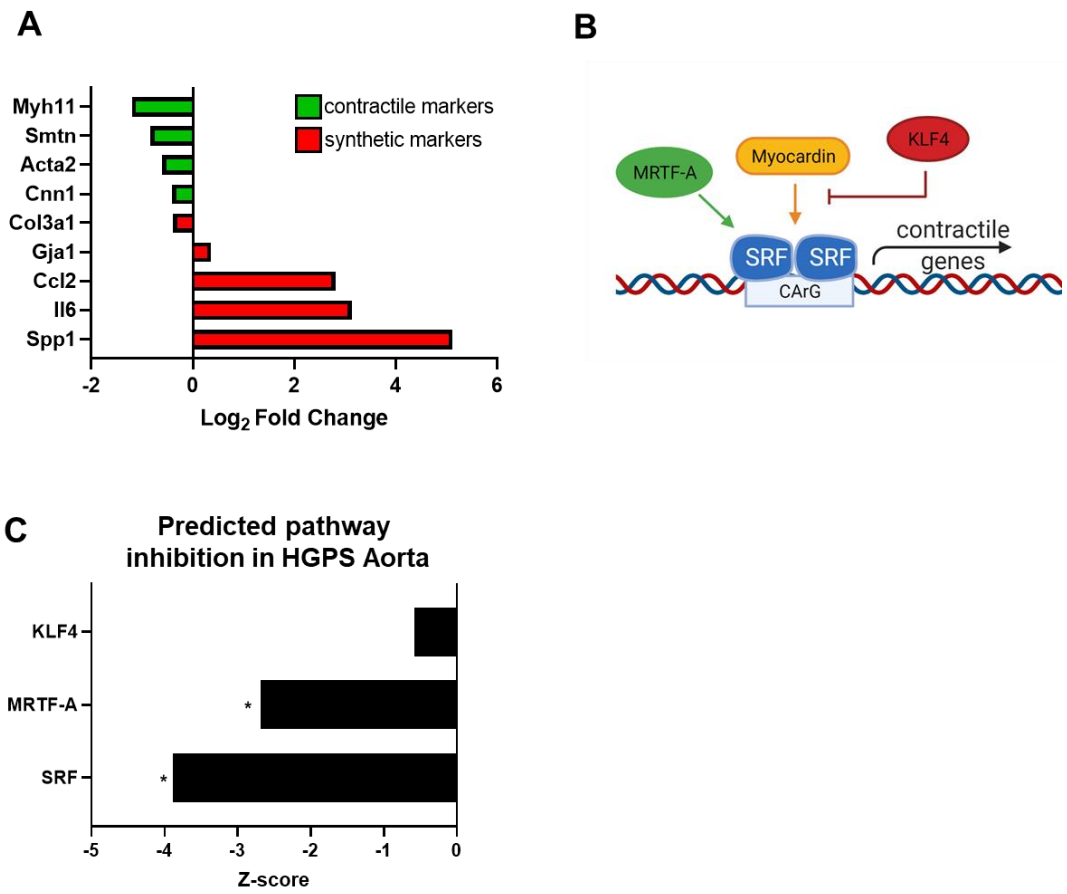

Figure 4.02. Reduced MRTF-A signature in HGPS aorta. (A) Significantly altered contractile (green) and synthetic (red) SMC markers as determined by genome-wide transcriptome analysis of WT and HGPS aortas (n=6 per genotype). **(B)** Schematic depicting serum response factor (SRF) binding to CArG elements in DNA which are responsible for the regulation of SMC contractile genes. Myocardin binding further enhances SRF transcriptional activity. SRF can be directly positively modulated by myocardin-related transcription factor A (MRTF-A) or indirectly inhibited by Kruppel like factor 4 (KLF4). **(C)** Ingenuity pathway analysis (IPA) performed on genome-wide transcriptome analysis of 2-month WT and HGPS aorta (n=6 per genotype). Negative Z-scores suggest an inhibited signature as determined from enrichment of SRF, MRTF-A,

and KLF4 target genes. Asterisk denotes a significantly inhibited pathway as determined by IPA.

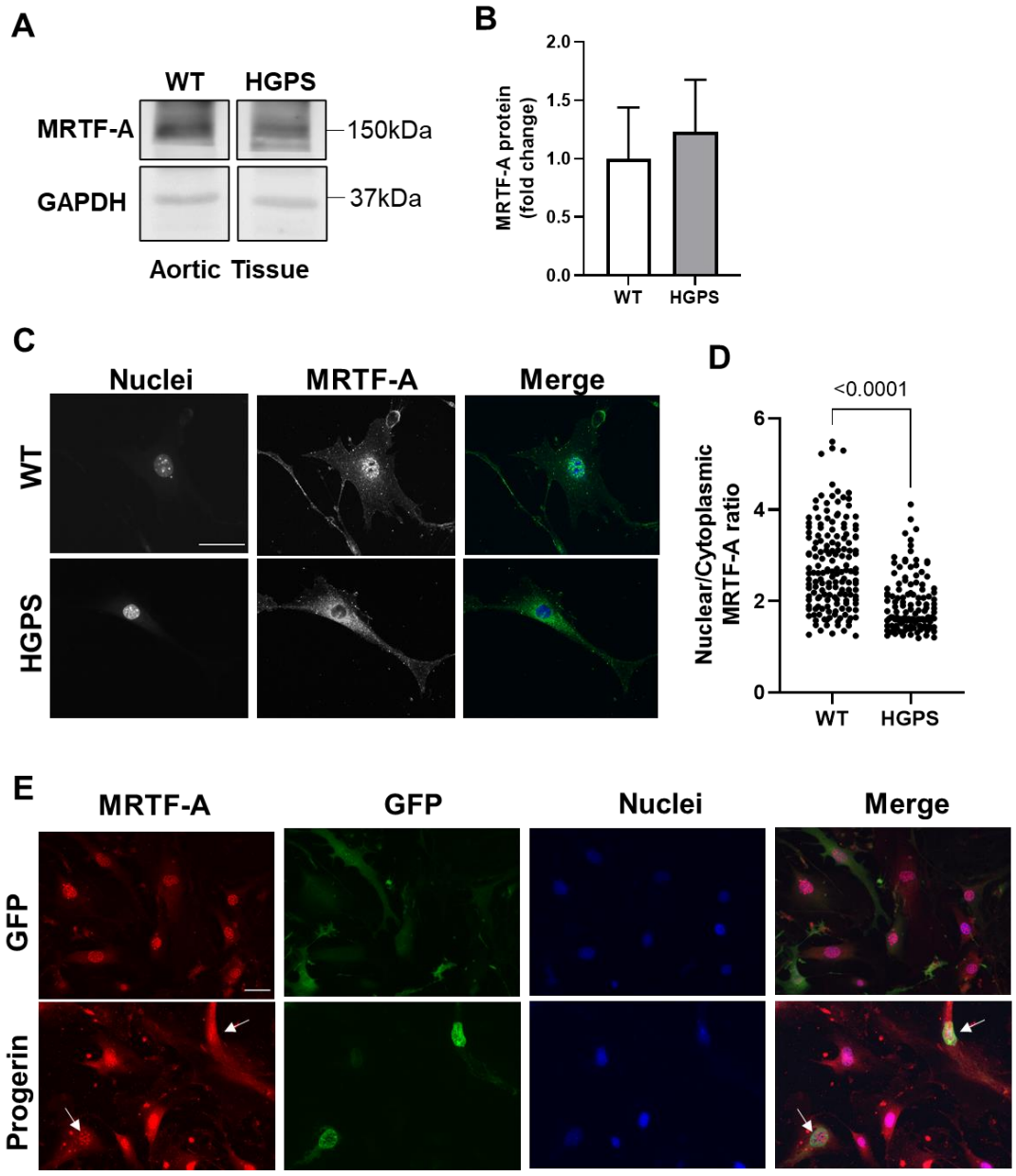

Figure 4.03. Reduced nuclear MRTF-A in HGPS smooth muscle cells (SMCs). (A-B) 2-month WT (n=3) and HGPS (n=4) aorta lysates were immunoblotted for MRTF-A and

GAPDH (loading control) and MRTF-A protein levels were quantified in panel B. Bar graph displays means ± SD **(C)** Primary aortic SMCs were isolated from 2-month WT and HGPS mice and immunostained for MRTF-A. **(D)** Quantification of nuclear-cytoplasmic MRTF-A ratio from immunostaining of WT and HGPS SMCs (n=~120-150 cells accrued over 4 independent experiments). Statistical significance determined by Mann-Whitney. **(E)** WT SMCs were incubated with adenovirus encoding GFP or GFP-Progerin for 72-hours. SMCs were immunostained for MRTF-A. White arrows point to progerin-containing nuclei to highlight the reduced nuclear MRTF-A present in progerin-expressing cells. Scale bars display 50μm. Images are representative of 2 independent experiments.

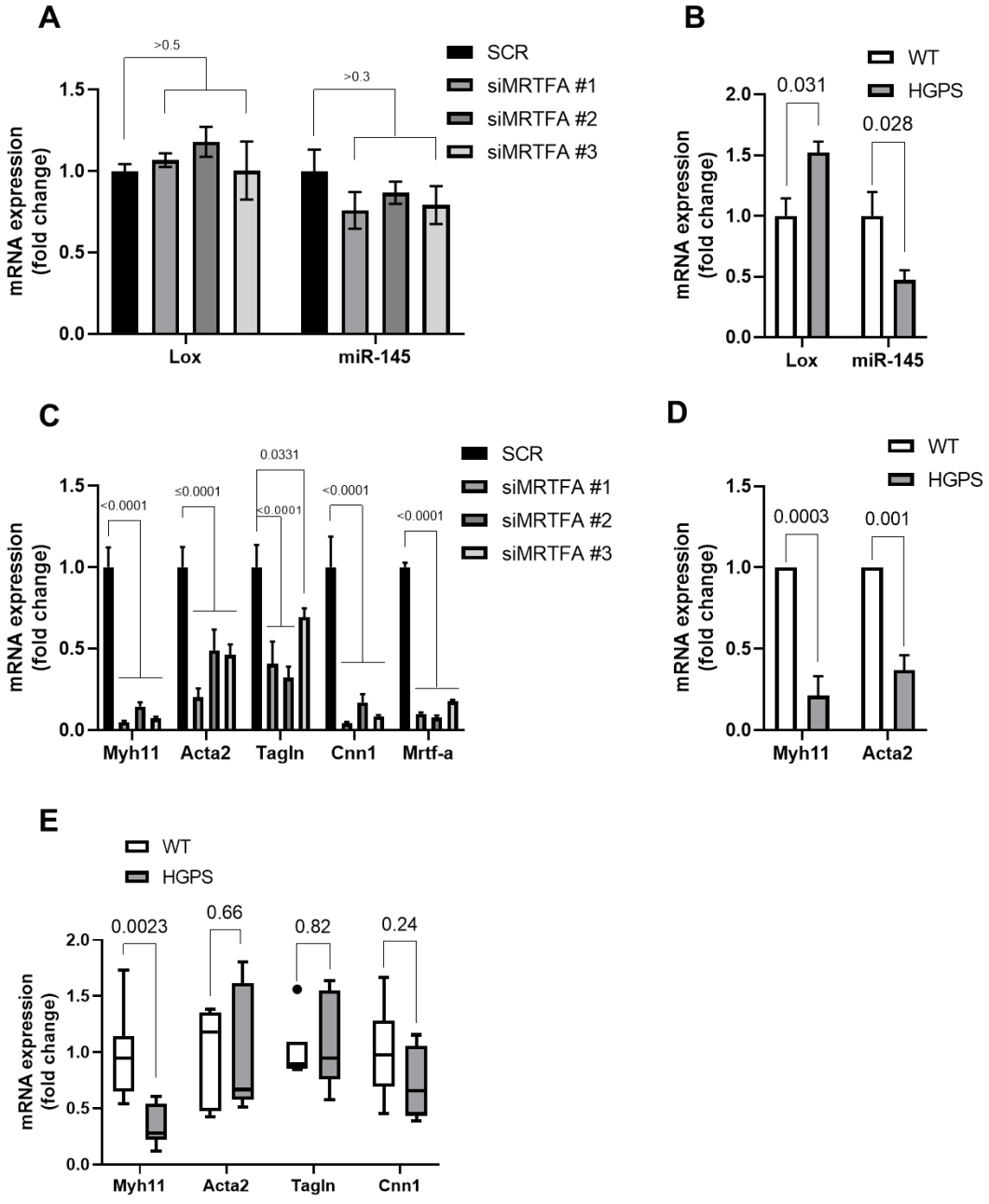

Figure 4.04. MRTF-A knockdown reduces SMC contractile gene mRNA levels. (A) WT SMCs were incubated with a scrambled (SCR, control) siRNA or three unique siRNAs toward MRTF-A for 72-hours (n=5). LOX mRNA and miR-145 expression levels

were quantified by RT-qPCR after MRTF-A knockdown and normalized to scrambled control. Statistical significance between SCR and siRNA-treated cells was determined by Two-way ANOVA with Sidak post-tests comparing each siRNA treatment to SCR control. **(B)** In an independent experiment, transcript levels of *Lox* and *miR-145* in HGPS SMCs were quantified by RT-qPCR ad normalized to WT SMC transcript levels (n=6-8). Statistical significance determined by Mann Whitney. **(C)** MRTF-A was knocked down in WT SMCs as described in panel A and mRNA levels for contractile genes were analyzed by qPCR and normalized to scrambled control. Statistical significance between SCR and siRNA-treated cells was determined by Two-way ANOVA with Sidak post-tests comparing each siRNA treatment to SCR control. **(D)** In an independent experiment, mRNA levels of *Myh11* and *Acta2* in HGPS SMCs were quantified by RT-qPCR ad normalized to WT SMC transcript levels (n=6-8). Statistical significance determined by one-sample t-test comparing to a theoretical mean of 1. **(E)** Contractile gene transcript levels in 2-month WT and HGPS aorta (reproduced from chapter 3). Statistical significance determined by Mann-Whitney.

4.7 References

Beamish JA, He P, Kottke-Marchant K & Marchant RE (2010) Molecular regulation of contractile smooth muscle cell phenotype: implications for vascular tissue engineering. *Tissue Eng. Part B. Rev.* 16, 467–91. Available at: http://www.ncbi.nlm.nih.gov/pubmed/20334504.

del Campo L, Sánchez-López A, González-Gómez C, Andrés-Manzano MJ, Dorado B & Andrés V (2020) Vascular Smooth Muscle Cell-Specific Progerin Expression Provokes Contractile Impairment in a Mouse Model of Hutchinson-Gilford Progeria Syndrome that Is Ameliorated by Nitrite Treatment. *Cells* 9, 656. Available at: https://pubmed.ncbi.nlm.nih.gov/32182706/.

del Campo L, Sánchez-López A, Salaices M, von Kleeck RA, Expósito E, González-Gómez C, Cussó L, Guzmán-Martínez G, Ruiz-Cabello J, Desco M, Assoian RK, Briones AM & Andrés V (2019) Vascular smooth muscle cell-specific progerin expression in a mouse model of Hutchinson–Gilford progeria syndrome promotes arterial stiffness: Therapeutic effect of dietary nitrite. *Aging Cell*, e12936.

Chen Z-J, Wang W-P, Chen Y-C, Wang J-Y, Lin W-H, Tai L-A, Liou G-G, Yang C-S & Chi Y-H (2014) Dysregulated interactions between lamin A and SUN1 induce abnormalities in the nuclear envelope and endoplasmic reticulum in progeric laminopathies. *J. Cell Sci.* 127.

Crisp M, Liu Q, Roux K, Rattner JB, Shanahan C, Burke B, Stahl PD & Hodzic D (2006) Coupling of the nucleus and cytoplasm: Role of the LINC complex. *J. Cell Biol.* 172, 41–53.

Cuff CA, Kothapalli D, Azonobi I, Chun S, Zhang Y, Belkin R, Yeh C, Secreto A, Assoian RK, Rader DJ & Puré E (2001) The adhesion receptor CD44 promotes atherosclerosis by mediating inflammatory cell recruitment and vascular cell activation. *J. Clin. Invest.* 108, 1031–1040.

Dahl KN & Kalinowski A (2011) Nucleoskeleton mechanics at a glance. *J. Cell Sci.* 124, 675–678. Available at: https://jcs.biologists.org/content/124/5/675.

Dahl KN, Ribeiro AJS & Lammerding J (2008) Nuclear shape, mechanics, and mechanotransduction. *Circ. Res.* 102, 1307–1318.

Dahl KN, Scaffidi P, Islam MF, Yodh AG, Wilson KL & Misteli T (2006) Distinct structural and mechanical properties of the nuclear lamina in Hutchinson-Gilford progeria syndrome. *Proc. Natl. Acad. Sci. U. S. A.* 103, 10271–6.

Davis-Dusenbery BN, Wu C & Hata A (2011) Micromanaging vascular smooth muscle cell differentiation and phenotypic modulation. *Arterioscler. Thromb. Vasc. Biol.* 31, 2370–2377.

Du KL, Chen M, Li J, Lepore JJ, Mericko P & Parmacek MS (2004) Megakaryoblastic Leukemia Factor-1 Transduces Cytoskeletal Signals and Induces Smooth Muscle Cell Differentiation from Undifferentiated Embryonic Stem Cells. *J. Biol. Chem.* 279, 17578–17586.

Eriksson M, Brown WT, Gordon LB, Glynn MW, Singer J, Scott L, Erdos MR, Robbins CM, Moses TY, Berglund P, Dutra A, Pak E, Durkin S, Csoka AB, Boehnke M, Glover TW & Collins FS (2003) Recurrent de novo point mutations in lamin A cause Hutchinson-Gilford progeria syndrome. *Nature* 423, 293–298.

Goldman RD, Shumaker DK, Erdos MR, Eriksson M, Goldman AE, Gordon LB, Gruenbaum Y, Khuon S, Mendez M, Varga R & Collins FS (2004) Accumulation of

mutant lamin A progressive changes in nuclear architecture in Hutchinson-Gilford progeria syndrome. *Proc. Natl. Acad. Sci. U. S. A.* 101, 8963–8968.

Grootaert MOJ & Bennett MR (2021) Vascular smooth muscle cells in atherosclerosis: time for a re-assessment. *Cardiovasc. Res.*

Guettler S, Vartiainen MK, Miralles F, Larijani B & Treisman R (2008) RPEL Motifs Link the Serum Response Factor Cofactor MAL but Not Myocardin to Rho Signaling via Actin Binding. *Mol. Cell. Biol.* 28, 732–742.

Gurbuz I, Ferralli J, Roloff T, Chiquet-Ehrismann R & Asparuhova MB (2014) SAP domain-dependent Mkl1 signaling stimulates proliferation and cell migration by induction of a distinct gene set indicative of poor prognosis in breast cancer patients. *Mol. Cancer* 13, 22.

Hamczyk M, del Campo L & Andrés V (2018) Aging in the Cardiovascular System: Lessons from Hutchinson-Gilford Progeria Syndrome. *Annu. Rev. Physiol.* 80, 27–48.

Hao H, Gabbiani G & Bochaton-Piallat ML (2003) Arterial smooth muscle cell heterogeneity: Implications for atherosclerosis and restenosis development. *Arterioscler. Thromb. Vasc. Biol.* 23, 1510–1520.

Hathaway DR, March KL, Lash JA, Adam LP & Wilensky RL (1991) Vascular smooth muscle. A review of the molecular basis of contractility. *Circulation* 83, 382–90.

Ho CY, Jaalouk DE, Vartiainen MK & Lammerding J (2013) Lamin A/C and emerin regulate MKL1-SRF activity by modulating actin dynamics. *Nature* 497, 507–513.

Jeon ES, Park WS, Lee MJ, Kim YM, Han J & Kim JH (2008) A rho kinase/myocardin-related transcription factor-a-dependent mechanism underlies the sphingosylphosphorylcholine-induced differentiation of mesenchymal stem cells into

contractile smooth muscle cells. *Circ. Res.* 103, 635–642.

Kelley JB, Datta S, Snow CJ, Chatterjee M, Ni L, Spencer A, Yang C-S, Cubenas-Potts C, Matunis MJ & Paschal BM (2011) The Defective Nuclear Lamina in Hutchinson-Gilford Progeria Syndrome Disrupts the Nucleocytoplasmic Ran Gradient and Inhibits Nuclear Localization of Ubc9. *Mol. Cell. Biol.* 31, 3378–3395.

Kim PH, Luu J, Heizer P, Tu Y, Weston TA, Chen N, Lim C, Li RL, Lin P-Y, Dunn JCY, Hodzic D, Young SG & Fong LG (2018) Disrupting the LINC complex in smooth muscle cells reduces aortic disease in a mouse model of Hutchinson-Gilford progeria syndrome. *Sci. Transl. Med.* 10, eaat7163.

Kim S, Ip HS, Lu MM, Clendenin C & Parmacek MS (1997) A serum response factor-dependent transcriptional regulatory program identifies distinct smooth muscle cell sublineages. *Mol. Cell. Biol.* 17, 2266–2278.

von Kleeck R, Roberts E, Castagnino P, Bruun K, Brankovic SA, Hawthorne EA, Xu T, Tobias JW & Assoian RK (2021) Arterial stiffness and cardiac dysfunction in Hutchinson–Gilford Progeria Syndrome corrected by inhibition of lysyl oxidase. *Life Sci. Alliance* 4, e202000997.

Klein EA, Yung Y, Castagnino P, Kothapalli D & Assoian RK (2007) Cell Adhesion, Cellular Tension, and Cell Cycle Control. *Methods Enzymol.* 426, 155–175.

Lee RT, Yamamoto C, Feng Y, Potter-Perigo S, Briggs WH, Landschulz KT, Turi TG, Thompson JF, Libby P & Wight TN (2001) Mechanical Strain Induces Specific Changes in the Synthesis and Organization of Proteoglycans by Vascular Smooth Muscle Cells. *J. Biol. Chem.* 276, 13847–13851.

Li L, Miano JM, Cserjesi P & Olson EN (1996) SM22α, a marker of adult smooth muscle, is expressed in multiple myogenic lineages during embryogenesis. *Circ. Res.* 78,

188–195.

Long X, Bell RD, Gerthoffer WT, Zlokovic B V. & Miano JM (2008) Myocardin Is Sufficient for a Smooth Muscle-Like Contractile Phenotype. *Arterioscler. Thromb. Vasc. Biol.* 28.

Mack CP & Owens GK (1999) Regulation of smooth muscle α-actin expression in vivo is dependent on CArG elements within the 5' and first intron promoter regions. *Circ. Res.* 84, 852–861.

Martino F, Perestrelo AR, Vinarský V, Pagliari S & Forte G (2018) Cellular mechanotransduction: From tension to function. *Front. Physiol.* 9, 824.

Merideth MA, Gordon LB, Clauss S, Sachdev V, Smith ACM, Perry MB, Brewer CC, Zalewski C, Kim HJ, Solomon B, Brooks BP, Gerber LH, Turner ML, Domingo DL, Hart TC, Graf J, Reynolds JC, Gropman A, Yanovski JA, Gerhard-Herman M, Collins FS, Nabel EG, Cannon RO, Gahl WA & Introne WJ (2008) Phenotype and Course of Hutchinson–Gilford Progeria Syndrome. *N. Engl. J. Med.* 358, 592–604.

Miano JM (2003) Serum response factor: Toggling between disparate programs of gene expression. *J. Mol. Cell. Cardiol.* 35, 577–593.

Mu X, Tseng C, Hambright WS, Matre P, Lin C, Chanda P, Chen W, Gu J, Ravuri S, Cui Y, Zhong L, Cooke JP, Niedernhofer LJ, Robbins PD & Huard J (2020) Cytoskeleton stiffness regulates cellular senescence and innate immune response in Hutchinson–Gilford Progeria Syndrome. *Aging Cell* 19, e13152.

Olive M, Harten I, Mitchell R, Beers JK, Djabali K, Cao K, Erdos MR, Blair C, Funke B, Smoot L, Gerhard-Herman M, Machan JT, Kutys R, Virmani R, Collins FS, Wight TN, Nabel EG & Gordon LB (2010) Cardiovascular Pathology in Hutchinson-Gilford Progeria: Correlation With the Vascular Pathology of Aging. *Arterioscler. Thromb.*

Vasc. Biol. 30.

Onoue N, Nawata J, Tada T, Zhulanqiqige D, Wang H, Sugimura K, Fukumoto Y, Shirato K & Shimokawa H (2008) Increased Static Pressure Promotes Migration of Vascular Smooth Muscle Cells: Involvement of the Rho-kinase Pathway. *J. Cardiovasc. Pharmacol.* 51, 55–61.

Osmanagic-Myers S, Kiss A, Manakanatas C, Hamza O, Sedlmayer F, Szabo PL, Fischer I, Fichtinger P, Podesser BK, Eriksson M & Foisner R (2018) Endothelial progerin expression causes cardiovascular pathology through an impaired mechanoresponse. *J. Clin. Invest.* 129, 531–545.

Osorio FG, Navarro CL, Cadinanos J, Lopez-Mejia IC, Quiros PM, Bartoli C, Rivera J, Tazi J, Guzman G, Varela I, Depetris D, de Carlos F, Cobo J, Andres V, De Sandre-Giovannoli A, Freije JMP, Levy N & Lopez-Otin C (2011) Splicing-Directed Therapy in a New Mouse Model of Human Accelerated Aging. *Sci. Transl. Med.* 3, 106ra107-106ra107.

Owens GK, Kumar MS & Wamhoff BR (2004) Molecular regulation of vascular smooth muscle cell differentiation in development and disease. *Physiol. Rev.* 84, 767–801.

Rensen SSM, Doevendans PAFM & van Eys GJJM (2007a) Regulation and characteristics of vascular smooth muscle cell phenotypic diversity. *Neth. Heart J.* 15, 100–8.

Rensen SSM, Doevendans PAFM & van Eys GJJM (2007b) Regulation and characteristics of vascular smooth muscle cell phenotypic diversity. *Neth. Heart J.* 15, 100–8.

Rzucidlo EM, Martin KA & Powell RJ (2007) Regulation of vascular smooth muscle cell differentiation. *J. Vasc. Surg.* 45, A25–A32.

De Sandre-Giovannoli A, Bernard R, Cau P, Navarro C, Amiel J, Boccaccio I, Lyonnet S, Stewart CL, Munnich A, Le Merrer M & Lévy N (2003) Lamin A truncation in Hutchinson-Gilford progeria. *Science (80-.).* 300, 2055.

Saxena S & Kumar S (2020) Pharmacotherapy to gene editing: potential therapeutic approaches for Hutchinson–Gilford progeria syndrome. *GeroScience* 42, 467–494.

Sinha JK, Ghosh S & Raghunath M (2014) Progeria: A rare genetic premature ageing disorder. *Indian J. Med. Res.* 139, 667–674.

Sit B, Feng Z, Xanthis I, Marhuenda E, Zingaro S, Shanahan C, Jones GE, Yu CH & Iskratsch T (2020) Matrix stiffness and blood pressure together regulate vascular smooth muscle cell phenotype switching and cofilin dependent podosome formation. *bioRxiv*, 2020.12.27.424498.

Takahashi Y, Hiratsuka S, Machida N, Takahashi D, Matsushita J, Hozak P, Misteli T, Miyamoto K & Harata M (2020) Impairment of nuclear F-actin formation and its relevance to cellular phenotypes in Hutchinson-Gilford progeria syndrome. *Nucleus* 11, 250–263.

Talwar S, Kant A, Xu T, Shenoy V & Assoian RK (2021) Mechanosensitive smooth muscle cell phenotypic plasticity emerging from a null state and the balance between Rac and Rho. *Cell Rep 35, 3.*

Verstraeten VLRM, Ji JY, Cummings KS, Lee RT & Lammerding J (2008) Increased mechanosensitivity and nuclear stiffness in Hutchinson-Gilford progeria cells: effects of farnesyltransferase inhibitors. *Aging Cell* 7, 383–93.

Wang Y, Cao W, Cui J, Yu Y, Zhao Y, Shi J, Wu J, Xia Z, Yu B & Liu J (2018) Arterial Wall Stress Induces Phenotypic Switching of Arterial Smooth Muscle Cells in Vascular Remodeling by Activating the YAP/TAZ Signaling Pathway. *Cell. Physiol.*

Biochem. 51, 842–853.

Webb RC (2003) Smooth muscle contraction and relaxation. In *American Journal of Physiology - Advances in Physiology Education*. American Physiological Society, pp.201–206.

Chapter 5: Discussion and future directions

5.1 Overview

Although the genetic basis of the mutation causing Hutchinson-Gilford Progeria Syndrome (HGPS) has been well studied, how this mutation severely affects the vasculature, and in particular the vascular smooth muscle cell (SMC) population, has remained elusive. The HGPS vasculature has been characterized as a collagen-dense, fibrotic environment with a significant loss of SMCs from the medial layer of large arteries (Gerhard-Herman et al. 2011; Merideth et al. 2008; Olive et al. 2010). HGPS children are highly susceptible to accumulation of atherosclerotic plaques in which vessel occlusion or plaque rupture leads to heart attack or stroke (Gerhard-Herman et al. 2011; Merideth et al. 2008; Olive et al. 2010). So far, the link between the progressive cardiovascular disease in HGPS and progerin, the mutated Lamin A protein, has not been functionally characterized.

In Chapter 2 of this thesis, I evaluated the progressive arterial stiffening that takes place in HGPS by using a mouse model to study the disease. I found that arterial stiffening takes place much earlier than others have reported - before the onset of severe HGPS phenotypes such as SMC depletion (del Campo et al. 2019; Murtada et al. 2020). Instead of arterial stiffness originating from high abundance of collagens like has been reported in aged HGPS mice (del Campo et al. 2019; Murtada et al. 2020), I found that arterial stiffening at an early timepoint correlates with an upregulation of the collagen cross-linking enzyme lysyl oxidase (LOX). Furthermore, I found that HGPS arteries and SMCs present with decreased miR-145, a known regulator of LOX transcript levels, and restoration of miR-145 reduced LOX expression in HGPS SMCs to WT levels. Intriguingly, in addition to regulating LOX expression, miR-145 is also a marker of the

contractile phenotype of SMCs. Decreased miR-145 led me to hypothesize that HGPS SMCs may exist in a less contractile, or synthetic, state in HGPS arteries.

Thus, in Chapter 3, I characterized arterial contractility at the same timepoint I reported increased arterial stiffening in HGPS. Interestingly, HGPS arteries present with decreased contractile ability at an early age of 2-months, and the decreased contraction of HGPS arteries is likely not due to increased arterial stiffness, as reducing arterial stiffness did not restore vessel contractility. Rather, transcriptome profiling of HGPS aortas revealed a decrease in expression of the SMC contractile machinery – especially that of smooth muscle myosin heavy chain (SM-MHC), which was one of the most down-regulated contractile genes in the analysis. Isolated primary HGPS SMCs showed reduced force generation, and restoration of SM-MHC corrected traction force to near WT levels.

In preliminary findings in Chapter 4, I show that reduced traction force and decreased SM-MHC, but not miR145 or LOX regulation, are direct effects of progerin. This finding prompted me to explore the MRTF-A signaling pathway as a potential explanation for how progerin may be altering contractile gene expression. My bioinformatic analysis of transcriptome-wide profiling in HGPS aortas showed a decreased MRTF-A target-gene signature, and this correlated with a decreased nuclear-cytoplasmic ratio of MRTF-A in isolated HGPS SMCs. Knockdown of MRTF-A in WT SMCs resulted in decreased expression of many SMC contractile genes but did not perfectly recapitulate the selective decrease in SM-MHC seen in HGPS SMCs. These results suggest that other signaling pathways in addition to MRTF-A must also be at play to downregulate SM-MHC. Furthermore, reduced MRTF-A does not alter LOX mRNA or

miR-145 expression, so there must be additional pathways independently promoting arterial stiffening and decreased contractility in HGPS (Fig. 5.01).

The following sections of the discussion will focus on the topics of arterial stiffening and contractility in HGPS to discuss potential future directions for this work as well as outstanding questions that still remain to be addressed in the field of HGPS cardiovascular biology. Lastly, I will touch on the similarities and differences I have found between premature aging and natural aging, and what our understanding of HGPS may mean for insights into arterial stiffening in the aging population.

5.2 Arterial stiffening in HGPS

Arterial stiffening is a major cholesterol-independent risk factor for cardiovascular disease that increases naturally with age (Mitchell et al. 2010). Increased arterial stiffness is associated with impaired lung function, slower gait speed, and diminishing physical functioning in day-to-day life (Laurent et al. 2019). Although genetic factors certainly dictate arterial stiffening (Laurent et al. 2005; Lacolley et al. 2009; Logan et al. 2015), environmental factors such as aerobic fitness condition, low body fat, low cholesterol, and low salt are associated with decreased arterial stiffening in populations around the world (Laurent et al. 2019). However, understanding genetic predisposition to arterial stiffening will help to develop targeted therapeutics to reduce arterial stiffening in both HGPS as well as natural and ultimately reduce the burden of cardiovascular disease.

In the case of HGPS, progerin expression specifically in the vascular SMC population has been connected to the elevated arterial stiffness (del Campo et al. 2019). Intriguingly, mice expressing progerin under an endothelial-specific promotor did not develop arterial stiffening (del Campo et al. 2019), suggesting a specific role for the SMC population. Furthermore, collagenase degradation of the arterial matrix *ex vivo* resulted in a reduction in arterial stiffening in HGPS mice, indicating a role for collagens in the stiffening of HGPS vessels (del Campo et al. 2019). In collaboration with del Campo et al. (2019), I observed an increase in collagens-III, IV, V, and XII in 14-week HGPS mice. However, the increased collagens in HGPS mouse arteries were reported in vessels near the end of the HGPS mouse lifespan, but work reported in this thesis is the first to analyze mice at a very early timepoint before the onset of serious HGPS pathology. Interestingly, I found arterial stiffening in HGPS begins with increased expression of LOX rather than the canonically expected increase in fibrillar collagens. LOX has not been previously implicated in HGPS pathology. Collectively, my results and those of del Campo et al. (2019) indicate that, while collagen abundance may increase during the HGPS mouse lifespan, initial arterial stiffening is due to increased collagen cross-linking.

Although I have demonstrated that LOX is a key protein in promoting the initial arterial stiffening of HGPS, LOX inhibition with BAPN did not fully reduce circumferential stiffness of HGPS arteries to WT levels, suggesting that additional ECM remodeling events are contributing to the stiffening process. Future work to characterize changes in ECM composition, advanced glycosylation end products, proteoglycans, and other cross-linking enzymes such as transglutaminases, all of which have been associated with increased tissue stiffening (Steppan et al. 2017; Oh et al. 2017; Goldin et al. 2006;

Barkovskaya et al. 2020; Chen et al. 2020), will help to provide a more thorough picture of arterial stiffening in HGPS. Additional work elucidating the initiation of arterial stiffening would benefit from unbiased proteomics methods to understand how the ECM composition changes over time and correlate changes in ECM protein abundance with myographic analysis of HGPS arteries in a time-course manner. Pairing a time course of bi-weekly myography with proteomic analyses of the ECM of HGPS arteries would allow for correlation of proteins that are associated with arterial stiffening. Although we used genome-wide transcriptome profiling to infer altered ECM proteins, future studies should focus on using proteomic approaches to understand ECM composition as transcript levels do not always correlate with ECM deposition, as I observed in aged WT aorta which displayed low LOX transcript but high LOX protein abundance.

In addition to aberrant ECM, HGPS SMCs could also be contributing to a stiffer microenvironment through increased cellular stiffness. Indeed, it has been shown that arterial stiffness in aged monkeys is correlated with increased stiffness of isolated SMCs from aged monkeys (Sehgel et al. 2015; Qiu et al. 2007; Qiu et al. 2010). However, as cells are delicately entwined in their microenvironment, the contribution of cells versus ECM may be hard to tease out. Work not shown in this thesis attempting to pressurize decellularized carotids using pressure myography was unsuccessful, as vessels either ruptured or developed large leaks upon pressurization.

Although I have identified the deregulated miR-145-LOX expression as causal for arterial stiffening in HGPS mice, an essential question that remains is how progerin expression is causing deregulation of this pathway and increased LOX abundance. As reported in Chapter 4, I surprisingly saw that acute progerin expression in WT SMCs did

not alter miR-145 levels or change LOX protein abundance. This likely suggests that the altered miR-145-LOX signaling is either due to cell extrinsic mechanisms or the long-term presence of progerin during development. Additionally, the altered miR-145-LOX abundance in HGPS is likely not due to the signaling or communication from other arterial cell types, such as endothelial cells, as primary cultured SMCs also displayed increased LOX mRNA in the absence of other cell types normally present in arteries.

A potential hypothesis for the deregulated miR145-LOX pathway in HGPS is that the ECM deposited by HGPS SMCs may influence the high LOX expression. Growing HGPS SMCs on ECM derived from WT SMCs or vice versa would help to evaluate whether the ECM influences LOX abundance. In addition, circulating factors in HGPS mice and patients may impact LOX levels. Bloodwork from HGPS mice evaluating transforming growth factor-β (TFG-β), platelet derived growth factor (PDGF), or glucose levels may provide insight as all have been shown to regulate LOX (Fang et al. 2016; Green et al. 1995; Chronopoulos et al. 2010). However, whether these signaling pathways are miR-145 dependent or independent have yet to be evaluated.

An additional overarching question that remains is why are HGPS SMCs stiffening their environment, and is this possibly a beneficial adaptation? The nuclei of HGPS cells are brittle and fragile, as has been previously reported in HGPS skin fibroblasts (Verstraeten et al. 2008). Kim et al. (2018) have shown that HGPS SMCs are more susceptible to DNA damage and death due to biaxial strain. I hypothesize that in order to protect the fragile nucleus from the constant strain of pulsatile blood flow on the arterial network, HGPS SMCs may be secreting and remodeling the ECM to stiffen the environment and reduce the amount of strain. Thus, this arterial stiffening seen in HGPS

might be a protective mechanism to preserve the fragile HGPS SMCs for an extended period of time. To test this hypothesis, it would be of interest to reduce arterial stiffening, either with BAPN or new generation LOX-inhibitors (see below), and evaluate the progressive loss of SMCs with arterial softening. If increased matrix stiffness is a protective mechanism for HGPS SMCs to survive longer, decreasing arterial stiffness would place the HGPS SMCs under increased strain as the artery circumferentially distends more due to pulsatile blood flow, causing SMC loss at an earlier timepoint. Although the cardiovascular community generally regards arterial stiffening as a co-morbidity during normal aging, it is worth considering that arterial stiffening may be playing a protective role in pathological genetic conditions such as HGPS. As such, it is critical to consider the negative impacts of arterial softening just as much as the beneficial effects.

Interestingly, I did not observe that reducing arterial stiffness through chronic BAPN administration extends lifespan in HGPS mice. Aside from the simple explanation that arterial stiffness has little influence on lifespan in HGPS, alternative explanations and potential future directions merit further exploration. The toxic side effects of BAPN, as discussed in Chapter 2, may offset the beneficial effects of reducing arterial stiffness. A new pan-LOX inhibitor, PXS-5505, has recently passed Phase 1 clinical trials with an excellent safety profile (How et al. 2020). Using a daily dosing regimen of PXS-5505 in place of BAPN would eliminate the uncertainties caused by the toxicity of BAPN.

An additional complication when studying HGPS mouse survival after arterial softening is that mice are highly resistant to develop and die of cardiovascular disease. For example, to study atherosclerosis in mice, the field has used Apolipoprotein E

(Apoe) null or Low-density lipoprotein receptor (LDLR) deletion to generate non-HDL hyperlipidemia in mice (Getz & Reardon 2012). Indeed, HGPS mice on the Apoe-null background and HGPS mice expressing progerin driven under a SMC-specific promotor on the Apoe-null background developed more severe atherosclerosis and died earlier than control Apoe-null mice (Hamczyk, Villa-Bellosta, et al. 2018). Interestingly, our lab has shown that treating Apoe-null mice with BAPN and reducing arterial stiffness significantly reduced monocyte recruitment and lesion area in aortas (Kothapalli et al. 2012; Liu et al. 2019). It may be of interest to understand if reducing arterial stiffness can prolong the lifespan of HGPS mice on the Apoe-null background. However, as LDL-cholesterol is not altered in human HGPS patients (Szamosi et al. 1984; Gordon et al. 2005), studying mice on an Apoe-null background may not provide a certain explanation for what is happening in the human syndrome. Newer animal models such as minipigs and monkeys, which have more human-like lipoprotein profiles (Getz & Reardon 2012), have now been developed to study HGPS (Dorado et al. 2019; Wang et al. 2020). Although arterial stiffening and cardiovascular disease have not been fully characterized in these models yet, they may provide a more similar phenotype to the human syndrome.

Lastly, I may have not observed BAPN-induced increases in HGPS mouse lifespan because HGPS mice may not be dying from cardiovascular consequences. In fact, the cause of death in $LMNA^{G609/G609G}$ HGPS mice is not well understood. Recently, Kreienkamp (2019) showed that HGPS mice succumb to starvation and cachexia, and placing HGPS mice on a high-fat diet increased lifespan and further exacerbated cardiovascular pathology as HGPS mice lived longer (Kreienkamp et al. 2019).

Reducing arterial stiffness may have not improved lifespan because HGPS mice were dying from starvation and cachexia before the onset of severe cardiovascular complications. Placing HGPS mice on a high-fat diet and performing chronic BAPN or PXS-5505 administration may provide a better way to understand how reducing arterial stiffness can benefit the cardiovascular system as HGPS mice display more overt cardiovascular phenotypes the longer they survive (Kreienkamp et al. 2019). However, as in all pharmacology, drug administration will be a delicate balance about finding the proper therapeutic window. The LOX inhibitor dose and regimen must be sufficient to reduce arterial stiffness but not induce aorta rupture or aortic aneurysm (consequences of long-term BAPN administration (Ren et al. 2016)) or have other systemic effects.

5.3 Arterial contractility in HGPS

My studies show that the decreased arterial contractility of HGPS arteries is a very early event which precedes the loss of SMCs from the large arteries. Although others have demonstrated decreased arterial contractility, they have done so at a late stage in the lifespan of HGPS mice where decreased SMC number and additional HGPS pathologies complicate the cause of reduced contractility (del Campo et al. 2020; Murtada et al. 2020). Because HGPS arteries presented with severe arterial stiffening at the early timepoint in which we evaluated contractility, I hypothesized that increased arterial stiffness may prevent HGPS arteries from properly contracting. However, reducing arterial stiffness by BAPN treatment did not restore arterial contractility in response to KCl. Thus, the reduction in contractility observed in HGPS mice is likely not

due to increased arterial stiffness. An alternative hypothesis is that reduced contractility in HGPS arteries is instead due to altered SMC force generation. Supporting this hypothesis, I found that primary HGPS SMCs are defective for expression of SMC contractility genes (particularly *Myh11*), that they show decreased force generation by traction force microscopy, and that overexpression of SM-MHC increased traction force. As a further study, it would be of interest to mate HGPS mice with SM-MHC transgenic mice to understand if restoration of SM-MHC can restore arterial contractility *in vivo*, and if rescuing the reduced contractility observed in HGPS corrects any pathologies that are typically found in the disease.

However, it is worth noting that forced expression of SM-MHC did not completely restore traction force of HGPS SMCs to WT levels, suggesting that defective expression of contractile proteins other than SM-MHC may also contribute to the phenotype. In Chapter 3, I mention that genes such as MYL9, the smooth muscle myosin light chain, and MYLK, the smooth muscle myosin light chain kinase, are also reduced in HGPS arteries, although not to the same extent as SM-MHC. Indeed, the majority of genes that appeared in the SMC contractility category from KEGG analysis of transcriptome-wide profiling of aortas were downregulated in HGPS aortas. Intriguingly those profiling results also indicated that the mRNA levels of ADRA1D, the alpha-1D adrenergic receptor, was downregulated to a similar extent as SM-MHC in HGPS arteries. Although I used a vasoconstrictor that acts through membrane depolarization (KCl) and not G-protein signaling to evaluate arterial contractility in HGPS, it may be of interest to study if HGPS mice and children have a reduced response to adrenergic signaling due to decreased abundance of ADRA1D.

One major additional question that remains is why the reduction in SM-MHC is restricted to the vascular SMC population, as intestine and bladder tissue (which also contain SMCs) did not show a reduction in SM-MHC, nor do HGPS children show any serious issues with either organ. I had originally hypothesized that this was likely due to the high mechanical stress that vascular SMCs are under in comparison to other SMC types in the body. As strain propagates mechanical information to vascular SMCs through mechanotransduction (Goldschmidt et al. 2001), including information about the expression of contractile genes (Reusch et al. 1997; Reusch et al. 1996), it could be that progerin's role in interrupting mechanotransduction signaling (Dahl et al. 2006; Verstraeten et al. 2008) has a bigger effect in tissues that are undergoing the highest amounts of mechanical stress. However, an issue complicating this interpretation is that acute progerin expression in primary cultured SMCs, which are not subjected to cyclic strain, also expressed decreased levels of SM-MHC (Chapter 4). It is possible that vascular SMCs may be inherently different and more susceptible to progerin expression than other SMC types.

Intriguingly, HGPS mice expressing a dominant negative KASH domain under a SMC-specific promoter, thus disrupting the LINC complex in SMCs *in vivo*, do not display the typical arterial fibrosis and SMC loss, suggesting that progerin's role in altering nuclear mechanotransduction is critical to the HGPS phenotype (Kim et al. 2018). It would be of interest to see if these HGPS mice expressing the dominant negative KASH have restored arterial expression of *Myh11* mRNA and contractility. This would link the decreased SM-MHC to disrupted mechanosensing in HGPS vascular

SMCs as well as provide insight into a possible mechanism of how progerin is causing altered contractility.

HGPS pathology may be associated with abundance of progerin, as disease progression in homozygous progerin mice is much faster than that of heterozygous progerin mice. Lamin A expression scales with tissue stiffness, and tissues subjected to high levels of mechanical stress tend to have higher levels of Lamin A (Swift et al. 2013). It would be of interest to compare Lamin A, and thus progerin, expression levels between different subtypes of SMCs to understand if the vascular SMC population inherently produces more Lamin A, or progerin, than other subtypes, potentially explaining why they are more susceptible. Indeed, Kim et al. (2018) found that the aorta had one of the highest levels of Lamin A expression in comparison to other tissue types (Kim et al. 2018).

Although it may be that HGPS pathology is associated with progerin abundance, it is also possible that presence of WT Lamin A can protect against progerin's effects, which could explain why heterozygous progerin mice develop pathology more slowly. Interestingly, de la Rosa (2013) et al. found that mosaic mice in which approximately 50% of the cells were deficient for ZMPSTE24, the enzyme critical for pre-Lamin A processing (see Introduction), develop normally and do not possess a progeria phenotype (whereas full ZMPSTE24 knockout mice develop a severe progeria phenotype). ZMPSTE24 knockout fibroblasts, which normally have a slower proliferation rate, thrived when co-cultured with WT fibroblasts. Mosaic mice did not display changes in tissue health or plasma concentrations of IGF1 or blood glucose, which were significantly lowered in ZMPSTE24 knockout mice (De La Rosa et al. 2013). These

results suggest that extrinsic factors from healthy Lamin A-expressing cells may protect against the detrimental effects of prelamin-A-expressing cells. This idea provides exciting opportunities for gene-editing techniques, in which a long-term disadvantage has been their inability to incorporate into a large number of cells in the body (Koblan et al. 2021; Santiago-Fernández et al. 2019; Beyret et al. 2019). De la Rosa et al. (2013) demonstrated that it may be possible to alleviate the progeria phenotype by correcting the mutation in just half of the body's cells.

In Chapter 4, I show that decreased nuclear MRTF-A may be responsible for reducing many contractility genes in HGPS SMCs, but why SM-MHC is downregulated more than others remains a question to be answered. Epigenetic silencing of specific contractile genes may provide an explanation for the selective decrease. It may be of value to understand the methylation status of the *Myh11* promoter or enhancer regions at upstream CpG islands. Additionally, it is possible that the *Myh11* promoter or enhancers, which have been shown to be critical for transcription of the gene (Manabe & Owens 2001; Madsen et al. 1997), may have altered histone modifications . Furthermore, genes associated with the nuclear lamina are highly heterochromatic and generally silenced (van Steensel & Belmont 2017; Bank & Gruenbaum 2011; Shevelyov & Ulianov 2019). It would be of interest to see if the region of chromatin containing the *Myh11* gene has an altered association with the nuclear lamina in HGPS, as chromatin association studies with progerin have revealed highly altered binding in HGPS dermal fibroblasts (Köhler et al. 2020).

It would also be beneficial to evaluate arterial contractility and SM-MHC abundance in mice treated with the only FDA-approved therapy for HGPS – Lonafarnib

(Voelker 2021). Lonafarnib is a farnesyltransferase inhibitor that restores genome organization and corrects nuclear blebbing in HGPS fibroblasts (Bikkul et al. 2018; Gabriel et al. 2017). In clinical trials, lonafarnib reduced pulse-wave velocity measurements of arterial stiffness, and decreased carotid artery wall echo density (Gordon et al. 2018). Lonafarnib is predicted to work by preventing farnesylation of progerin, causing the unfarnesylated progerin protein to be degraded (Columbaro et al. 2005). As lonafarnib reduces the abundance of progerin, I would expect the drug to restore vessel contractility as I have shown progerin expression is directly associated with decreased force generation. Treating HGPS primary SMCs with lonafarnib and evaluating traction force would be one way to test this idea and understand the drug's effect.

5.4 Smooth muscle differentiation in HGPS

SMCs can undergo phenotypic switching from contractile to synthetic, ECM producing cells (see Introduction). Intriguingly, the observations I have reported in HGPS SMCS and arteries, such as decreased contractile proteins and increased ECM/arterial stiffening, are very consistent with what the literature has reported from "synthetic", or dedifferentiated, SMCs. I hypothesize that progerin expression is promoting the transition of SMCs to a more synthetic state, whether it be through direct modification of gene expression or through alterations in the microenvironment and signaling pathways (Fig. 5.01).

As a first example, miR-145 is a marker of the contractile cell type, and I have reported reduced miR-145 in HGPS SMCs (Davis-Dusenbery et al. 2011; Cheng et al. 2009; Hutcheson et al. 2013). Secondly, Osteopontin (gene *Spp1*), a key marker of the synthetic SMC population (Shanahan et al. 1993; Wang et al. 2012), is one of the most significantly elevated genes in HGPS arteries as determined by our transcriptome-wide profiling. Lastly, I have observed reduced MRTF-A signaling, a key regulator of the contractile SMC phenotype (Jeon et al. 2008; Du et al. 2004), in HGPS aorta and SMCs. However, it is likely that altered MRTF-A signaling alone is not sufficient to explain all of these observations: although I observed that MRTF-A knockdown produced a decrease in SMC contractile gene expression, knockdown did not affect LOX or miR-145 transcript levels. This suggests other deregulated events in HGPS must also be playing a role in modulating the synthetic gene profile. Aside from intracellular signaling pathways, feedback from the ECM can also promote phenotypic switching of SMCs (Hedin & Thyberg 1987; Yamamoto et al. 1993), so the altered ECM of HGPS arteries may contribute to the increased dedifferentiation phenotype of HGPS SMCs. A careful proteomics study evaluating the composition of the arterial ECM in comparison to the decrease in contractile proteins as the HGPS mouse ages may help to identify ECM proteins responsible for altering SMC phenotypic state. Conversely, the phenotypic state of SMCs can influence secretion of ECM. Thus, the decreased contractility and increased arterial stiffness observed in HGPS may not be entirely independent. However, because of the tight connection between these two phenomena, it may be very hard to tease apart whether dedifferentiation of HGPS SMCs drives ECM remodeling or whether ECM remodeling drives dedifferentiation of HGPS SMCs.

5.5 Similarities and differences between HGPS and normal aging

As there are many described similarities between the cardiovascular pathologies of HGPS and normal aging including increased arterial stiffness, calcification, and atherosclerosis (see introduction; Hamczyk, del Campo, et al. 2018), I postulated that studying the rapid cardiovascular complications in HGPS may provide insight into the mechanism of arterial aging in healthy individuals. Indeed, I observed highly elevated circumferential arterial stiffening in both young HGPS and 24-month WT mouse carotid arteries. However, young HGPS mice did not display significant axial stiffening while 24-month WT mice displayed severe axial stiffening, suggesting that the mechanisms are not the same. However, it is important to note that in late-stage HGPS mice, severe axial stiffening has been reported (Murtada et al. 2020). This implies that in the HGPS model, circumferential stiffness occurs first, followed by axial stiffening at a later timepoint. In contrast, work by Brankovic et al. (2019), which studied mechanics of WT carotid arteries at 2, 6, 12, and 24-months, showed that onset of arterial stiffening occurred simultaneously in both the axial and circumferential directions starting as early as 12-months (Brankovic et al. 2019). They also showed that knockout of matrix metalloproteinase 12 (MMP12), a potent elastase, decreased axial stiffening due to age but had little effect on circumferential mechanics (Brankovic et al. 2019). As collagen deposition and arterial fibrosis are common to both HGPS (Olive et al. 2010; Gerhard-Herman et al. 2011; Merideth et al. 2008) and normally aged arteries (Kohn et al. 2015;

Tsamis et al. 2013), altered elastin degradation dynamics may underlie the differential axial stiffening seen in normal aging and HGPS.

Further evidence that differential mechanisms are driving arterial stiffening and fibrosis in HGPS versus normal aging comes from my work with miR-145, which showed decreased expression in the medial layer of HGPS aortas but not in 24-month WT aortas. Additionally, in normally aged arteries LOX protein was upregulated in both the media and adventitial layers, whereas elevated LOX expression was restricted to the medial layer in HGPS. Nevertheless, the similarity of increased LOX abundance in both premature and normal aging suggests that LOX inhibition may be a potential therapeutic approach to target arterial stiffening in both cases.

Additionally, I reported that decreased contractility in both HGPS and normal mouse aging was associated with less SM-MHC and postulated that the reduced contractility may be due to a more synthetic population of SMCs. Intriguingly, miR-145 has been identified as a marker of the contractile state of SMCs. Although I observed decreased contractility in 24-month WT carotids, I did not observe decreased miR-145 levels. This further supports the hypothesis that although the end readout of decreased arterial contractility may be similar in HGPS and normal aging, the contractile gene profile of the arteries is likely different and the mechanisms underlying the decreased contractility may be diverse.

As a limitation of this dissertation, it is important to note that many arterial comparisons were performed between young (1- or 2-month) HGPS mice and old WT mice (24-month, a timepoint at the end of the WT mouse lifespan). The young HGPS timepoint was chosen so that I could observe the initial driving factors of cardiovascular

pathology. However, when making comparisons between young HGPS arteries and naturally aged arteries, the selected timepoints may not be analogous. For example, the cardiovascular pathology of young 2-month HGPS mice may more so resemble that of 12-month WT mice, while 3-month HGPS mice (a time point more toward the end of HGPS mouse lifespan) may better resemble the 24-month WT mouse. An in-depth study evaluating a progression of arterial aging in both HGPS and WT mice would further shed light on potential comparable timepoints to understand similarities and differences in cardiovascular pathologies.

Overall, although the end read-outs of increased arterial stiffness and decreased contractility may be the same, I believe the mechanisms underlying these processes are inherently different in HGPS and normal aging. In HGPS, arterial aging happens rapidly, and I believe genetic factors are much more prominent in promoting cardiovascular pathologies. In WT aging, cardiovascular pathologies develop over a much more extended period of time, and although genetics certainly have an effect, the extended period of time allows for environmental factors such as diet, physical activity, hormone levels, stress, and inflammation to also play a very powerful role in vascular pathologies. Nevertheless, work presented in this thesis gives new insights into the increased arterial stiffening and decreased arterial contractility in premature and natural aging and sheds light on potential therapeutic approaches to reduce the burden of cardiovascular disease.

5.6 Figures

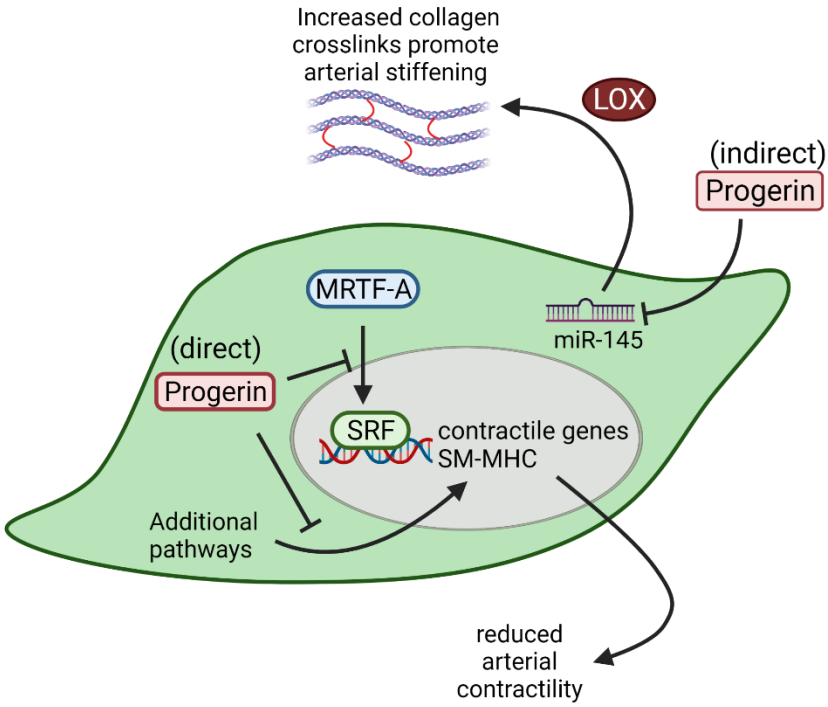

Figure 5.01. Proposed model of progerin's mechanism of action in promoting increased arterial stiffness and decreased arterial contractility in HGPS. In healthy SMCs, progerin inhibits nuclear localization of MRTF-A to reduce contractile gene expression through a direct effect. Additional pathways critical for expression of SM-MHC are also directly inhibited by progerin, contributing to the reduced arterial contractility observed in HGPS arteries. Progerin also indirectly decreases miR-145 levels to cause elevated LOX and promote arterial stiffening.

5.7 References

Bank EM & Gruenbaum Y (2011) The nuclear lamina and heterochromatin: A complex relationship. In *Biochemical Society Transactions*. Biochem Soc Trans, pp.1705–1709.

Barkovskaya A, Buffone A, Žídek M & Weaver VM (2020) Proteoglycans as Mediators of Cancer Tissue Mechanics. *Front. Cell Dev. Biol.* 8, 569377.

Beyret E, Liao HK, Yamamoto M, Hernandez-Benitez R, Fu Y, Erikson G, Reddy P & Izpisua Belmonte JC (2019) Single-dose CRISPR–Cas9 therapy extends lifespan of mice with Hutchinson–Gilford progeria syndrome. *Nat. Med.* 25, 419–422.

Bikkul MU, Clements CS, Godwin LS, Goldberg MW, Kill IR & Bridger JM (2018) Farnesyltransferase inhibitor and rapamycin correct aberrant genome organisation and decrease DNA damage respectively, in hutchinson-gilford progeria syndrome fibroblasts. *Biogerontology* 19, 579–602.

Brankovic S, Hawthorne EA, Yu X, Zhang Y & Assoian RK (2019) MMP12 preferentially attenuates axial stiffening of aging arteries. *J. Biomech. Eng.*.

del Campo L, Sánchez-López A, González-Gómez C, Andrés-Manzano MJ, Dorado B & Andrés V (2020) Vascular Smooth Muscle Cell-Specific Progerin Expression Provokes Contractile Impairment in a Mouse Model of Hutchinson-Gilford Progeria Syndrome that Is Ameliorated by Nitrite Treatment. *Cells* 9, 656.

del Campo L, Sánchez-López A, Salaices M, von Kleeck RA, Expósito E, González-Gómez C, Cussó L, Guzmán-Martínez G, Ruiz-Cabello J, Desco M, Assoian RK, Briones AM & Andrés V (2019) Vascular smooth muscle cell-specific

progerin expression in a mouse model of Hutchinson–Gilford progeria syndrome promotes arterial stiffness: Therapeutic effect of dietary nitrite. *Aging Cell*, e12936.

Chen D, Smith LR, Khandekar G, Patel P, Yu CK, Zhang K, Chen CS, Han L & Wells RG (2020) Distinct effects of different matrix proteoglycans on collagen fibrillogenesis and cell-mediated collagen reorganization. *Sci. Rep.* 10, 1–13.

Cheng Y, Liu X, Yang J, Lin Y, Xu DZ, Lu Q, Deitch EA, Huo Y, Delphin ES & Zhang C (2009) MicroRNA-145, a novel smooth muscle cell phenotypic marker and modulator, controls vascular neointimal lesion formation. *Circ. Res.* 105, 158–166.

Chronopoulos A, Tang A, Beglova E, Trackman PC & Roy S (2010) High glucose increases lysyl oxidase expression and activity in retinal endothelial cells: Mechanism for compromised extracellular matrix barrier function. *Diabetes* 59, 3159–3166.

Columbaro M, Capanni C, Mattioli E, Novelli G, Parnaik VK, Squarzoni S, Maraldi NM & Lattanzi G (2005) Rescue of heterochromatin organization in Hutchinson-Gilford progeria by drug treatment. *Cell. Mol. Life Sci.* 62, 2669–2678.

Dahl KN, Scaffidi P, Islam MF, Yodh AG, Wilson KL & Misteli T (2006) Distinct structural and mechanical properties of the nuclear lamina in Hutchinson-Gilford progeria syndrome. *Proc. Natl. Acad. Sci. U. S. A.* 103, 10271–6.

Davis-Dusenbery BN, Wu C & Hata A (2011) Micromanaging vascular smooth muscle cell differentiation and phenotypic modulation. *Arterioscler. Thromb. Vasc. Biol.* 31, 2370–2377.

Dorado B, Pløen GG, Barettino A, Macías A, Gonzalo P, Andrés-Manzano MJ, González-Gómez C, Galán-Arriola C, Alfonso JM, Lobo M, López-Martín GJ, Molina A, Sánchez-Sánchez R, Gadea J, Sánchez-González J, Liu Y, Callesen H,

Filgueiras-Rama D, Ibáñez B, Sørensen CB & Andrés V (2019) Generation and characterization of a novel knockin minipig model of Hutchinson-Gilford progeria syndrome. *Cell Discov.* 5, 1–15.

Du KL, Chen M, Li J, Lepore JJ, Mericko P & Parmacek MS (2004) Megakaryoblastic Leukemia Factor-1 Transduces Cytoskeletal Signals and Induces Smooth Muscle Cell Differentiation from Undifferentiated Embryonic Stem Cells. *J. Biol. Chem.* 279, 17578–17586.

Fang Y, Chang HM, Cheng JC, Klausen C, Leung PCK & Yang X (2016) Transforming growth factor-β1 increases lysyl oxidase expression by downregulating MIR29A in human granulose lutein cells. *Reproduction* 152, 205–213.

Gabriel D, Shafry DD, Gordon LB & Djabali K (2017) Intermittent treatment with farnesyltransferase inhibitor and sulforaphane improves cellular homeostasis in Hutchinson- Gilford progeria fibroblasts. *Oncotarget* 8, 64809–64826.

Gerhard-Herman M, Smoot LB, Wake N, Kieran MW, Kleinman ME, Miller DT, Schwartzman A, Giobbie-Hurder A, Neuberg D & Gordon LB (2011) Mechanisms of Premature Vascular Aging in Children With Hutchinson-Gilford Progeria Syndrome. *Hypertension* 59.

Getz GS & Reardon CA (2012) Animal models of Atherosclerosis. *Arterioscler. Thromb. Vasc. Biol.* 32, 1104–1115.

Goldin A, Beckman JA, Schmidt AM & Creager MA (2006) Advanced glycation end products: Sparking the development of diabetic vascular injury. *Circulation* 114, 597–605.

Goldschmidt ME, McLeod KJ & Taylor WR (2001) Integrin-mediated mechanotransduction in vascular smooth muscle cells: Frequency and force

response characteristics. *Circ. Res.* 88, 674–680.

Gordon LB, Harten IA, Patti ME & Lichtenstein AH (2005) Reduced adiponectin and HDL cholesterol without elevated C-reactive protein: Clues to the biology of premature atherosclerosis in Hutchinson-Gilford Progeria Syndrome. *J. Pediatr.* 146, 336–341.

Gordon LB, Shappell H, Massaro J, D'Agostino RB, Brazier J, Campbell SE, Kleinman ME & Kieran MW (2018) Association of Lonafarnib Treatment vs No Treatment With Mortality Rate in Patients With Hutchinson-Gilford Progeria Syndrome. *JAMA* 319, 1687.

Green RS, Lieb ME, Weintraub AS, Gacheru SN, Rosenfield CL, Shah S, Kagan HM & Taubman MB (1995) Identification of lysyl oxidase and other platelet-derived growth factor- inducible genes in vascular smooth muscle cells by differential screening. *Lab. Investig.* 73, 476–482.

Hamczyk M, del Campo L & Andrés V (2018) Aging in the Cardiovascular System: Lessons from Hutchinson-Gilford Progeria Syndrome. *Annu. Rev. Physiol.* 80, 27–48.

Hamczyk MR, Villa-Bellosta R, Gonzalo P, Andrés-Manzano MJ, Nogales P, Bentzon JF, López-Otín C & Andrés V (2018) Vascular Smooth Muscle-Specific Progerin Expression Accelerates Atherosclerosis and Death in a Mouse Model of Hutchinson-Gilford Progeria Syndrome. *Circulation*, CIRCULATIONAHA.117.030856.

Hedin U & Thyberg J (1987) Plasma fibronectin promotes modulation of arterial smooth-muscle cells from contractile to synthetic phenotype. *Differentiation* 33, 239–246.

How J, Liu Y, Lombardi Story J, Neuberg DS, Ravid K, Jarolimek W, Charlton B & Hobbs GS (2020) Evaluation of a Pan-Lysyl Oxidase Inhibitor, Pxs-5505, in

Myelofibrosis: A Phase I, Randomized, Placebo Controlled Double Blind Study in Healthy Adults. *Blood* 136, 16–16.

Hutcheson R, Terry R, Chaplin J, Smith E, Musiyenko A, Russell JC, Lincoln T & Rocic P (2013) MicroRNA-145 restores contractile vascular smooth muscle phenotype and coronary collateral growth in the metabolic syndrome. *Arterioscler. Thromb. Vasc. Biol.* 33, 727–736.

Jeon ES, Park WS, Lee MJ, Kim YM, Han J & Kim JH (2008) A rho kinase/myocardin-related transcription factor-a-dependent mechanism underlies the sphingosylphosphorylcholine-induced differentiation of mesenchymal stem cells into contractile smooth muscle cells. *Circ. Res.* 103, 635–642.

Kim PH, Luu J, Heizer P, Tu Y, Weston TA, Chen N, Lim C, Li RL, Lin P-Y, Dunn JCY, Hodzic D, Young SG & Fong LG (2018) Disrupting the LINC complex in smooth muscle cells reduces aortic disease in a mouse model of Hutchinson-Gilford progeria syndrome. *Sci. Transl. Med.* 10, eaat7163.

Koblan LW, Erdos MR, Wilson C, Cabral WA, Levy JM, Xiong ZM, Tavarez UL, Davison LM, Gete YG, Mao X, Newby GA, Doherty SP, Narisu N, Sheng Q, Krilow C, Lin CY, Gordon LB, Cao K, Collins FS, Brown JD & Liu DR (2021) In vivo base editing rescues Hutchinson–Gilford progeria syndrome in mice. *Nature* 589, 608–614.

Köhler F, Bormann F, Raddatz G, Gutekunst J, Corless S, Musch T, Lonsdorf AS, Erhardt S, Lyko F & Rodríguez-Paredes M (2020) Epigenetic deregulation of lamina-associated domains in Hutchinson-Gilford progeria syndrome. *Genome Med.* 12, 46.

Kohn JC, Lampi MC & Reinhart-King CA (2015) Age-related vascular stiffening: causes and consequences. *Front. Genet.* 06, 112.

Kothapalli D, Liu S-L, Bae YH, Monslow J, Xu T, Hawthorne EA, Byfield FJ, Castagnino P, Rao S, Rader DJ, Puré E, Phillips MC, Lund-Katz S, Janmey PA & Assoian RK (2012) Cardiovascular Protection by ApoE and ApoE-HDL Linked to Suppression of ECM Gene Expression and Arterial Stiffening. *Cell Rep.* 2, 1259–1271.

Kreienkamp R, Billon C, Bedia-Diaz G, Albert CJ, Toth Z, Butler AA, McBride-Gagyi S, Ford DA, Baldan A, Burris TP & Gonzalo S (2019) Doubled lifespan and patient-like pathologies in progeria mice fed high-fat diet. *Aging Cell* 18.

De La Rosa J, Freije JMP, Cabanillas R, Osorio FG, Fraga MF, Fernández-García MS, Rad R, Fanjul V, Ugalde AP, Liang Q, Prosser HM, Bradley A, Cadiñanos J & López-Otín C (2013) Prelamin A causes progeria through cell-extrinsic mechanisms and prevents cancer invasion. *Nat. Commun.* 4, 1–9.

Lacolley P, Challande P, Osborne-Pellegrin M & Regnault V (2009) Genetics and pathophysiology of arterial stiffness. *Cardiovasc. Res.* 81, 637–648.

Laurent S, Boutouyrie P, Cunha PG, Lacolley P & Nilsson PM (2019) Concept of Extremes in Vascular Aging. *Hypertension* 74, 218–228.

Laurent S, Boutouyrie P & Lacolley P (2005) Structural and genetic bases of arterial stiffness. *Hypertension* 45, 1050–1055.

Liu S lin, Bajpai A, Hawthorne EA, Bae Y, Castagnino P, Monslow J, Puré E, Spiller KL & Assoian RK (2019) Cardiovascular protection in females linked to estrogen-dependent inhibition of arterial stiffening and macrophage MMP12. *JCI Insight* 4.

Logan JG, Engler MB & Kim H (2015) Genetic Determinants of Arterial Stiffness. *Adv. Data Anal. Classif.* 9, 23–43.

Madsen CS, Hershey JC, Hautmann MB, White SL & Owens GK (1997) Expression of the smooth muscle myosin heavy chain gene is regulated by a negative-acting GC-

rich element located between two positive-acting serum response factor-binding elements. *J. Biol. Chem.* 272, 6332–40.

Manabe I & Owens GK (2001) CArG elements control smooth muscle subtype-specific expression of smooth muscle myosin in vivo. *J. Clin. Invest.* 107, 823–834.

Merideth MA, Gordon LB, Clauss S, Sachdev V, Smith ACM, Perry MB, Brewer CC, Zalewski C, Kim HJ, Solomon B, Brooks BP, Gerber LH, Turner ML, Domingo DL, Hart TC, Graf J, Reynolds JC, Gropman A, Yanovski JA, Gerhard-Herman M, Collins FS, Nabel EG, Cannon RO, Gahl WA & Introne WJ (2008) Phenotype and Course of Hutchinson–Gilford Progeria Syndrome. *N. Engl. J. Med.* 358, 592–604.

Mitchell GF, Hwang SJ, Vasan RS, Larson MG, Pencina MJ, Hamburg NM, Vita JA, Levy D & Benjamin EJ (2010) Arterial stiffness and cardiovascular events: the Framingham Heart Study. *Circulation* 121, 505–511.

Murtada S-I, Kawamura Y, Caulk AW, Ahmadzadeh H, Mikush N, Zimmerman K, Kavanagh D, Weiss D, Latorre M, Zhuang ZW, Shadel GS, Braddock DT & Humphrey JD (2020) Paradoxical aortic stiffening and subsequent cardiac dysfunction in Hutchinson–Gilford progeria syndrome. *J. R. Soc. Interface* 17, 20200066.

Oh YJ, Pau VC, Steppan J, Sikka G, Bead VR, Nyhan D, Levine BD, Berkowitz DE & Santhanam L (2017) Role of tissue transglutaminase in age-associated ventricular stiffness. *Amino Acids* 49, 695–704.

Olive M, Harten I, Mitchell R, Beers JK, Djabali K, Cao K, Erdos MR, Blair C, Funke B, Smoot L, Gerhard-Herman M, Machan JT, Kutys R, Virmani R, Collins FS, Wight TN, Nabel EG & Gordon LB (2010) Cardiovascular Pathology in Hutchinson-Gilford Progeria: Correlation With the Vascular Pathology of Aging. *Arterioscler. Thromb.*

Vasc. Biol. 30.

Qiu H, Depre C, Ghosh K, Resuello RG, Natividad FF, Rossi F, Peppas A, Shen YT, Vatner DE & Vatner SF (2007) Mechanism of gender-specific differences in aortic stiffness with aging in nonhuman primates. *Circulation* 116, 669–676.

Qiu H, Zhu Y, Sun Z, Trzeciakowski JP, Gansner M, Depre C, Resuello RRG, Natividad FF, Hunter WC, Genin GM, Elson EL, Vatner DE, Meininger GA & Vatner SF (2010) Short communication: Vascular smooth muscle cell stiffness as a mechanism for increased aortic stiffness with aging. *Circ. Res.* 107, 615–619.

Ren W, Liu Y, Wang X, Jia L, Piao C, Lan F & Du J (2016) β-Aminopropionitrile monofumarate induces thoracic aortic dissection in C57BL/6 mice. *Sci. Rep.* 6.

Reusch HP, Chan G, Ives HE & Nemenoff RA (1997) Activation of JNK/SAPK and ERK by mechanical strain in vascular smooth muscle cells depends on extracellular matrix composition. *Biochem. Biophys. Res. Commun.* 237, 239–244.

Reusch P, Wagdy H, Reusch R, Wilson E & Ives HE (1996) Mechanical strain increases smooth muscle and decreases nonmuscle myosin expression in rat vascular smooth muscle cells. *Circ. Res.* 79, 1046–1053.

Santiago-Fernández O, Osorio FG, Quesada V, Rodríguez F, Basso S, Maeso D, Rolas L, Barkaway A, Nourshargh S, Folgueras AR, Freije JMP & López-Otín C (2019) Development of a CRISPR/Cas9-based therapy for Hutchinson–Gilford progeria syndrome. *Nat. Med.* 25, 423–426.

Sehgel NL, Vatner SF & Meininger GA (2015) "Smooth Muscle Cell Stiffness Syndrome"-Revisiting the Structural Basis of Arterial Stiffness. *Front. Physiol.* 6, 335.

Shanahan CM, Weissberg PL & Metcalfe JC (1993) Isolation of gene markers of

differentiated and proliferating vascular smooth muscle cells. *Circ. Res.* 73, 193–204.

Shevelyov YY & Ulianov S V. (2019) The Nuclear Lamina as an Organizer of Chromosome Architecture. *Cells* 8, 136.

van Steensel B & Belmont AS (2017) Lamina-Associated Domains: Links with Chromosome Architecture, Heterochromatin, and Gene Repression. *Cell* 169, 780–791.

Steppan J, Bergman Y, Viegas K, Armstrong D, Tan S, Wang H, Melucci S, Hori D, Park SY, Barreto SF, Isak A, Jandu S, Flavahan N, Butlin M, An SS, Avolio A, Berkowitz DE, Halushka MK & Santhanam L (2017) Tissue transglutaminase modulates vascular stiffness and function through crosslinking-dependent and crosslinking-independent functions. *J. Am. Heart Assoc.* 6.

Swift J, Ivanovska IL, Buxboim A, Harada T, Dingal PCDP, Pinter J, Pajerowski JD, Spinler KR, Shin J-W, Tewari M, Rehfeldt F, Speicher DW & Discher DE (2013) Nuclear Lamin-A Scales with Tissue Stiffness and Enhances Matrix-Directed Differentiation. *Science (80-.).* 341, 1240104–1240104.

Szamosi T, Szollár J, Meggyesi V, Wilhelm O, Bodánszky H & Mátyus J (1984) Serum cholesterol and triglyceride levels in progeria as a model of ageing. *Mech. Ageing Dev.* 28, 243–248.

Tsamis A, Krawiec JT & Vorp DA (2013) Elastin and collagen fibre microstructure of the human aorta in ageing and disease: a review. *J. R. Soc. Interface* 10, 20121004.

Verstraeten VLRM, Ji JY, Cummings KS, Lee RT & Lammerding J (2008) Increased mechanosensitivity and nuclear stiffness in Hutchinson–Gilford progeria cells: effects of farnesyltransferase inhibitors. *Aging Cell* 7, 383–393.

Voelker R (2021) First Progeria Drug Is Approved. *JAMA* 325, 20.

Wang F, Zhang W, Yang Q, Kang Y, Fan Y, Wei J, Liu Z, Dai S, Li H, Li Z, Xu L, Chu C, Qu J, Si C, Ji W, Liu GH, Long C & Niu Y (2020) Generation of a Hutchinson–Gilford progeria syndrome monkey model by base editing. *Protein Cell* 11, 809–824.

Wang L, Zhang J, Fu W, Guo D, Jiang J & Wang Y (2012) Association of smooth muscle cell phenotypes with extracellular matrix disorders in thoracic aortic dissection. *J. Vasc. Surg.* 56, 1698-1709.e1.

Yamamoto M, Yamamoto K & Noumura T (1993) Type I collagen promotes modulation of cultured rabbit arterial smooth muscle cells from a contractile to a synthetic phenotype. *Exp. Cell Res.* 204, 121–129.